INFORMATION TO USERS

This manuscript has been reproduced from the microfilm master. UMI films the text directly from the original or copy submitted. Thus, some thesis and dissertation copies are in typewriter face, while others may be from any type of computer printer.

The quality of this reproduction is dependent upon the quality of the copy submitted. Broken or indistinct print, colored or poor quality illustrations and photographs, print bleedthrough, substandard margins, and improper alignment can adversely affect reproduction.

In the unlikely event that the author did not send UMI a complete manuscript and there are missing pages, these will be noted. Also, if unauthorized copyright material had to be removed, a note will indicate the deletion.

Oversize materials (e.g., maps, drawings, charts) are reproduced by sectioning the original, beginning at the upper left-hand corner and continuing from left to right in equal sections with small overlaps.

ProQuest Information and Learning
300 North Zeeb Road, Ann Arbor, MI 48106-1346 USA
800-521-0600

CLASSICAL AND QUANTUM CHAOS: STRONGLY INTERACTING PARTICLES IN A CONFINED GEOMETRY.

by

Pavel S. Ivanushkin

A dissertation submitted to the Graduate Faculty in Physics in partial fulfillment of the requirements for the degree of Doctor of Philosophy, The City University of New York.

2003

UMI Number: 3103120

ProQuest Information and Learning Company
300 North Zeeb Road
P.O. Box 1346
Ann Arbor, MI 48106-1346

This manuscript has been read an accepted for the graduate Faculty in Physics in satisfaction of the dissertation requirements for the degree of Doctor of Philosophy.

SEPT. 15, 2003	
Date	Chair of Examining Committee
SEPT. 16, 2003	
Date	Executive Officer

Supervisory Commitee:

Bala Sundaram, Dissertation Supervisor

Mark Hillery

Anatoly Kuklov

Andrew Poje

William Screiber

THE CITY UNIVERSITY OF NEW YORK

Abstract

CLASSICAL AND QUANTUM CHAOS: STRONGLY INTERACTING PARTICLES IN A CONFINED GEOMETRY.

by

Pavel S. Ivanushkin

Dissertation Supervisor: Professor Bala Sundaram.

This dissertation details the classical and quantum dynamics of two mechanical systems. The first one represents a charged particle confined inside a square elastic boundary acted on by a uniform magnetic field - the Square Magnetic Billiard. The second system, called the Circular Coulomb Billiard, consists of two particles, interacting by virtue of the Coulomb potential, and enclosed inside a circular boundary. One of the particles is considered to be massive and remains stationary.

The first two chapters give a brief history of classical and quantum chaos, and review the major theoretical concepts. The third chapter analyzes the classical dynamics of the Square Magnetic Billiard. A number of approaches were used for numerical experiments:

which shows that the system's classical behavior ranges from completely integrable to fully chaotic, but then the system restores it's integrability as the magnetic field continues to grow.

The fourth chapter examines the Square Magnetic Billiard quantum mechanically. The eigenvalues for intermediate strengths of the magnetic field exhibit a great deal of an inter-level repulsion and the eigenfunctions demonstrate quantum scars. As the classical analogue restores its integrability, the quantum spectrum tends to Landau levels. The time evolution of the system also displays chaotic features for intermediate strength of the magnetic field. A model of a quantum dot based on the Square Magnetic Billiard show resonant character in the dependence of the transition.

The last two chapters focus on the Circular Coulomb billiard. The classical dynamics display a transition from integrability to a mixed phase space as a measure of asymmetry grows. A second parameter, the strength of interaction, suppresses chaos for small degrees of asymmetry and intensifies it for higher values. The quantum energy eigenvalues show strong correlation and eigenfunctions display quantum scars for a range of parameters corresponding to chaotic classical analogue. However, some uncorrelated levels persist in the spectrum, which can be attributed to the mixed phase space of the classical dynamics. A model of a quantum dot based on the Circular Coulomb Billiard displays an extremely sharp decay of a transport in a symmetric case.

Acknowledgments

No type of research endeavor is possible without collaboration with other people, and the work presented in this dissertation is certainly no exception. During the years at CUNY I had the great pleasure of working with a number of knowledgeable and enthusiastic people that I would like to acknowledge here.

First of all, I would like to thank my adviser, Bala Sundaram. His remarkable intuition, and outstanding talent in the creation of intriguing ideas is what formed the conceptual basis of this dissertation. Bala also provided all the necessary material support which made this research possible. His exceptional patience and genuine concern about people around him is what made my research work under his guidance a truly pleasant and creative endeavor.

I am very thankful to William Schreiber, who provided a helping hand from my first months of graduate study. His genuine kindness and exceptional intelligence is what earned him respect among all the graduate students, for whom he always made time to give advice when it is necessary. He never refused to offer a helping hand. I also attended Billy's lectures in classical mechanics during my graduate studies. I really enjoyed being his student and acquired a big deal of my knowledge of classical mechanics from him, which provided an essential part of this dissertation.

I also gained an inestimable amount of knowledge from my interactions with Anatoly Kuklov. Besides working with him on an intriguing Bose condensate problem, I had the pleasure of attending Anatoly's lectures in statistical mechanics during my graduate coursework. His outstanding feeling for the subject matter and enthusiasm is what

instantly sparks an interest in scientific problems he proposes to work on.

I also enjoyed interacting with Andrew Poje. He is a very nice person to communicate with in addition to being a knowledgeable scientist. I remember being impressed by his striking presentation in hydrodynamics, which taught me a lot on how the results of numerical experiments should be presented. Andrew has also been a great resource in numerical methods of solution of differential equations.

Special thanks to Lewis Carbonaro, a technical coordinator in the Mathematics department. The numerical data represented in this dissertation was acquired as a result of exploiting numerous computers that were made available due to his kind cooperation. Besides this he is person with a very good sense of humor and it was an overwhelming pleasure to communicate with him.

I would like to thank Benjamin Greenbaum for his kind help during the work on this dissertation. I particularly enjoyed my collaboration with him on some numerical experiments in chaotic dynamics.

Of course, I could not have come this far without a good start in physics, and the Moscow Institute of Physics and Technology is undoubtedly the best place that can provide this start. I will never forget the years I spent studying there, and my fellow students with whom I entered the beautiful path of physics.

I am especially grateful to Fedor Fedorovich Kamenez, a wonderful teacher who put me on this miraculous path of physics and taught me how to take my first steps in it. He led me along this path during my undergraduate and graduate years, and all of I have achieved and, perhaps, will achieve in the future is first of all due to him.

I want to express my thanks to Michail Michailovich Elyashevich, my adviser during my graduate studies in Moscow Institute of Physics and Technology. I learned a lot working with him on intriguing numerical experiments created due to his exceptional sense of interesting physical problems. I truly enjoyed working with him and greatly benefited from the years under his guidance.

The last 'thank you' in the list, which is the first one in my heart, is to my dear wife

Tatyana Ivanushkina. Her outstanding patience, her priceless help is what, first of all, made me capable of developing and completing the work in this dissertation.

Contents

Chapter 1

A Brief history: Classical Chaos.

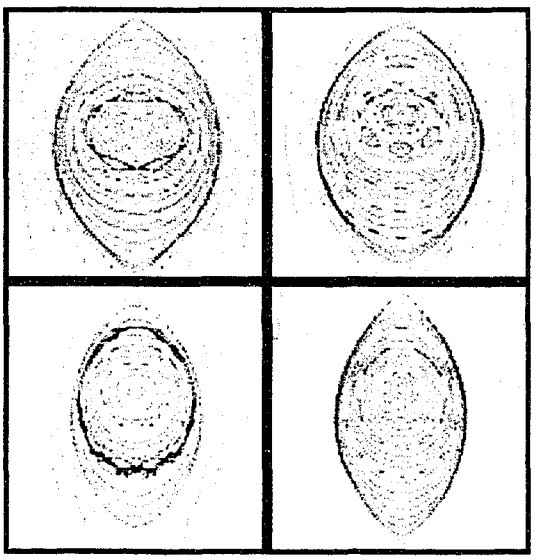

1.1 Deterministic system.

The study of chaos in dynamical systems was started relatively recently, during the middle of the 19th century. Before that Newtonian mechanics, based on a completely deterministic approach, had been the only guideline for physicists. The following excerpt from [20] gives an excellent explanation of *determinism*:

'**Determinism** is the philosophical belief that every event or action is

the inevitable result of preceding events and actions. Thus, in principle at least, every event or action can be completely predicted in advance, or in retrospect.'

Thus, according to the deterministic approach the time evolution of nature is like the operation of a perfect machine. The future of the universe is considered as being completely predetermined by the present, while the present is an inevitable result of the past.

As a philosophical belief about the material world, determinism can be traced to the time of Ancient Greece, several thousand years ago. However, it was at the time of Isaac Newton, about 300 years ago, when determinism was established as the basis of science. Newton discovered three laws of motion that he believed could predict the motion of any mechanical system based only upon an accurate measurement of its state at the current moment of time. Newton's three laws were extremely successful for several centuries after his discovery. Scientists believed in completely deterministic evolution of the universe even though they came across numerous problems that they failed to resolve based on the deterministic approach. Perhaps the most famous among them is the motion of the Moon around the Earth. The following quotation of Baron Gottfried Wilhelm Leibniz demonstrates how confident the scientists of the 18th century were in the ideas of determinism:

'That everything is brought forth through an established destiny is just as certain as that three times three is nine. If, for example, one sphere meets another sphere in free space and if their sizes and their paths and directions before collision are known, we can then foretell and calculate how they will rebound and what course they will take after the impact. Very simple laws are followed which also apply, no matter how many spheres are taken or whether objects are taken other than spheres. From this one sees then that everything proceeds mathematically that is, infallibly in the whole wide

world, so that if someone could have a sufficient insight into the inner parts of things, and in addition had remembrance and intelligence enough to consider all the circumstances and to take them into account, he would be a prophet and would see the future in the present as in a mirror.'

The formalism of classical mechanics was dramatically changed after Isaac Newton's time. Euler and Lagrange developed the methods that we are now using. A large number of complicated mechanical problems were successively solved. However, despite the efforts of physicists and mathematicians around the world, there were some problems that they were not able to resolve using the deterministic approach. Examples of such 'unsolvable problems' are *the three-body problem* and *the ergodic hypothesis.*

1.1.1 The three-body problem.

People have been trying to predict the motion of the Moon since antiquity. An accurate description of its motion was extremely important to determine the longitude of ships while traversing open seas. This motion is quite complicated as the orbit of the Moon cannot be approximated by an ellipse with the Earth as its focus: such an approximation would completely disregard the influence of the Sun on the motion of the Moon, which would lead to an extremely rough model. Therefore, at least three celestial bodies have to be taken into consideration and thus the three-body problem emerges.

The three-body problem also models another important concern in astronomy. According to Newtonian mechanics it is possible for one of planets in the solar system to leave its elliptical orbit around the Sun. This can happen because of a gravitational pull toward another planet in the vicinity. Being displaced from its stable elliptical orbit the planet can undergo a collision with the Sun or another planet. Knowing if any of the planets would do so became the problem of the stability of the solar system. Nothing like this would have been possible if the solar system consisted of just two celestial bodies, but whether it could happen in the three-body case remained unclear.

The question of the stability of the solar system was posed by Weierstrass in a mathematical competition. Poincaré's submission won the prize. He showed that conserved quantities that were analytic in the momenta and positions could not exist for the three-body problem. Then integration would seem unlikely from Poincaré's point of view due to the problem of small denominators. However the integration was accomplished by the Swedish mathematician Sundman. He showed that it is possible to integrate the three-body problem if one only takes into consideration two-body collisions. This way of attempting to prove the stability of the solar system resulted only in increasing doubts about the presence of such a stability.

For a long period of time, up to the second part of 20th century, scientists were uncertain about the stability of all planetary trajectories orbiting the Sun. The Kolmogorov-Arnold-Moser theorem gives us the proper tool to deal with non integrable systems. It was applied to examine the solar system and finally was proved that the later was a stable dynamical system. Discussion of this theorem is presented later in the chapter.

1.1.2 The ergodic hypothesis.

The second problem that played a key role in the development of chaotic dynamics was the ergodic hypothesis of Boltzmann. Maxwell and Boltzmann had combined the deterministic mechanics of Newton with statistical laws in order to create statistical mechanics. In this way, they derived thermodynamics based on Hamiltonian mechanics. To obtain results consistent with experimentally observed properties of macroscopic systems, Boltzmann had to make the great simplifying assumption of ergodicity: that the dynamical system would visit every part of the phase space allowed by conservation laws equally often.

This assumption of ergodicity seems to contradict the character of time evolution in Hamiltonian systems. The propagation in time of any system that obeys Hamiltonian equations is described in terms of an evolution operator $\hat{T}(t)$. Acting on an arbitrary point in 2N-dimensional phase space $(\vec{p}(0), \vec{q}(0))$ it propagates it to a new

point $(\vec{p}(t), \vec{q}(t))$:

$$(\vec{p}(t), \vec{q}(t)) = \hat{T}(t)(\vec{p}(0), \vec{q}(0)).$$

If one choses arbitrary a 2N-dimensional volume of initial conditions $V(0)$ then the evolution operator will propagate it in time to a new volume

$$V(t) = \hat{T}V(0).$$

Liouville's theorem (see [94]) states that for all Hamiltonian systems the time evolution operator preserves the volume: $|V(t)| = |V(0)|$. This means that at all future times a ball of initial conditions will be confined inside a ball of the same 2N-dimensional volume. This statement causes an apparent contradiction with the ergodic hypothesis - which claims that during its evolution a system visits with equal probability all the states that are not forbidden by energy conservation. Hence an arbitrary small volume of initial conditions must be spread through all the available 2N-dimensional dynamical phase space.

A proof of the ergodic hypothesis faces extensive mathematical difficulties. Up to now it was only shown to be true for just a few dynamical systems and appeared to be wrong for others.

The following example from reference [94] outlines qualitatively the character of dynamics for an ergodic Hamiltonian system. **Figure 1.1** demonstrates the character of the time evolution of the same ball of initial conditions under different types of Hamiltonians. Evolution of the first ball corresponds to the deterministic case (a) while the second ball is propagated by the Hamiltonian of an ergodic dynamical system (b). We see that the initial phase volume is conserved on both occasions, however for the ergodic evolution the topology of the shape becomes dramatically changed. This means that instead of computing an exact phase volume of this shape we have to consider its

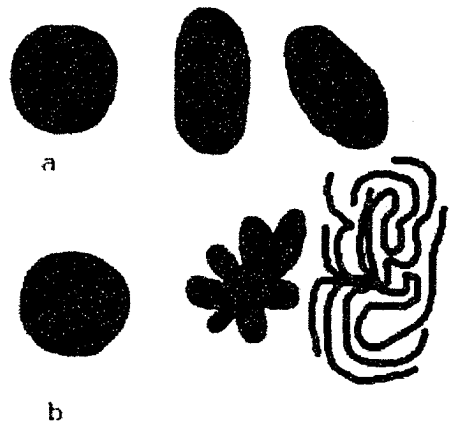

Figure 1.1: Sketch of the time evolution of a small ball of initial conditions for a deterministic (a) and an ergodic (b) Hamiltonian system. Initial volume is preserved, but the resultant shape in the case of the ergodic evolution is such that, for its proper description, we have to consider its envelope and compute an effective volume confined inside that envelope. This effective volume is growing with time, eventually spreading throughout the entire phase space.

envelope and determine an effective volume - the one bounded by the envelope. This way, while the Liouville's theorem for Hamiltonian systems still holds, the effective phase volume visited by the ergodic system is growing and eventually the system visits equally often all the available points in the phase space in agreement with the Boltzmann's ergodic hypothesis.

1.2 Dependence upon measurements of the initial state. Dynamical instability.

A basic principle of experimental science is that no real measurement is infinitely precise, but instead every measurement is obtained with some uncertainty. This is a consequence of the fact that all measuring devices - even perfectly designed ones - can only record results of their measurement within a finite amount of significant figures. Hence, even if one imagines that a perfect measuring device exists - the rounding error in its reading

would produce an uncertainty. Therefore, while progress in developing more accurate devices can reduce experimental error, nevertheless, even theoretically, error can never be completely eliminated.

In dynamics, the presence of uncertainty in the results of measurements means that the initial conditions of all real dynamical systems are obtained with a certain amount of error. As the dynamical system is developing in time, the presence of uncertainty in the initial conditions results in an erroneous prediction of the state of the system at all the future moments of times. It is important to notice that the final uncertainty arises not from any randomness contained in the Hamiltonian equations - these are completely deterministic. The uncertainty in the measurement of the initial conditions is what produces an inevitable error in prediction of the future state of the dynamical system. Newtonian mechanics implies that the final uncertainty can always be reduced to any desired value by measuring the initial conditions with greater accuracy. In other words, by putting more precise information into Newton's laws, it was believed that it is always possible to obtain more precise output for any later time.

Poincaré was first to notice that in some astronomical dynamical systems, shrinking the initial conditions does not always lead to the shrinking of errors in the final prediction in a corresponding way. He was working on mathematical equations to describe the motion of planets around the Sun. These equations resulted from applications of Newton's laws, and therefore were completely deterministic. However, Poincaré found that a large number of such systems do not obey the rule that shrinking the error in initial conditions leads to a corresponding shrinking of error in their outcomes. Moreover, he observed that for a great number of dynamical equations, a very tiny imprecision in the initial conditions would grow in time at an enormous rate. Thus two nearly-indistinguishable sets of initial conditions for the same dynamical system would result in completely different sets of trajectories in the future. Poincaré observed such enormous sensitivity to uncertainty in initial conditions for dynamical systems consisting of three or more interacting astronomical objects. He called this kind of behavior **dynam-**

ical instability or simply **chaos**. Poincaré demonstrated that for systems that exhibit dynamical instability any imprecision in measurement of initial conditions, no matter how small, results in such uncertainty in the deterministic prediction of the future that it is as if the prediction was made by random chance.

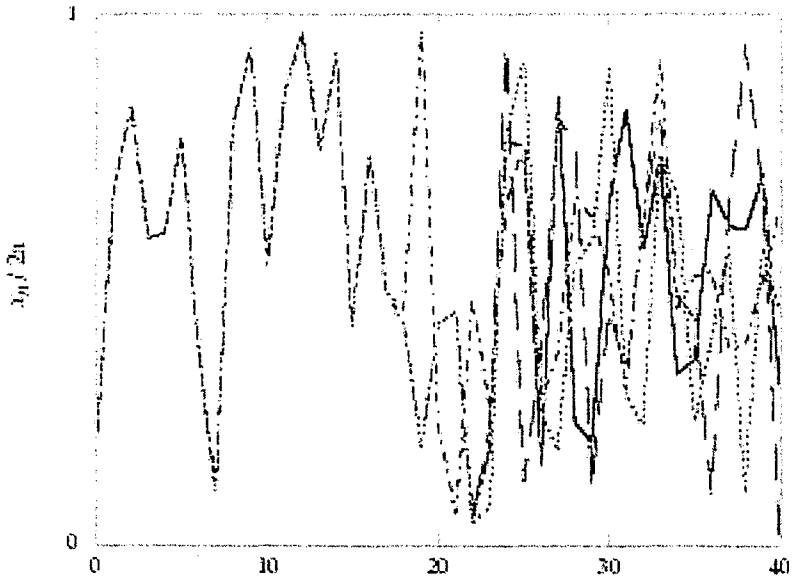

Figure 1.2: Numerical iteration of the standard map, illustrating the inherently unpredictable nature of chaotic systems. The same FORTRAN77 code was executed on four modern computers to iterate the standard map for $K = 10$ and the initial condition $(x_0, p_0) = (1, 1)$. The spatial coordinate x_n (taken modulo 2) is plotted for the first 40 iterations of the standard map. Although nominally the same (64-bit, or around 15-digit) double precision numerical representation was used on the different computers, slight differences in the numerical rounding methods among the processors are rapidly amplified as the iterations progress. *(The picture was taken from the reference [84]).*

Below is represented one more remarkable demonstration of dynamical instability described in reference [84]. Consider the "standard map", defined by the pair of iteration equations

$$p_{n+1} = p_n + K \sin x_n$$

$$x_{n+1} = x_n + p_{n+1}.$$

This system was shown to be chaotic for sufficiently large values of parameter K. These equations are, of course, deterministic, in the sense that there is no random element presented. Despite the apparent simplicity of this map, it gives rise to quite complicated dynamics. The lack of predictability in this map is illustrated in **Figure (1.2)**, which represents the results of iteration of the standard map with the same initial condition on four different computers. The important thing is that even though the results should be identical among the four computers, they only agree for around 16 iterations. After this point the trajectories diverge, and any prediction becomes completely meaningless.

Such an extreme sensitivity to initial conditions was also called the **"Butterfly Effect"** (see [52]). The name is due to a fact that such extreme unpredictability of this kind of systems gives rise to the idea of a butterfly flapping it's wings in one area of the world causing a tornado or similar disastrous weather in another remote area of the world.

Systems that exhibit the "Butterfly Effect" are called chaotic or stochastic systems. Thus an extreme sensitivity to initial conditions is one of major manifestations of chaotic dynamics. The following excerpt from [20] briefly summarizes our introductory discussion of chaotic and deterministic systems and gives a short definition of chaotic (stochastic) dynamical systems:

> *'A deterministic system is a system whose present state is fully determined by its initial conditions, in contra-distinction to a stochastic system, for which the initial conditions determine the present state only partially, due to noise, or other external circumstances beyond our control. For a stochastic system, the present state reflects the past initial conditions plus the particular realization of the noise generated.'*

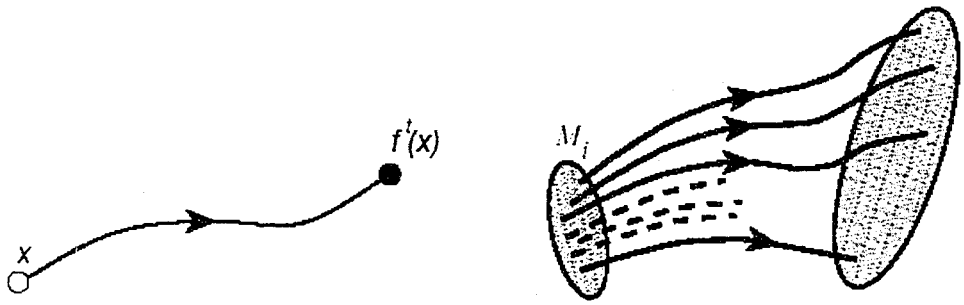

Figure 1.3: An evolution of dynamical system can be represented as the *dynamical flow* in 2N-dimensional dynamical phase space analogous to the flow of a fluid.

1.3 Dynamical Phase Space. Poincaré Sections.

To deal with dynamical problems in classical as well as in quantum mechanics it is extremely useful to introduce the phase space of a system. This is because in order to give complete information about a Hamiltonian system one has to specify all of its coordinates and momenta. Thus, the complete description of the state of a Hamiltonian system with N degrees of freedom can be represented by a set of all its coordinates and momenta which yields a point in 2N-dimensional phase space, $X(\vec{q},\vec{p})$. As the system is evolving in time the point representing it travels along some curve in the dynamical phase space

$$X(\vec{q},\vec{p},t) = \hat{T}X(\vec{q},\vec{p},0).$$

Simultaneous time evolution of an ensemble of initial conditions produces *dynamical flow* in the 2N-dimensional phase space **(Figure 1.3)**.

The introduction of phase space is a powerful step from a mathematical point of view, but it complicates a diagrammatic representation of the dynamics. Let us take as an example a dynamical system with three degrees of freedom. The dynamical phase of such a system is 6-dimensional. Humans are not able to visualize 6 dimensions. Hence, to facilitate a reading of all the relevant information about the system we need

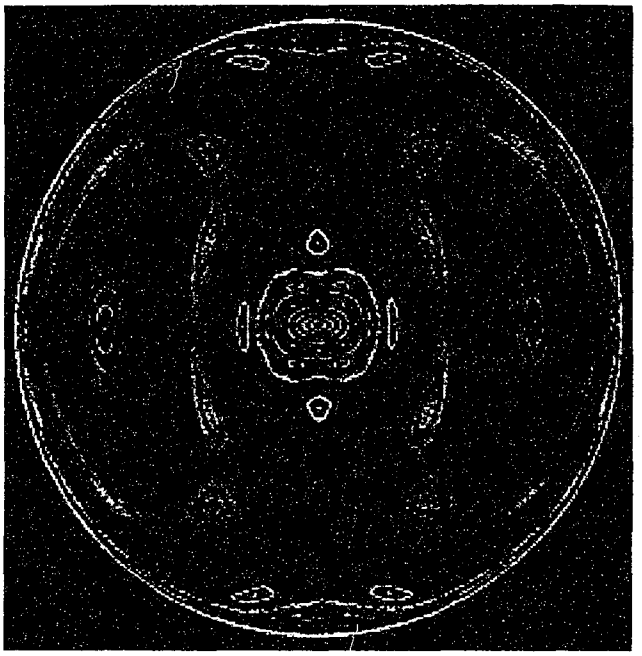

Figure 1.4: Poincaré section of an electron in a hydrogen atom in a strong magnetic field. The picture demonstrates a mixed phase space - coexistence of regular and chaotic motion *(The picture was taken from the reference [33]).*

to develop procedures that reduce the dimensionality of its phase portrait to three or, even better, two dimensions.

One example of how this reduction works is described in reference [33]. The authors examine the behavior of a hydrogen atom in a strong magnetic field. The hydrogen atom is a highly desirable system for classical as well as for quantum mechanics because of its simplicity. A single electron moves around a single proton. However, the classical motion of the electron becomes chaotic if an external electromagnetic field is applied (see as examples [70], [81]).

To visualize the dynamics of this system we must reduce the dimension of phase space. The following excerpt from [33] describes how it was done:

> 'The first step is to note that the applied magnetic field defines an axis of symmetry through the atom. The motion of the electron takes place effectively in a two-dimensional plane, and the motion around the axis can

be separated out; only the distances along the axis and from the axis matter. The symmetry of motion reduces the dimension of the phase space from six to four. Additional help comes from the fact that no outside force does any work on the electron. As a consequence, the total energy does not change with time. By focusing attention on a particular value of the energy, one can take a three-dimensional slice-called an energy shell-out of the four-dimensional phase space. The energy shell allows one to watch the twists and turns of the electron, and one can actually see something resembling a tangled wire sculpture. The resulting picture can be simplified even further through a simple idea that occurred to Poincaré. He suggested taking a fixed two-dimensional plane (called a Poincaré section, or a surface of section) through the energy shell and watching the points at which the trajectory intersects the surface. The Poincaré section reduces the tangled wire sculpture to a sequence of points in an ordinary plane.'

The resultant Poincaré section (or Poincaré map) for a highly excited hydrogen atom in a strong magnetic field is shown in **Figure 1.4**. The regions of the Poincaré section where the points appear to be randomly scattered indicate initial conditions that lead to stochastic trajectories, while continuous curves show regions where system's behavior is regular and thus completely predictable. This kind of dynamical phase space, which displays a coexistence of regular and chaotic regions, is called *a mixed phase space.*

The above quotation from Martin Gutzwiller's book brilliantly introduces the method of Poincaré maps and demonstrates the convenience of the method as it provides a clear visualization of multidimensional dynamics. The formal introduction of the Poincaré sectioning method is quite straightforward and can be done as follows: Given a Hamiltonian dynamical systems with N degrees of freedom, its dynamical phase space is 2N-dimensional. Thus the corresponding dynamical flow is represented by a curve in the 2N-dimensional space

$$X(\vec{q},\vec{p},t) = f^t(X(\vec{q},\vec{p},0)).$$

Successive intersections of this curve with the n-dimensional hypersurface ($n < 2N$) define the Poncaré map. In Gutzwiller's example above it was the projection of a trajectory in the 6-dimensional phase space on a 2-dimensional hypersurface.

1.4 The Lyapunov Exponent

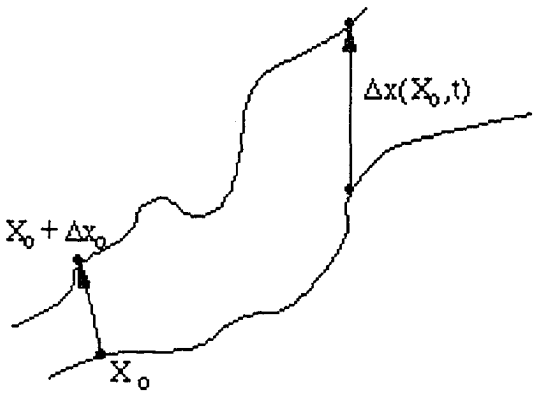

To obtain clear quantitative characteristics of dynamical instability we consider two trajectories that start out very close to each other. The initial separation between them in the phase space is

$$\Delta_0 = ||\vec{X}_1^0 - \vec{X}_0^0||.$$

The notation $\vec{X}_i$ is used to indicate the vector in the 2N-dimensional dynamical phase space, that means the composition of all the positions and momenta. As the system evolves in time the separation between trajectories changes to

$$\Delta_t = ||\vec{X}_1^t - \vec{X}_0^t||.$$

The property of sensitivity to initial conditions can be defined in the following way:

$$\Delta_t = \Delta_0 e^{\lambda t},$$

where λ, the mean rate of separation of nearest trajectories of the system, is called the **Lyapunov exponent**. For any finite accuracy in the measurements of initial conditions, the dynamics is predictable only up to a finite **Lyapunov time**

$$T_{Lyap} \approx -\frac{1}{\lambda} \ln \frac{\Delta_0}{L}.$$

In the expression above, L denotes the characteristic linear extent of the whole system. Thus the Lyapunov time shows a time during which a minimal uncertainty grows to the entire size of a system.

The correct mathematical definition of the Lyapunov exponent is slightly different in the sense that it involves a limiting procedure:

$$\lambda = \lim_{t\to\infty} \frac{1}{t} \lim_{|\Delta_0|\to 0} \ln \frac{|\Delta_t|}{|\Delta_0|}. \tag{1.1}$$

The Lyapunov exponent helps us to distinguish among the various types of trajectories in the following way:

- $\lambda < 0$ The orbit attracts to a stable fixed point or stable periodic orbit. Negative Lyapunov exponents are characteristic of dissipative or non-conservative systems (such as the damped harmonic oscillator). Such systems exhibit asymptotic stability, i. e. the more negative the exponent, the greater degree of stability. A limiting case $\lambda = -\infty$ corresponds to a critically damped oscillator. In such a case, the system tends to its equilibrium point as quickly as possible.

- $\lambda = 0$ The orbit is a neutral fixed point. Such systems exhibit Lyapunov stability. An example is a simple harmonic oscillator. As the frequency is independent of

the amplitude, its phase portrait is represented by a combination of concentric ellipses. The orbits in this situation maintain a constant separation.

- $\lambda > 0$ The orbit is unstable and chaotic. Nearby points, no matter how close, will diverge to an arbitrary separation. If all the points have a positive Lyapunov exponent then the entire dynamical phase space will eventually be visited. These points are said to be unstable, presence of unstable points leads to chaos.

Local values of the Lyapunov exponent differ for different regimes of a dynamical system. However, it has been proved that for a sufficiently large time evolution only a maximal value out of all the local Lyapunov exponents indicates stochasticity of the system and that is what the limit **(1.1)** converges to (see [72]). Numerical computations of Lyapunov exponents turned out to be impossible using the formal definition **(1.1)**. This is because the the function $\frac{|\Delta_t|}{|\Delta_0|}$ is extremely irregular and, moreover, does not increase after some saturation time, depending on initial conditions. To avoid this we have to consider only a short time evolution and average the results for an ensemble of trajectories. A practical realization of this was used in this dissertation for the computation of a Lyaponov exponent and can be found in reference [72]. The computational procedure itself was performed the following way: two close trajectories are taken at the initial moment of time: $\vec{X_0}|_{t=0}$ and $\vec{X_1}|_{t=0}$. The distance between them is $d_0 = ||\vec{X_0} - \vec{X_1}||$. After one iteration of length τ these two trajectories arrive at two new points in the phase space: $\vec{X_0}'|_{t=\tau}$ and $\vec{X_1}'|_{t=\tau}$. The distance between them becomes $d_1 = ||\vec{X_0}' - \vec{X_1}'||$. Before the next iteration the point $\vec{X_1}'$ is moved along the direction of the vector $(\vec{X_1}' - \vec{X_0}')$ so that the distance $||\vec{X_0}' - \vec{X_1}'||$ is again adjusted to be equal to d_0. After this the new iteration brings trajectories to two new points in the phase space and the distance d_2 between the points is calculated. Eventually after N iterations of this type the Lyapunov exponent is taken as the limit

$$\Lambda = \frac{1}{N\tau} \sum_{j=1}^{N} \ln(\frac{d_j}{d_0}). \tag{1.2}$$

The proof that the last expression eventually tends to the maximal Lyapunov exponent can be found in the references [14] [6].

1.5 Kolmogorov entropy.

A positive Lyapunov exponent does not by itself imply chaos. A trivial case is an unbounded dynamical system described by the equation:

$$\frac{d\vec{X}}{dt} = \lambda\vec{X}$$

if $\lambda > 0$ all the nearest trajectories separate exponentially, however, this system is not chaotic, trajectories just separate, but do not meet again. Chaotic dynamics is characterized not just by local exponential separation of nearby trajectories, but also by *mixing* means their re-approaching each other arbitrary closely, infinitely many times. Only in this way can any trajectory of a dynamical system fill, in an ergodic manner, all of the available phase space.

Kolmogorov entropy (also called K-entropy) is a quantitative characteristic of a dynamical system which characterizes its degree of mixing. Thus, it is the major indicator of chaos in Hamiltonian systems. The Kolmogorov entropy was introduced in 1959 by Kolmogorov ([45]). His formal procedures contain a great deal of sophisticated mathematics that are not presented in this dissertation. A convenient qualitative description of the concept of the K-entropy is given by Zaslavsky (see [93]). Let us outline his definition of this essential concept for chaotic dynamics. The time evolution of a system that exhibits mixed phase space is diagrammatically represented in **Figure 1.5**. A ball of initial conditions evolves in an extremely complicated way, eventually forming a shape with complex topology. The exact value of the phase volume V_0 is conserved according to the Liouville's theorem. However, this value does not describe adequately a measure of the shape with such complicated topology. We have to approximate the structure by considering an envelope that embraces all the tangled structure and then computing

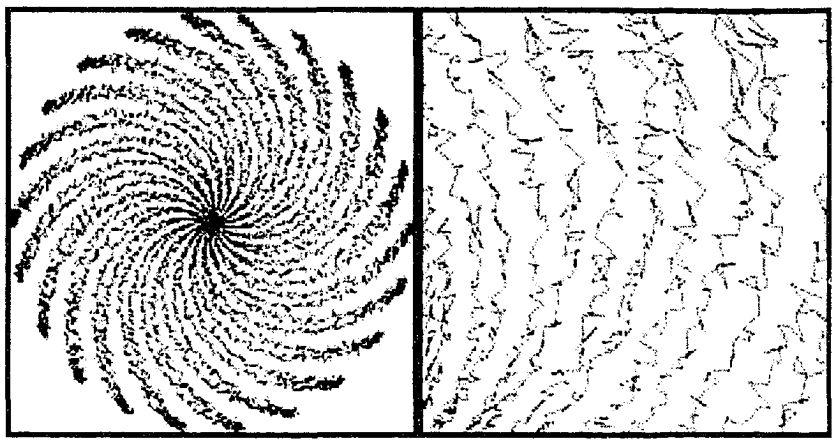

Figure 1.5: A diagram that displays the character of the dynamical evolution of a ball of initial conditions in a case of mixed dynamical phase space. The picture on the right displays a magnified view of a small rectangular region from the picture on the left. The topology of the shape becomes so complicated that to compute its volume correctly an envelope would have to be considered that confines all this complex topology. The volume embraced by the envelope is what is considered as the volume visited by the system.

the volume of a shape confined inside the envelope V_t. A measure of growth of such an effective volume is the Kolmogorov entropy of the system:

$$V_t = V_0 e^{ht} \quad h > 0 \text{ is the Kolmogorov entropy.}$$

Thus the Kolmogorov entropy measures the ergodicity of the system, showing how fast a ball of initial conditions spreads throughout the available dynamical phase space. It becomes a global characteristic of stochasticity in a dynamical system, in contrast with the Lyapunov exponent - the local characteristic of the chaos, based on a local divergence of nearest trajectories.

1.6 Chaos and Integrability

Let us consider the Hamiltonian dynamics of a bounded system with N degrees of freedom. The system is called *integrable* if there exist N independent functions of gen-

eralized coordinates and momenta $f_j(\vec{q},\vec{p})$ that remain constant along the trajectories

$$\dot{f}_j(\vec{q},\vec{p}) = 0.$$

The functions f_j are called *integrals of motion* (for details see as an example [47] or [30]).

The choice of mutually independent sets of integrals of motion is not unique. The fact is that any combination of them will produce another one. However, there exist a most convenient set of integrals of motion for analysis - called *actions*. The analytical expression for actions is

$$J_j(\vec{q},\vec{p}) = \frac{1}{2\pi}\oint p_j dq_j.$$

The integral is taken for one complete period of change of a dynamical coordinate q_j. Now let us assume that we consider an integrable dynamical system. This means that there exist N (equal to an amount of degrees of freedom) integrals of motion and N actions which prove to be constants of dynamical evolution as well (for proof see as an example [30]). Now let us perform a canonical transformation using the actions as the new canonical momenta

$$P_j = J_j(\vec{q},\vec{p}). \tag{1.3}$$

It was proved (see [47]) that in new canonical variables the Hamiltonian of an integrable dynamical system will be of the form $H = H(J_1, J_2, \ldots, J_N)$. The generalized coordinates conjugate to the actions are called *angles*, θ_j.

The Hamiltonian equations for the system in terms of the angle-action variables turn out to have an extremely simple form:

$$\dot{J}_j = -\frac{\partial H}{\partial \theta_j} = 0$$
$$\dot{\theta}_j = \frac{\partial H}{\partial J_j} = \omega_j.$$

Leading to the solution

$$\begin{aligned} J_j &= const \\ \theta_j &= \omega_j t. \end{aligned} \tag{1.4}$$

Equation **(1.4)** yields a possible indicator of the integrability of the system. The fact that actions are constant means that if we consider actions of the system during its time evolution as a random value, then its distribution must represent just a single vertical line as the result of the integrability. In the case of a non integrable systems, actions are no longer integrals of motion. Their distribution becomes broader as the degree of non integrability grows. Thus the width of the distribution of the actions becomes a possible indicator of the extent to which the dynamical system is non integrable. In the case where a distribution of actions is relatively uniform without sharp maxima presented, a variance σ^2 can be used as an indicator of the width of the distribution and hence as a quantitative measure of the degree of the non integrability:

$$\sigma^2 = \frac{1}{N}\sum_j (x_j - \langle x \rangle)^2$$
$$\langle x \rangle = \frac{1}{N}\sum_j x_j.$$

Another convenient indicator of non integrability can be obtained if we consider an inverse transformation of **(1.4)** to the original generalized positions and momenta:

$$q_j = q_j(\omega_1 t, \omega_2 t, \ldots, \omega_N t, J_1, J_2, \ldots, J_N). \tag{1.5}$$

All J_j in the expression **(1.5)** are constant. The Fourier transform of expression **(1.5)** will contain frequencies Ω_j that will represent various linear combinations of the

frequencies ω_j with integer coefficients:

$$q_j(t) = \sum A_j e^{-i\Omega_j t} \quad \Omega_j = \sum_i n_i \omega_i \quad n_i \text{ -all integers.}$$

Therefore, the Fourier spectrum will be discrete.

Thus the time evolution of an integrable system can be represented in the form of a discrete trigonometric series. Such a form of the solution has no provision for an exponential divergence of trajectories and, hence - *chaos does not exist in integrable Hamiltonian systems.*

Thus a discrete Fourier spectrum of trajectories is one more possible indicator of the integrability and, therefore, of regular dynamics. The opposite situation, a continuous spectrum of the time evolution, is a clear indicator that the dynamical system is non integrable and, perhaps, chaotic. However, as described as an example in reference [93] a continuous Fourier spectrum of time evolution appears to be a necessary, but not sufficient condition for a dynamical system to exhibit chaos. Its presence guarantees that the corresponding dynamics is non integrable, but not that it is chaotic. Once the continuous Fourier spectrum of a time evolution is observed we need additional tests to be certain about whether a system really exhibits a chaotic dynamical phase space or not. Two possible reliable tests have already been mentioned in the earlier sections - Poincaré maps and exponential divergence.

1.7 The KAM Theorem.

The Kolmogorov-Arnold-Moser (KAM) Theorem was stated in 1954 by Kolmogorov ([43]), then subsequently proved in the 1960-s by Arnold and Moser (see as an example [89]). This theorem describes the transition of an integrable system to chaos, or, on the other hand, it gives conditions under which chaos is restricted in its extent.

The theorem considers an *almost integrable* dynamical system, this means its Hamiltonian consist of an integrable part and a small perturbation. Conventional perturbation

theory *(see for example [72])* gives the following expression for the Hamiltonian

$$H = H_0(J_1, J_2) + \epsilon V(J_1, J_2, \theta_1, \theta_2). \tag{1.6}$$

For simplicity a dynamical system with 2 degrees of freedom is considered. The part $H_0(J_1, J_2)$ indicates the integrable part of the Hamiltonian which always can be expressed in terms of the actions (see [30] or [47]). The remaining part represents a small perturbation. For an integrable case the solution of the Hamiltonian equations is

$$\begin{aligned} J_1 &= const \qquad J_2 = const \\ \theta_1 &= \omega_1 t + \theta_1^0 \quad \theta_2 = \omega_2 t + \theta_2^0. \end{aligned} \tag{1.7}$$

The trajectories in a phase space lies on 4-dimensional tori, each parametrized by conditions $J_1 = const \quad and \quad J_2 = const$. In the case when frequencies corresponding to a particular torus are commensurate,

$$n_1\omega_1 + n_2\omega_2 = 0 \quad n_1, n_2\text{-integers},$$

the corresponding trajectory is closed and its motion is periodic. Otherwise, the trajectory never closes, but it fills the surface of the torus uniformly. This type of motion is called quasiperiodic.

The system becomes non integrable if a perturbation is applied, however:

- *The KAM theorem guarantees preservation of most invariant tori under a sufficiently small and smooth (but otherwise arbitrary) perturbation.*

The theorem also gives a hint as to which irrational tori are the most robust. This is the case because small denominators can occur for perturbed rational tori, causing their quick destruction even for small values of the perturbation.

As was already mentioned, the KAM theorem is relevant to the question of the stability of the solar system, which is a nearly integrable system. Therefore, the relatively weak mutual interactions of the planets, compared with the force exerted by the Sun,

cause some deformations of their orbits but not their destruction. The solar system represents a non integrable dynamical system, but the Kolmogorov-Arnold-Moser theorem proves its stability.

Chapter 2

Quantum Chaos

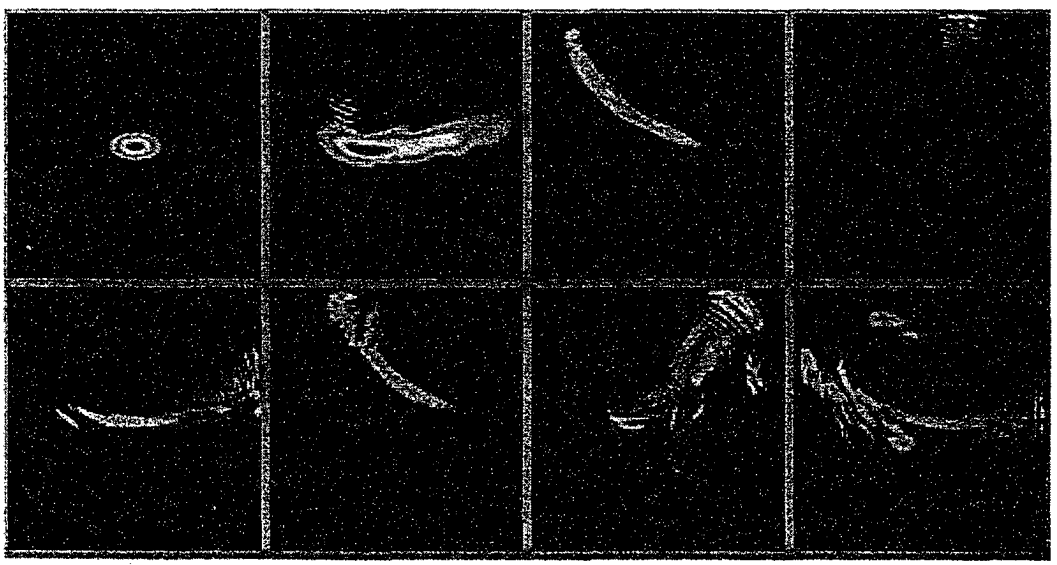

2.1 Separation of quantum wave packets.

Perhaps the most outstanding feature of the quantum world is its smooth and wave-like nature. This feature leads to the question of how chaos makes itself felt when a stochastic classical dynamical system is transported to the quantum world. How can the extremely irregular character of classical chaotic motion be transmitted into the smooth and wavelike motion of the atomic scale? Does chaos exist in the quantum world?

One reason why it is difficult to look for chaos in quantum systems is that chaos in the classical mechanics is defined in terms of the separation of the nearest trajectories. Therefore, the first attempt to introduce chaos in quantum mechanics is to do something analogous. A measure of a 'distance' between two wave packets - is their overlap integral:

$$\langle \psi_1(t) | \psi_2(t) \rangle. \tag{2.1}$$

The time evolution of the wave packet under Hamiltonian $\hat{H}$ is defined in terms of a unitary time-evolution operator

$$|\psi_j(t)\rangle = e^{-i\frac{\hat{H}t}{\hbar}} |\psi_j^0\rangle.$$

This way the time evolution of an overlap integral of two quantum states is:

$$\langle \psi_1(t) | \psi_2(t) \rangle = \langle \psi_1^0 | e^{i\frac{\hat{H}t}{\hbar}} e^{-i\frac{\hat{H}t}{\hbar}} | \psi_2^0 \rangle = \langle \psi_1^0 | \psi_2^0 \rangle.$$

This means that due to the unitarity of the time-evolution operator the overlap integral is preserved. Thus two wave packets do not separate.

The second apparently simple way to introduce chaos analogously to how it was done in classical mechanics is to look for a continuous energy spectrum as this was a convenient indicator of stochasticity in the classical case. However, this approach can not succeed either. This is a fact, because all the time-independent quantum mechanical bounded systems have discrete spectra (see [49]). It is worth mentioning that, on the other hand, the spectrum of any bounded quantum system becomes continuous in the classical limit. This indicates the weakness of such an approach for finding signatures of chaotic dynamics in the quantum case.

Therefore, attempts to directly translate elements of classical chaos into quantum dynamics are too simplistic to be valid. The fact is that the quantum wave functions are not exactly comparable to trajectories. The overlap integral of two quantum wave

functions is analogous to the overlap integral of two classical distributions rather than two classical trajectories. On the other hand the overlap integral of two classical distributions is also preserved according to Liouville's theorem.

However, there exist an indicator of classical chaos in quantum systems in terms of the overlap integral **(2.1)**, suggested by Asher Peres (see[64]). His idea was to to consider an overlap of two identical wave packets, but under the evolution of two slightly different Hamiltonians. It was observed for classically chaotic systems that the overlap decays exponentially, while for classically stable systems the overlap remains close to unity or may at most exhibit a power-law decay **(see [22])**. Such a sensitivity of the quantum evolution to perturbations is now called *the Loschmidt Echo* and it can be considered as one of manifestations of chaotic behavior in the quantum case.

2.2 The Big Picture.

Preliminary work seems to show that some clear manifestations of chaotic behavior can be observed in quantum mechanics. Besides the extreme sensitivity to perturbations mentioned in previous chapter, remarkable signatures of the chaotic dynamics were found in the distribution of energy levels of certain atomic systems ([70]). It even appears to affect the wave patterns associated with those levels. Stochastic behavior is also observed when electrons scatter from small molecules. It has to be emphasized, however, that the term 'quantum chaos' serves more to describe a puzzle than to state a well-defined problem.

Following Martin Gutzwiller (see [32]) it is helpful to consider such an interpretation of the bigger picture in order to recognize the concept of quantum chaos. All the theoretical discussions of mechanics can be artificially divided into three compartments (see **Figure 2.1**):

• Elementary classical mechanics is placed in the first compartment. It contains all the integrable systems that exhibit deterministic and regular behavior. This container

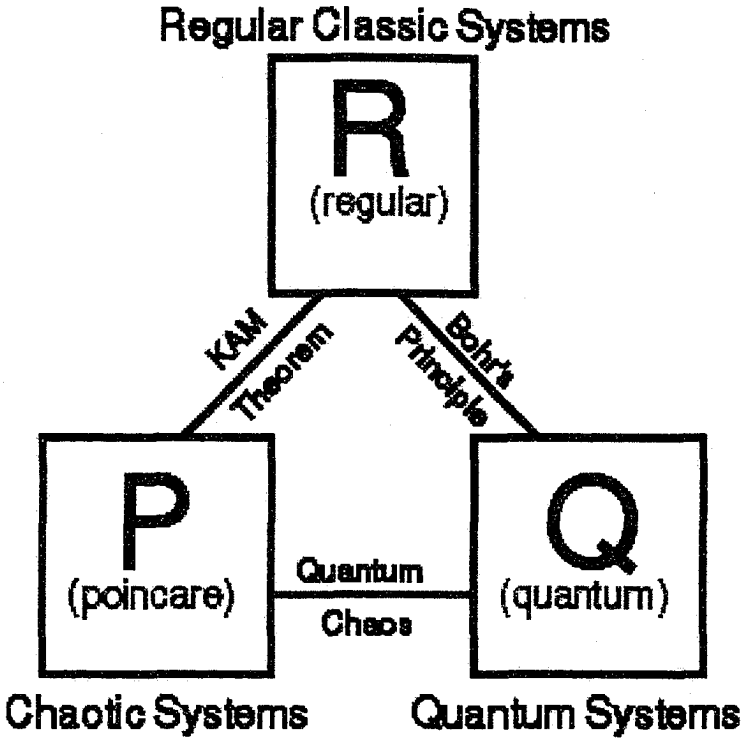

Figure 2.1: **The 'Big Picture'.**

is labeled by the letter **R**, which means regular. Besides this we put into this box all the dynamical systems that are not integrable, but can be accurately described using conventional perturbation theory for calculations of the effects of small disturbances. One example of such a dynamical system is the Moon orbiting around the Earth. The influence of the Sun in this case can be considered as a small perturbation, which causes just a mild modification of the time evolution of an integrable dynamical system.

- Chaotic classical dynamical systems can not be described adequately by means of conventional perturbation theory, therefore we have to place them into a separate compartment. Since the first detailed analysis of chaotic systems was done by Póincare, the corresponding container is labeled **P** in his honor. All systems that exhibit eruptive nondeterministic behavior are placed in this second box. Among them are all the fundamental problems of mechanics, starting with three, rather than only two bodies

interacting with one another, such as the Earth, Moon and Sun, or three atoms in the water molecule, or the three quarks in the proton.

• All quantum mechanical systems belong to the third container, labeled **Q**. According to Dirac this box contains 'most of physics and all of chemistry'. However, only a relatively small amount of special problems have been solved in quantum mechanics in the form designed by Niels Bohr, Werner Heisenberg, Erwin Schrodinger, Max Born and many others. Among these resolved problems is the hydrogen atom, which is a quantum analogue of the two-body problem. However, there exist an overwhelming amount of dynamical systems that quantum mechanics, as it was initially designed, is not able to treat adequately. One of the numerous examples of those systems is the helium atom, which is analogous to the three-body problem in classical mechanics - the one that was placed into the compartment **P**.

The three boxes **R**, **P** and **Q** are linked by several connections. The connection between **R** and **Q** is provided by Bohr's correspondence principle. The principle states that classical mechanics must be contained in quantum mechanics in the limiting case when the total energy of objects become much larger than the characteristic scale of energies of atoms and molecules (which is of an order of Plank's constant $\hbar$). The main connection between **R** and **P** is the Kolmogorov-Arnold-Moser (KAM) theorem that was mentioned in Section (1.7). The theorem provides a tool for calculating how much of the regular structure of a system withstands perturbation, and therefore helps to identify the way a regular system starts to exhibit chaotic behavior. Thus the two boxes that are not linked yet are **P** and **Q** - the link between them has to describe the transition of classically stochastic nondeterministic systems to a smooth and wavelike quantum world. Establishing such a link is the major concern of 'quantum chaos'.

As we already discussed in Section 1.6 the major feature of classically chaotic systems is a lack of integrability. This means that the number of integrals of motion for such systems is less than their dimensionality. It is known from the theory of canonical quantization (see for example [49] or [59]) that the existence of a conserved quantity I_j

in classical mechanics leads to the commutation of a corresponding operator $\hat{I}_j$ with the Hamiltonian:

$$[\hat{I}_j, \hat{H}] = 0.$$

As a result of this commutation the energy eigenfunctions must also be eigenfunctions of $\hat{I}_j$. This eigenfunction must then be of a separable form and thus we can reduce the number of variables in the Schrodinger equation by one, replacing the operator $\hat{I}_j$ by its corresponding quantum number. If the classical problem has a complete set of the integrals of motion, then the Schrodinger equation, for the corresponding quantum problem is completely separable and therefore has a complete set of quantum numbers as well as corresponding complete set of eigenfunctions, ordered by these quantum numbers. Based on this we can conclude that Quantum Chaos deals with systems that are described by the Schrodinger equation where the complete separation of variables is impossible. Such systems do not have well defined and ordered set of good quantum numbers. Study of behavior of such kind of systems is major concern of Quantum Chaos.

To complete this discussion below are given some examples of quantum dynamical systems. Classical analogues of all of them exhibit chaotic behavior, and studying their quantum dynamics is the concern of quantum chaos.

- Helium atom. *The classical analogue is the three body problem.*
- Rydberg atom in an electromagnetic field. *The classical analogue exhibits a mixed phase space* **(see Figure 1.4)**.
- Many body problems. *The classical analogues can be described only by means of siatistical methods.*
- Quantum billiards - two-dimensional confined motion. *The classical analogues exhibit behavior that essentially depends upon a geometry of the confinement and*

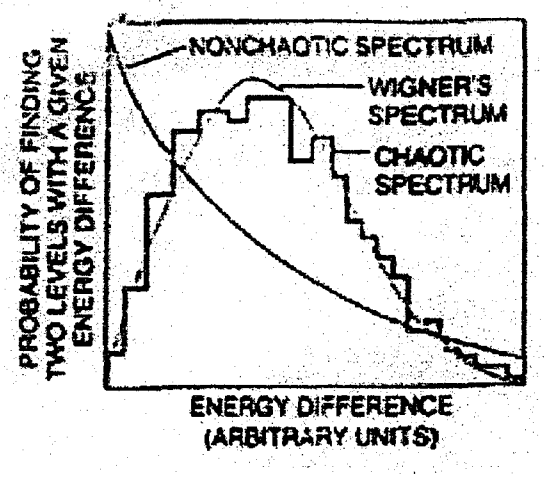

Figure 2.2: ENERGY SPECTRUM or distribution of energy levels, differs markedly between chaotic and non-chaotic quantum systems. For a non-chaotic system such as a molecular hydrogen ion (H_2^+), the probability of finding two energy levels close to each other is quite high. In the case of a chaotic system levels like 'keep safe distance' from one another. *(The picture was taken from the reference [33]).*

external forces applied:

- *Integrable dynamics (rectangular and elliptical billiards without external field).*
- *Mixed phase space (rectangular and elliptical magnetic billiards, mushroom billiards).*
- *Chaotic phase space (Stadium billiard, Sinai billiard).*

- Mesoscopic systems, quantum dots. Practical realizations of quantum billiards. A detailed description is given later in this chapter.

2.3 Level-Spacing Distribution.

One of the trademarks of a quantum mechanical system is quantized energy levels, which is the first place to look for quantum chaos. Chaos does not make itself felt for a particular energy level, rather its presence is seen in the entire spectrum, and, in statistical distributions of the level spacings.

Let us revisit the Rydberg atom **(Figure 1.4)**, but this time quantum mechanically. Theoretically the energy-levels using perturbation methods were found by Solovyov V.A. and Braun P.A. The complete description is presented in references [81], [82] and [83]. As the theory of the quantum states of the Rydberg atom in an electromagnetic field was being developed, some experimental results ([70] and [71]) confirmed what was predicted by the theoreticians. Somewhat paradoxically, what was observed is that for a non-chaotic quantum system the energy levels are distributed randomly and without correlation. However, the energy levels of a chaotic system in the quantum case exhibit strong correlations. The picture from the reference [33] demonstrates this **(Fig. 2.2)**. The levels of the regular system are often close to one another, because a regular system consists of a composition of completely decoupled subsystems, the consequence of the separation of variables. On the other hand the energy levels of a chaotic system seems to be aware of one another and try to keep a safe distance. This is a clear consequence of non integrability - a chaotic system cannot be decomposed, hence its properties versus all the general coordinates and momenta are strongly correlated.

As one can see from the figure **(Fig. 2.2)** the distribution of the energy level spacing for the classically chaotic system is close to the Wigner distribution, the one that describes the spacing of energy levels in random matrices. To obtain an expression for the Wigner's distribution let us consider 2x2 random symmetric matrix

$$\begin{pmatrix} h_{11} & h_{12} \\ h_{21} & h_{22} \end{pmatrix} \qquad h_{12} = h_{21}.$$

All the elements h_{ij} are random numbers. The characteristic equation

$$(h_{11} - E)(h_{22} - E) - h_{21}h_{12} = 0$$

has two solutions

$$E_{12} = \frac{1}{2}(h_{11} + h_{22} \pm \sqrt{{h_{11}}^2 + 4{h_{12}}^2 - 2h_{11}h_{22} + {h_{22}}^2}).$$

The spacing between the levels is

$$\Delta E = \sqrt{{h_{11}}^2 + 4{h_{12}}^2 - 2h_{11}h_{22} + {h_{22}}^2} = \sqrt{(h_{11} - h_{22})^2 + 4{h_{12}}^2}.$$

All the h_{ij} are random. Therefore the distribution of level spacing is equivalent to the distribution of $\sqrt{\xi^2 + \chi^2}$ of the random values ξ and χ. The probability of finding levels in a small interval between s and $s + ds$ is proportional to sds.

Let the probability of finding no levels between $0 \rightarrow s$ be $F_{no}(s)$. Then the probability $F_{no}(s + ds)$ can be written

$$F_{no}(s + ds) = F_{no}(s)(1 - Csds).$$

In the last expression C is a constant of proportionality and $(1 - Csds)$ is the probability of finding no levels between s and $s + ds$. We expand $F_{no}(s + ds)$ in Fourier series and integrate, obtaining

$$F_{no}(s) \approx e^{-\frac{1}{2}Cs^2}.$$

Let $P(s)ds$ be the probability of finding the spacing between two neighboring energy levels in a range s and $s + ds$. It can be written

$$P(s)ds = F_{no}(s) - F_{no}(s + ds).$$

Expand $F_{no}(s + ds)$ in a Taylor series and integrating gives

$$P(s) = Cse^{-\frac{1}{2}Cs^2}.$$

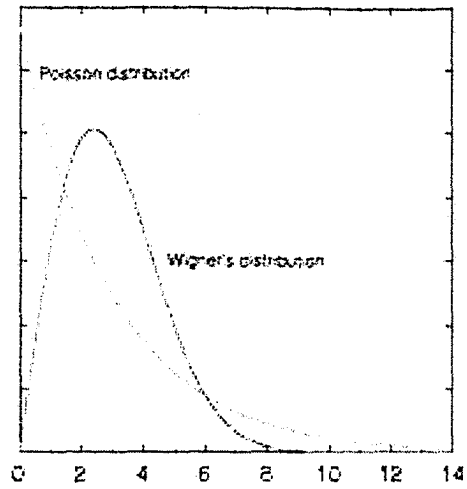

Figure 2.3: Plots of Wigner's and Poisson distribution. Both plots correspond to the same mean value.

We can express the constant C in terms of the average spacing D

$$D = \int_0^\infty ds \;\; sP(s) = \sqrt{\frac{\pi}{2C}}.$$

Thus, the final expression for the Wigner's distribution is

$$P_W(s) = \frac{\pi s}{2D^2} e^{-\frac{\pi s^2}{4D^2}}. \tag{2.2}$$

The probability of finding neighboring energy levels within very small spacing is very small since $P_W(s)$ is proportional to s. Thus the energy levels repel each other and therefore are correlated.

Let us note that if we would assume the purely random level distribution we would obtain the Poisson distribution for the level spacing

$$P_P(s) = \frac{1}{D} e^{-\frac{s}{D}}. \tag{2.3}$$

The figure **(Fig. 2.3)** shows plots of the Wigner and Poisson distributions for the same average value. We see that the Poisson distribution has the maximum probability

at the origin. This means that uncorrelated levels have a high probability of a small level spacing. In contrast the correlated levels seems to repel each other, keeping some certain spacing between.

2.4 Random Matrix Theory.

The example discussed above can be considered as the simplest case of the application of *Random Matrix Theory.* This theory was developed by Wigner for application to nuclear eigenvalues. The reason for use of random values in Hamiltonian matrices was a lack of reliable experimental results in measurements of nuclear excited energy levels due to instrumental resolution failings.The following excerpt summarizes Wigner's motivation for the use of statistical methods ([24]or [72])

> *Recent theoretical analysis have had impressive success in interpreting the detailed structure of the low-lying excited states of complex nuclei. Still, there must come point beyond which such analysis of individual cannot usefully go. It is impossible that level assignment based on shell structure and collective of individual-particle quantum numbers can ever be pushed as far as the millionth level. It is therefore reasonable to inquire whether the highly excited states may be understood from the diametrically opposite point of view, assuming as a working hypothesis that all the shell structure is washed out and that no quantum numbers other than spin and parity remains good. The result of such an inquiry will be a statistical theory of energy levels. The statistical theory will not predict the detailed sequence of in any one nucleus, but it will describe the general appearance and the degree of irregularity of the level structure that is expected in any nucleus which is too complicated to be understood in details.*

Thus Wigner's first basic assumption was that the matrix elements of the Hamiltonian matrix of the system are unknown and unknowable. All the elements of the

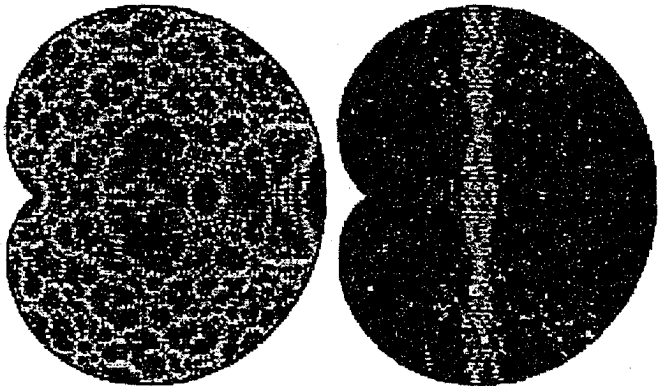

Figure 2.4: Probability density of the 1,816th and 1,817th eigenstate of a quantum particle trapped in a chaotic heart-shaped region with Dirichlet boundary conditions. *The picture was taken from the reference [3].*

Hamiltonian matrix are considered to be random. The additional constraints that each particular system imposes on the elements of the Hamiltonian matrix are based on the symmetry properties of a particular dynamical system.

Random Matrix Theory proved to be extremely powerful for dealing with quantum chaotic systems. It was originally used for analysis of the spectra of heavy nuclei ([26]). These are many-particle systems whose interaction, according to Wigner, is so complex that the Hamiltonian representing the system should behave like a large random matrix.

However, it was discovered later that even simple one-particle quantum systems exhibit random matrix statistics, if the classical limit of the system is chaotic. An example of such a system is the electron in the heart-shaped region represented on a picture **(Figure 2.4)**, studied in reference [3]. Using this method the properties of the energy levels of some quantum chaotic billiards were studied in details. The major approach is to represent quantum eigenfunctions as a random composition of plane-waves with fixed energy (see [10]). As an example in reference [12] the energy spectrum of a chaotic Sinai billiard was found using Random Matrix Theory. More examples of chaotic quantum systems investigated by Random Matrix Theory can be found in [16].

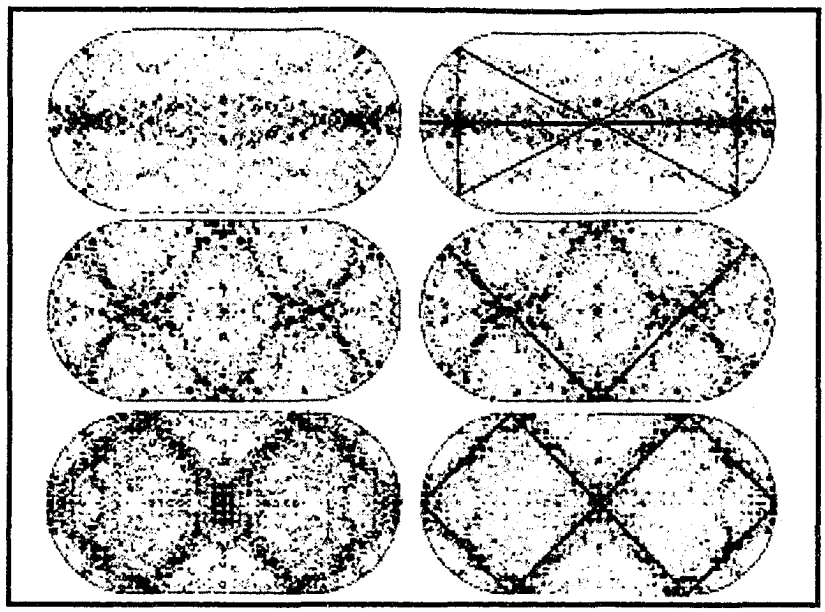

Figure 2.5: Particle in a stadium-shaped box has chaotic stationary states with associated wave patterns that look less random than one might expect. Most of the states are concentrated around narrow channels that form simple shapes, that were called scars *(The picture was taken from the reference [37]).*

The major drawback of Random Matrix Theory is the fact that it is suitable only for chaotic systems. Random Matrix Theory cannot be applied to study dynamical systems with mixed phase space, where chaotic dynamics coexist with regular motion. However, all dynamical systems examined in this dissertation exhibit mixed phase space, therefore methods other than Random Matrix Theory were developed and used to deal with these systems.

2.5 Quantum Scars.

As was mentioned in a previous section the quantum eigenfunctions of classically chaotic dynamical system do not always look like random superpositions of plane waves with fixed energy. Instead, many eigenfunctions display a concentration of amplitudes around short unstable periodic orbits. Such a concentration contradicts with predictions made by Random Matrix Theory.

The first surprising discovery was made by Eric Heller ([37]). He and his students calculated a series of stationary states for a two-dimensional cavity in the shape of a stadium. The corresponding problem in classical mechanics was known to be chaotic, as a typical trajectory quickly covers most of the available phase space quite evenly. Such behavior suggests that the stationary states might also look random, as if they had been designed without any rhyme or reason. In contrast, Heller discovered that most stationary states are concentrated around narrow channels that form simple shapes inside the stadium. The channels are aligned along classical periodic orbits **(Figure 2.5)**. He called these channels 'quantum scars'.

Similar structure can also be found in the stationary states of a hydrogen atom in a strong electromagnetic field **(Figure 2.6)**. As was mentioned earlier the corresponding classical problem is chaotic. A comprehensive theoretical description of its classical dynamics can be found in reference [23], while a theoretical solution of the quantum problem is described in references [92] and [81]. The quantum eigenfunctions of the electrons were found to exhibit an extensive concentration along classical trajectories **(Figure 2.6)**. Thus the second remarkable signature of quantum chaos - the quantum scars were first observed for this classically chaotic system.

Its worth mentioning that the energy level statistics for Rydberg Atom inside a magnetic field was obtained not only theoretically. Simultaneously, there were a series of experiments performed (see [70] and [71]). As was expected, the level-spacing distribution demonstrates strong level correlation for the classically chaotic regime **(Figure 2.2)**. Thus for Rydberg Atoms in a strong magnetic field, such manifestation of chaos in quantum mechanics as the strong level repulsion was not just predicted theoretically; its existence was proved by numerous experiments.

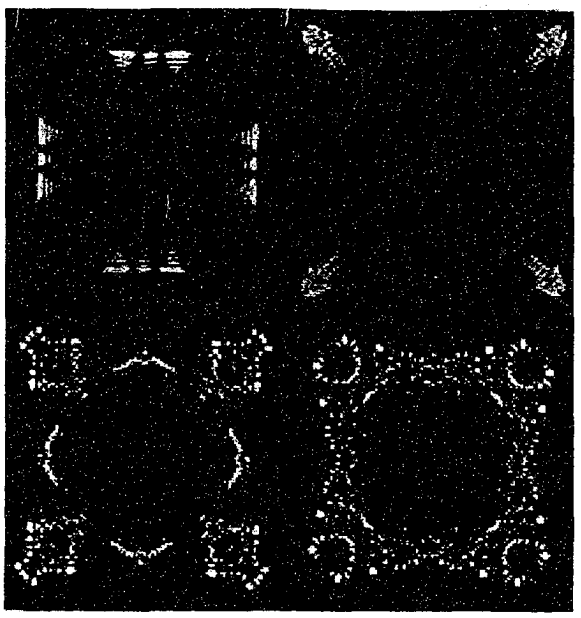

Figure 2.6: Stationary states or wave patterns, associated with the energy levels of a Rydberg atom (a highly excited hydrogen atom) in a strong magnetic field. *(The picture was taken from the reference [33])*

2.6 Dynamical Localization

The first amazing feature of the quantum behavior of a classically chaotic system is so called *Dynamical Localization.* An excellent demonstration of this phenomenon is the problem of the $\delta-$kicked rotor, solved and discussed in details in [17] or [84].

2.6.1 The kicked rotor. Classical case.

The kicked rotor is described by the Hamiltonian

$$H(x,p,t) = \frac{p^2}{2} + K\cos x \sum_n \delta(t - nT), \tag{2.4}$$

which is just the Hamiltonian for a simple pendulum, but with the potential turned on in $\delta-$function pulses every unit of time.

The Hamiltonian equations are

$$\dot{p} = K \sin x \sum_n \delta(t - nT) \quad \dot{x} = p. \tag{2.5}$$

Integrating these equations on the interval $(t_n - \epsilon, t_{n+1} - \epsilon)$ - this means *from just before n-th to just before (n+1)-th kick* will give

$$p_{n+1} = p_n + K \sin x_n \qquad x_{n+1} = x_n + p_{n+1}. \tag{2.6}$$

This is the standard map that was already mentioned in the **Section 1.2**. The character of dynamics in this system is governed by parameter K. Then, the authors of [17] considered the behavior of the average energy of the system

$$E_n = \langle \frac{{p_n}^2}{2} \rangle. \tag{2.7}$$

In the last expression $\langle\rangle$ brackets denote averaging with respect to the initial distribution of trajectories. This distribution was taken to be uniform, then the averaging of trigonometric functions in **2.6** yields the final result

$$E_n = \frac{K^2}{4} n. \tag{2.8}$$

This implies the diffusive growth of the energy (linear in time) with diffusion rate $\frac{K^2}{4}$.

2.6.2 The kicked rotor. Quantum case.

Looking for correspondence between classical and quantum dynamical systems, the authors of [17] considered the quantum mechanical equation of motion of the $\delta-$kicked rotor. To integrate the time-dependent Schrodinger equation they used the evolution operator (see for example [9]):

$$U(t, t_0) = e^{-\frac{i}{\hbar}\int_{t_0}^{t} \tilde{H}(\tau)d\tau}. \tag{2.9}$$

Similar to the classical case, the integration is performed *from just before n-th to just before (n+1)-th kick.* This yields the evolution operator

$$U(t_{n+1}, t_n) = e^{-\frac{ip^2}{2\hbar} - \frac{iK\cos x}{\hbar}}. \tag{2.10}$$

The above exponential operator was split in two parts - the Cartesian part that is diagonal in the configuration space and the momentum part that is diagonal in the momentum space. As a result the following quantum map was obtained and integrated

$$|\psi_{n+1}\rangle = e^{-\frac{ip^2}{2\hbar}} e^{-\frac{iK\cos x}{\hbar}} |\psi_n\rangle. \tag{2.11}$$

In correspondence with the classical case, the diffusive growth of energy was as well expected in the quantum case. However, the authors of [17] discovered that the quantum kicked rotor gains energy as in the classical case only for a short time, after which the diffusion is suppressed. This effect has come to be known as *dynamical localization*, and is dramatic example of how quantum effects suppress classical chaos.

One more striking numerical demonstration of the suppression of chaos in the quantum kicked rotor was done by Shepelyansky in [78]. Results of his numerical computations are illustrated in **Figure 2.7**. The classical and quantum systems start their time evolution from the same initial condition.The suppression of energy growth by dynamical localization is evident in the quantum case. After evolving for some duration, a time-reversal is performed. In principle, both models should reverse their behavior and return to their initial conditions. The classical system only successfully contracts for a short time, though, and due to the buildup of numerical roundoff errors, the trajectories "forget" their history and the ensemble resumes diffusive, as expected for chaotic dynamics. The quantum system, on the other hand, makes a clean return to the initial

state indicating a robustness against perturbation and thus an absence of chaos.

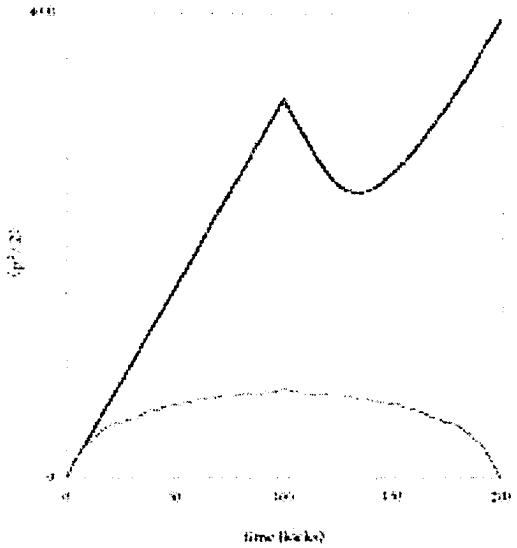

Figure 2.7: Comparison of classical (heavy solid line) and quantum (thin solid line) momentum transport in the kicked rotor for $K = 10$ and scaled Planck constant $\hbar = 1$ (simulation). The kinetic energy $p^2/2$ in both cases is plotted as a function of time. The classical transport is diffusive, as characterized by the linear growth of energy. The quantum transport only shows diffusion for short times, and localization for longer times. At 100 kicks (marked by the dashed line), the direction of time is reversed. The classical ensemble resumes diffusive behavior after numerical errors build up in the simulation (thus converting the special trajectories that evolve back to the initial condition into generic, diffusive trajectories), which is typical for chaotic dynamics. The quantum system, on the other hand, retraces its step back to its initial condition, indicating a lack of chaos. *(The picture was taken from the reference [84]).*

2.7 Semi-classical quantization. The Gutzwiller trace formula.

As was discussed in Section 2.5, classically chaotic systems display a concentration of the quantum wave function around short unstable periodic orbits - 'quantum scars' (see [37]). Similar concentration was observed in the energy space (see [58]) - highly excited quantum energy levels of a classically chaotic system demonstrate a strong concentration near values corresponding to semi-classical energy levels obtained as the

result of quantization of the short unstable periodic orbits.

All this indicates the importance of classical short unstable periodic orbits for the purposes of semi-classical dynamics for classically chaotic systems. Perhaps, the most remarkable demonstration of the key role of classical periodic orbits in stochastic classical systems transmitted into the quantum mechanics is associated with the Gutzwiller trace formula (see [33] and [55]). For reasons explained later in this section, the formula is not used in this dissertation, and that is why it is not represented here. However, we outline the basic concepts related to the Gutzwiller trace formula because of the importance of these concepts for a general picture of quantum chaos.

Mathematically, the Gutzwiller trace formula represents the limit of the quantum mechanical Green's Function (propagator of the quantum system) $G(q'', q', E)$ as the constant $\hbar$ becomes small. As the result of such a limiting procedure it was proved by Martin Gutzwiller that the quantum Green's Function can be represented as the summation of $\delta-$functions, each concentrated along unstable periodic orbits. Therefore, solution of a quantum dynamical problem by means of the Gutzwiller trace formula requires knowledge and clear unambiguous ordering of all the classical unstable closed orbits at energy E. Once such orbits are identified and ordered, an application of the Gutzwiller trace formula involves computation of the actions $\oint p_j dq_j$ related to each of the classical unstable closed trajectories and then summation of certain functions of these actions. This way all the quantum dynamics of a classically chaotic system become completely determined by classical unstable periodic orbits.

The fact that the Gutzwiller trace formula requires simple classification of all the classical short periodic orbits makes impossible to apply it for dynamical systems examined in this dissertation. For the systems we are going to deal with in this thesis an unambiguous classification of all the classical periodic orbits seems to be impossible. Therefore, to describe these systems adequately we are going to develop and apply methods other than the Gutzwiller trace formula.

2.8 Mesoscopic systems. Quantum dots.

The recent rapid progress in submicron lithography arises interest to study the classical and quantum chaotic billiards. Mesoscopic systems that are less than one micron in size, were produced. Such systems are able to confine a small amount of electrons inside an enclosure. Walls of such a container represent an impurity inserted in semiconductor heterostructure. An interaction between enclosed electrons and walls represent specular reflection. For high temperatures such systems behaves like a two-dimensional classical billiard, while for small temperatures quantum effects must be taken into account. In this way study of quantum billiards acquired an important experimental, not just theoretical, context. Let us discuss some examples of the mesoscopic systems.

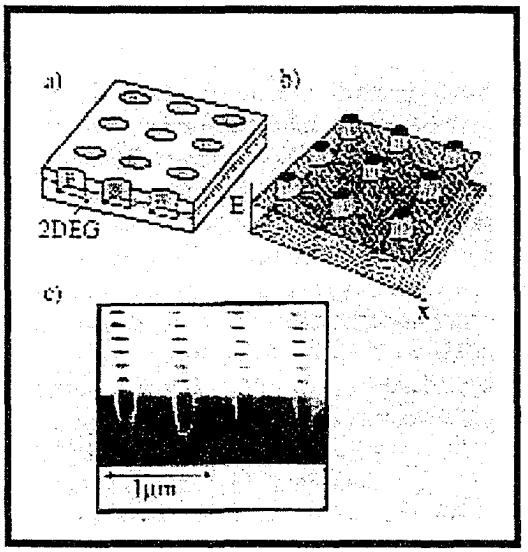

Figure 2.8: Sketch of an array of periodically arranged nanometer-sized holes etched into a semiconductor sandwich structure and the corresponding electrostatic antidot potential (b.). *(The picture was taken from the reference [75]).*

The **Figure 2.8** represents one of realizations of mesoscopic systems (see [91] for details). The structure consists of a periodic array of nanometer-sized holes etched into a semiconductor sandwich structure. This results in a periodic potential for a two-dimensional electron gas at the interface of a heterojunction. The effective potential looks similar to an egg carton. The electrons move at a constant Fermi energy in between

the periodically arranged potential posts. If the antidots are steep, a unit cell of the antidot crystal may be regarded as an experimental realization of the Sinai billiard.

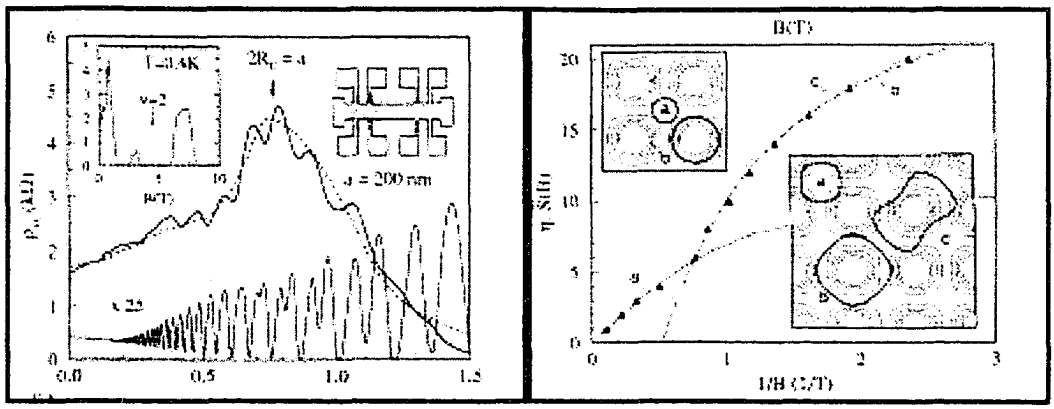

Figure 2.9: Resistivity measured for patterned (on the left) and unpatterned (on the right) segment of the same sample temperature. The left curve show a broad resistivity peak due to quantum resonance effects. *(The picture was taken from the reference [90]).*

In the reference [90] is described an experimental study of the resistivity of this system versus the magnitude of an external magnetic field. Experiments were carried out under $T = 4.7\ K$, thus the system's behavior is equivalent to the diffraction of a two-dimensional quantum wave-packet on a periodic potential. Experimental results demonstrate quantum resonance phenomenon just the way it was expected. An experimental curve, pictured on the left side of **Figure 2.9** demonstrates the resonant peak in resistivity for a certain value of the external magnetic field. The left graph on the same picture represents the behavior of the same semiconducting heterostructure without impurities. Increasing the external magnetic field in this case leads to monotonic growth of the resistivity.

Another example of a mesoscopic system is a 'quantum dot'. It is produced by impurities inserted in a semiconducting heterojunction, experimentally realizing two-dimensional billiards containing few particles. As an example, reference [56] experimentally investigated the quantum dot represented in **Figure 2.10**. GaAs and AlGaAs were used as semiconductors to produce a two-dimensional electron gas on their junction. Confinement of an electron is produced by additional negatively charged surface

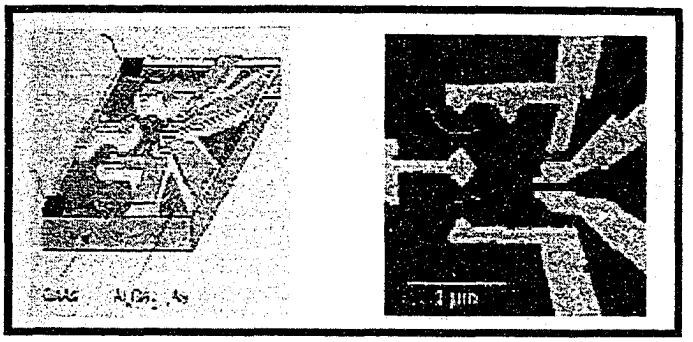

Figure 2.10: A lateral quantum dot made by confining electrons a at two-dimensional interface between GaAs and AlGaAs by adding negatively charged surface gates. The right figure shows a micrograph of such an electron billiard where an electron is allowed to pass in and out of the dot only through two left leads. *(The picture was taken from the reference [75]).*

gates. An electron is allowed to pass in and out of the dot only through two left leads. Depending upon the geometry of the confinement and the external magnetic field that can be applied, for certain cases, the transition properties of the dot differ significantly.

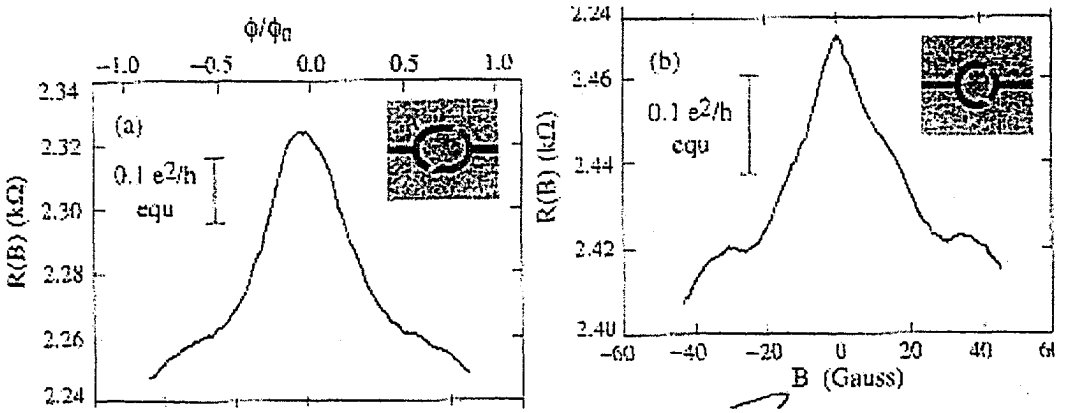

Figure 2.11: A resistance of a stadium shaped cavity (on the left) and a circular shaped cavity (on the right) depending upon an external magnetic field applied perpendicular to the shape of the confinement. In both cases a resonance behavior of the resistance is observed. However for the case of the chaotic stadium shaped cavity, the resonance curve is smooth, while for the integrable case the shape of the curve is extremely unusual - triangle like. *(The picture was taken from the reference [19]).*

In a reference [19] two quantum dots of different enclosure geometry were investigated. The confinement of the first structure had a circular shape, which represents the

case of an integrable billiard, while the second 'quantum dot' had an enclosure in the shape of a stadium, a well known example of essentially chaotic dynamics. The authors of [19] were measuring resistivity of this quantum dot depending upon the external magnetic field applied perpendicularly. In both cases, resonance behavior in the resistivity was observed by exhibiting a maximum for certain values of the external magnetic field **(see Figure 2.11)**. However, for the case of the chaotic billiard, which means the stadium shaped confinement, the resonance peak of the resistivity obtained showed a smooth Lorentzian curve, while for the case of circular container the resonance curve showed an unusual triangular behavior. This was considered by the authors of [19] as one of the signatures signature of the chaos.

2.9 The single electron transistor and artificial atoms.

Another important experimental motivation of the work represented in this dissertation is a single electron transistor. Before describing its details let us first represent the following excerpt taken from an on-line technical news journal (`http://news.zdnet.co.uk`):

> `June 21-st 2001`
>
> `Cambridge researchers have demonstrated a nine-bit memory device that uses between one and ten electrons per bit. This is around 100,000 times fewer electrons than are used in current dynamic memory devices, and is close to the theoretical limit for electronic storage. Commercial devices based on this technology would have massively reduced power consumption and improved speed.`

A schematic of one kind of single electron transistor is represented in **Figure 2.12**, taken from [54]. A two-dimensional electron gas is confined perpendicular to GaAs and AlGaAs interface, and the confinement in the other directions is accomplished with negative potential applied to small confinement electrodes. Basically, it represents a quantum dot with ability to vary the electrostatic energy of the enclosed electrons.

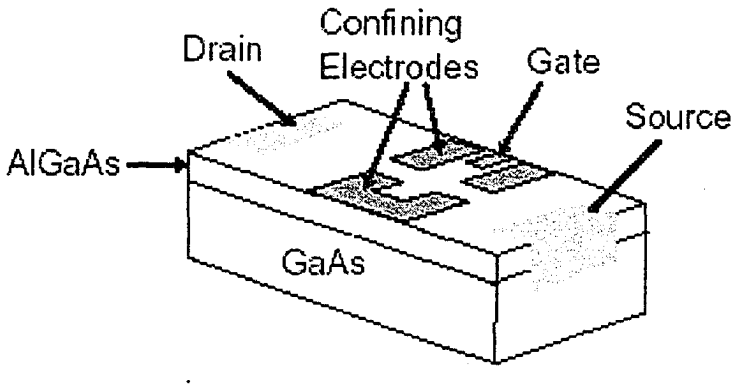

Figure 2.12: Schematic drawing of a single electron transistor (SET). Potential applied to confining electrodes changes the electrostatic energy of confined electrons, which affects the tunneling of electrons between source and drain. *(The picture was taken from the reference [54]).*

As the potential applied to the confining electrodes changes, it affects the electrostatic energy of the confined electrons. The source and drain contacts allow to drive electrons from an external circuit through the quantum dot. The rate of a tunneling of the external electrons between the source and the drain depends upon the electrostatic potential energy of the electrons confined inside the quantum dot.

The electrostatic potential energy experienced by an electron moving from the source to the drain is represented on the left part of **Figure 2.13**, taken from [60]. The right part of the **Figure 2.13** shows the conductance as the function of gate voltage. The conductance increases and decreases by several orders of magnitude almost periodically versus the gate voltage. Such a fine resonant structure of the conductance resembles lines of atomic spectra. That's why the single electron transistors were called artificial atoms.

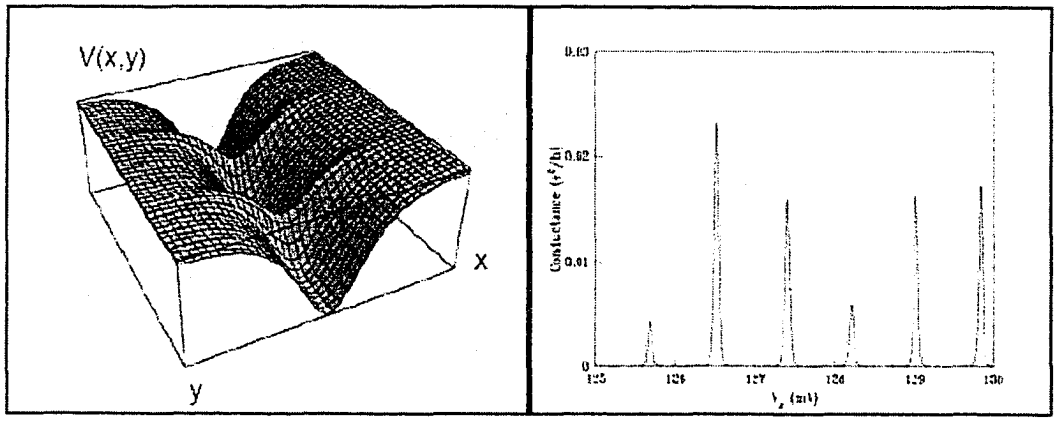

Figure 2.13: The electrostatic potential energy experienced by an electron moving from the source to the drain *(left figure)*. The conductance of the single electron transistor as the function of a gate voltage *(right figure)*. The conductance increases and decreases by several orders of magnitude almost periodically. Such type of dependence resembles lines of atomic spectra. As the result the single electron transistors were called artificial atoms. *(The picture was taken from the reference [60]).*

Chapter 3

Charged particle inside a square billiard: Classical case.

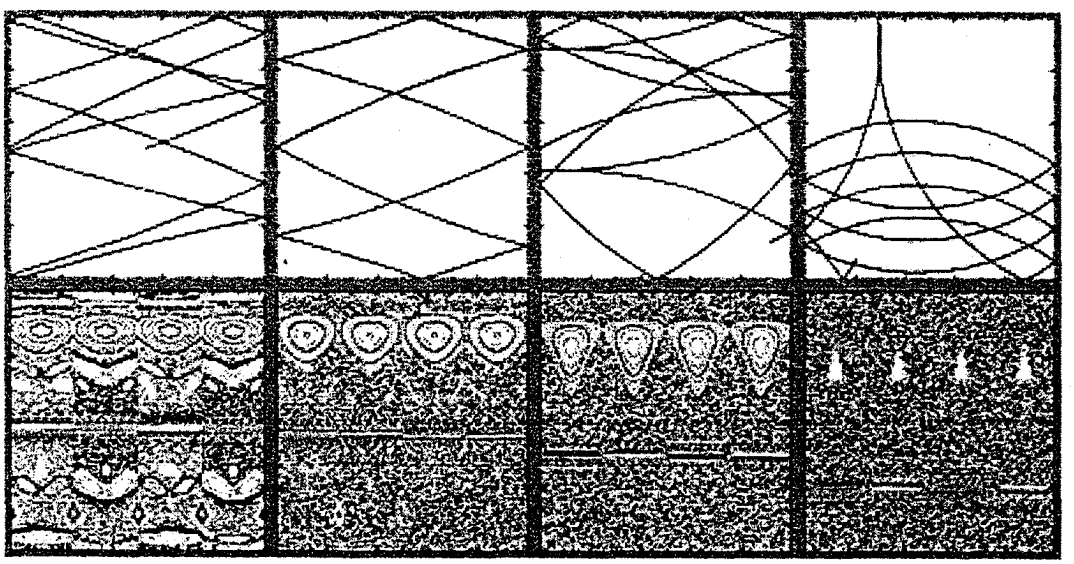

The first dynamical system detailed in this dissertation is called the Square Magnetic Billiard. It represents a two-dimensional charged particle confined inside a square enclosure with perfectly elastic walls. A perpendicular magnetic field of a variable intensity is applied perpendicularly to the plane of the confinement. The character of the dynamics of the system as well as the character of it's possible interaction with exter-

nal objects are completely determined by the strength of the magnetic field. In terms of the experimental motivation the Square Magnetic Billiard represents a model of a quantum dot maintained under sufficiently high temperature, which provides possibility of classical treatment of the dynamics of the system.

3.1 The Square Magnetic Billiard.

The Squáre Magnetic Billiard consists of a charged particle of charge q and mass m enclosed inside a square confinement. The length of the sides of the billiard is taken to be unity. The walls of the billiard are perfectly elastic. A uniform magnetic field $\vec{B}$ perpendicular to the plane of the billiard exerts a force on the particle.

The billiard is placed in the $xy-plane$, so the vector of the magnetic field is pointing in the $z-$direction. The Hamiltonian of a charged particle in an electromagnetic field is

$$\hat{H} = \frac{1}{2m}(\vec{p} - \frac{q}{c}\vec{A})^2 + q\phi. \tag{3.1}$$

We use the Landau gauge for the vector potential (see [48])

$$\vec{A} = \vec{A_L} = \begin{pmatrix} -By \\ 0 \\ 0 \end{pmatrix} \quad \phi = 0.$$

The Hamiltonian becomes

$$\hat{H} = \frac{1}{2m}(p_x + \frac{qB}{c}y)^2 + \frac{{p_y}^2}{2m}. \tag{3.2}$$

After substitution the **cyclotron frequency** $\omega_c = \frac{qB}{mc}$

$$\hat{H} = \frac{1}{2m}(p_x + m\omega_c y)^2 + \frac{{p_y}^2}{2m},$$

Hamilton's equations are

$$\begin{aligned} \dot{x} &= \tfrac{p_x + m\omega_c y}{m} \qquad & \dot{y} &= \tfrac{p_y}{m} \\ \dot{p_x} &= 0 \qquad & \dot{p_y} &= -\omega_c(p_x + m\omega_c y). \end{aligned} \tag{3.3}$$

Solutions of this Hamiltonian system are well known. A trajectory represents a circular path with the parameters of a circle adjusted according to the initial Cauchy conditions. In the case of the boundary presented, a trajectory consists of circular segments of cyclotron radius R_c between the points of specular reflection. An expression for the cyclotron radius as can be found by solving **(3.3)** is

$$R_c = \frac{1}{\omega_c}\sqrt{\frac{2E}{m}} = \frac{c}{qB}\sqrt{2mE}. \tag{3.4}$$

A few such trajectories for some arbitrary values of the cyclotron radius are represented in **Figure 3.1**.

The cyclotron radius is a convenient parameter for study of the character of the dynamics of the system.

3.2 Poincaré Sections.

Let us first consider Poincaré sections in order to investigate the character of the dynamics of the system. The Poincaré maps were plotted in terms of Birkhoff coordinates (Q, P) (see as an example [72]). The coordinate Q - is the coordinate of the bounce along the perimeter of the billiard normalized to unity. The second coordinate (P) is equal to the cosine of a bouncing angle. The Poincaré sections were obtained and plotted for different values of the cyclotron radius R_c. Some of the maps are represented in **Figure 3.2**. An extensive collection of the Poincaré sections for a wide range of parameters of the system are shown in **Appendix A**.

From the Poincaré sections **(Figure A)** the following can be concluded about the general features of the dynamics of the system with changing the cyclotron radius R_c:

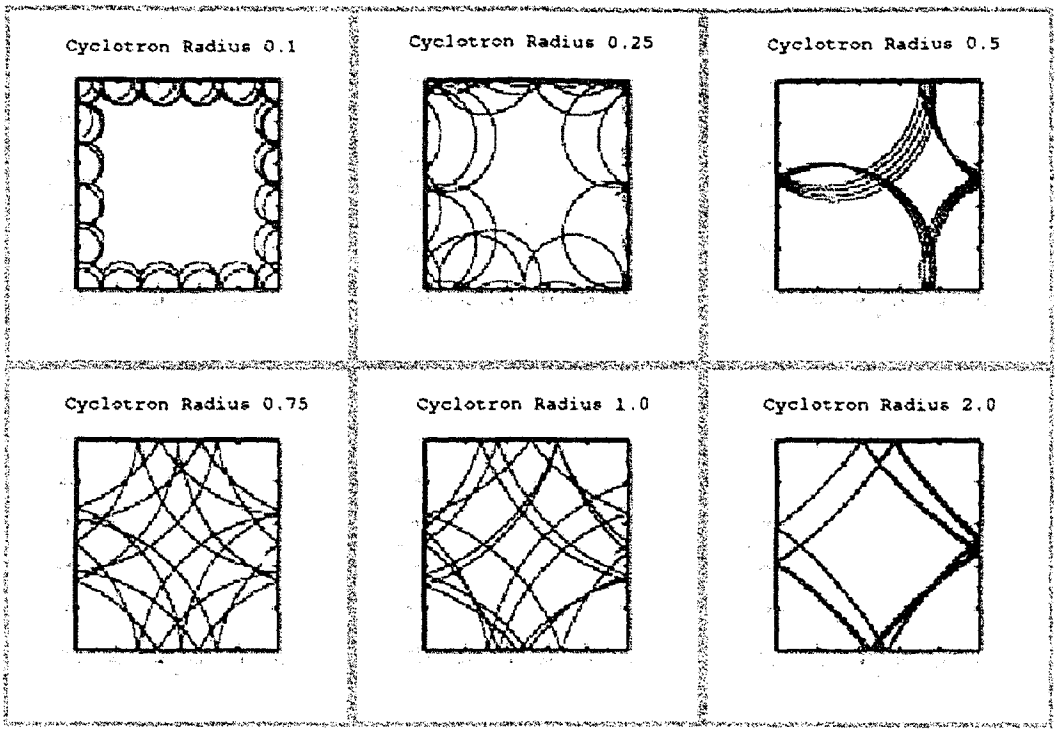

Figure 3.1: Sampling of trajectories for a particle inside a square magnetic billiard. The walls of the billiard are perfectly elastic. Trajectories of the particle between bounces are circles with radius equal to the *cyclotron* radius R_c

• For the case of a weak magnetic field (as the cyclotron radius is large $R_c \to \infty$) the dynamics of the system are regular - the Poincaré sections consist initially of straight lines that eventually becomes slightly bent, representing the KAM surfaces.

• As the magnitude of the magnetic field increases, but the value of the cyclotron radius remains larger than a characteristic scale of the system (in a range $3 < R_c < 100$), the system exhibits a mixed phase space. The Poincaré sections show the coexistence of chaotic and regular regions (the KAM tori) in the phase space. However, as the magnitude of the magnetic field increases more, KAM surfaces are destroyed and the degree of stochasticity of the system increases monotonically.

• As the magnitude of the magnetic field is such that a value of the cyclotron radius is of the same order as the size of the system (in a range $0.8 < R_c < 3$) nearly all the KAM tori are destroyed, and the system becomes almost totally chaotic. The highest

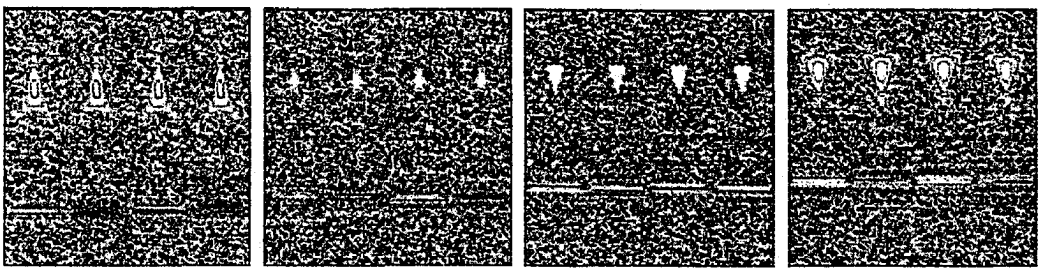

Figure 3.2: Four Poincaré sections for the values of the cyclotron radius that result in the mostly chaotic phase space $R_c = 0.9$ $R_c = 1.1$ $R_c = 1.3$ $R_c = 1.5$ The phase space is almost entirely chaotic except small, almost point-size islands of regularity remaining present in the top part of each map, as well as thin linear segments in the bottom part. The former correspond to trajectories of period 4, while the latter correspond to trajectories of period 2.

degree of stochasticity occurs when the cyclotron radius is approximately $R_c \approx 1.1$ **(see Figure 3.2)**. For this case, small almost point-size islands of regularity remain in the top of Poincaré map. Besides this, thin linear segments in the bottom part of each Poincaré section are formed by another regular trajectory. Detailed description of trajectories forming regular parts of the Poincaré maps is given later in this chapter.

- As the magnitude of the magnetic field continues to grow and thus the cyclotron radius becomes less than a characteristic size of the system (approximately $0.5 < R_c < 0.8$), the islands of regularity start to grow, suppressing the chaotic sea. Therefore as the cyclotron radius becomes smaller than the size of the system the chaos is suppressed and the system acquires a tendency to restore regularity.

- As the cyclotron radius lays in a range $R_c < 0.5$ the Poincaré sections do not correctly represent the character of the dynamics. This is the case because of the existence of closed circular trajectories that do not undergo bounces. The Poincaré map does not represent such trajectories, however as the cyclotron radius continues to decrease the relative amount of trajectories not undergoing any bounces increases and tends to unity (as $R_c \to 0$). All these trajectories are integrable, hence, as their relative volume grows, the system again acquires integrability.

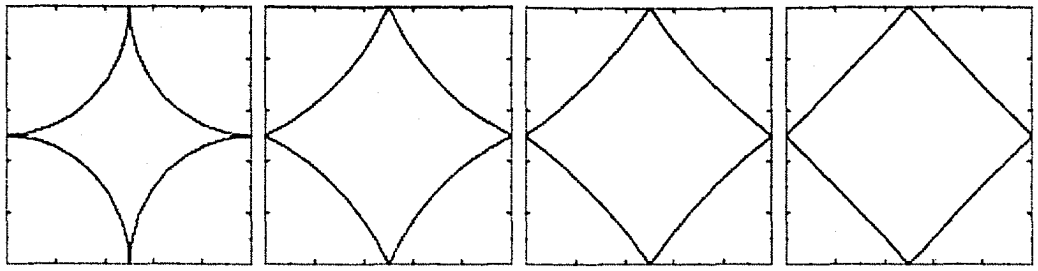

Figure 3.3: The periodic trajectories of period 4 for the values of the cyclotron radius corresponding to $R_c = 0.5,\ 1.0\ 2.0\ 10.0$. These sorts of trajectories form four islands at the top part of each Poincaré section. The islands become maximally squeezed for the mostly chaotic case, $R_c \approx 1.1$.

3.3 Periodic trajectories.

What kind of trajectories form the islands of integrability observed on the Poincaré maps **(see Figure 3.2)**? Four islands presented at the top part of each Poincaré section are formed by period four trajectories. Each of these trajectories start at the middle of the sides of the square . Few of these trajectories are represented in **Figure 3.3**. It can be found from geometric consideration that the bounce angle of such a trajectory is:

$$\theta_0^4 = \frac{\pi}{4} + \arcsin\frac{1}{2R_c\sqrt{2}}.$$

Another remarkable feature of all Poincaré sections corresponding to sufficiently large cyclotron radius ($R_c > 0.5$) are linear portions at the bottom part. This portion of the maps is formed by periodic trajectories of period 2. Some of these corresponding to different values of the cyclotron radius are represented in **Figure 3.4**. The bounce angle of this kind of trajectory is $\theta_0^2 = \frac{\pi}{2} + \arcsin\frac{1}{2R_c}$. An essential feature of the period 2 trajectories is translational symmetry: their shape does not depend upon the position of the bouncing point, but only upon the value of the bouncing angle. As the result they form linear segments on the Poncaré section.

If a value of the angle θ differs from the equilibrium value, the periodic trajectories are deformed and eventually completely destroyed. To examine this destruction we take

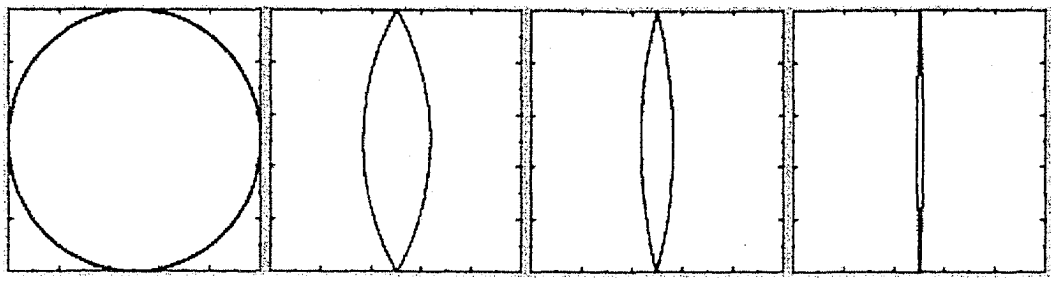

Figure 3.4: The periodic trajectories of period 2 for the values of the cyclotron radius corresponding to $R_c = 0.5,\ 1.0\ 2.0\ 10.0$. These types of trajectories form linear segments on each of the Poincaré sections. An essential feature of these sorts of trajectories is their translational symmetry. That is why they form linear segments, not isolated points on the Poincaré maps.

an initial angle to be slightly different from its equilibrium value corresponding to one or another type of the periodic trajectories $\theta = \theta_0 + \delta\theta$. As a consequence of such a deflection the periodic trajectories become deformed and eventually for sufficiently large values of deflection and sufficient time they leave the regular region and enter the chaotic one. The example evolution of periodic trajectories for the case of $R_c = 1.1$ is shown in **Figure 3.5**. An important feature of this trajectory is the fact that it becomes destroyed much faster and for smaller values of the initial deflection $\delta\theta$ compared with the destruction of trajectories of a similar kind, but corresponding to different values of the cyclotron radius. This is one more indication that the mostly chaotic the dynamics is for the case when the cyclotron radius $R_c \approx 1.1$. Deflection from this critical value leads to a growth of the robustness of the periodic trajectories of period 4. As for the periodic trajectories of period 2 (destruction is represented in Figure 3.6), their robustness does not depend dramatically upon a deflection of the cyclotron radius from its critical value. For a wide range of values of R_c these types of trajectories are destroyed similarly and equally fast.

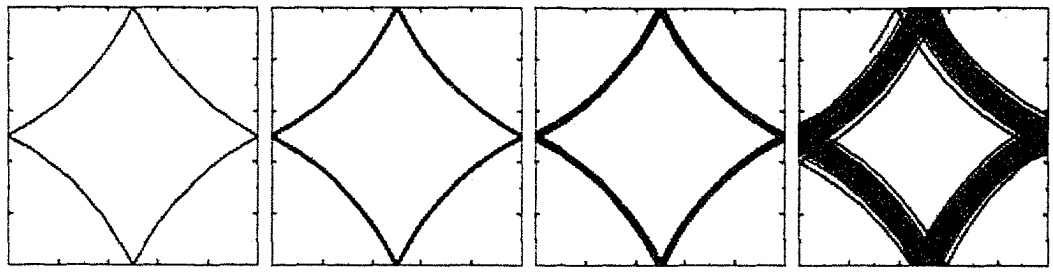

Figure 3.5: Destruction of period 4 trajectory for the cyclotron radius $R_c = 1.1$. For other values of the cyclotron radius the destruction develops in a similar way, but more slowly. To destroy the periodic trajectory as the value of the cyclotron radius differs from the critical value, a greater time as well as a greater values of the initial displacement from equilibrium are required.

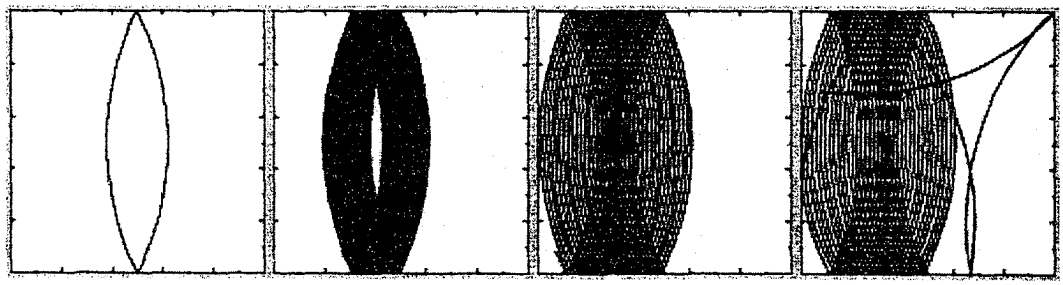

Figure 3.6: Destruction of period 2 trajectory for the cyclotron radius $R_c = 1.1$. For other values of the cyclotron radius the destruction develops in a similar way. Robustness of the period 2 trajectory is not sensitive to the value of the cyclotron radius. For a wide range of values of R_c the destruction happens equally fast.

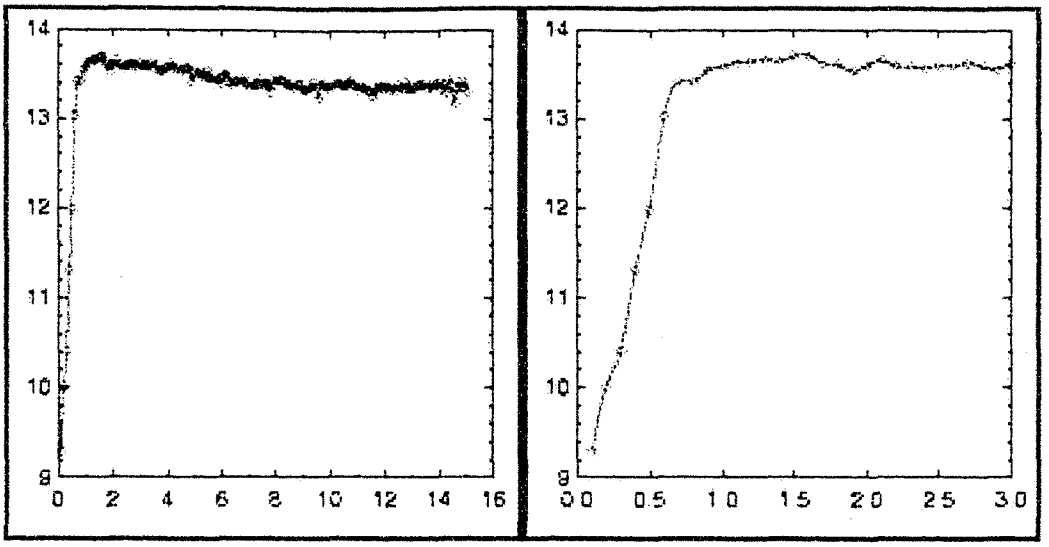

Figure 3.7: Lyapunov exponent versus cyclotron radius R_c. The picture on the right represents the initial portion of a complete graph placed on the left. The maximal Lyapunov exponent corresponds to $R_c \approx 1.1$ - when the cyclotron radius is the same order of magnitude as size of the system. Its value for this case is approximately equal to $\lambda_{max} \approx 13.6$. Results are consistent with those obtained by study of the Poncaré sections.

3.4 Lyapunov Exponent.

To get a better quantitative idea of the chaotic behavior of the system let us investigate how the Lyapunov exponent depends upon the cyclotron radius. To compute the Lyapunov exponent numerically we use the theorem stated and described in the Introduction **(Chapter 1.4)**.

Results of computations are represented in **Figure (3.7)**. The results are totally consistent with those obtained from analysis of the Poincaré sections (see Chapter 3.2). The system is mostly chaotic as the value of the cyclotron radius is approximately equal to the size of the system ($R_c \approx 1.1$). The maximal value of the Lyapunov exponent exists for this range of values of the cyclotron radius and it is approximately equal to $\lambda_{max} \approx 13.6$. The Lyapunov exponent quickly tends to zero as the cyclotron radius tends to zero which is the case of a strong magnetic field. On the other hand the right portion of the graph shows a monotonic decrease of the Lyapunov exponent as

the cyclotron radius is growing, meaning that the magnetic field tends to zero. Results are consistent with those obtained from the analysis of the Poincaré Sections (Chapter 3.2). The system is mostly chaotic when a value the cyclotron radius is of the order of the size of the system. As the cyclotron radius goes either far below or far above this critical value - the system acquires regularity and eventually becomes integrable for the both of the limiting cases ($R_c \to 0$ as well as $R_c \to \infty$).

3.5 Angle Action variables.

Angle Action variables (see references [30] or [47]) can be used to display a character of the dynamics of the system. If no external magnetic field is applied then the system is integrable. The actions in such a case are equal to

$$J_x = \frac{1}{2\pi} \oint p_x dx = \frac{|p_x|}{\pi}$$
$$J_y = \frac{1}{2\pi} \oint p_y dy = \frac{|p_y|}{\pi},$$

where it was taken into account that the side of the billiard is of the unit length. In terms of the actions the Hamiltonian is:

$$H = \frac{\pi^2}{2m} {J_x}^2 + \frac{\pi^2}{2m} {J_y}^2,$$

with corresponding frequencies:

$$\omega_x = \frac{\partial H}{\partial J_x} = \frac{\pi^2}{m} J_x \quad \omega_y = \frac{\partial H}{\partial J_y} = \frac{\pi^2}{m} J_y.$$

If the ratio of frequencies $\frac{\omega_x}{\omega_y}$ is a rational number, the motion is periodic - which means the trajectory is closed. Otherwise the trajectory is not closed and the motion is quasiperiodic. Some examples of closed as well as not closed (quasiperiodic) trajectories can be seen in the picture **(Fig. 3.8)**.

For the case of integrable motion the pair of actions (J_x, J_y) are constants of motion

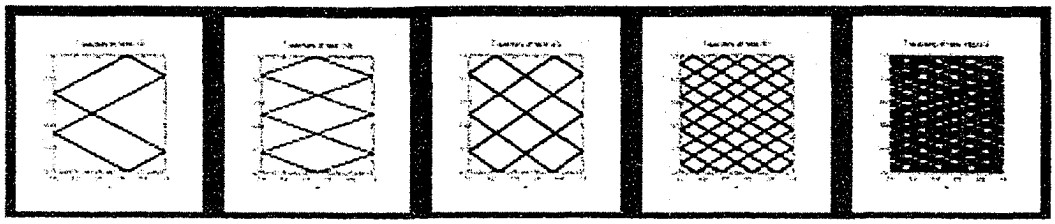

Figure 3.8: Periodic and quasiperiodic trajectories of the particle inside a square billiard without a magnetic field. The ratios of frequencies shown in the picture are correspondingly $\frac{1}{2}$ $\frac{1}{3}$ $\frac{2}{3}$ $\frac{4}{7}$ $\frac{1}{\pi}$

and they uniquely identify each trajectory. When a nonzero magnetic field is applied the actions are no longer integrals of motion. However, their statistical analysis could give important features of the dynamics.

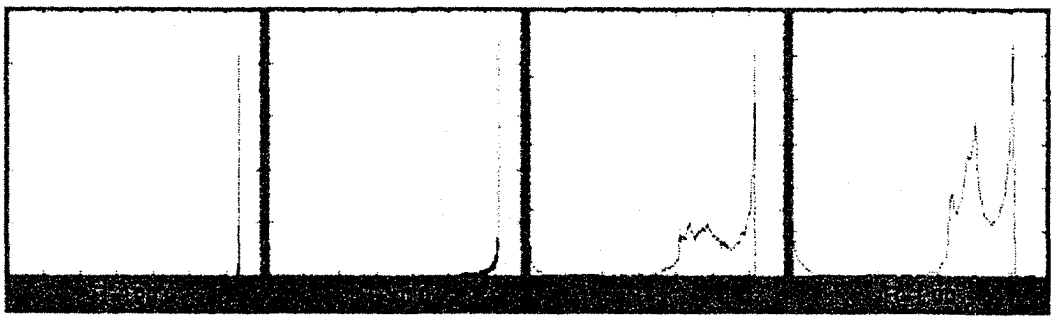

Figure 3.9: Histogram of action for various values of the cyclotron radius R_c. The first two pictures correspond to cases of a relatively small magnetic field as the result the histograms of actions are extremely narrow - close to a single vertical line. As the value of the cyclotron radius becomes comparable with the size of the system, the actions exhibit a broad distribution, which is an indicator of a high degree of stochasticity for the system.

Let us compute actions $J_j = \frac{1}{2\pi} \oint p_j dq_j$ for trajectories corresponding to various values of the cyclotron radius. Some results of the computations are represented in **Figure 3.9**. A more extensive collection of results, obtained for a wide range of the parameter α, is in Appendix A **(Figure A.4)**. It can be seen on the histograms that as the magnetic field is small the histogram of actions is extremely narrow, close to a single vertical line. This indicates that the system is initially integrable. As the magnetic field increases it can be seen that behavior of the actions becomes increasingly random. A

spectrum of possible values of actions for the single trajectory becomes broader as the cyclotron radius decreases. However, we always observe a sharp maximum on the right side of the histogram. To figure out what kind of trajectories form those maxima let us evaluate the action for the periodic trajectories (Figure 3.4)

$$J_x = \frac{1}{2\pi}\oint p_x dx \quad J_y = \frac{1}{2\pi}\oint p_y dy.$$

For the circular segments of the trajectories

$$y = y_C + R_c \sin(\omega_c t + \phi_0) \quad p_y = m\omega_c R_c \cos(\omega_c t + \phi_0),$$

therefore,

$$J_y = \frac{1}{2\pi} m(\omega_c R_c)^2 \oint \cos(\omega_c t + \phi_0)^2 dt = \frac{m}{4\pi}(\omega_c R_c)^2 (\oint dt + \oint \cos(2(\omega_c t + \phi_0))dt).$$

The first integral is just equal to a period T of the trajectory. Thus we have

$$J_y = \frac{TE}{2\pi} + \frac{m}{4\pi}(\omega_c R_c)^2 \oint \cos(2(\omega_c t + \phi_0))dt. \tag{3.5}$$

In the expression above E stands for the kinetic energy of the particle.

The second integral is

$$(\omega_c R_c)^2 \oint \cos(2(\omega_c t + \phi_0))dt = \frac{1}{m^2}\oint ({p_y}^2 - {p_x}^2)dt.$$

Thus the result is

$$J_y = \frac{TE}{2\pi} + \frac{1}{4\pi m}\oint ({p_y}^2 - {p_x}^2)dt. \tag{3.6}$$

Let us evaluate this integral for the trajectory of period 2 for limiting cases. First let us consider the case when $R_c \to \infty$. The period 2 trajectory in such a case is

R_c	10	5	2	1.5	1.1	1	0.9	0.8	0.7	0.6	0.5
J	0.318	0.317	0.313	0.301	0.309	0.298	0.293	0.286	0.275	0.258	0.250

Table 3.1: Actions for the period two trajectories.

represented by the straight line segment perpendicular to the horizontal side. Therefore $p_x = 0$ ${p_y}^2 = 2mE$, thus

$$J_y = \frac{TE}{2\pi} + \frac{TE}{2\pi} = \frac{TE}{\pi}.$$

Another limiting case is $R_c = 0.5$. The trajectory in this occasion represents a circle inscribed inside the billiard. The second integral becomes

$$\oint ({p_y}^2 - {p_x}^2)dt = \oint (\cos(\phi)^2 - \sin(\phi)^2)d\phi = 0.$$

Therefore the action $J_y = \frac{TE}{2\pi}$.

The value of the action for arbitrary values of R_c lies between these two limiting cases and can be computed numerically. Results of computations are shown in **Table 3.1**. The mass and the speed of the particle was taken to be equal to one. Therefore for large R_c we expect the action to be equal to $\frac{1}{\pi}$ and this agrees with the tabular data. As for the other limiting case, $R_c = 0.5$, the expected value is $\frac{1}{4}$. This as well agrees with the numerical data.

Now let us carry out similar computations for trajectories of period four. Trajectories of this kind have two axes of symmetry. This leads to the fact that a combination of dynamical variables ${p_y}^2 - {p_x}^2$ becomes a periodic function oscillating between maximal and minimal values that are equal in absolute values, but opposite in signs. Some examples of this dynamical function are represented in **Figure 3.10**. This sort of behavior leads to the fact that $\oint ({p_y}^2 - {p_x}^2)dt$ vanishes and actions for these types trajectories are equal to

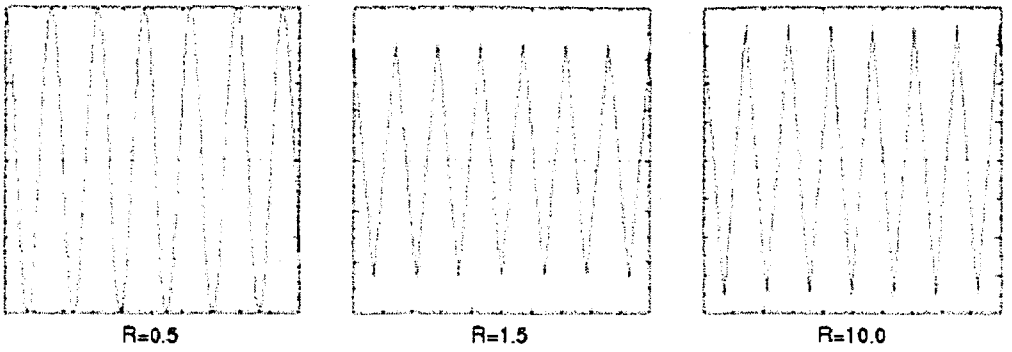

Figure 3.10: Time evolution of the dynamical function ${p_y}^2 - {p_x}^2$ along the trajectory of period four. The average value computed for one period is equal to zero as the function oscillates periodically between its maximal and minimal values. These values are equal in absolute value, but opposite in sign.

R_c	10	5	2	1.5	1.1	1	0.9	0.8	0.7	0.6	0.5
J	0.225	0.225	0.226	0.227	0.229	0.230	0.231	0.232	0.235	0.240	0.250

Table 3.2: Actions for the period four trajectories

.

$$J_x = J_y = \frac{TE}{2\pi}. \tag{3.7}$$

For the limiting case of a large cyclotron radius the trajectory represents a square inscribed inside the billiard. If the speed and the mass are equal to unity the period $T = 2\sqrt{2}$. Therefore, the actions become $J_x = J_y = \frac{\sqrt{2}}{2\pi}$.

For the case of $R_c = 0.5$ the trajectory represents the circle inscribed inside the billiard but being cut on four parts,each part reflected. Therefore we expect the action to be equal to the action of the period two trajectory of the same radius $J_x = J_y = \frac{1}{4}$.

For arbitrary values of the cyclotron radius actions were computed numerically. The results are represented in **Table 3.2.** We can see that for the special cases our results agree with what was expected.

The values of actions shown in the Tables **(3.1) and (3.2)** can be compared with sharp peaks that are seen on the histograms **(Figure A.4 Appendix A)**. These values in the table **(3.1)** correspond to the values of the maxima on the right side of each of

the histograms. Therefore, the most of the time during its motion the particle spends in the vicinity of the period 2 trajectory. This trajectory becomes highly visited, or, as this effect is called in references [95] and [96] - it becomes sticky. As the cyclotron radius lies in a range that corresponds to mostly stochastic behavior of the system - R_c is of the order of the size of the system - the other maxima appears to be noticeable to the left of the first one. Similar comparisons with the Table **(3.2)** show that this maxima are formed by the periodic trajectories of period 4 (Figure 3.3). Hence as the system becomes more chaotic the key role of all of its periodic trajectories becomes more evident. This is in complete agreement with the theory of ergodic systems developed and described in reference [20]. All the statistical behavior of the stochastic system can be obtained by computing some averages along the shortest periodic trajectories, which form the skeleton of each chaotic system.

3.6 Spectral characteristics

The spectral method is another way to distinguish chaotic dynamics. It is based on the fact of existence of integrals of motion expressible in terms of the action-angle variables for integrable dynamical systems. Let us consider an arbitrary trajectory of an integrable dynamical system. Using a canonical transformation (see for details [30] or [47]) any trajectory can be expressed in terms of the action-angle variables. This yields a simple form for the time evolution equation:

$$\theta_j(t) = \omega_j t \quad \omega_j = \frac{\partial H}{\partial J_j}.$$

In the case of finite motion the inverse canonical transformation to the Cartesian coordinates will yield in two dimensions:

$$x_j = \sum_{k=-\infty}^{+\infty} \sum_{n=-\infty}^{+\infty} a_{kn}(J_x, J_y) e^{ik\omega_x t} e^{in\omega_y t}.$$

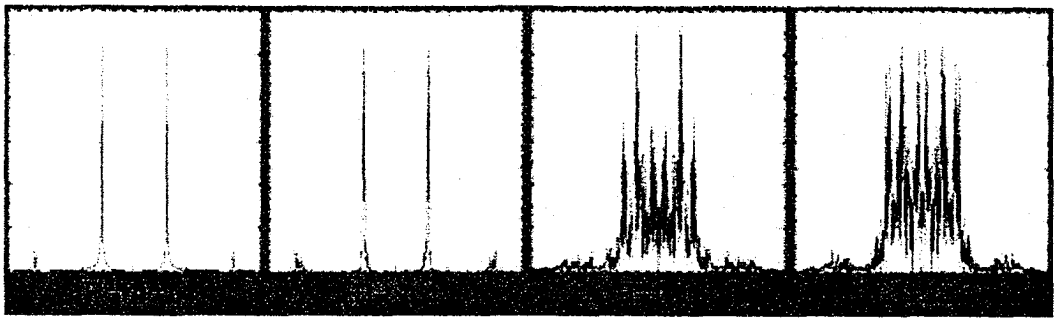

Figure 3.11: Fourier spectrum of a single trajectory for various values of the cyclotron radius R_c. The first two pictures correspond to cases of a relatively weak magnetic field. As a result the spectra are discrete - an indicator of the integrability of the system. As the value of the cyclotron radius becomes comparable with the size of the system - the Fourier spectra become continuous, which is an indicator of a high degree of stochasticity in the system.

This functions is represented by the sum of harmonics, therefore its Fourier spectrum must be discrete. As the dynamics becomes more and more chaotic, the actions exhibit a random behavior, and the Fourier spectrum of the trajectory becomes continuous. Fourier spectra of some trajectories for various values of the cyclotron radius were computed numerically and some results are represented in the pictures **(Figure 3.11)**. A more extensive collection of the computational results is placed in the Appendix A **(Figure A)**.

What is seen is exactly what was anticipated. Initially, for small magnetic fields (as the cyclotron radius is large), the motion is close to integrable and the Fourier spectrum is discrete. As the cyclotron radius decreases, the Fourier spectrum becomes continuous and acquires mostly uniform continuous shape when the value of the cyclotron radius becomes equal to the size of the system. As the cyclotron radius continues to reduce its value, coming far below the size of the system, the Fourier spectrum is being again separated on thin isolated strips, becoming discrete again for large values of the magnetic field (as $R_c \to 0$).

This way the study of the system dynamics by means of the Fourier transform of a single trajectory confirms results obtained in previous sections of this chapter. The

system is integrable when no external magnetic field applied, then its stochasticity growth up to some critical value of the cyclotron radius (as before this critical value is $R_c \approx 1.1$). As the magnetic field continuous to grow, the systems starts to restore its integrability and becomes integrable again as $R_c \to 0$.

3.7 Summary

The dynamics of the classical square magnetic billiard was studied in details in this chapter. Different methods were applied and the results of all of them illustrated the following general features of the dynamics of the system:

- When no external magnetic field is applied the system is integrable. As a weak magnetic field is applied (such as $R_c >\approx 100$) the system's dynamics still continues to be regular. Then its KAM surfaces are slightly deformed.

- As the magnitude of the magnetic field increases but the value of the cyclotron radius remains larger than a characteristic scale of the system (lies in a range $2 < R_c < 100$), the system exhibits a mixed phase spaces. The stochasticity increases as the cyclotron radius continues to decrease. The mixed phase space is continuously transmitted to the chaotic one as more and more of the KAM surfaces are destroyed. The Lyapunov exponent of the system keeps growing approximately linearly.

- As the value of the cyclotron radius is of the same order as the size of the system (approximately in a range $0.8 < R_c < 2$) the system is mostly chaotic. Almost all the KAM tori are destroyed. The maximal degree of the destruction as well as the maximal value of the Lyapunov exponent corresponds to an approximate value of the cyclotron radius $R_c \approx 1.1$. The maximal Lyapunov exponent is approximately equal to $\lambda_{max} \approx 13.6$.

- As the value of the cyclotron radius continues to decrease, the system starts to restore its integrability. The Lyapunov exponent quickly goes to zero as $R_c \to 0$. This happens because almost all trajectories with very small cyclotron radius do not undergo

collisions. Therefore, they move in circular trajectories with constant energy and angular momentum. Hence, the dynamics becomes integrable.

Study of the actions revealed stickiness of short periodic trajectories, especially of the period 2 trajectories. However, for the mostly chaotic case, this essentially increases stickiness of other short periodic trajectories, in particular of a 'diamond-looking' periodic trajectory of period 4. Thus the growth of an ergodicity of the system increases the key role of its shortest periodic trajectories (see reference [20]).

Chapter 4

Charged particle inside a square billiard: Quantum case.

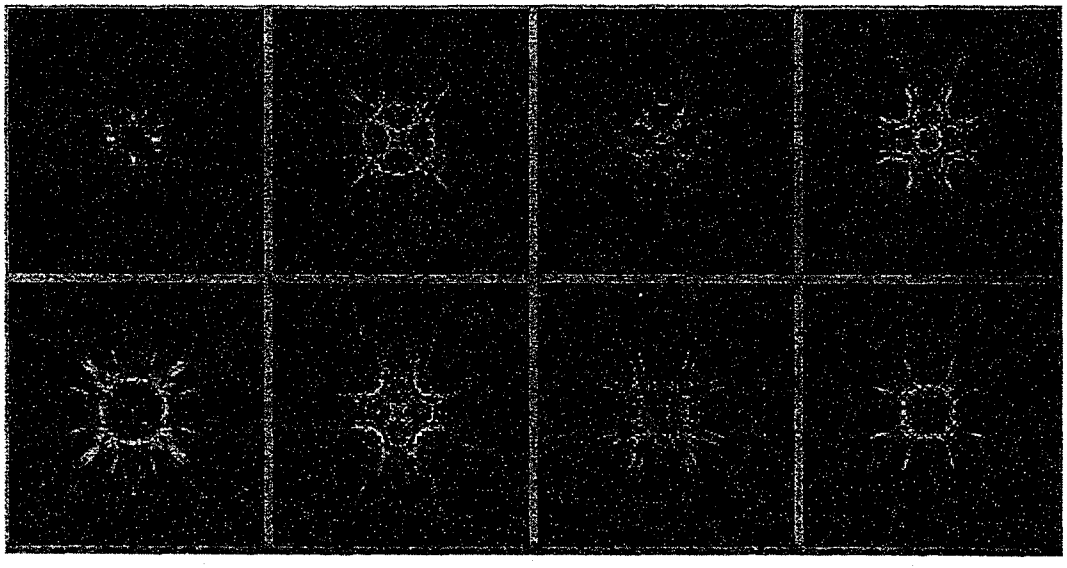

This chapter represents the quantum mechanical treatment of the dynamical system examined in the previous chapter. In terms of the experimental motivation, the Square Magnetic Billiard solved quantum mechanically represents a model of a quantum dot maintained under sufficiently low temperature. To determine the character of the dynamics of the system as well as its possible interaction with external objects, we need to

solve the Schrodinger equation, and determine a spectrum of the energy eigenvalues and examine the structure of the corresponding eigenfunctions of the system. The methods, developed and tested in this chapter will be used later to study more realistic models of quantum dots, ones containing two or more strongly interacting particles.

4.1 Quantum Square Magnetic Billiard.

We start with the Hamiltonian **(3.2)**

$$\hat{H} = \frac{1}{2m}(p_x + \frac{qB}{c}y)^2 + \frac{{p_y}^2}{2m} \ ,$$

and use the symmetric gauge for the vector potential (see [48])

$$\vec{A} = \begin{pmatrix} -\frac{By}{2} \\ \frac{Bx}{2} \\ 0 \end{pmatrix} \qquad \phi = 0.$$

Replacing the dynamical variables by their operators

$$x_j \to x_j \quad p_j \to -i\hbar\frac{\partial}{\partial x_j},$$

and using the same expression for the cyclotron frequency as in the previous chapter

$$\omega_c = \frac{qB}{mc}.$$

Therefore the quantum Hamiltonian of the system becomes:

$$\begin{aligned} &\hat{H} = -\tfrac{\hbar^2}{2m}\nabla^2 - i\hbar\tfrac{\omega_c}{2}(y\tfrac{\partial}{\partial x} - x\tfrac{\partial}{\partial y}) + \tfrac{m{\omega_c}^2}{8}(x^2+y^2) \\ &\nabla^2 = \tfrac{\partial^2}{\partial x^2} + \tfrac{\partial^2}{\partial y^2}. \end{aligned} \tag{4.1}$$

As before, we consider a particle placed inside a perfectly elastic two-dimensional

square billiard whose sides equal to unity. Therefore, the boundary conditions are:

$$\Psi(t,x,y)|_{x=-0.5} = \Psi(t,x,y)|_{x=0.5} \Psi(t,x,y)|_{y=-0.5} = \Psi(t,x,y)|_{y=0.5} = 0.$$

In order to understand some general properties of the dynamics of the confined charged particle in the presence of the external magnetic field, let us start with the application of simple perturbative methods (see [59]).

4.2 Perturbation Theory: weak magnetic field.

The time-independent Schrodinger equation $\hat{H}\psi = E\psi$ is

$$-\frac{\hbar^2}{2m}\nabla^2\psi - i\hbar\frac{\omega_c}{2}(y\frac{\partial}{\partial x} - x\frac{\partial}{\partial y})\psi + \frac{m\omega_c{}^2}{8}(x^2+y^2)\psi = E\psi$$
$$\nabla^2 = \frac{\partial^2}{\partial x^2} + \frac{\partial^2}{\partial y^2}.$$

Introducing parameters

$$\alpha = \frac{m\omega_c}{\hbar} \qquad \epsilon = \frac{2mE}{\hbar^2} \qquad R_c = \frac{1}{\omega_c}\sqrt{\frac{2E}{m}} = \frac{\sqrt{\epsilon}}{\alpha}$$

the Schrodinger equation becomes

$$-\nabla^2\psi - i\alpha(y\frac{\partial}{\partial x} - x\frac{\partial}{\partial y})\psi + \frac{\alpha^2}{4}(x^2+y^2)\psi = \epsilon\psi. \tag{4.2}$$

Let us split the Hamiltonian into two parts

$$\hat{H}_0 = -\nabla^2 \quad \hat{H}_1 = -i\alpha(y\frac{\partial}{\partial x} - x\frac{\partial}{\partial y}) + \frac{\alpha^2}{4}(x^2+y^2),$$

and consider $\hat{H}_1$ as a perturbation with a small parameter α (how small will be clarified later).

The solutions of unperturbed equation $\hat{H}_0\psi = \epsilon\psi$ that satisfy the Dirichlet boundary conditions on the square of the unit side are well known. The normalized eigenfunctions

Level (k_x, k_y)	(1,1)	(2,2)	(3,3)
Energy	$19.739 + 0.0163\alpha^2$	$78.957 + 0.0353\alpha^2$	$177.653 + 0.0388\alpha^2$
Level (k_x, k_y)	(4,4)	(6,6)	(7,7)
Energy	$315.827 + 0.0401\alpha^2$	$710.611 + 0.0410\alpha^2$	$967.22 + 0.0411\alpha^2$

Table 4.1: Non-degenerate energy levels.

of $\hat{H}_0$ are

$$\phi_{kn} = \frac{1}{2}\sin(\pi k(x+0.5))\sin(\pi n(y+0.5)) \quad k = 1,2,\ldots \quad n = 1,2,\ldots ,$$

where the center of the billiard is taken to be the point $(0,0)$. The corresponding eigenvalues of $\hat{H}_0$ are

$$\epsilon_{kn} = \pi^2(k^2+n^2) \quad k = 1,2,\ldots \quad n = 1,2,\ldots$$

According to time-independent perturbation theory, the first order correction to an energy eigenvalue of *a non-degenerate state* ϵ_j is

$$\Delta\epsilon_j = \langle\phi_j|\hat{H}_1|\phi_j\rangle ,$$

which for the ground state leads to

$$\Delta\epsilon_0 = \frac{1}{4}\int_{-0.5}^{0.5} dx \int_{-0.5}^{0.5} dy \ \sin(\pi(x+0.5))\sin(\pi(y+0.5))\hat{H}_1(\sin(\pi(x+0.5))\sin(\pi(y+0.5))).$$

Numerical evaluation of the last integral yields:

$$\Delta\epsilon_0 \approx 0.0163\alpha^2.$$

In exactly the same manner corrections to all other non-degenerate states can be computed. The numerical results for the first few non-degenerate states are shown in Table 4.1

At this point, we can find the range of parameter values for which that perturbation theory yields reliable results. To do this, we apply the condition that the corrections to each of the energy eigenvalues is much less than the energy eigenvalue itself. This gives (we use results for the ground state): $0.0163\alpha^2 \ll 19.739$. Thus the range of parameters such that time-independent perturbation method yields reliable results is

$$\alpha \ll 35.$$

Let us now apply the method to degenerate levels. Consider an unperturbed N-times degenerate level. There exist N orthonormal eigenfunctions that belong to this level $\phi_1, \ldots, \phi_N$. We are looking for a solution of the perturbed equation of the form

$$\psi = \sum a_j \phi_j.$$

In the last expression a_j are undefined coefficients. Substitution into the Schrodinger equation yields

$$\hat{H}_0\psi + \hat{H}_1\psi = E\psi \implies (\epsilon - E)\sum a_j\phi_j + \hat{H}_1\psi = 0.$$

We multiply both parts by $\langle\phi_i|$, integrate and use the closure relation. This yields:

$$(\epsilon - E)\sum a_j\delta_{ij} + \sum a_j h_{1ij} = 0.$$

In the last expression h_{1ij} denotes matrix elements of the perturbation $h_{1ij} = \langle\phi_i|\hat{H}_1|\phi_j\rangle$. Labeling the correction to the energy level as ΔE we obtain a matrix equation

$$\sum a_j(h_{1ij} - \Delta E\delta_{ij}) = 0.$$

A homogeneous matrix equation has nontrivial solutions if its determinant is zero. Hence the condition $\det(h_{1ij} - \Delta E\delta_{ij}) = 0$ gives us corrections to the degenerate energy levels.

Thus as an example for the first excited levels ($\epsilon_{12} = \epsilon_{21} = 5\pi^2$) the matrix of perturbation is

$$\begin{pmatrix} 0.02583\alpha^2 + 0\,i & 0 - 0.96067\alpha\,i \\ 0 + 0.96067\alpha\,i & 0.02583\alpha^2 + 0\,i \end{pmatrix}.$$

Therefore the equation for ΔE is

$$(0.02583\alpha^2 - \Delta E)^2 = (0.96067\alpha)^2$$

and thus initially degenerate energy levels becomes split on two separate levels

$$\epsilon_1^{\pm} = 5\pi^2 + 0.02583\alpha^2 \pm 0.96067\alpha\,.$$

If the same procedure is performed for the second excited levels $\epsilon_{13} = \epsilon_{31} = 10\pi^2$ the matrix of perturbation is

$$\begin{pmatrix} 0.02759\alpha^2 + 0i & 0 + 0i \\ 0 + 0i & 0.02759\alpha^2 + 0i \end{pmatrix}$$

and the energy levels continue to be degenerate, both energy values quadratically depending upon α as

$$\epsilon_3^{\pm} = 10\pi^2 + 0.02759\alpha^2.$$

Similarly, corrections to the other degenerate energy levels were computed. A summary of the results for the few lowest energy levels is represented in **Figure 4.1**. The general picture of the behavior of the energy levels under the action of a weak magnetic field can be outlined as follows:

• The energy eigenvalues of all the non-degenerate states ($\psi_{00}, \psi_{11} \ldots$) grow quadratically with α. This results from the fact that the perturbation is increasing quadratically with α.

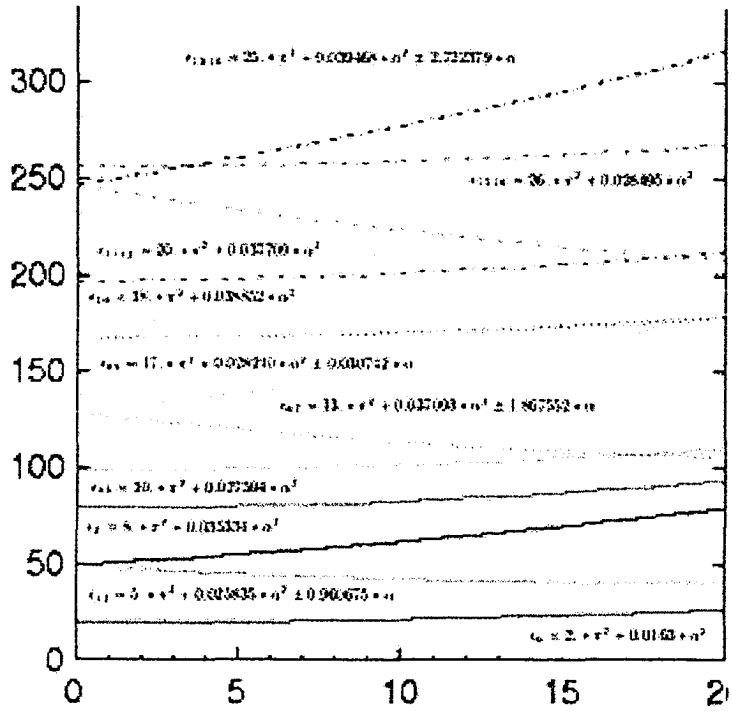

Figure 4.1: Energy values ϵ versus α for the few lowest energy states. The energy values of all the non-degenerate states are growing quadratically with α. Some of the initially degenerate states become split due to the action of the magnetic field. In this case the energy of one of them is growing quadratically, while the energy of the second one is linearly decreasing. Some of the initially degenerated levels continue to be degenerated, the energy values of the both of them growing as α^2.

- The degeneracy is not completely broken as the perturbation is applied. Some of the levels continue to be degenerate (as an example the second excited level (ψ_{13}, ψ_{31})). In this case the energy eigenvalues of both of states that belong to the degenerate level grow quadratically with α.

- Some of the initially degenerate levels become split (as an example the first excited level (ψ_{12}, ψ_{21})). In this case one of the energy eigenvalues grows quadratically with α, while the other exhibits a linear decrease in its value.

The results obtained in this section are valid for small values of the parameter α, which means a weak external magnetic field. As the magnetic field becomes stronger, perturbation methods do not give reliable results. Other methods will be developed

later in this chapter to deal with the case of a strong magnetic field. However, the results obtained in this section can be used as an indicator of the reliability of future methods, in the sense that they have to give results consistent with those obtained in this section for small values of parameter α.

4.3 Time-independent Schrodinger equation - case of an unconfined particle: Separation of variables.

Consider the time-independent Schrodinger equation **(4.2)**

$$-\frac{\hbar^2}{2m}\nabla^2\psi - i\hbar\frac{\omega_c}{2}(y\frac{\partial}{\partial x} - x\frac{\partial}{\partial y})\psi + \frac{m{\omega_c}^2}{8}(x^2+y^2)\psi = E\psi$$
$$\nabla^2 = \frac{\partial^2}{\partial x^2} + \frac{\partial^2}{\partial y^2}.$$

In polar coordinates

$$x = \rho\cos\theta \quad y = \rho\sin\theta$$
$$\nabla^2 = \frac{\partial^2}{\partial\rho^2} + \frac{1}{\rho}\frac{\partial}{\partial\rho} + \frac{1}{\rho^2}\frac{\partial^2}{\partial\theta^2}$$
$$x\frac{\partial}{\partial y} - y\frac{\partial}{\partial x} = \frac{\partial}{\partial\theta}$$

the Schrodinger equation becomes

$$-\frac{\hbar^2}{2m}\nabla^2\psi + i\hbar\frac{\omega_c}{2}\frac{\partial}{\partial\theta} + \frac{m{\omega_c}^2}{8}\rho^2\psi = E\psi. \tag{4.3}$$

This equation allows for the separation of variables. Looking for a solution in the form $\psi = f(\rho)e^{iM\theta}$, we obtain the following equation for the radial part $f(\rho)$

$$-\frac{\hbar^2}{2m}(f'' + \frac{1}{\rho}f' - \frac{1}{\rho^2}M^2 f) - \hbar M\frac{\omega_c}{2}f + \frac{m{\omega_c}^2}{8}\rho^2 f = Ef.$$

For eigenfunction ψ to be single-valued we impose the requirement that M is a positive integer $M = 0, \pm1, \pm2, \pm3\ldots$ We use parameters as previously defined:

$$\epsilon = \frac{2mE}{\hbar^2} \quad \alpha = \frac{m\omega_c}{\hbar}.$$

The radial equation becomes

$$f'' + \frac{1}{\rho}f' - \frac{M^2}{\rho^2}f + \alpha M f - \frac{(\alpha\rho)^2}{4}f + \epsilon f = 0. \tag{4.4}$$

Transformation of variables

$$\chi = \frac{\alpha\rho^2}{2}$$

yields

$$2\chi f'' + 2f' - \frac{M^2}{2\chi}f + Mf - \frac{\chi}{2}f + \frac{\epsilon}{\alpha}f = 0.$$

Substituting

$$f = \chi^{\lambda} e^{-\frac{\chi}{2}}\phi\,,$$

and combine like terms, we obtain

$$2\chi\phi'' + (4\lambda + 2 - 2\chi)\phi' + (2\lambda^2 - \frac{M^2}{2})\frac{\phi}{\chi} + (M - 1 - 2\lambda + \frac{\epsilon}{\alpha})\phi = 0.$$

Substituting $\lambda = \frac{|M|}{2}$ yields

$$\chi\phi'' + (|M| + 1 - \chi)\phi' + (\frac{\epsilon}{2\alpha} - \frac{|M| + 1 - M}{2})\phi = 0, \tag{4.5}$$

which has the form of the well-known **confluent hypergeometric equation** (see [1])

$$xy'' + (c - x)y' - ay = 0. \tag{4.6}$$

The solution of **(4.6)** (finite at the origin) is the **confluent hypergeometric function**

of the first kind ${}_1F_1(a,b,x)$ (see [1])

$$ {}_1F_1(a,b,x) = 1 + \frac{a}{b}x + \frac{a(a+1)}{b(b+1)}\frac{x^2}{2!} + \frac{a(a+1)(a+2)}{b(b+1)(b+2)}\frac{x^3}{3!} + \ldots = \sum_{k=0}^{\infty}\frac{(a)_k}{(b)_k}\frac{x^k}{k!} \tag{4.7} $$

$(a)_k$ $(b)_k$ are Pochhammer symbols.

Therefore, an unnormalized set of solutions of equation **(4.3)** is given by:

$$ \psi_{\epsilon M}(\rho,\theta) = (\frac{\alpha\rho^2}{2})^{\frac{|M|}{2}} e^{-\frac{\alpha\rho^2}{4}} {}_1F_1(\frac{|M|+1-M}{2} - \frac{\epsilon}{2\alpha}, |M|+1, \frac{\alpha\rho^2}{2})e^{iM\theta}. $$

It is known from the properties of hypergeometric functions (see [1]) that the series **(4.7)** diverges unless truncated to a finite number of terms. Hence, in the absence of boundary conditions the series **(4.7)** must terminate. This leads to the condition:

$$ \frac{|M|+1-M}{2} - \frac{\epsilon}{2\alpha} = -n \;\; n = 0,1,2,\ldots $$

This last condition helps to allocate the spectrum of energy eigenvalues in the absence of the boundary conditions:

$$ \epsilon = \begin{cases} \alpha \;\; M \geq 0 \\ \alpha + 2|M|\alpha \;\; M < 0. \end{cases} $$

The equidistant set of energy levels is well known (see as an example [49]) and are called **Landau levels**:

$$ \epsilon_n = \alpha(2n+1) \;\; n = 0,1,2,\ldots $$
$$ E_n = \frac{\hbar^2}{2m}\alpha(2n+1) = \hbar\omega_c(n+\tfrac{1}{2}) \;\; n = 0,1,2,\ldots $$

Each Landau level is infinitely degenerate. The unnormalized eigenfunctions corresponding to the n-th Landau level $\epsilon_n = \alpha(2n+1)$ are

$$\psi_{nM} = \begin{cases} (\frac{\alpha\rho^2}{2})^{\frac{M}{2}} e^{-\frac{\alpha\rho^2}{4}} \, {}_1F_1(-n, M+1, \frac{\alpha\rho^2}{2}) e^{iM\theta} & M = 0, 1, 2, 3, \ldots \\ (\frac{\alpha\rho^2}{2})^{\frac{|M|}{2}} e^{-\frac{\alpha\rho^2}{4}} \, {}_1F_1(|M| - n, |M|+1, \frac{\alpha\rho^2}{2}) e^{iM\theta} & M = -1, -2, \ldots, -n+1. \end{cases} \tag{4.8}$$

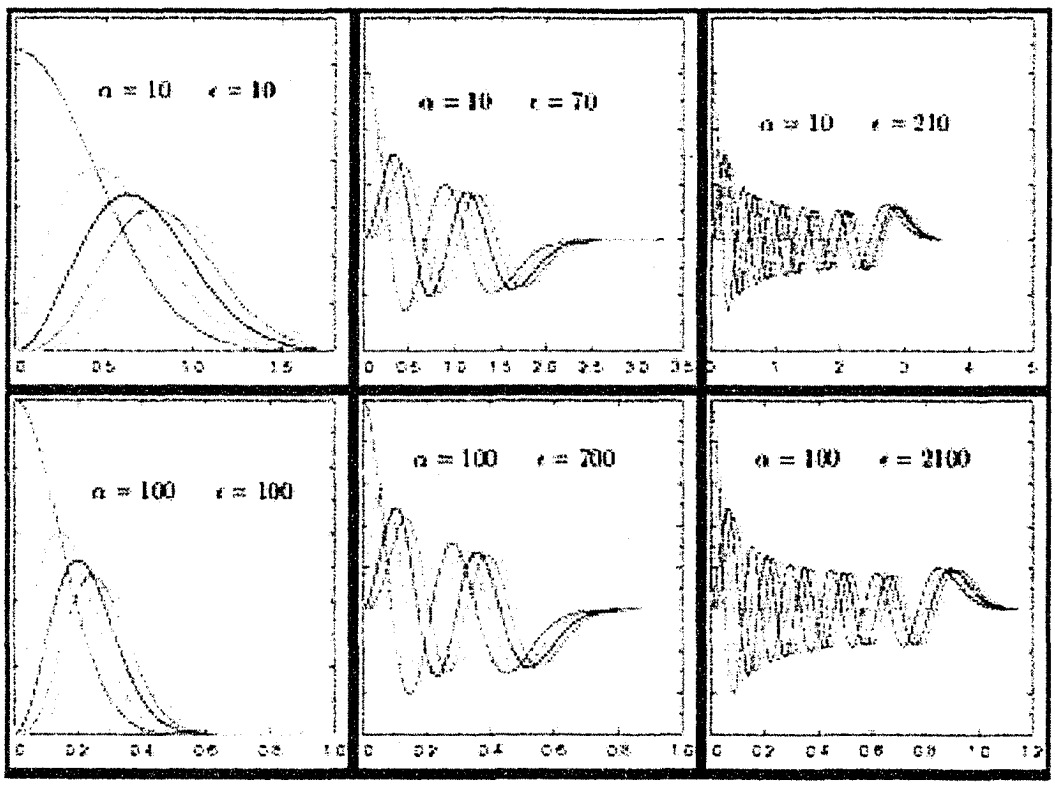

Figure 4.2: Radial part of Landau Levels. It can be seen that as the magnetic field is increased, each Landau level peaks closer to the origin.

The radial part of Landau levels for various values of parameters is represented in **Figure 4.2**. The general feature of all Landau Levels is that as the magnetic field becomes stronger (the parameter α increases), the wavefunctions peaks closer to the origin and quickly decay as you move outward. This leads to the fact that for a strong enough magnetic field the Landau Levels can be used as a good approximation to a solution of the problem with boundary conditions.

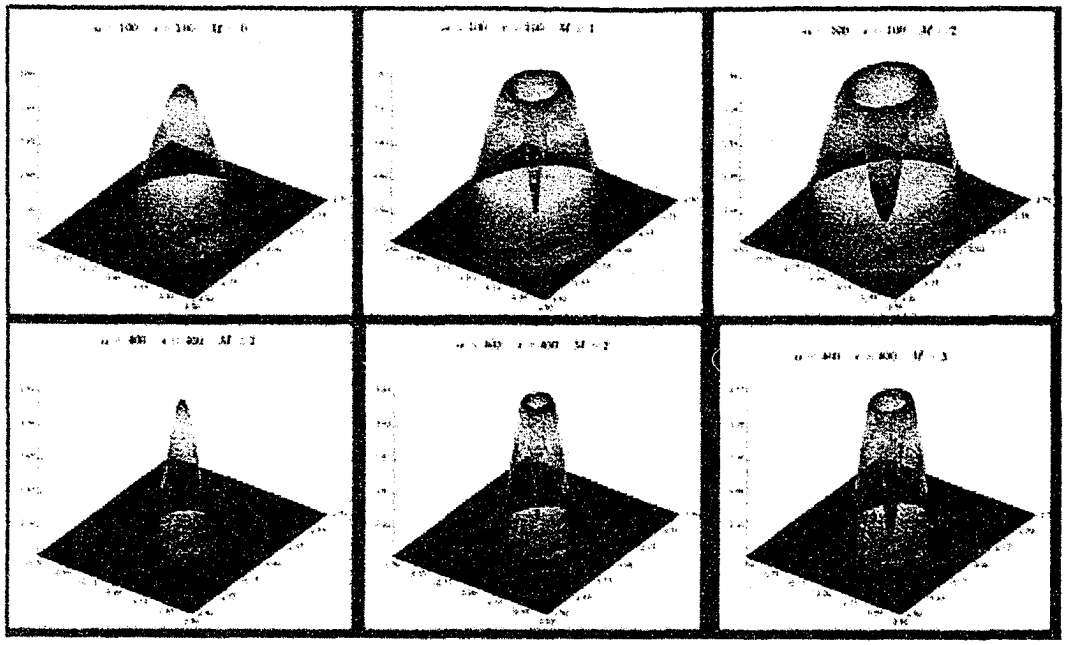

Figure 4.3: Landau Levels for $\alpha = 100$ and $\alpha = 400$.

4.4 Perturbation theory: strong magnetic field.

The radial part of the wave function describing a free particle (Landau Levels) is proportional to the term $e^{-\frac{\alpha\rho^2}{4}}$. This means that for a sufficiently strong magnetic field ($\alpha \to \infty$) the wave function quickly decays toward the boundary. The graphs **(4.3)** demonstrate this fact - an increase in parameter α leads to a greater degree of localization of the wavefunction near the center of the billiard. Therefore, for large enough values of parameter α, the wavefunctions describing Landau Levels can be used as approximate solutions to the problem with boundary conditions.

We are going to apply methods of time independent perturbation theory (see [49]) assuming that the magnetic field is sufficiently strong such that the lowest Landau Levels are localized close to the center of the billiard. The unperturbed Hamiltonian **(4.1)** is

$$\hat{H_0} = -\frac{\hbar^2}{2m}\nabla^2 + i\hbar\frac{\omega_c}{2}\frac{\partial}{\partial\theta} + \frac{m{\omega_c}^2}{8}\rho^2\psi = \frac{\hbar^2}{2m}(-\nabla^2 + i\alpha\frac{\partial}{\partial\theta} + \frac{\alpha^2}{4}\rho^2).$$

A perturbation $\hat{H_1}$ acts in such a way that it suppresses the action of the unper-

turbed Hamiltonian $\hat{H}_0$ outside the boundary. To define an operator of the perturbation formally, let us introduce two operators $\hat{\Gamma}$ and $\hat{\Phi}$ such that

$$\begin{cases} \hat{\Gamma}\psi = \hat{H}_0\psi \ \text{ outside the billiard} \\ \hat{\Gamma}\psi = 0 \ \text{ inside the billiard} \end{cases}$$

$$\begin{cases} \hat{\Phi}\psi = 0 \ \text{ outside the billiard} \\ \hat{\Phi}\psi = \hat{H}_0\psi \ \text{ inside the billiard.} \end{cases}$$

In terms of $\hat{\Gamma}$ the perturbed Hamiltonian is

$$\hat{H} = \hat{H}_0 - \hat{\Gamma}.$$

Therefore the perturbation $\hat{H}_1 = -\hat{\Gamma}$. The matrix elements of the perturbation are

$$\langle\phi_i|\hat{H}_1|\phi_j\rangle = -\langle\phi_i|\hat{\Gamma}|\phi_j\rangle.$$

For purposes of numerical integration it is much more convenient to integrate inside the region confined by the boundary, which is achieved using the following transformation:

$$-\langle\phi_i|\hat{\Gamma}|\phi_j\rangle = -\langle\phi_i|\hat{H}_0|\phi_j\rangle + \langle\phi_i|\hat{\Phi}|\phi_j\rangle.$$

Using $\hat{H}_0\phi_j = \epsilon_j\phi_j$ and the closure relation $\langle\phi_i|\phi_j\rangle = \delta_i^j$ the last expression can be rewritten as

$$\langle\phi_i|\hat{H}_1|\phi_j\rangle = \langle\phi_i|\Phi|\phi_j\rangle - \epsilon_j\delta_i^j.$$

All the eigenstates of $\hat{H}_0$ **(Landau Levels (4.8))** are infinitely degenerate, hence we

have to apply perturbation theory to degenerate states. Let us consider first of all the lowest Landau Levels that correspond to the energy value $\epsilon_0 = \alpha$. The eigenfunctions of this degenerate level are

$$\psi_{nM} = (\frac{\alpha\rho^2}{2})^{\frac{M}{2}} e^{-\frac{\alpha\rho^2}{4}} {}_1F_1(0, M+1, \frac{\alpha\rho^2}{2}) e^{iM\theta} \quad M = 0, 1, 2, 3, \ldots$$

As an example we consider the case $\alpha = 100$. The unperturbed lowest Landau Level has an energy eigenvalue $\epsilon = 100$. As described above we computed the matrix of the perturbation:

$$V_{ij} = \langle \phi_i | \hat{H}_1 | \phi_j \rangle.$$

then we solved numerically the characteristic equation

$$V_{ij} - \Delta E \delta_{ij} = 0 \, .$$

Solutions of this equation give us corrections to the energy eigenvalues of an initially degenerate level. For the case discussed ($\alpha = 100$), the circular equation has seven solutions, thus seven perturbed energy eigenvalues were obtained. The corrections turned out to be very small. The initial state $\epsilon = 100$ becomes split into seven levels with the following energy eigenvalues 99.967 99.996 100.000 100.029 100.062 100.115 100.216. The perturbed eigenfunctions have the same shapes as the first seven eigenfunctions shown in **Figure (B)** in Appendix B. These profiles coincide with the shapes of the seven Landau Levels with $\epsilon = 100$ and the magnetic quantum numbers correspondingly $M = 0, 1, \ldots 6$. Therefore, the seven Landau Levels with the highest degree of localization at the center of the billiard turn out to be a good approximation for the seven eigenfunctions corresponding to the lowest states of the boundary value problem. As the magnetic field becomes stronger, more Landau levels become approximate solutions to the problem with boundary conditions. Thus as the strength of the magnetic field

increases, the behavior of the particle in the square billiard becomes more like the behavior of the same particle without any confinement. This is consistent with what was observed in the classical case: ,where with an increase of the magnetic field the number of trajectories that do not undergo any collisions grows.

However, the perturbative method just described cannot be used to obtain highly excited states. Neither can it be applied for the case of intermediate strength magnetic fields. To examine these cases, other methods are needed. However, the results of this section are useful as the limiting case of strong magnetic fields. All the results of future methods must be consistent with what was obtained in this section as the parameter α becomes extremely large.

4.5 Time-independent Schrodinger equation. Rayleigh-Ritz Method.

The perturbation methods discussed in the previous sections describe adequately the behavior of the system only for limiting cases. The first one works for a weak magnetic field. The classical analogue that corresponds to this limit is nearly integrable motion for large values of the cyclotron radius. On the other hand, the perturbative method of the previous section is valid only if the magnetic field is sufficiently strong and only for the lowest eigenstates. The classical analogue is a set of trajectories that do not undergo collisions with the boundary. Both of these limiting cases correspond to a regular behavior of the classical analogue. However, our major goal is to describe the quantum dynamics of the system when the classical analogue is essentially chaotic, which means when the values of the classical cyclotron radius is approximately equal to the size of the system. This range of the cyclotron radius corresponds to a medium strength of the external magnetic field, when neither of the perturbation methods is valid. The first method that can be used when perturbation methods fail is the Rayleigh-Ritz method (see [59]).

The Hamiltonian of the system in Cartesian coordinates is

$$\hat{H} = \frac{\hbar^2}{2m}(\Delta^2 - i\alpha(y\frac{\partial}{\partial x} - x\frac{\partial}{\partial y}) + \frac{\alpha^2}{4}(x^2 + y^2))$$
$$\alpha = \frac{m\omega_c}{\hbar}.$$

As the set of the Rayleigh-Ritz trial functions it is convenient to use a normalized set of sinusoidal standing waves.

$$\phi_{ij}(x,y) = \frac{1}{2}\sin(\pi k_x(x+0.5))\sin(\pi k_y(y+0.5))$$
$$k_x = \pm 1, \pm 2, \ldots \quad k_y = \pm 1, \pm 2, \ldots$$

$\phi_{ij}(x,y)$ form complete set and they satisfy the boundary conditions, therefore any linear combination of them satisfies the boundary conditions as well. We reorder the set $\phi_{ij}(x,y)$ in ascending order of the values ${k_x}^2 + {k_y}^2$ and in this way introduce the single index n for counting the trial functions $\phi_n(x,y)$. The Hamiltonian matrix is

$$H_{mn} = \langle\phi_m|\hat{H}|\phi_n\rangle.$$

If we multiply both parts of the Schrodinger equation **(4.2)** by $\langle\phi_m|$, integrate and use the closure relation $\langle\phi_i|\phi_j\rangle = \delta_i^j$ then the Schrodinger equation will be transformed into a matrix eigenvalue equation:

$$H_{mn}\vec{\xi} = \lambda\vec{\xi}. \tag{4.9}$$

As known from the theory of the Rayleigh-Ritz Method (see [59]) the set of the eigenvalues of (4.9) tends to the set of the eigenvalues of the original Schrodinger equation as we increase the number of trial functions ($N \to \infty$). On the other hand the eigenvectors $\vec{\xi}$ yield the eigenfunctions of the Schrodinger equation in the following way

$$\psi_j(x,y) = \sum_{n=0}^{N} \xi_j^n \phi_n(x,y).$$

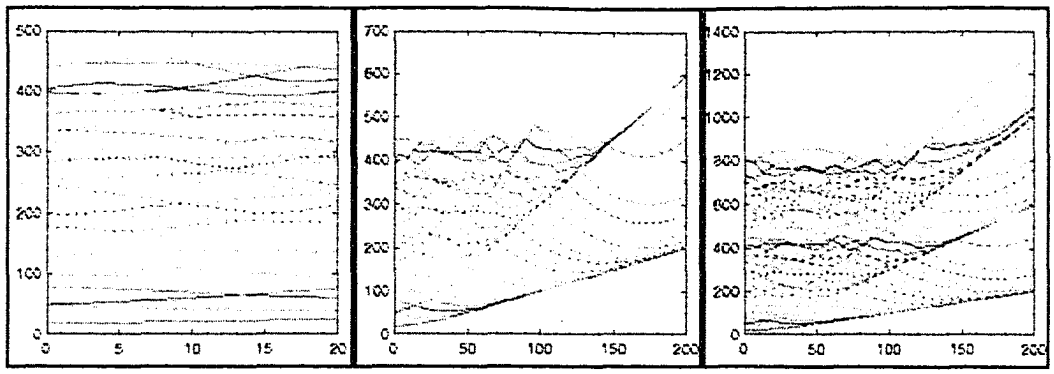

Figure 4.4: Energy levels of the quantum square magnetic billiard versus the constant α. Initially the levels behave the same way as obtained using time independent perturbation theory **(see Figure 4.1)**. As the magnetic field increases, the energy levels start to exhibit a great deal of randomness. As observed, the randomness occurs due to inter-level repulsion - i. e. the levels repel each other to avoid crossing. This type of behavior leads to strong correlation between the levels, a well established manifestation of quantum chaos. Finally, as the magnetic field becomes sufficiently strong, all the levels smoothly approach lines $\epsilon = (2n+1)\alpha$ - the energy values of the rotationally symmetric Landau Levels. Therefore, the system changes the type of its symmetry and restores its integrability.

To test the reliability of the method we perform computations for various values of N - the amount of the trial functions used. If an increase in N leads to a considerable change in results of the computations, then the results acquired are not realistic. We have to keep increasing N until the results become robust to changes in the number of the trial functions used.

The results reported later in this section were acquired using $N = 900$ trial functions. The major procedure was to compute and diagonalize a 900x900 matrix. The preliminary procedure was performed as described above to test the reliability of the results. The data for the lowest 600 energy levels turned out to be robust to subsequent increases in N. The use of a larger number of trial functions would provide us with a greater number of reliably computed energy eigenvalues as well as the corresponding eigenfunctions. However, it requires much more powerful computing facilities than were available.

Plots of the energy levels versus the parameter α are represented in **Figure 4.4**. In

order to describe the general character of the behavior of the energy spectrum of the quantum system and compare it with the classical analogue we need an expression for the classical cyclotron radius **(3.4)** in terms of the quantum parameters:

$$R_c = \frac{1}{\omega_c}\sqrt{\frac{2E}{m}} = \frac{\sqrt{\epsilon}}{\alpha}.$$

The general features of the energy spectrum as illustrated in **Figure 4.4** are the following:

- When the magnetic field is relatively small, $\alpha < 15$, the energy spectrum looks like the one represented in **Figure 4.1**, obtained using time-independent perturbation theory for small strength of the magnetic field. However, as the magnetic field increases the levels obtained by simple perturbation theory exhibit a lot of crossings, while the levels in **Figure 4.4** do not cross. Instead, they exhibit strong repulsion. The strong level correlation is one of the remarkable features of a classically chaotic system in the quantum case. It is worth mentioning that time independent perturbation theory gives reliable results before the first occurrences of the repulsion. This reinforces the fact that a classically chaotic system cannot be solved by methods of perturbation theory.

- As the magnetic field becomes sufficiently strong (approximately $15 < \alpha < 3\sqrt{\epsilon}$) the highest degree of the level correlations can be observed. The levels repel each other, making the general appearance of the energy spectrum mostly irregular. In order to compare this with the corresponding classical analogue we notice that the inequality $\alpha < 3\sqrt{\epsilon}$ leads to $R_c > \frac{1}{3}$, which is approximate condition for the system to start exhibiting chaos in the classical case.

- As the magnetic field becomes relatively large (approximately $\alpha > 3\sqrt{\epsilon}$) the energy spectrum appears to restore its regularity. The energy levels smoothly approach lines $\epsilon = (2n+1)\alpha$ which are the energies of the Landau Levels. The Landau

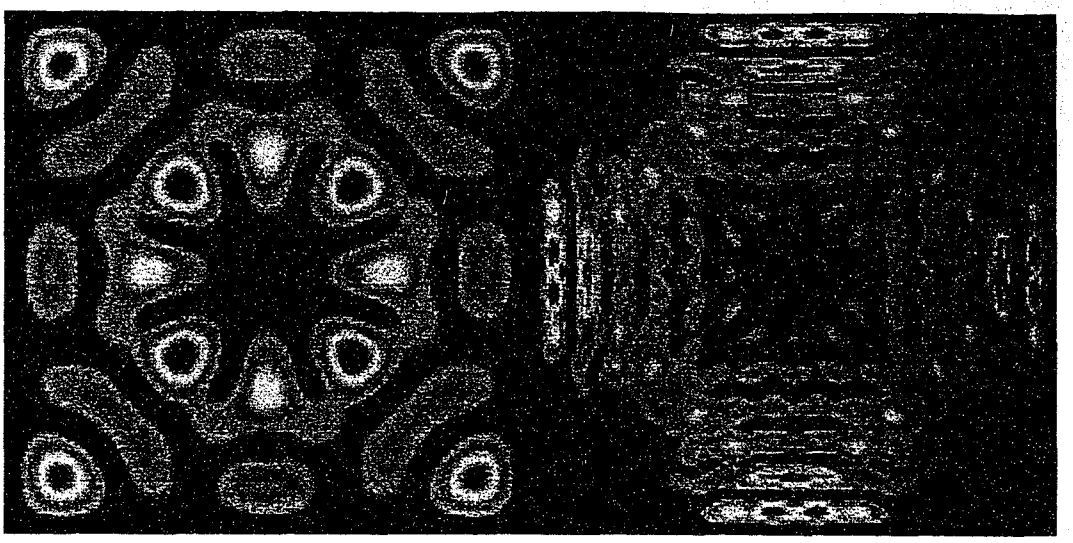

Figure 4.5: The wavefunctions corresponding to the mostly classically chaotic case ($R_c \approx 1.1$) the left screenshot represents the level number 32 for the case $\alpha = 20$, the second one represents the level number 223 for the case $\alpha = 50$. The shape of the wavefunctions exhibits concentration of the amplitude of probability along narrow channels - the quantum scars. The shape of the scars is similar to the shape of a classical period-four trajectory corresponding to $R_c = 1.1$.

Levels are rotationally symmetric. Hence the system eventually changes its type of symmetry and restores its integrability. Classically, this case corresponds to the case of a strong magnetic field, when integrable circular trajectories of small radius appears, which do not undergo collisions with the boundary.

An extensive presentation of wavefunctions of the system for various values of the parameter α is given in Appendix B (**Figures ??**). Let us now identify wavefunctions, corresponding to the mostly chaotic classical analogue. It was shown in the previous chapter that the classical system is mostly chaotic if $R_c \approx 1.1$. The corresponding condition for the quantum case yields $\epsilon \approx 1.21\alpha^2$. Eigenfunctions for the cases $\alpha = 20$ and $\alpha = 50$ are shown in **Figure 4.5**. The shape of these eigenfunctions demonstrate a strong concentration of the probability along narrow channels - the 'quantum scars' ([37]). The concentration happens among the 'diamond-shaped' period-four trajectory that was discussed in detail in the previous chapter. Thus, as the classical analogue

exhibits mostly chaotic dynamics - the quantum eigenfunctions are concentrated along narrow channels, corresponding to the classical periodic orbits.

4.6 Matching Boundary Conditions: Allocating Energy Spectrum.

The Rayleigh-Ritz method described in the previous section requires diagonalization of large matrices in order to obtain highly excited energy levels. As mentioned earlier, the computing facilities used for this work provided reliable computations of only the lowest 600 levels. In contrast, a method of matching of the boundary conditions allows computations of much more higher excited levels using the same computing power. This method does not guarantee that we obtain all the subsequent energy levels, and some of the levels could be missed. However, levels obtained proved to be the real energy levels of the quantum system and they could be obtained to much higher order than by means of the Rayleigh-Ritz Method.

As before, we look for solutions of the time-independent Schrodinger equation **(4.3)**

$$-\frac{\hbar^2}{2m}\nabla^2\psi + i\hbar\frac{\omega_c}{2}\frac{\partial}{\partial\theta}\psi + \frac{m{\omega_c}^2}{8}\rho^2\psi = E\psi$$

of the form

$$\psi(\rho,\theta) = f(\rho)e^{iM\theta}.$$

Substitution into **(4.3)**, and using the same parameters as before

$$\epsilon = \frac{2mE}{\hbar^2} \quad \alpha = \frac{m\omega_c}{\hbar}$$

leads to the following equation for the radial part $f(\rho)$:

$$f'' + \frac{1}{\rho} f' - \frac{M^2}{\rho^2} f + \alpha M f - \frac{(\alpha\rho)^2}{4} f + \epsilon f = 0. \tag{4.10}$$

An asymptotic form of **(4.10)** as $\rho \to 0$ is

$$f'' + \frac{1}{\rho} f' - \frac{M^2}{\rho^2} f = 0.$$

The last equation has two linearly independent solutions. However, only one of them is finite at the origin: $f(\rho) = r^{|M|}$. This asymptotic solution was used as a Cauchy condition for numerical solution of the equation **(4.10)**

$$f(0) = \begin{cases} 1 & M = 0 \\ 0 & M \neq 0 \end{cases}, \qquad f(\delta\tau) = \begin{cases} 1 & M = 0 \\ (\delta\tau)^{|M|} & M \neq 0. \end{cases} \tag{4.11}$$

Numerical integration of **(4.10)** was accomplished using an embedded 8th order Runge-Kutta method (see [68]). To express the result of the integration in the Cartesian rather than the polar coordinate system, the points between the grid were interpolated using a cubic spline interpolation method. Let us denote the result of the numerical integration as $f_{M\epsilon}(\rho)$. Thus the solution of the two-dimensional Schrodinger equation for the certain values of M and ϵ is the product

$$\psi_{M\epsilon} = f_{M\epsilon}(\rho) e^{iM\theta}.$$

For the solution to be single-valued, the quantum number M must be an integer. Thus the function $\psi_{M\epsilon}$ for arbitrary integer M satisfies the Schrodinger equation **(4.10)** with the eigenvalue ϵ, and so does any linear combination of these functions with an arbitrary set of coefficients C_M

$$\psi_\epsilon = \sum_{M=-\infty}^{+\infty} \psi_{M\epsilon} = \sum_{M=-\infty}^{+\infty} C_M f_{M\epsilon}(\rho) e^{iM\theta}.$$

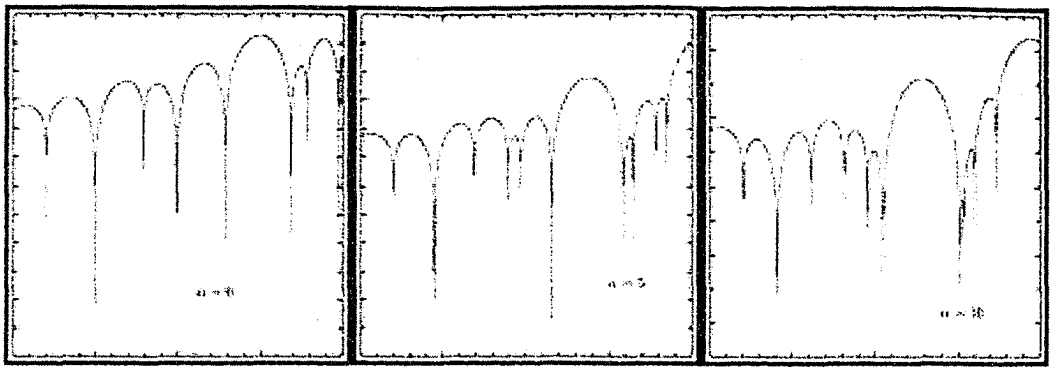

Figure 4.6: Determinant of the matrix of **(4.13)** versus ϵ for various values of α. The sharp minima correspond to values of ϵ that make the system of homogeneous equations **(4.13)** resolvable, thus allocating the energy eigenvalues ϵ_j. The y-scale is logarithmic.

Next, we choose N points X_j on the boundary and try to adjust N coefficients C_M in such a way that

$$\sum C_M \psi_{M\epsilon}(X_j) = 0 \text{ at all the points } X_j. \tag{4.12}$$

This results in a system of N homogeneous complex equations.

$$\sum C_M \psi_{M\epsilon}(X_j) = 0 \;\; j = 1, 2, 3, \ldots N. \tag{4.13}$$

For a homogeneous system of equations to have nontrivial solutions the determinant of coefficients must be zero. This provides us with a criterion that helps us allocate the energy eigenvalues, i.e.

$$\det(\psi_{M\epsilon}(X_j)) = 0.$$

A few graphs of $\det(\psi_{nM}(X_j))$ are shown in Figure 4.6. We see that these graphs have extremely sharp minima. This minima correspond to values of ϵ_j that make possible a simultaneous solution of the system of homogeneous equations **(4.13)**, and thus identifies the energy eigenvalues.

After we allocate the energy eigenvalues, we look for a nontrivial solution of the homogeneous system **(4.13)** in order to find the corresponding eigenfunctions. We have to set one of the coefficients C_M to be equal to some nonzero value to make the system non-homogeneous. To decide which one of C_M to use as predefined, we compute a norm of each column of the matrix of the system **(4.13)**

$$S_M = \sum_{j=1}^{N} |\psi_{M\epsilon}(X_j)|,$$

then we determine the M_0 that corresponds to a minimal norm

$$S_{M_0} = \min(S_M),$$

and impose the corresponding coefficient C_{M_0} to be equal to one. Then, making the substitution $C_{M_0} = 1$, we obtain an inhomogeneous system of $N - 1$ complex equations that we solved using the *LU-decomposition method* (see [68]). Finally a linear combination

$$\psi_{\epsilon_j} = \sum C_M \psi_{M\epsilon}$$

yields an unnormalized wavefunction corresponding to the eigenvalue ϵ_j.

The eigenfunctions and the energy values obtained by this method corresponds well to those obtained earlier by the Rayleigh-Ritz Method. However, matching of the boundary conditions does not provide all the energy eigenvalues. The number of losses can be reduced as we increase the number N of the functions $\psi_{M\epsilon}$ used. The major advantage of the method of matching boundary conditions is that it yields extremely highly excited energy levels together with their corresponding eigenfunctions. As an example, eigenfunctions corresponding to highly excited levels are represented in **Figure (4.12)**. Shapes of these semi-classical levels resemble classical period-four trajectories. Another demonstration of highly excited levels (starting with a level number approximately 2000) is presented in Appendix B **(Figures (??))**.

In the last two sections, we have developed two methods that helps us to examine properties of the system for intermediate values of the external magnetic field. The energy spectra corresponding to this range of parameters exhibit a great deal of inter-level repulsion and the eigenfunctions display a strong concentration along the classical periodic orbits. All these features are well known manifestations of classically chaotic dynamics in the quantum case.

4.7 Study of the energy spectrum.

The previous chapters showed clear quantum manifestations of classically chaotic behavior for certain values of the parameter α. The energy spectrum exhibited a great deal of randomness for $\alpha < 3\sqrt{\epsilon}$. As mentioned, this condition is consistent with the corresponding condition for chaos in the classical case - the system becomes chaotic as the cyclotron radius becomes approximately equal to the size of the system. In this chapter we analyze the level spacing distribution, as it provides a quantitative characteristic of the level correlation.

For the case of a free particle inside the square billiard with no magnetic field, the normalized eigen functions are

$$\psi_{ij}(x,y) = \frac{1}{2}\sin(\pi k_x(x+0.5))\sin(\pi k_y(y+0.5))k_x = \pm 1, \pm 2, \ldots \quad k_y = \pm 1, \pm 2, \ldots$$

and the corresponding energy levels are

$$E_{ij} = \frac{(\hbar\pi)^2}{2m}({k_x}^2 + {k_y}^2).$$

Denoting $E = \frac{\hbar^2}{2m}\epsilon$, the energy spectrum

$$\epsilon_{ij} = \pi^2({k_x}^2 + {k_y}^2).$$

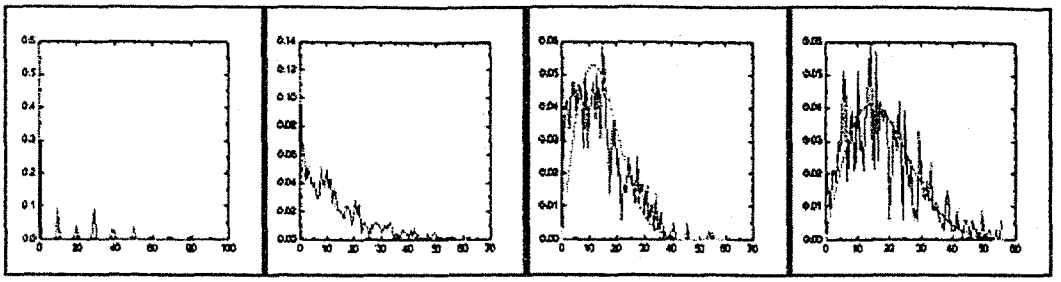

Figure 4.7: The level spacing distributions for various values of the parameter α. The first picture corresponds to the integrable case in the absence of magnetic field. Other pictures correspond to $\alpha = 20, 50, 100$. The last two histograms are very close to the corresponding Wigner's distributions (the green line). Thus, the last two level spacing distributions exhibit what is called *the quantum manifestation of the classically chaotic system* - a strong level correlation. The neighbor energy levels 'keep distance' between each other. The classical cyclotron radius, corresponding to the last two pictures is of an order of the size of the system, which corresponds to the most classically chaotic case.

All the energy levels with $k_x \neq k_y$ are degenerate, as an interchange k_x and k_y leads to a different eigenstate, but does not change an energy eigenvalue. Therefore, the histogram of the level spacing has a sharp peak at the origin. All the other level spacings are integer multipliers of π^2. Therefore, in the absence of magnetic field we expect the distribution of level spacings to be a combination of equidistant δ-peaks, with the first peak at the coordinate origin. The distance between closest peaks is π^2

A plot for this case ($\alpha = 0$) as well as plots for other values of the parameter α are represented in **Figure 4.7**. A more comprehensive collection of the level spacing distributions can be found in Appendix B **(Figure B)**. It can be clearly seen from the graphs that the level spacing distribution tends to a Wigner distribution as the parameter α is increased. To make the connection to the classical case, we must obtain *a range of values* of the classical parameter R_c that corresponds to each plot in **Figure (4.7)**. As was shown in Section (4.5) R_c can be expressed in terms of the parameters of the quantum system in the following way

$$R_c = \frac{\sqrt{\epsilon}}{\alpha}.$$

The general features of the level spacing distribution versus parameters of the quantum system as seen in Figure 4.7 can be summarized as follows:

- The first histogram corresponds to the classically integrable case when no external magnetic field exists inside the billiard. The levels are uncorrelated, a sharp maximum in the origin indicates a high probability for two different states to have the same energy.

- The second histogram corresponds to $\alpha = 20$. The energy levels range between $\epsilon_0 = 25.82$ and $\epsilon_1 = 8637$. The corresponding classical cyclotron radius ranges between ≈ 0.25 and ≈ 4.6468. An average value of R_c is larger than the size of the system. The classical analogue exhibits mixed phase space with a great deal of regularity. The level spacing distribution shows some correlation, however, maximal probability corresponds to zero level spacing, meaning that there is no significant level repulsion.

- The third histogram corresponds to $\alpha = 50$. The energy levels range between $\epsilon_0 = 50.4$ and $\epsilon_1 = 9679$. This means that the corresponding classical cyclotron radius ranges between ≈ 0.14 and ≈ 1.97 and for the fourth histogram $\alpha = 100$ and energy levels range between $\epsilon_0 = 100.0$ and $\epsilon_1 = 11868$, thus the corresponding classical cyclotron radius ranges between ≈ 0.1 and ≈ 1.01. Both cases are analogous to mostly chaotic dynamical phase space as the average R_c that they correspond to is of the order of the size of the system. As a result, strong level repulsion is observed, which is a signature of classical chaos in the quantum case. The green line on the last two graphs shows the corresponding Wigner distribution which agrees with the numerical results.

Thus the study of the level spacing distribution in this section quantitatively demonstrates correlations of energy levels for the quantum analogue of a classically chaotic system. In the next section we are going to examine the time evolution of a quantum

system, looking for signatures of classical chaos in the time propagation of an initial wave packet.

4.8 Time-dependent Schrodinger equation: The Split Operator Method.

We now consider the time-dependent Schrodinger equation

$$i\hbar\frac{\partial}{\partial t}\Psi = \hat{H}\Psi.$$

The expression for the Hamiltonian is given by **(4.1)**. Introducing the dimensionless time $\tau = \frac{\hbar}{m}t$ and, again the parameter

$$\alpha = \frac{m\omega_c}{\hbar}$$

the time-dependent Schrodinger equation becomes

$$i\frac{\partial}{\partial\tau}\Psi = (-\tfrac{1}{2}\nabla^2 - \tfrac{i\alpha}{2}(y\tfrac{\partial}{\partial x} - x\tfrac{\partial}{\partial y}) + \tfrac{\alpha^2}{8}(x^2+y^2))\Psi.$$

The Hamiltonian now consists of three operators

$$\hat{T} = -\tfrac{1}{2}\nabla^2 \text{ - an operator of kinetic energy,}$$
$$\hat{L_z} = -\tfrac{i\alpha}{2}(y\tfrac{\partial}{\partial x} - x\tfrac{\partial}{\partial y}) \text{ - an operator of angular momentum,}$$
$$\hat{V} = \tfrac{\alpha^2}{8}(x^2+y^2) \text{ - an operator of potential energy.}$$

The formal solution of this equation is (see [59])

$$\Psi(\vec{r}, \tau_0 + d\tau) = e^{-i(\hat{T}\,d\tau + \hat{L_z}\,d\tau + \hat{V}\,d\tau)}\Psi(\vec{r}, 0).$$

We can use an approximation for the exponential operator which is correct up to

order $d\tau^3$ (see [59])

$$e^{-i(\hat{T}\,d\tau+\hat{L}_z\,d\tau+\hat{V}\,d\tau)} \approx e^{-i\frac{d\tau}{2}\hat{V}}e^{-i\frac{d\tau}{2}\hat{L}_z}e^{-id\tau\hat{T}}e^{-i\frac{d\tau}{2}\hat{L}_z}e^{-i\frac{d\tau}{2}\hat{V}}.$$

This last expression gives us an approximate evolution operator. If the initial wavefunction is $\Psi(\vec{r},\tau_0)$, then the expression for the wavefunction $\Delta\tau$ later is computed as

$$\Psi(\vec{r},\tau_0+\Delta\tau) = e^{-i\frac{\Delta\tau}{2}\hat{V}}e^{-i\frac{\Delta\tau}{2}\hat{L}_z}e^{-i\Delta\tau\hat{T}}e^{-i\frac{\Delta\tau}{2}\hat{L}_z}e^{-i\frac{\Delta\tau}{2}\hat{V}}\Psi(\vec{r},\tau_0).$$

The advantage of this form is that each exponential operator is applied in a space where it is diagonal:

- The first exponential operator $e^{-i\frac{\Delta\tau}{2}\hat{V}}$ is diagonal in the configuration space therefore its action leads to multiplication of initial wavepacket by the complex exponential function

$$\Psi_1 = e^{-i\frac{\Delta\tau}{2}\hat{V}}\Psi(\vec{r},\tau_0) = e^{-i\frac{\Delta\tau}{2}\frac{\alpha^2}{8}(x^2+y^2)}\Psi(\vec{r},\tau_0).$$

- The second exponential operator involves an angular momentum operator which is diagonal in the polar coordinates

$$\hat{L}_z = -\frac{i\alpha}{2}(y\frac{\partial}{\partial x} - x\frac{\partial}{\partial y}) = \frac{i\alpha}{2}\frac{\partial}{\partial\phi}$$
$$x = r\cos\phi \quad y = r\sin\phi.$$

Normalized single-valued eigenfunctions of this operator are

$$\Phi_M = \frac{1}{\sqrt{2\pi}}e^{iM\phi} \quad \hat{L}_z\Phi_M = -\frac{M\alpha}{2}\Phi_M.$$

Therefore to apply the second exponential operator we first have to represent the

wavefunction in polar coordinates. This was done using the cubic spline interpolation (see [68]). After that the function was expanded in the series

$$\Psi_1(\rho,\phi) = \sum B(\rho,M)\Phi_M,$$

where the coefficients of this expansion are

$$B(\rho,M) = \int_0^{2\pi} \frac{1}{\sqrt{2\pi}} e^{-iM\phi}\Psi_1(\rho,\phi)d\phi.$$

Application of the exponential operator leads to multiplication of each expansion coefficient by the complex exponential factor

$$\tilde{B}(\rho,M) = e^{i\frac{M\alpha\Delta\tau}{4}}B(\rho,M).$$

Finally an inverse transform yields the result of application of the second exponential operator

$$\Psi_2(\rho,\phi) = \sum \tilde{B}(\rho,M)\frac{1}{\sqrt{2\pi}}e^{iM\phi}.$$

- The third exponential operator is diagonal in momentum space. To apply it we first represent $\Psi_2(\rho,\phi)$ in Cartesian coordinates, using the cubic spline procedure one more time, and then we perform a Fast Fourier Transform (see [28]). To ensure that the solution satisfies the boundary conditions, the Fast Fourier Transform was performed in terms of trigonometric sines with a period commensurate with the period of the billiard. Thus the Fourier expansion is

$$\Psi_2(x,y) = \textstyle\sum_{k_xk_y} A_{k_xk_y} \sin(\pi k_x(x+0.5)) \sin(\pi k_y(y+0.5))$$
$$A_{k_xk_y} = \tfrac{1}{2}\textstyle\int_{-0.5}^{0.5} dx \int_{-0.5}^{0.5} dy\ \sin(\pi k_x(x+0.5)) \sin(\pi k_y(y+0.5))\Psi_2(x,y).$$

Application of the third exponential leads to multiplication of each expansion coefficient by the complex exponential factor

$$\tilde{A}_{k_x k_y} = e^{i\frac{\pi^2({k_x}^2+{k_x}^2)\Delta\tau}{2}} A_{k_x k_y}.$$

Then the Inverse Fast Fourier Transform yields the final result of the third iteration

$$\Psi_3(x,y) = \sum_{k_x k_y} \tilde{A}_{k_x k_y} \sin(\pi k_x(x+0.5)) \sin(\pi k_y(y+0.5)).$$

The remaining two iterations involve applications of the exponential operators $e^{-i\frac{\Delta\tau}{2}\hat{L}_z}$ and $e^{-i\frac{\Delta\tau}{2}\hat{V}}$ the same way as discussed above. Results of computations are shown in **Figures (B)** that are placed in Appendix B.

The two figures represent successive screenshots of the time evolutions of two initial minimal uncertainty wavepackets:

$$\Psi(x,y) = \frac{1}{\sqrt{2\pi\Delta x\Delta y}} e^{-\frac{(x-<x>)^2}{4(\Delta x)^2} - \frac{(y-<y>)^2}{4(\Delta y)^2} + ik_x x + ik_y y}.$$

To look for classical correspondence let us express the classical cyclotron radius in terms of the parameters of the quantum system. We use the expression **(3.4)** for the classical cyclotron radius:

$$R_c = \frac{1}{\omega_c}\sqrt{\frac{2E}{m}} = \frac{m}{\hbar\alpha}\sqrt{\frac{2E}{m}},$$

When the energy of the wave packet is

$$E = \frac{\hbar^2({k_x}^2 + {k_y}^2)}{2m},$$

thus

$$R_c = \frac{m}{\hbar\alpha}\frac{\hbar k}{m} = \frac{k}{\alpha} \quad k = \sqrt{{k_x}^2 + {k_y}^2}.$$

The **Figures (B)** show time evolutions of the same minimal uncertainty wavepacket under two different Hamiltonians. The results can be described as follows:

- The first figure represents a time evolution that corresponds to the following set of parameters: $k = 20$ $\alpha = 100$. Hence $R_c = \frac{1}{5}$. The corresponding classical case is known to be mostly regular, as there exist a vast majority of trajectories that do not undergo collisions. The wave pattern evolving on the picture represents clearly regular evolution. The initial wave packet periodically shrinks and expands its shape altogether with a general translation of the whole pattern along the circular path of the classical cyclotron radius.

- The second figure represents a time evolution that corresponds to the following set of parameters: $k = 100$ $\alpha = 100$. Hence $R_c = 1$. The corresponding classical case is now fully chaotic. The initial wave packet is quickly destroyed, giving rise to a completely irregular pattern. However some elements of a circular structure can be observed in the pattern evolving and the curvature of these elements is equal to the classical cyclotron radius.

In this way the time evolution of a quantum system that has a chaotic classical analogue was found to exhibit chaotic behavior in contrast with a system whose classical analogue is regular. The later displays a regular character of the time evolution, i.e. a combination of smooth oscillations with regular translational motion.

4.8.1 The energy spectrum of an evolving wave pattern.

We have shown that an evolving wave pattern carries clear signatures of the classical chaos in the quantum mechanics. We are now going to look for manifestations of

the underlying chaos in the energy spectrum of an evolving pattern. To get the energy spectrum we use the solution of the time-dependent Schrodinger equation $\Psi(t)$, obtained in the previous section. We assume that there exists a complete set of orthonormal eigenfunctions of the system ϕ_j. Let us label the corresponding eigenvalues by E_j. Consider a series expansion of the initial wave pattern $\Psi(0) = \sum C_j \phi_j$. The Hamiltonian of the system is diagonal in terms of ϕ_j, therefore the exponential operator $e^{-\frac{i\hat{H}}{\hbar}\Delta t}$ leads to multiplication of each term of the expansion by a complex phase. Therefore, the solution of the time-dependent Schrodinger equation is:

$$\Psi(t) = e^{-\frac{i\hat{H}}{\hbar}t}\Psi(0) = \sum C_j \phi_j e^{-\frac{iE_j}{\hbar}t}. \tag{4.14}$$

Computing the correlation function $< \Psi(0)|\Psi(t) >$ and using the closure relation $< \phi_i|\phi_j >= \delta_i^j$ we obtain

$$\langle\Psi(t)|\Psi(0)\rangle = \langle\sum C_j \phi_j e^{-iE_j t}|\sum C_k \phi_k\rangle = \sum C_j{}^* C_j e^{iE_j t}. \tag{4.15}$$

The Fourier spectrum of the last expression consists of peaks corresponding to consecutive energy eigenvalues of the system. Thus the energy spectrum of the quantum Hamiltonian system can be found from the Fourier transform of the expression $\langle\Psi(t)|\Psi(0)\rangle$.

For better resolution we took an initial wave pattern containing a limited amount of harmonics. Thus, $\Psi(0)$ was chosen in the following form

$$\Psi(0) = \sum_{k=1}^{N}\sum_{n=1}^{N} \sin(\pi k(x+0.5))\sin(\pi n(y+0.5)). \tag{4.16}$$

The results of the computations for various values of the parameter α are shown in **Figure 4.8**. An initial wave pattern consisted of 6^2 sinusoidal harmonics. This means that the parameter N in the expression **(4.8)** is equal to 6. All the terms of the series **(4.8)** are exact eigenfunctions of the Schrodinger equation for the case when no

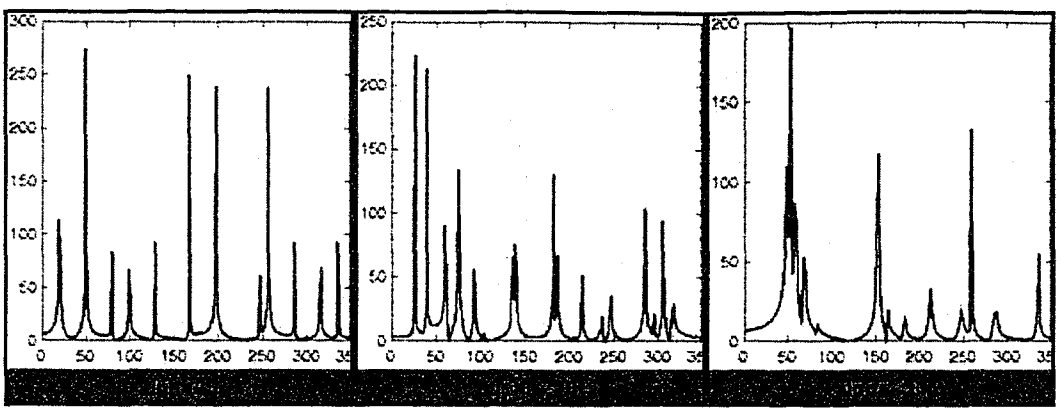

Figure 4.8: Energy spectra obtained using the time evolution of an initial wave pattern for various values of parameter α.

magnetic field exists inside the billiard. Therefore for a case $\alpha = 0$ we expect to obtain a linear spectrum of the correlation function with peaks corresponding to the following values:

$$\epsilon_{kn} = \pi^2(k^2 + n^2) \quad k, n = 1, 2, \ldots 6.$$

The first graph shown in **Figure 4.8** reproduces this spectrum. As the magnetic field grows we see that the resultant spectrum changes its character. The last picture for $\alpha = 50$ shows that the lines of the initially discrete spectrum become broader as the system's spectrum becomes more continuous. The fact that we obtained continuous spectrum means that our starting assumption which implies the existence of a complete set of the eigenfunctions of the Hamiltonian was incorrect. As mentioned in **Section 2.2**, if a classical analogue has no complete set of integrals of motion then the corresponding quantum Schrodinger equation is non-separable. Therefore the time evolution of this system can not be represented as a combination of harmonically evolving terms **(4.14)**. As a consequence the resultant spectrum is continuous.

To end this section, it is worth mentioning that the energy values obtained here **(Figure 4.8)** are in a good correspondence with those obtained by other methods. In other words, all data obtained in this chapter by various methods agree with each other,

giving us a completely consistent description of the system from different points of view.

4.9 Semi-classical case.

In order to ascertain the accuracy of all the methods used throughout this chapter, and to obtain some additional features of the quantum dynamics of the square magnetic billiard, we are going to examine the problem semi-classically (see [49]), using an approach valid only for the highly excited levels. The expression for the semi-classical energy eigenvalues is given by the Bohr-Sommerfeld quantization rule (with Einstein correction)

$$\frac{1}{2\pi\hbar}\sum_j \oint p_j dq_j = n + \frac{1}{2}.$$

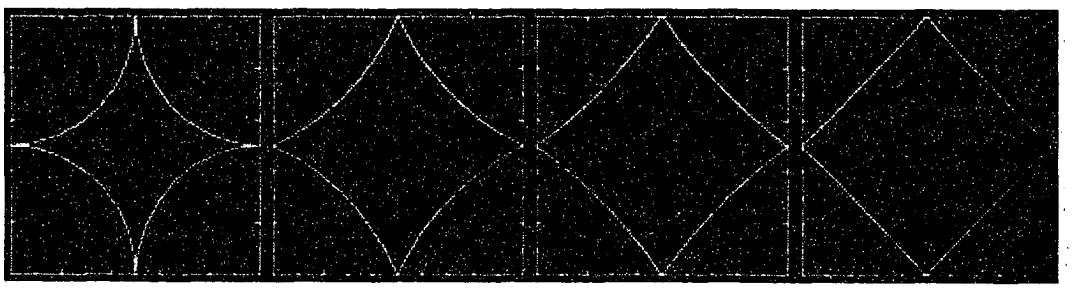

Figure 4.9: The classical period four trajectories.

Integration has to be performed along the classical closed path. Let us choose for example the classical period 4 trajectory as one, shown in **Figure 4.9**.

It was found in the previous chapter **(3.7)** that the actions for this sort of trajectory are equal to

$$J_x = J_y = \frac{1}{2\pi}\oint p_j dq_j = \frac{TE}{2\pi}.$$

Therefore the semi-classical quantization rule yields

$$TE = \pi\hbar(n + \frac{1}{2}). \tag{4.17}$$

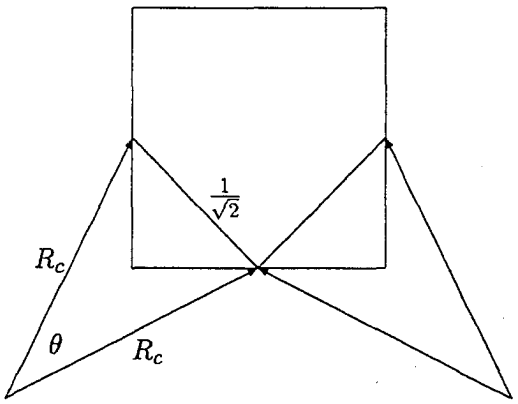

Figure 4.10: A diagram of the period four trajectory.

Let us introduce a parameter θ - the central angle subtended by the circular segment of the trajectory. R_c - labels the classical cyclotron radius (see diagram in **Figure 4.10**). During one period, the trajectory sweeps an angle (4θ), hence $\omega_c T = 4\theta$. Substitution into **(4.17)** yields

$$4\theta E = \pi\hbar\omega_c(n + \frac{1}{2}).$$

On the other hand $R_c \sin(\frac{\theta}{2}) = \frac{1}{2\sqrt{2}}$ therefore

$$8 \sin^{-1}(\frac{1}{2R_c\sqrt{2}})E = \pi\hbar\omega_c(n + \frac{1}{2}).$$

Using the familiar parameters

$$E = \frac{\hbar^2}{2m}\epsilon \text{ and } \alpha = \frac{m\omega_c}{\hbar},$$

we obtain

$$4\sin^{-1}(\frac{1}{2R_c\sqrt{2}})\epsilon = \pi\alpha(n+\frac{1}{2}).$$

Finally the semi-classical quantization is

$$\epsilon_n = \frac{\pi\alpha}{4\sin^{-1}(\frac{1}{2R_c\sqrt{2}})}(n+\frac{1}{2}) \quad n = 0,1,2,\ldots \tag{4.18}$$

On the other hand for the cyclotron radius we have, according to the classical dynamics,

$$m(\omega_c R_c)^2 = 2E,$$

which can be rewritten as

$$(\alpha R_c)^2 = \epsilon_n. \tag{4.19}$$

Thus in order to find the quantum parameters corresponding to the classical period-4 trajectory we have to simultaneously find solutions to the equations **(4.18)** and **(4.19)**. The graphical solution of this equations for the case $\alpha = 100$ is shown in **Figure 4.11**.

We use the semi-classical energy eigenvalues obtained and substitute them into **the equation (4.12)** of the method of matching boundary conditions. Some wavefunctions obtained this way are represented in **Figure 4.12**. We see that the shape of the wavefunctions represented corresponds to the shape of the period-4 classical trajectory we started with. This fact demonstrates one more time the correctness and consistency of the methods used throughout this chapter. The values of the parameter α and the energy values used for computations of the results shown in **Figure 4.11** were adjusted so that the corresponding cyclotron radius is of the order of the size of the system. Therefore the classical analogue is chaotic. The wave functions also display 'quantum scars', a quantum signature of the underlying classical stochasticity.

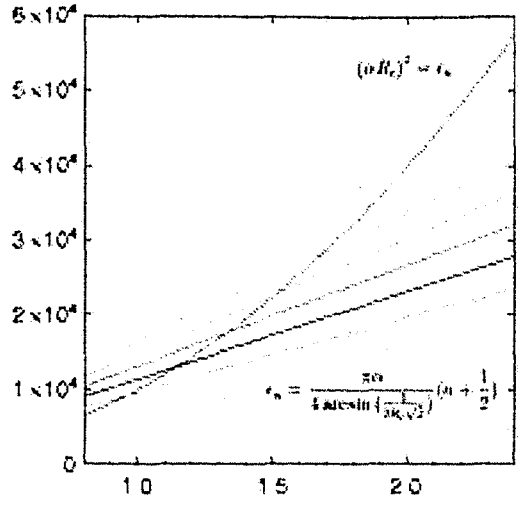

Figure 4.11: Simultaneous solution of the equations **(4.18)** and **(4.19)** for $\alpha = 100$.

4.10 Transport properties.

Let us consider a simple model of a quantum dot that confines an electron in a square two-dimensional domain **(Figure 4.10)**. An external magnetic field is directed perpendicular to the plane of confinement. Two tiny gates are made in the boundary, the electron enters the cavity through a gate placed at the point (x_0, y_0), and we expect it to leave the dot through the gate at the point (x_1, y_1).

We approximate a wavefunction of the entering electron by a minimal uncertainty wavepacket localized at the point (x_0, y_0) with uncertainties in coordinates $\Delta x, \Delta y$ (see [59])

$$\Psi_0(x,y) = \sqrt{\frac{1}{2\pi\Delta x\Delta y}} e^{-(\frac{x-x_0}{2\Delta x})^2 - (\frac{y-y_0}{2\Delta y})^2 + ik_{x0}x + ik_{y0}y}. \tag{4.20}$$

Using the complete set of eigenfunctions of an electron inside the cavity as found in Section 4.6, we can write down an expression for the time evolution of the entering

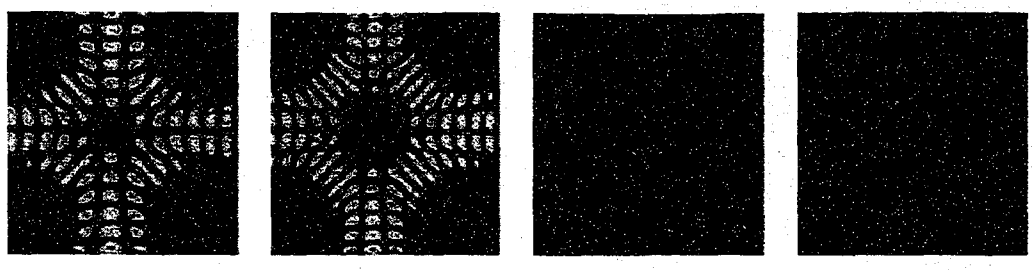

Figure 4.12: Quantum 'scars'. Narrow channels of high quantum probability along classical periodic orbits

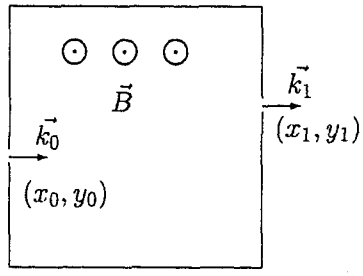

Figure 4.13: A model of a "quantum dot" using the square magnetic billiard as a confinement for an electron. A charged particle enters the dot through the gate (x_0, y_0) and leaves it through the gate (x_1, y_1).

electron. To do this we first expand $\Psi_0(x, y)$ in a series in terms of eigenfunctions ϕ_j

$$\Psi_0(x, y) = \sum_j C_j \phi_j \qquad C_j = \langle \phi_j | \Psi_0(x, y) \rangle. \tag{4.21}$$

The time evolution of initial wavepacket becomes

$$\Psi(t, x, y) = \sum_j C_j \phi_j e^{-\frac{iE_j t}{\hbar}}. \tag{4.22}$$

The probability density for the electron to escape from the cavity through the second gate is equal to a projection of $\Psi(t, x, y)$ on a minimal uncertainty wavepacket localized at the point (x_1, y_1). Let us denote such an outgoing packet as Ψ_1 and we again expand it in series in terms of the eigenfunctions ϕ_j

$$\Psi_1(x,y) = \sum_j D_j \phi_j \qquad D_j = \langle \phi_j | \Psi_1(x,y) \rangle. \tag{4.23}$$

The projection of $\Psi(t,x,y)$ on Ψ_1 is given by

$$\langle \Psi(t,x,y) | \Psi_1 \rangle = \langle \sum_j C_j \phi_j e^{-\frac{iE_j t}{\hbar}} | \sum_n D_j \phi_n \rangle = \sum_j C_j^* D_j e^{\frac{iE_j t}{\hbar}}. \tag{4.24}$$

To obtain the probability for the electron to escape the cavity through the second gate we square the last expression and take its time average. All the oscillating terms will disappear and the expression for the transition of the dot becomes:

$$T = |\langle \Psi(t,x,y) | \Psi_1 \rangle|^2 = \sum_j |C_j|^2 |D_j|^2. \tag{4.25}$$

The last expression was used for numerical computations. We considered the quantum dots with three different positions of the entrance gate. The outgoing wavepacket for all three of the cases was taken to be at the middle of the right wall (the point $(1.0, 0.5)$). To distinguish the transport properties corresponding to different positions of the entrance gate we use the following notation:

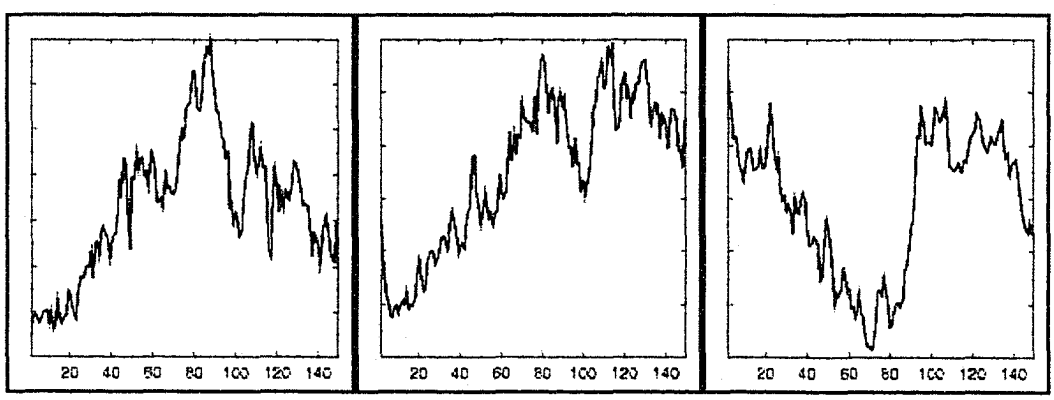

Figure 4.14: The transport properties of the quantum dot based on the square magnetic billiard. The three graphs correspond to different mutual orientations of incoming and outgoing waves. According to a notation introduced in the text the graphs represented correspond to the transport coefficients T_1, T_2 and T_3.

- T_1 labels the transition probability when the entering wavepacket is localized at the middle of the left wall (the point $(0.0, 0.5)$)
- T_2 labels the transition probability when the entering wavepacket is localized at the middle of the top wall (the point $(0.5, 1.0)$)
- T_3 labels the transition probability when the entering wavepacket is localized at a point on the bottom wall with coordinates $(0.1, 0.0)$. The relevant feature of this case is that it is asymmetric as compared with the other two cases.

Results of the computations are represented in **Figure 4.14**. The three graphs in the figure represent the transport coefficients corresponding to T_1, T_2 and T_3.

A common feature of the first two graphs is that they have a maximum corresponding to $\alpha \approx 90$. Let us compute the corresponding strength of the magnetic field:

$$B = \frac{mc\omega_c}{q} = \frac{\hbar\alpha c}{q} \approx 2 \cdot 10^{-7}\alpha.$$

Thus the observed maximum corresponds to the strength of the external magnetic field $B \approx 1.8 \cdot 10^{-5}\ T$. The asymmetric case shows a maximum for approximately the same strength of the magnetic field. As a consequence, an explanation of the appearance of this maximum based on a shape of the shortest classical periodic orbits seems to be impossible. An explanation of the observed resonant structure of the conductivity of the quantum dot requires additional careful examination, which the author of this dissertation is planning to start in the near future.

4.11 Summary.

The dynamics of the quantum square magnetic billiard was studied in detail in this chapter. Various methods were applied and the results of all of them illustrate the following general features of the quantum dynamics of the system:

- When no external magnetic field is applied the Schrodinger equation of the system is separable and the system is integrable. The wavefunctions in this case are sinusoidal standing waves. The energy levels are degenerate and they are totally uncorrelated. The time evolution of an initial wave pattern displays smooth oscillatory motion. The classical analogue of this case is the integrable regular motion of a particle inside the square billiard not subject to any external fields.

- As a weak external magnetic field is applied, $\alpha < 10$, the dynamics of the system can be well described by perturbative methods. Some of the initially degenerate states become split, while others remain degenerate. This leads to the fact that the energy levels still remain uncorrelated. The wave functions are close in shape to sinusoidal standing waves, but keep being reshaped as the magnetic field keeps growing. The time evolution for this case represents a wavelike oscillatory motion, the energy spectrum of an evolving in time wave pattern has a clear discrete character which indicates that the time evolution of the whole system in this case can be decomposed into the vibrational evolution of a set of mutually independent harmonics, which is characteristic of a separable Schrodinger equation. The classical analogue for this case is the regular nearly integrable motion for large values of the cyclotron Radius.

- For magnetic fields of intermediate strength, $10 < \alpha < 100$, the system exhibits a number interesting properties that can be related to the underlying chaotic dynamics of the classical analogue. The energy values become strongly correlated. This correlation can be observed visually in the spectrum. The closest levels 'repel' each other leading to 'avoiding crossings'. The level spacing distribution for this range of parameters is close to a Wigner distribution - which means that nearest levels maintain a certain distance between each other. The energy eigenfunctions display a strong degree of concentration of the probability along narrow channels corresponding to unstable classical periodic orbits, called 'quantum scars'.

Additional signatures of the underlying chaos for this range of parameters were obtained by solving the time dependent problem. An initial wave packet becomes quickly destroyed giving rise to irregular structures. The energy spectrum obtained based on the time evolution turned out to have a continuous component, which is the result of the non integrability of the corresponding dynamical equations. Interesting resonant properties of conductivity are exhibited in a quantum dot based on the square magnetic billiard maintained in this range of parameters. Regardless of the positions of gates, the quantum dot has a maximal conductivity when $\alpha \approx 90$. This value of the parameter α corresponds to a magnetic field $B \approx 1.8 \cdot 10^{-5}\ T$. The position of the resonance does not depend upon the energy of an electron entering the dot, which appear to make it impossible to explain this phenomenon in terms of the classical periodic orbits.

- As the external field becomes extremely strong, $\alpha > 150$, all the lowest eigenstates are well approximated by the Landau Levels. They are equidistant, infinitely degenerate, uncorrelated levels of unconfined charged particle in the magnetic field. The wavefunctions of the Landau Levels have a circular shape. Thus, as the magnetic field becomes extremely strong, the system acquires a new type of the symmetry which restores its integrability. The classical analogue of Landau Levels are trajectories that do not undergo any bounces with the boundary.

  However, it should be mentioned that the highly excited levels can not be approximated by the Landau Levels. These levels exhibit a strong correlation in the energy space and their eigenfunctions display 'quantum scars'. The same feature is seen in the classical case - the trajectories that are subjected to collisions are stochastic for all values of the cyclotron radius. Another relevant fact is that the relative amount of these trajectories tends to zero as the strength of the magnetic field increases farther. Similarly in the quantum case **(see Figure 4.4)** the relative number of energy levels that approach Landau Levels quickly increases as

the magnetic field grows. Thus, the dynamics of the system tends to the regular dynamics of an unconfined particle acted on by a magnetic field.

Chapter 5

Interacting Particles inside a circular billiard: Classical dynamics.

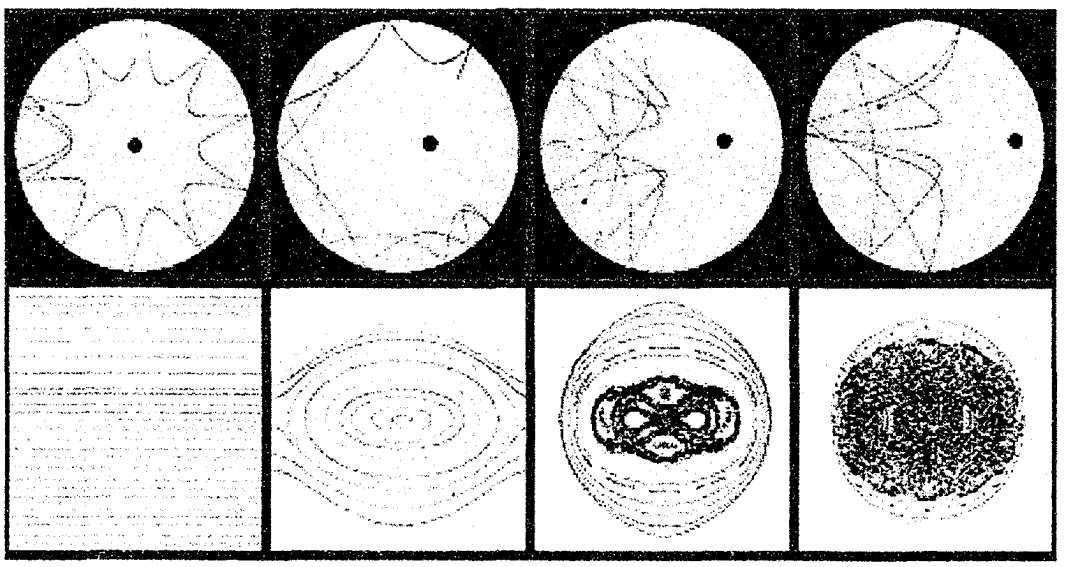

The second dynamical system studied in this dissertation is the so-called Circular Coulomb Billiard. It represents a charged particle confined inside a circular enclosure with perfectly elastic walls. Another stationary particle of infinite mass is placed inside

the confinement. The two particles interact by means of a repulsive electrostatic force. The strength of the Coulomb's repulsion and the location of the massive particle are the parameters that determine the character of the dynamics of the system. In terms of an experimental context, this system models a quantum dot enclosing several particles. Another experimental motivation for this dynamical system is that it can serve as a model of a single electron transistor (artificial atom). If the temperature is sufficiently high, the particles inside a quantum dot exhibit classical dynamics.

5.1 The Circular Coulomb Billiard.

The Circular Coulomb Billiard consists of a charged particle of mass m and charge q moving inside a circular billiard. The radius of the billiard is taken to be unity. The walls of the billiard are perfectly elastic. Another particle of charge Q and infinite mass stays stationary inside the billiard. The coordinates of the second (massive) particle are (x_0, y_0). The particles repel each other according to Coulomb's law. Thus the Hamiltonian of the system is

$$H = \frac{{p_x}^2}{2m} + \frac{{p_y}^2}{2m} + \frac{qQ}{\sqrt{(x-x_0)^2 + (y-y_0)^2}} \tag{5.1}$$

which yields the Hamiltonian equations

$$\dot{x} = \frac{p_x}{m} \qquad \dot{y} = \frac{p_y}{m}$$
$$\dot{p_x} = \frac{qQ(x-x_0)}{((x-x_0)^2+(y-y_0)^2)^{\frac{3}{2}}} \quad \dot{p_y} = \frac{qQ(y-y_0)}{((x-x_0)^2+(y-y_0)^2)^{\frac{3}{2}}}.$$

In terms of velocities $v_i = \frac{p_i}{m}$ the equations become

$$\dot{x} = v_x \qquad \dot{y} = v_y$$
$$\dot{v_x} = \frac{\gamma(x-x_0)}{((x-x_0)^2+(y-y_0)^2)^{\frac{3}{2}}} \quad \dot{v_y} = \frac{\gamma(y-y_0)}{((x-x_0)^2+(y-y_0)^2)^{\frac{3}{2}}}.$$

The parameter $\gamma = \frac{qQ}{m}$ characterizes the strength of the Coulomb repulsion.

The character of the dynamics in this system depends on two parameters - γ and the displacement of the Coulomb center from the center of the billiard. The latter breaks the symmetry of the system and in this way acts as an effective stochasticity parameter. The character of the dynamics does not depend upon the direction in which the Coulomb center is displaced, but only upon the absolute value of such a displacement. Therefore, we can move the repulsive center in any conveniently chosen direction, say, the positive direction of the x-axis. This way the coordinates of the Coulomb center (the massive particle) become $(X_0, 0)$ and the value X_0 represents a displacement of the Coulomb center from the center of symmetry. The Hamiltonian becomes

$$\dot{x} = v_x \qquad \dot{y} = v_y$$
$$\dot{v_x} = \frac{\gamma(x-X_0)}{((x-X_0)^2+y^2)^{\frac{3}{2}}} \qquad \dot{v_y} = \frac{\gamma y}{((x-X_0)^2+y^2)^{\frac{3}{2}}}.$$

The last equations can be integrated numerically using the embedded eight order Runge Kutta, Prince-Dormand method with 9th order error estimate (see [68]).

5.2 Poncaré sections.

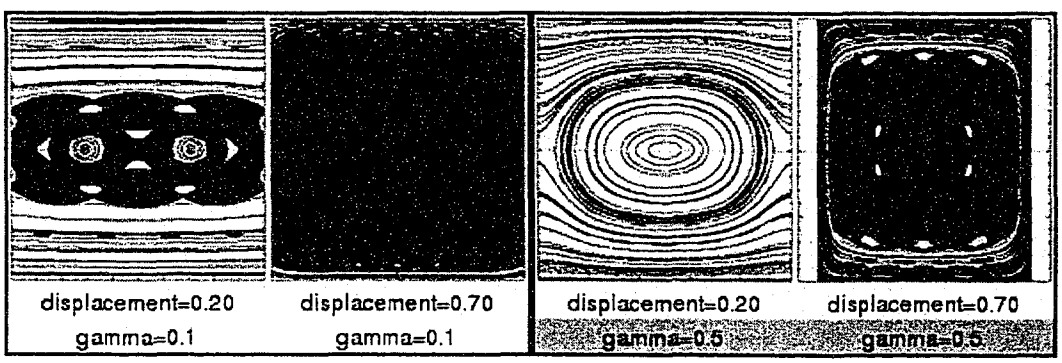

The first way to investigate the dynamics of the system is to look at its Poncaré sections corresponding to different sets of parameters. As in the case of the Square Magnetic Billiard (see Chapter 3.1), a pair of Birkhoff coordinates (P, Q) was chosen. Recall that the coordinate Q - is the coordinate of the bounce along the perimeter of

the billiard normalized to unity, while the second coordinate P is equal to the cosine of the bouncing angle. The Poicaré sections were obtained for various sets of parameters. Some resultant pictures are shown in **Figure (5.2)**. A comprehensive collection of Poncaré sections corresponding to a wide range of system parameters are included in Appendix C (**Figure C**). From these plots we can see the following general features of the dynamics of the system:

- When the Coulomb center is situated at the symmetry point of the billiard, the dynamics of the system are completely integrable. This fact is just a consequence of the symmetry of the system: *as the repulsive center is placed in the center of the billiard, the system is invariant under rotations, hence the angular momentum is conserved (see as an example [47]).*

- As the Coulomb center is displaced from the center of the billiard, the system continues to be regular up to some critical value of the displacement. This critical value depends upon the strength of the Coulomb repulsion. Its approximate value can be estimated visually and grows linearly with the growth of the value of the constant γ: $\Delta_{cr} \approx \gamma$. Thus, the strength of the repulsion suppresses chaos for a small degree of asymmetry.

- As the displacement of the repulsive center becomes greater than the critical value Δ_{cr}, the system exhibits a mixed phase space. With continued increase of the asymmetry all the KAM tori are eventually destroyed and the phase space becomes entirely chaotic. The greater the value of the parameter γ, the faster the transition to chaotic behavior. This means that the strength of repulsion reduces stochasticity for a small degree of asymmetry, but makes the system more chaotic in the case of large displacement.

5.3 Lyapunov Exponent.

Let us now study the dynamics of the system in terms of the Lyapunov exponent. The procedure used for the numerical computation of the Lyapunov exponent was outlined in the **Section 1.4**. The Lyapunov exponent of the system was computed for different values of the strength of the Coulomb interaction (parameter γ) as well as for different values of the displacements of the Coulomb center (parameter X_0). The results of the computations are represented in **Figure 5.1**. Computed values of the Lyapunov Exponent versus displacement of the Coulomb center are plotted with best fit curves of the logarithmic interpolation:

$$y = A \ln(\frac{s}{s_0}).$$

The interpolation coefficient A and x_0 were found using the least square, method, this means that for each computed set of the points (x_k, y_k) minimization was performed of the expression

$$\Sigma_2 = \sum_k (y_k - A \ln(\frac{x_k}{s_0}))^2.$$

The interpolating functions that describe the Lyapunov exponent versus displacement of the repulsive center, for some values of parameter γ, are

$$\begin{aligned} \lambda &\approx 28.56 \ln(\tfrac{X_0}{0.002}) \quad \gamma = 0.1, \\ \lambda &\approx 68.96 \ln(\tfrac{X_0}{0.013}) \quad \gamma = 0.2, \\ \lambda &\approx 131.51 \ln(\tfrac{X_0}{0.11}) \quad \gamma = 0.5. \end{aligned} \tag{5.2}$$

The denominators of the logarithmic expression grow very fast as γ increases. This means that the strong repulsion suppresses chaos for small values of X_0. On the other hand the multiplier of the logarithmic expression is increasing as γ grows. As the result, the Lyapunov exponent grows much faster for strong values of the Coulomb repulsion.

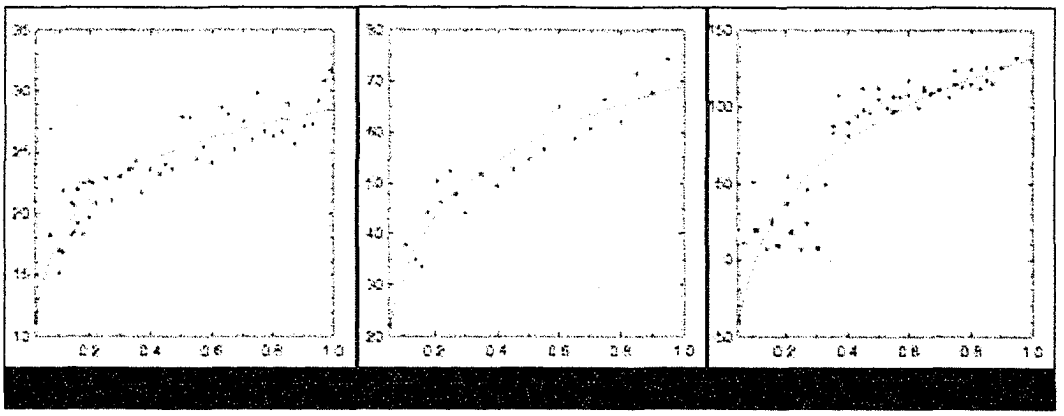

Figure 5.1: Lyapunov exponent versus displacement of the Coulomb center from the center of the billiard. Computations are presented for different values of the strength of the Coulomb interaction (parameter γ). The best fit curves of the logarithmic interpolation are indicated on each graph. It can be seen that the basic features of the dynamics are as follows: The greater the asymmetry of the system - the more chaotic the system becomes. As for the dependence upon the strength of the interaction the situation is more complicated. First of all, for small values of the displacement the strong Coulomb repulsion suppresses chaos. On the other hand, for stronger repulsion - stochasticity of the system grows much faster and eventually becomes higher. The maximal value of the Lyapunov exponent (one that corresponds to the placement of the Coulomb center close to the edge of the billiard) grows linearly with the growth of the strength of the repulsion.

The maximal Lyapunov exponent, i. e. the one that corresponds to the placement of the Coulomb center close to the edge of the billiard grows approximately linearly with the growth of the strength of the repulsion.

Thus, in summary - *an increase of the strength of the Coulomb interaction suppresses chaos for small values of the displacement, but quickly makes the system chaotic with a larger degree of stochasticity for sufficiently large degree of the symmetry break.*

5.4 Action-Angle variables.

Now, let us examine the dynamics of the system in terms of the action-angle variables. Due to circular symmetry the radial action:

$$J_r = \oint p_r dr = m \oint \dot{r} dr = m \oint \frac{x\dot{x}y\dot{y}}{r} dr \ ,$$

is best for the computations. The last integral can be computed numerically where a complete cycle for variable r corresponds to motion between two successive bounces. For the case when the Coulomb repulsive center is situated at the center of the billiard, the system is integrable, hence $J_r = const$. The histogram of the action in such a case shows just a single vertical line corresponding to the single constant action. Then, as the repulsive center is displaced from the center of the billiard, the system becomes non-integrable and action J_r has a randomly distributed value. The histograms of the distributions of J_r for different values of parameters are represented in **Figure (5.2)**.

It can be clearly seen that as the system is nearly integrable the action's distribution is narrow, and becomes broader as the system becomes more chaotic. Another relevant feature is that as the strength of the Coulomb interaction is increasing, the system starts to exhibit chaos starting from some critical value of the displacement. The value of such a critical displacement grows with increasing strength of the Coulomb repulsion. On the other hand, the system's sensitivity to the stochasticity parameter is much greater for greater values of the parameter γ.

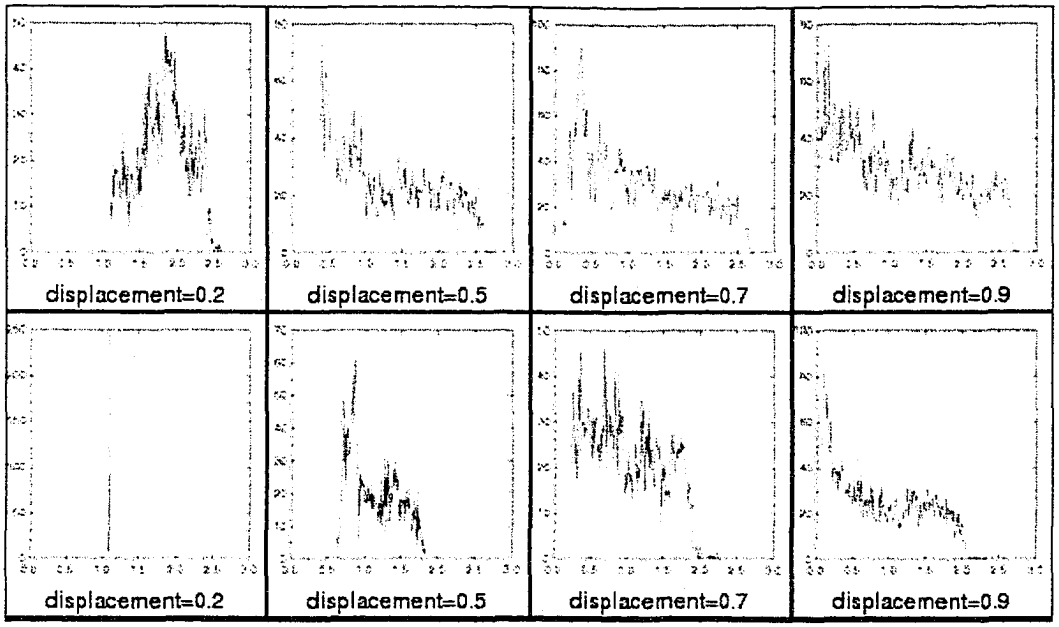

Figure 5.2: Histograms of actions J_r for $\gamma = 0.1$ and $\gamma = 0.5$. The displacement of the repulsive center from the center of the billiard is acting as the parameter of stochasticity. It can be clearly seen that as the displacement is increasing, the behavior of the action J_r increases its randomness.

The degree of stochasticity can be quantitatively estimated in terms of the variance $\hat{\sigma}^2$ of the distribution of J_r as a function of the displacement of the repulsive center from the center of the billiard.

$$\hat{\sigma}^2 = \frac{1}{N-1} \sum (x_i - x_{average})^2.$$

Graphs corresponding to different values of displacements are represented in **Figure 5.4**. The graphs clearly demonstrate that the system becomes chaotic above some threshold value of the displacement Δ_{cr}. To ascribe a physical meaning to this threshold parameter let us find the condition for the trajectory of the particle to cross the center of the billiard when the value of the displacement of the coulomb center from the center of the billiard is δ and the total energy $E = 1$. The energy conservation leads to

$$\frac{\gamma}{\delta} = 1.$$

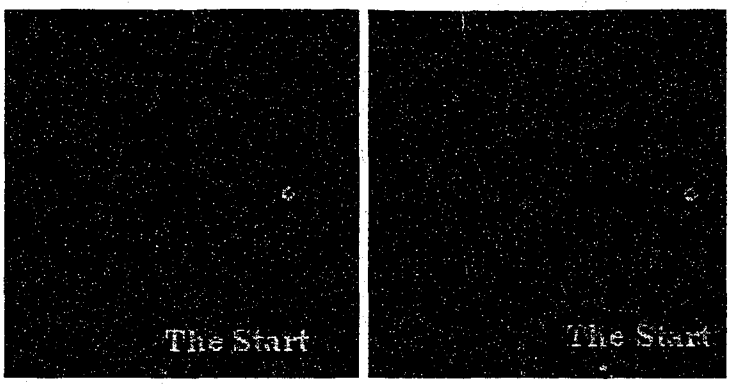

Figure 5.3: Trajectories that pass between the center of the billiard and the repulsive Coulomb center. The presence of such trajectories affects the character of the dynamics of the system, increasing its stochasticity.

Therefore, trajectories of the particle start to pass between the center of the billiard and the repulsive center (as shown in **Figure 5.3**) when $\delta > \gamma$. On the other hand it can be clearly seen from **Figure 5.4** that the variance starts to grow and thus the system starts to exhibit stochasticity as $\delta > \approx \gamma$. Thus, the clear conclusion is that trajectories passing between the center of the billiard and the repulsive center are those making the system mostly chaotic. As the strength of interaction increases, the moving particle is pushed off center and fewer trajectories are able to pass between the repulsive center and the center of the billiard. Hence, the system appeared to be regular for a greater range of the displacement of the Coulomb center.

The general results are exactly the same as those obtained in the previous chapter: *an increase in the strength of the Coulomb interaction suppresses chaos for small values of the displacement, but quickly makes the system chaotic with a larger degree of stochasticity for a sufficiently large break of the symmetry.*

5.5 Summary.

The classical dynamics of two strongly interacting particles billiard was studied in detail from a number of different points of view: Poncaré sections, Lyapunov exponents and the action variables. All these different approaches lead to the same conclusion about

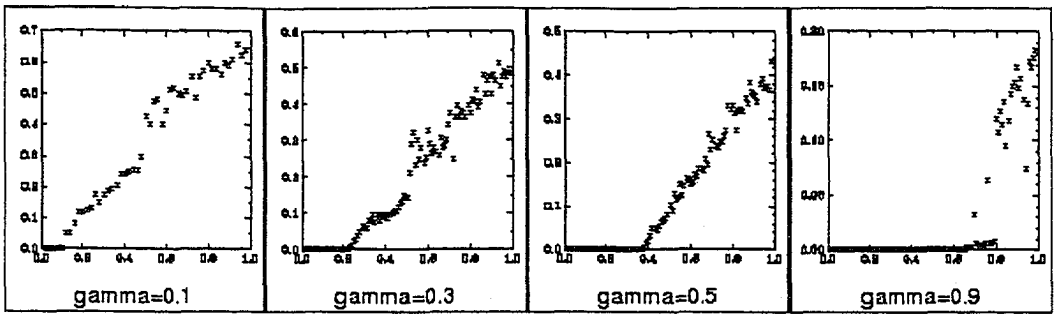

Figure 5.4: Variances $\hat{\sigma}^2$ of distributions of the actions J_r versus displacement of the Coulomb center for different values of the strength of the Coulomb interaction γ. It can be seen from the graphs that as the strength of the interaction is increasing the system starts to exhibit stochastic behavior starting with larger values of the stochastic parameter (asymmetry of the system). On the other hand, the stochasticity of the system appears to be more extensive with the growth of the Coulomb constant.

properties of the dynamics of the system depending upon the strength of the Coulomb interaction (parameter γ) and the degree of asymmetry of the system (parameter X_0):

- The system is integrable when the repulsive center coincides with the center of the billiard.

- When the Coulomb center is displaced from the center of the billiard and the value of displacement is less than some critical value $X_0 < \Delta_{cr}$, the motion continues to be regular. The Poncaré sections for this case represent projections of the KAM tori. The value of the critical parameter Δ_{cr} depends approximately linearly upon the strength of the Coulomb repulsion $\Delta_{cr} \approx \gamma$. Thus the strength of the Coulomb repulsion suppresses chaos for the case of the small degree of the asymmetry of the system.

- When the displacement of the Coulomb center becomes larger than the critical parameter $X_0 > \Delta_{cr}$, some of the KAM tori become destroyed and the system exhibits a mixed phase space. Farther growth of the asymmetry leads to destruction of the remaining KAM surfaces. This destruction happens faster for larger values of the Coulomb repulsion. Finally, as the repulsive center moves close enough to the boundary, the system exhibits a chaotic phase space. The value of the Lyapunov exponent of the system is growing logarithmically versus displacement and arrives to its maximal value

as the Coulomb center is placed near the edge of the billiard. The maximal value of the Lyapunov exponent grows approximately linearly versus the growth of the strength of the Coulomb repulsion. This way, the strength of the Coulomb repulsion increases the degree of the stochasticity of the system in the case when the symmetry is sufficiently broken.

Chapter 6

Interacting Particles inside a circular Coulomb billiard: Quantum Dynamics.

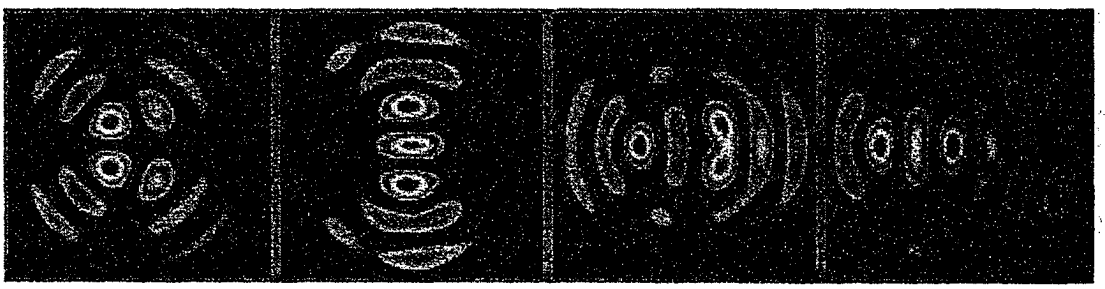

This chapter discusses the quantum mechanical treatment of the Circular Coulomb Billiard. The experimental motivation for the quantum mechanical approach in description of this system comes from artificial atoms at law temperatures, when the character of the dynamics is essentially quantum mechanical. Methods, developed and tested in this chapter will be used later to study more realistic models of many particle systems in confined geometries, which are maximally close to realistic models of artificial atoms, as well as quantum dots with two or more interacting particles.

6.1 Quantum Circular Coulomb Billiard.

Starting with the classical Hamiltonian **(5.1)**

$$H = \frac{{p_x}^2}{2m} + \frac{{p_y}^2}{2m} + \frac{\gamma}{\sqrt{(x-x_0)^2 + (y-y_0)^2}},$$

we again use the parameter

$$\gamma = \frac{qQ}{m}.$$

Replacing the dynamical variables by their operators

$$x_j \to x_j \quad p_j \to -i\hbar\frac{\partial}{\partial x_j},$$

we obtain the quantum Hamiltonian:

$$\begin{aligned} \hat{H} &= -\tfrac{\hbar^2}{2m}\nabla^2 + \frac{\gamma}{\sqrt{(x-x_0)^2+(y-y_0)^2}} \\ \nabla^2 &= \tfrac{\partial^2}{\partial x^2} + \tfrac{\partial^2}{\partial y^2}. \end{aligned} \tag{6.1}$$

Thus the time-independent Schrodinger equation is

$$-\frac{\hbar^2}{2m}\nabla^2\psi + \frac{\gamma}{\sqrt{(x-x_0)^2 + (y-y_0)^2}}\psi = E\psi.$$

Introducing the parameters

$$\epsilon = \tfrac{2mE}{\hbar^2} \quad \alpha = \tfrac{2m\gamma}{\hbar^2} \tag{6.2}$$

the Schrodinger equation becomes

$$-\nabla^2\psi + \frac{\alpha}{\sqrt{(x-x_0)^2 + (y-y_0)^2}}\psi = \epsilon\psi. \tag{6.3}$$

Confinement of the system inside the circular elastic billiard of unit radius leads to the following boundary conditions:

$$\Psi(t,x,y)|_{x^2+y^2=1}=0.$$

6.2 Perturbation method: case of weak electrostatic repulsion.

First, in order to observe some general features of the quantum dynamics, we apply the time independent perturbation method (see [49] or [59]) under the assumption of weak electrostatic repulsion. The exact range of the parameter α for which the perturbation approach yields reliable results will be clarified later. Following the standard procedure of time-independent perturbation theory, we split the Hamiltonian into two parts

$$\hat{H}_0=-\nabla^2 \quad \hat{H}_1=\frac{\alpha}{\sqrt{(x-x_0)^2+(y-y_0)^2}}.$$

An expression for the unperturbed Hamiltonian in polar coordinates is

$$\hat{H}_0=-\frac{\partial^2}{\partial\rho^2}-\frac{1}{\rho}\frac{\partial}{\partial\rho}-\frac{1}{\rho^2}\frac{\partial^2}{\partial\theta^2}.$$

The eigenfunctions of $\hat{H}_0$ that satisfy the Dirichlet boundary conditions on the unit circle are

$$\phi_{nm}=J_m(\mu_n^m\rho)e^{im\theta} \quad n=1,2,3,\ldots \quad m=0,\pm1,\pm2,\ldots$$

In the expression above $J_m(x)$ denotes the Bessel functions of the first kind (see [1]) and μ_n^m labels the $n-$th zero of the Bessel function $J_m(x)$. The energy eigenvalues of the unperturbed Hamiltonian are $(\mu_n^m)^2$. The perturbation is

$$\hat{H}_1 = \frac{\alpha}{\sqrt{(x-x_0)^2 + (y-y_0)^2}}.$$

The eigenfunctions of $\hat{H}_0$ corresponding to $m = 0$ are not degenerate, therefore the corrections to the corresponding energy levels are equal to matrix elements of the perturbation

$$\Delta\epsilon_{nondegenerate} = \langle\phi_{n0}|\hat{H}_1|\phi_{n0}\rangle.$$

If $m \neq 0$ the energy levels are degenerate and in order to find general corrections to them we have to diagonalize the matrix of the perturbation. However, we can use the symmetry of the system. The displacement of the Coulomb center can be taken taken along the $x-$axis. In such a case, the matrix of the perturbation is diagonal if we choose the following pair of the eigenfunction as a basis of the degenerate state:

$$\phi_{ne} = J_m(\mu_n^m \rho)\cos(m\theta) \quad \phi_{no} = J_m(\mu_n^m \rho)\sin(m\theta).$$

The graphs of a few eigenfunctions ϕ_{ne} and ϕ_{no} are represented in **Figure 6.1.**

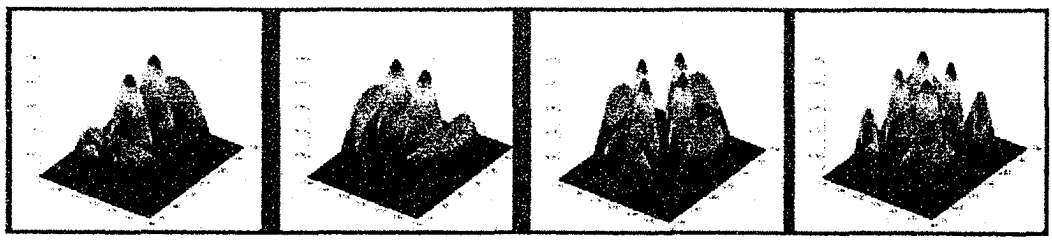

Figure 6.1: The pairs of eigenfunctions ϕ_{ne} and ϕ_{no} for energy values $\epsilon = \mu_1^{12}$ and $\epsilon = \mu_1^{22}$

Initially degenerate energy levels become split and the resultant corrections to the states ϕ_{ne} and ϕ_{no} are

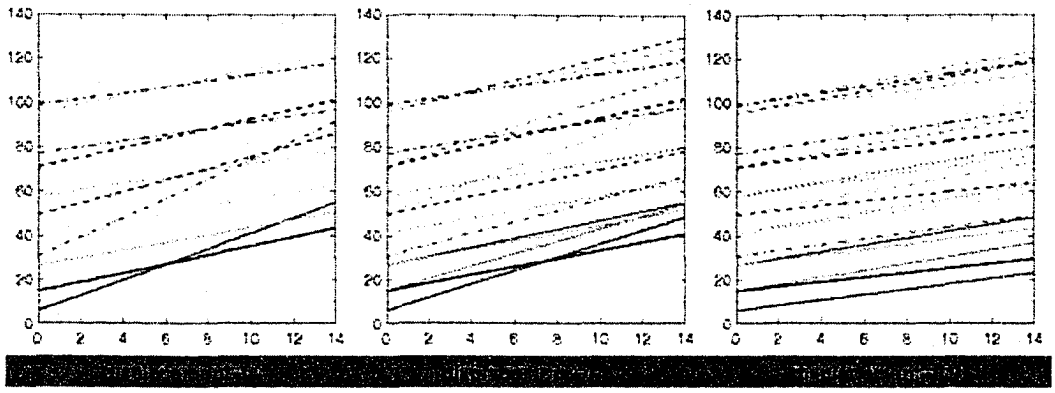

Figure 6.2: Energy Levels for various values of the displacement of the center of the Coulomb field versus strength of the Coulomb field α acquired using time independent perturbation theory.

$$\Delta\epsilon_{ne} = \langle\phi_{ne}|\hat{H}_1|\phi_{ne}\rangle \quad \Delta\epsilon_{no} = \langle\phi_{no}|\hat{H}_1|\phi_{no}\rangle.$$

The eigenfunctions of the unperturbed Hamiltonian $\langle\phi_{ne}|$ and $\langle\phi_{no}|$ remain first order approximate eigenfunctions of the perturbed system. The graphs of the energy versus the parameter α for few values of the displacement of the repulsive center are represented in **Figure 6.2**. We see that the energy eigenvalues increase proportionally to α. Let us estimate a range of parameters when the perturbation approach gives an adequate description of the system. Time-independent perturbation theory yields valid results if $\Delta\epsilon \ll \epsilon$ (see [49]). The ground state of the system is the state mostly affected by the perturbation. Hence, we use the results obtained for this state to estimate accuracy of the method. The correction to the energy for this state turned out to be

$$\Delta\epsilon_0 = 3.513510 \cdot \alpha.$$

The energy eigenvalue of the unperturbed ground state is $\epsilon_0 = 5.783186$. Therefore, the perturbation approach is valid if

$$\alpha \ll 1.65 \, .$$

All energy levels **(Figure 6.2)** display a simple linear increase as the result of proportionality of the perturbation $\hat{H}_1$ to the value of the parameter α. Such behavior does not exhibit any degree of randomness or inter-level correlation as we expect to observe in the case of the quantum correspondence of the classically chaotic dynamics. Let us determine the classical analogue of the quantum system which evolves in the quantum case according to the perturbative methods. All the classical computations were carried out with the constant value of the total energy $E = 1$, substituted into **(6.2)** to obtain the following relationship between the classical and quantum parameters used:

$$\gamma = \frac{\alpha}{\epsilon}.$$

As before, for an estimation of the accuracy of the perturbative method we use the minimal value of the energy $\epsilon_0 = 5.783186$ which corresponds to the ground state of the system where no Coulomb repulsion is present. Therefore, the quantum mechanical condition $\alpha \ll 1.65$ emerges in the classical case as $\gamma \ll\approx 0.1$. This corresponds to the case of an extremely weak Coulomb repulsion, where the force exerted by the Coulomb center is so weak that it does not strongly affect the dynamics of the system.

As it was expected, the results of perturbation theory are valid only when the classical analogue of the system exhibits regular dynamics. Therefore, data obtained in this section has no connection to the underlying classical chaos. However, the results obtained here can be used as the limiting values corresponding to the case of weak repulsion to check the correctness of methods that will be introduced in the coming parts of this chapter.

6.3 Application of the Rayleigh-Ritz method.

In this section we solve the time-independent Schrodinger equation **(6.3)**

$$-\Delta^2\psi + \frac{\alpha}{\sqrt{(x-x_0)^2+(y-y_0)^2}}\psi = \epsilon\psi$$

using the Rayleigh-Ritz method **(see [59])**, which yields good results for quite a wide range of quantum mechanical Hamiltonian systems. As an orthonormal set of Rayleigh-Ritz trial functions we use

$$\phi_{nm}(\rho,\theta) = C_m J_m(\mu_n^m \rho)e^{im\theta} \quad m = 0, \pm 1, \pm 2, \ldots \quad n = 1, 2, 3, \ldots$$

In the expression above $J_m(x)$ are the Bessel functions of an integer order, μ_n^m denotes the n-th root of an equation $J_m(\mu) = 0$ and C_m is the normalization constant. As known from the theory of Bessel functions (see [1]) ϕ_{nm} form a complete set. Besides that, the boundary conditions $\phi_{nm}|_{\rho=1} = 0$ are satisfied, and as a consequence, this is true for arbitrary linear combination $\sum A_{nm}\phi_{nm}$. Therefore, we look for a solution of the form

$$\psi(\rho,\theta) = \sum_{nm} A_{nm}\phi_{nm}(\rho,\theta),$$

where A_{nm} in the last expression are undefined coefficients. To obtain a summation governed by a single index, we reorder the trial functions in ascending order of the values μ_n^m. This yields a slightly different form of the solution:

$$\psi(\rho,\theta) = \sum_i A_i\phi_i(\rho,\theta). \tag{6.4}$$

Next we substitute $\psi(\rho,\theta)$ into the Schrodinger equation **(6.3)**, multiply by $\langle\phi_j|$, integrate and use the closure relation $\langle\phi_j|\phi_i\rangle = \delta_{ji}$. This produces a matrix equation

$$H_{ji}A_i = \epsilon A_j. \tag{6.5}$$

In the expression above H_{ji} denotes the Hamiltonian matrix:

$$H_{ji} = \langle \phi_j | \hat{H} | \phi_i \rangle.$$

We solve **(6.5)** using the *LU decomposition method* (see [68]). The matrix eigenvalues obtained are the Rayleigh-Ritz approximation for eigenvalues of the Schrodinger equation. Substituting components of the eigenvectors $\vec{A}$ of the matrix equation into **(6.4)** give the Rayleigh-Ritz approximation for the eigenfunctions of the Hamiltonian. The more trial functions we use, the more accurate the results are. To test the reliability of the method we perform a procedure, similar to that described in the **Section 4.5**. We increase the amount of trial functions used (N) until the results start to be independent of N.

The computations were carried out using $N = 196$ trial functions. The lowest 150 energy levels appeared to be independent of N, therefore the lowest 150 eigenfunctions obtained can be considered as the realistic set of eigenfunctions of the system. A further increase of N would provide reliable results for a larger amount of eigenfunctions. However, it would require much more powerful computers than those available for work on this dissertation.

6.3.1 Energy eigenlevels of the system.

Figure 6.3 represents a few of the lowest energy levels versus α for various values of the displacement obtained using the Rayleigh-Ritz method. Compared with the analogous spectrum acquired using perturbation theory **(Figure 6.2)** we can see that for very small values of α the results obtained by these two methods agree - all the energy eigenvalues in both figures display a linear increase, proportional to α. Later on, the energy levels obtained by the perturbative method start to cross each other, while the Rayleigh-Ritz method shows that the levels avoid crossing, repelling each other.

Unlike the above set of graphs, we represent the energy spectrum versus the dis-

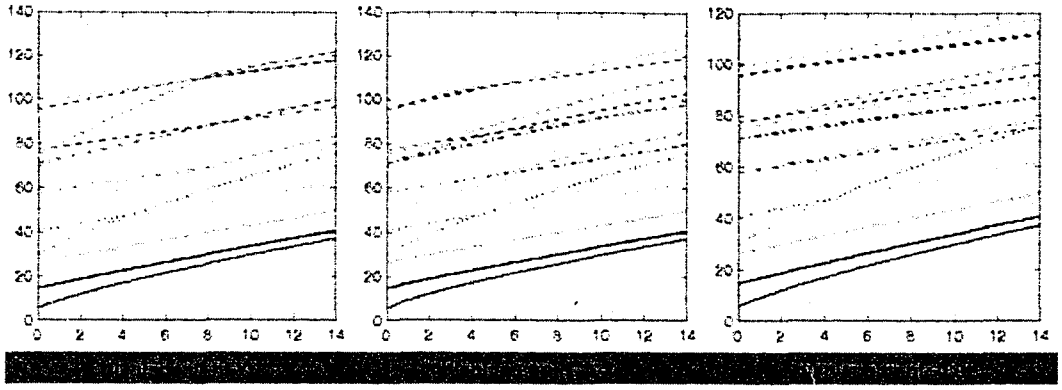

Figure 6.3: Energy Levels for different values of displacement of the center of the Coulomb field versus strength of the Coulomb field α

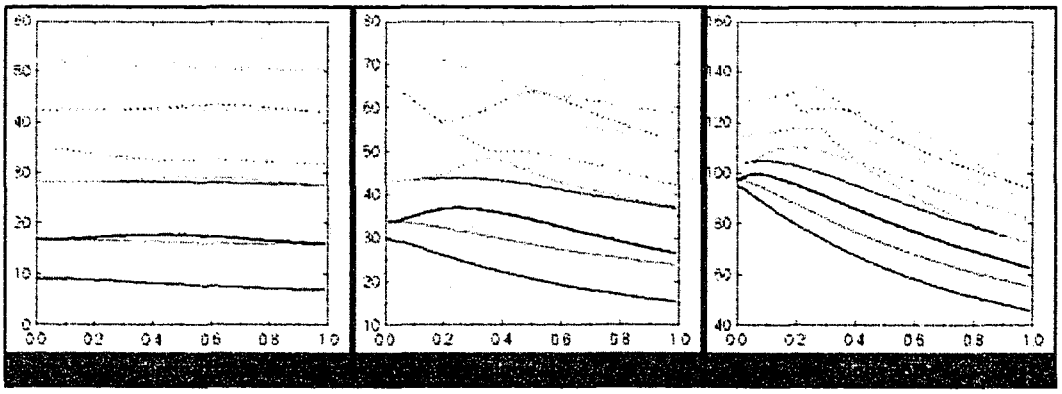

Figure 6.4: The lowest ten levels of the energy eigenspectrum versus displacement of the Coulomb center for various values of the strength of the Coulomb repulsion (parameter α).

placement of the Coulomb center for various values of the strength of the Coulomb repulsion in Figures **(6.4) and (6.5)**. The following general description of the system in terms of its energy spectrum can be given based on these pictures:

- As the Coulomb repulsion is weak $\alpha <\approx 2$, the dynamics of the system can be well approximated by perturbative methods. The energy levels show at a small rate proportionally to α, and there is no correlation between them. The classical analogue of this case is regular motion, when the Coulomb repulsion is too small to significantly affect the dynamics of the system.

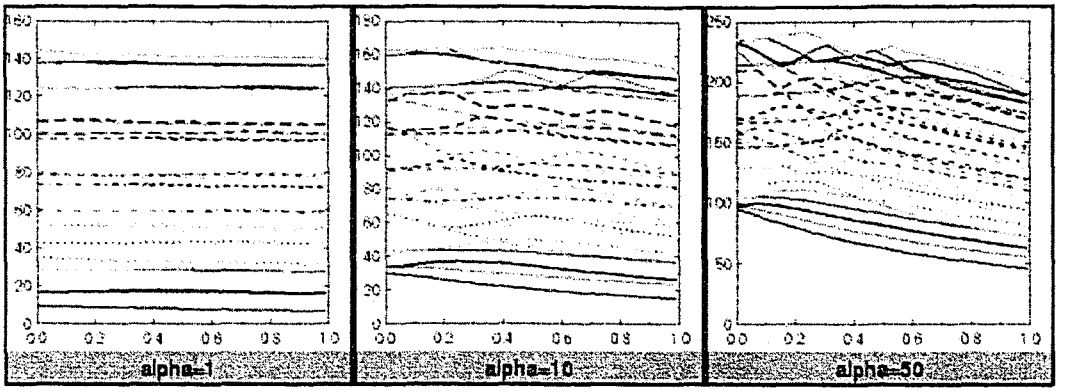

Figure 6.5: The lowest thirty levels of the energy eigenspectrum versus displacement of the Coulomb center for various values of the strength of the Coulomb repulsion (parameter α).

- When the Coulomb repulsion is sufficiently strong, but a displacement of the repulsive center from the center of the billiard is smaller than some threshold value, the energy levels are not correlated and they change approximately in proportion to the displacement of the Coulomb center. The threshold value of the displacement that puts a limit to this sort of behavior is $X_0 \approx \frac{\alpha}{\epsilon}$. The last equation corresponds classically to $X_0 \approx \gamma$. In the classical case this condition indicates a transition from regular to chaotic character of the dynamics for a certain degree of asymmetry. Thus we obtain one more example that, when the classical dynamical system exhibits regular dynamics, the energy levels of its quantum analogue are uncorrelated.

- As the displacement of the repulsive center from the center of the billiard becomes sufficiently large, $X_0 >\approx \frac{\alpha}{\epsilon}$, the picture of the energy spectrum shows a great deal of a randomness due to numerous repulsions of the closest levels. This means that different eigenstates of the system become strongly correlated. The quantum condition $X_0 >\approx \frac{\alpha}{\epsilon}$ classically means $X_0 > \gamma$. The classical dynamics for this range of parameters exhibits a mixed phase space that eventually becomes chaotic. Thus, we observe that when the classical analogue of the quantum system exhibits chaotic dynamics, the quantum energy levels start to display strong inter-level

correlation.

6.3.2 Level spacing statistics.

As already mentioned (Chapter 2.3) and revisited in the previous subsection the energy-level statistics can be an important indicator of an underlying classical chaos emerging from the quantum mechanics. A common feature of quantum systems that have chaotic classical analogues is 'level repulsion', while a lack of such a repulsion, or Poisson statistics indicates that the classical counterpart of the quantum system is regular.

We are going to examine the energy-level statistics of the quantum Coulomb billiard analyzed in this chapter. We take an ordered set of the energy levels of the system, and compute spacings of the neighbor levels:

$$\Delta_k = \epsilon_{k+1} - \epsilon_k.$$

The values Δ_k appear to be distributed randomly and we compute a histogram of this distribution. Some results are represented in **Figure 6.6**. They correspond to $\alpha = 50$ and various values of the displacement of the Coulomb center. A large collection of the histograms obtained for quite a wide range of parameters of the system is placed in Appendix D (**Figure D.7**). The general features of the level spacing distribution can be summarized as the following:

- When the Coulomb center is placed close to the center of the billiard all the histograms show an extremely sharp maximum at the origin. This is a consequence of an infinite degree of degeneracy in terms of the angular momentum of the system with axial symmetry.

- As the displacement of the Coulomb center grows, the probability for two neighboring levels to have equal values of the energy becomes relatively smaller. However, this probability does not completely disappear - it remains equal to some nonzero value even for the highest degree of the asymmetry when the repulsive center is

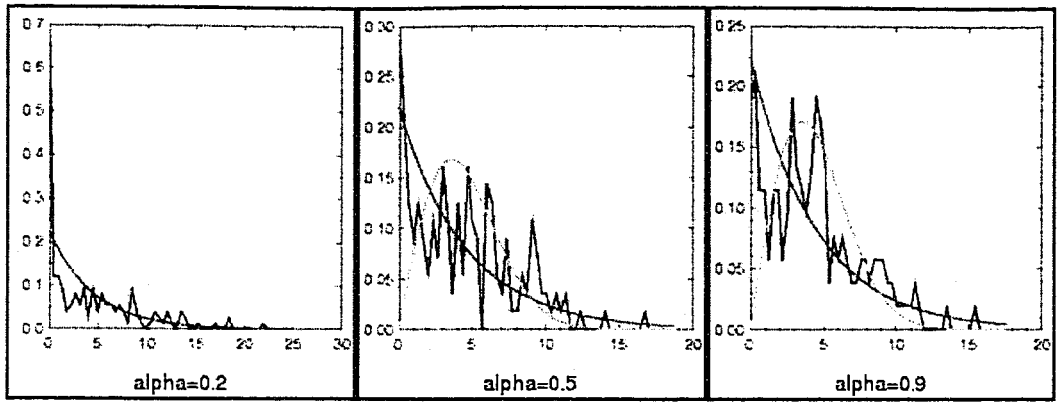

Figure 6.6: Histograms of the level-spacing distribution (the dark-blue lines) of the quantum circular Coulomb billiard with $\alpha = 50$. The violet lines represent the corresponding Poisson distributions, while the light-blue lines represent the Wigner distribution. It can be seen that as the displacement of the Coulomb center is small, the distribution exhibits a sharp maximum at the origin. This is the result of an infinite degree of degeneracy of the integrable case. As the degree of an asymmetry is growing the energy levels become correlated, thus the probability for two close levels to have equal energy values becomes relatively small. However, all the histograms show a nonzero value at the origin, therefore some uncorrelated energy levels remain presented. The shape of the histograms corresponding to large degrees of the asymmetry seem to be split on two parts: the left part tends to the Poisson random walk statistics while the right one approaches Wigner's distribution.

placed close to the boundary. The shape of the histograms for sufficiently large values of the displacement $\alpha > 0.4$ appears to consist of two pieces. A part corresponding to small values of the spacings ($\Delta <\approx 3$) seems to be described by the Poincare random walk statistics, while the right portion of the graph ($\Delta >\approx 3$) clearly approaches Wigner's distribution.

The above summary suggests a reason to think that the energy spectrum of the system consists of two distinct parts. The energy levels that belong to the first part are uncorrelated and spacings between them obey Poisson statistics, while the rest of the levels exhibits a strong inter-level correlation and their spacings are described by Wigner's distribution. This is consistent with what was observed in the previous subsection. As we noticed there, the energy levels exhibit a strong repulsion when $X_0 > \frac{\alpha}{\epsilon}$ **(Figure 6.5)**. This means that if we consider a hyperbola $\epsilon = \frac{\alpha}{X_0}$, then all the

states above this hyperbola display strong inter-level repulsion. To figure out what kind of energy levels correspond to a system with a certain strength of Coulomb repulsion and a certain degree of asymmetry we have to draw a vertical line $X_0 = const$ on one of the graphs in **Figure 6.5**. This line crosses numerous uncorrelated spectral curves situated below the hyperbola and then it penetrates into a region where a strong level repulsion is present. The lowest energy levels are situated below the hyperbola $\epsilon = \frac{\alpha}{X_0}$, and these levels have quite a smooth shape and do not display any correlation with each other. Thus the lowest spectral lines form an uncorrelated part of the energy spectrum, the one described by the Poisson random walk statistics. On the other hand all the energy levels above the hyperbola $\epsilon = \frac{\alpha}{X_0}$ form the correlated part of the spectrum, their statistics are described by Wigner's distribution.

6.3.3 Eigenfunctions of the system.

A large presentation of the eigenfunctions of the system obtained using the Rayleigh-Ritz method is given in Appendix D (**Figure D.1**). The eigenfunctions corresponding to the random part of the energy spectrum are what attract the most interest for the purpose of this dissertation. As it was shown in the previous subsection the inter-level repulsion becomes significant and the classical counterpart of the system is chaotic when

$$X_0 > \frac{\alpha}{\epsilon}.$$

A few of eigenfunctions with parameters satisfying the last relationship are represented in **Figure 6.7**. They display a strong concentration of the probability along narrow channels, corresponding to the classical periodic orbits. As it was already mentioned, this sort of eigenfunction is called a quantum scar and its presence indicates that the classical analogue of the quantum system is chaotic. Thus, the analysis of the wave functions of the system provides one more quantum manifestation of the underlying classical chaos - the quantum scars.

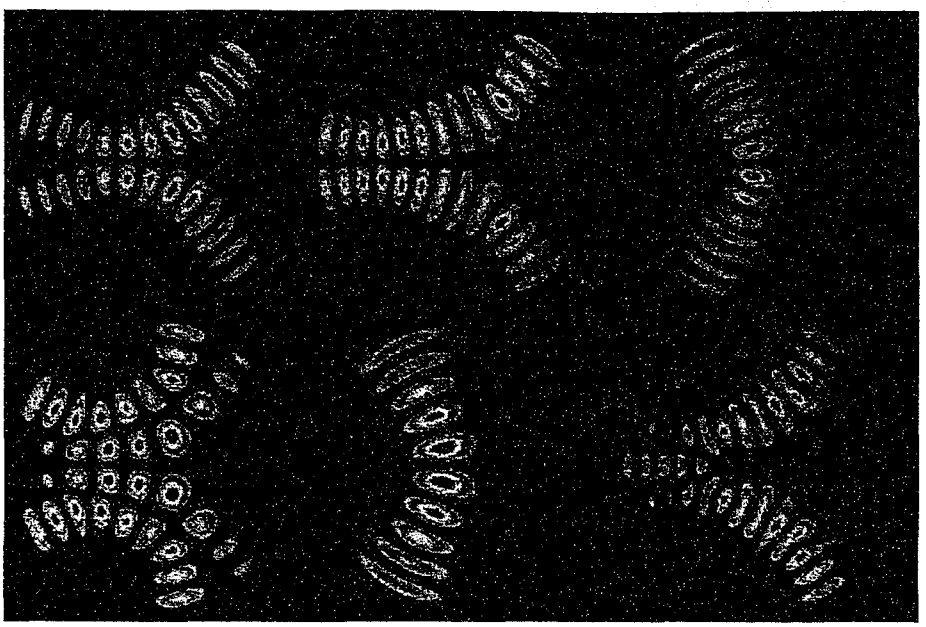

Figure 6.7: The wavefunctions of some of the quantum states with parameters obeying the relationship $X_0 > \frac{\alpha}{\epsilon}$. Thus the classical analogues of these states are chaotic. The wavefunctions in the Figure display a strong concentration of the probability along narrow channels - quantum scars. Shapes of the scars resemble shapes of the classical periodic orbits.

6.4 Solution of the problem with the axial symmetry.

As was discussed in the previous section the accuracy of the Rayleigh-Ritz method depends on the number of trial functions used (N). which is limited by the computational resources available. Therefore, the Rayleigh-Ritz approach can not be applied if we need to examine highly excited states. In the earlier chapters the method of matching of the boundary conditions was devised **(see Section 4.6)** to find the highly excited levels of the quantum square magnetic billiard. Now we are going to apply this method to the system examined in this chapter. First, we need to solve the problem with an axial symmetry to use its eigenfuctions as a set of trial functions for the method of matching of the boundary conditions.

The axial symmetry implies that the Coulomb center coincides with the center of the billiard. The Hamiltonian in this case is

$$\hat{H} = -\frac{\partial^2}{\partial\rho^2} - \frac{1}{\rho}\frac{\partial}{\partial\rho} - \frac{1}{\rho^2}\frac{\partial^2}{\partial\theta^2} + \frac{\alpha}{\rho}.$$

To find the eigenfunctions we use a separation of variables

$$\phi(\rho,\theta) = \Phi(\rho)e^{im\theta} \quad m = 0, \pm 1, \pm 2, \cdots$$

The requirement for ϕ to be single-valued leads to the fact that the quantum number m can be only an integer value. The radial part $\Phi(\rho)$ must satisfy the following equation:

$$\Phi'' + \frac{1}{\rho}\Phi' - \frac{m^2}{\rho^2}\Phi - \frac{\alpha}{\rho}\Phi + \epsilon\Phi = 0\,, \tag{6.6}$$

with the boundary condition $\Phi(1) = 0$ and the additional requirement that $\Phi(\rho)$ is finite at the origin $\rho \to 0$. Two asymptotic solutions of the equation **(6.6)** as $\rho \to 0$ are

$$\rho^{\pm|m|}.$$

However, for $|m| \neq 0$ only one of these functions is finite at the origin. Hence, we have to chose this one and obtain the asymptotic behavior of the radial part as $\rho \to 0$

$$\Phi(\rho) = \rho^{|m|} \quad \rho \to 0.$$

This consideration yields the Cauchy conditions for the numerical solution of the equation **(6.6)**.

$$\Phi(\rho) = \begin{cases} \Phi(0) = 1 \;\; \Phi(\delta\tau) = 1 & m = 0 \\ \Phi(0) = 0 \;\; \Phi(\delta\tau) = (\delta\tau)^{|m|} & m \neq 0. \end{cases}$$

Using this Cauchy conditions we apply the *embedded 8th order Runge-Kutta Prince-*

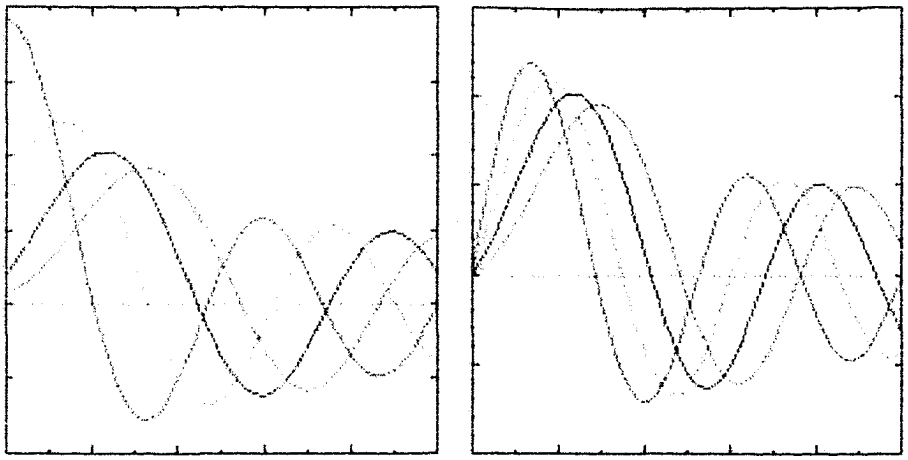

Figure 6.8: Results of the numerical solution of the equation **(6.6)**. The left graph corresponds to $m = 0$ and the right one to $m = 1$. Different curves on the same figure correspond to $\alpha = 0\ 10\ 20\ 30$.

Dormand method with 9th order error estimate (see [68]) to integrate **(6.6)**. The graphs of some of the solutions obtained this way are represented in **Figure 6.8**. The red curves on each picture correspond to $\alpha = 0$ and hence are the Bessel function of an integer order $J_m(x)$. As the parameter α grows - the particle becomes displaced farther from the repulsive center.

The next thing to do is to match boundary conditions. It can be done by adjusting the parameter ϵ. For each combination of the parameters α and m we determine numerically the values of ϵ such that the radial part vanishes on the boundary $\Phi(1) = 0$. In this way a discrete set of the energy eigenvalues, ϵ_j, was allocated each corresponding to the same quantum magnetic number m but to different **principal quantum numbers** K. The quantum number K is equal to the amount of zeros of the radial part of the wavefunction.

A few of the lowest energy levels are represented in **Figure 6.9**. An interesting feature to notice in the behavior of the spectral lines is that for sufficiently large values of the constant of interaction, α, the energy eigenvalues corresponding to the same principal quantum number K but to a different magnetic number m come extremely

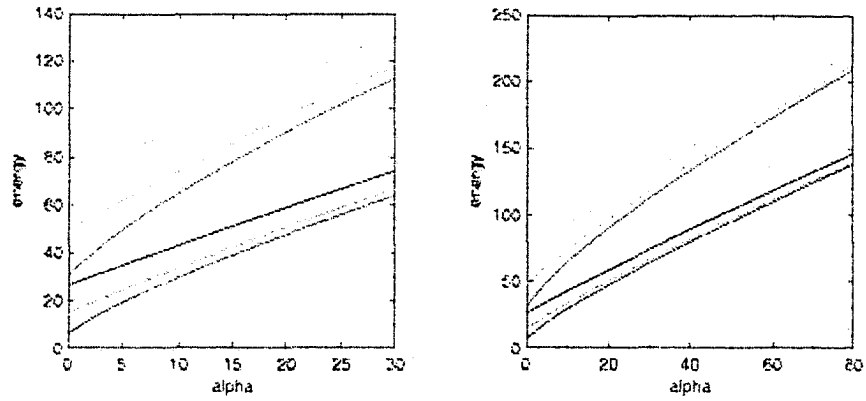

Figure 6.9: Energy spectrum versus the parameter of interaction α.

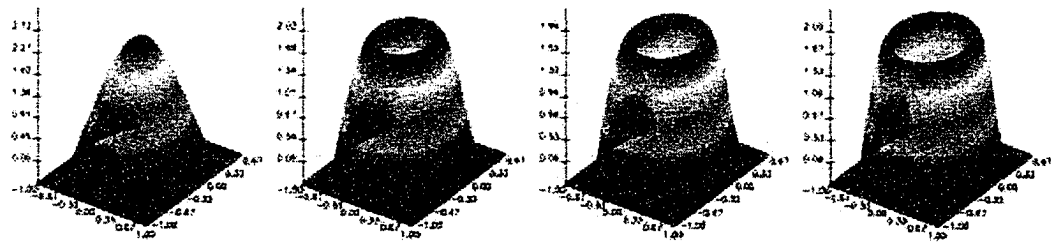

Figure 6.10: The wave functions of the ground state for different values of the strength of the repulsive potential $\alpha = 0\ 5\ 10\ 20$.

close to each other. This means that the strong interaction suppresses the degeneracy in terms of the angular momentum. Another interesting feature is that the energy levels corresponding to the magnetic quantum number $m = 0$ grow at much higher rate for small α ($\alpha <\approx 15$). They then reduce the rate of their growth, and eventually approach all the other lines with the same quantum number K. This type of behavior can be understood from the fact, that for this energy levels the maximum probability initially corresponds to $\rho = 0$. Therefore, as the repulsive pole appears at the center of the billiard, the potential energy of this levels acquires the highest value, hence this levels become mostly affected by the presence of the field. To minimize the energy the maximal probability becomes displaced from the position of the repulsive center. Eventually these levels change their shape as can be seen in the pictures **(6.10) (6.11)**

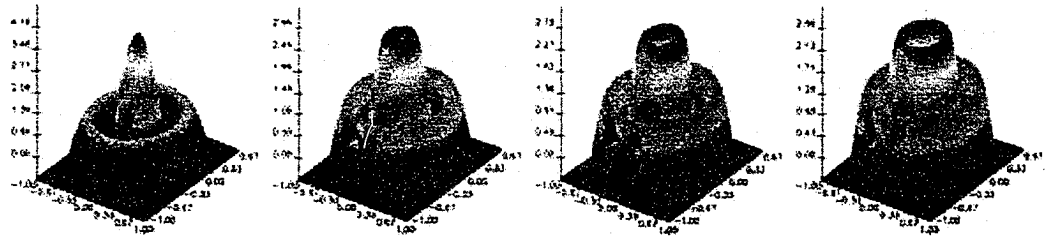

Figure 6.11: The wave functions corresponding to the quantum numbers $K = 2$ $M = 0$ for different values of the strength of the repulsive potential $\alpha = 0\ 5\ 10\ 20$.

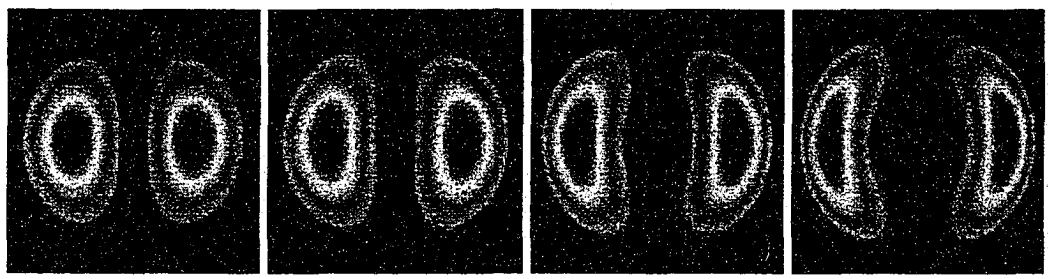

Figure 6.12: The wave functions of the first excited state $K = 1$ $M = 1$ for different values of the strength of the repulsive potential $\alpha = 0\ 5\ 20\ 50$.

and extreme growth of their energy values slows down.

6.5 Method of Matching of Boundary Conditions.

As illustrated in the case of the quantum square magnetic billiard, we are going to use the set of infinitely degenerate eigenfunctions, obtained in the previous section, as trial functions for the method of matching of the boundary conditions. The Hamiltonian of the system is

$$\hat{H} = -\frac{\partial^2}{\partial\rho^2} - \frac{1}{\rho}\frac{\partial}{\partial\rho} - \frac{1}{\rho^2}\frac{\partial^2}{\partial\theta^2} + \frac{\alpha}{\sqrt{(x-x_0)^2 + (y-y_0)^2}}. \tag{6.7}$$

We use the notation $\Phi(\rho, \alpha, \epsilon)e^{im\theta}$ for the eigenfunctions obtained in the previous section *(that satisfy the Schrodinger equation for the case with axial symmetry)*. As before we consider the displacement of the Coulomb center along the $x-$axis: $(y_0 = 0)$.

We are looking for a solution of the equation **(6.7)** in terms of a series

$$\psi(x,y) = \sum_{m=-N}^{N} C_m \Phi(\rho', \alpha, \epsilon) e^{im\theta'}. \tag{6.8}$$

In the expression above C_m are arbitrary coefficients and

$$\rho' = \sqrt{(x-x_0)^2 + (y-y_0)^2} \quad \theta' = \arctan \tfrac{y-y_0}{x-x_0}$$

are the polar coordinates in a polar coordinate system originated at the position of the repulsive center. Each term in the series **(6.8)** satisfies the Schrodinger equation with the parameters α and ϵ, as does their arbitrary linear combination. The next thing to do is to find a solution that satisfies the boundary conditions. This can be accomplished by adjusting the coefficients C_m in such a way that their linear combination **(6.8)** vanishes on the boundary. We choose $2N+1$ points on the boundary with coordinates ${\rho'}_i, {\theta'}_i$. Substitution of the coordinates of all these point into **(6.8)** and the requirement that the linear combination is equal to zero on the boundary produces $2N+1$ complex homogeneous equations with $2N+1$ unknown coefficients C_m.

$$\psi({\rho'}_i, {\theta'}_i) = \sum_{m=-N}^{N} C_m \Phi({\rho'}_i, \alpha, \epsilon) e^{im{\theta'}_i} = 0 \quad i,j = 0, \pm 1, \pm 2, \ldots \pm N. \tag{6.9}$$

The system of linear homogeneous equations has nontrivial solution if its determinant is zero. This way the condition

$$\det ||A_{im}|| = \det ||\Phi({\rho'}_i, \alpha, \epsilon) e^{im{\theta'}_i}|| = 0$$

helps to allocate the energy spectrum for every value of the parameter α.

Calculations were carried out for $N = 128$, producing operations on 257×257 matrices. It turned out that graphs of $\det ||A_{im}||(\epsilon)$ have extremely sharp minima at certain values of ϵ. Let us denote a set ϵ that corresponds to these minima as ϵ_j. The system of equations **(6.9)** has a nontrivial solution for these values of ϵ, while for the

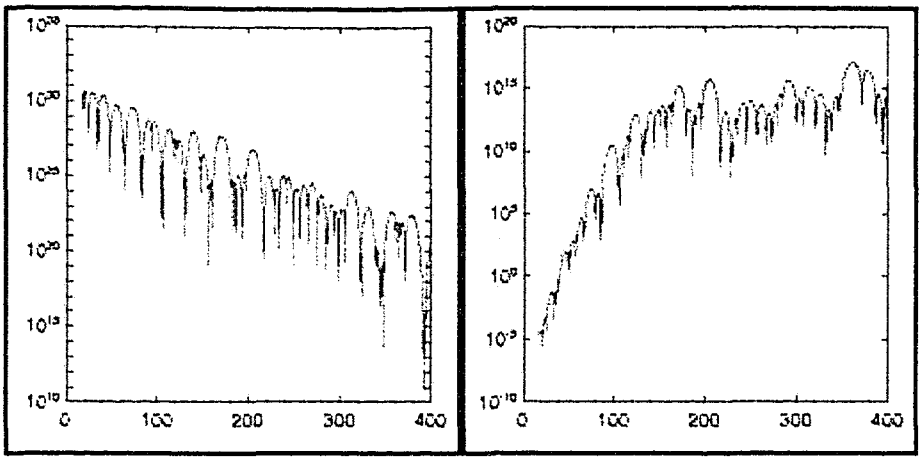

Figure 6.13: Plots of the dependence $\det||A_{im}||(\epsilon)$ for sets of parameters $\alpha = 5 \;\; X_0 = 0.10$ and $\alpha = 5 \;\; X_0 = 0.50$. The graphs are done in a logarithmic scale along the y-axis. Sharp minima on each of the graphs indicate a set of the energy eigenvalues ϵ_i.

original Schrodinger equation **(6.7)** the set ϵ_j represents the energy eigenvalues. Typical plots of the graphs $\det||A_{im}||(\epsilon)$ are represented in **Figure (6.13)**. Very clear minima on each of the graphs indicate the energy eigenvalues of the Hamiltonian.

Once energy eigenvalues are obtained, they are substituted into **(6.9)**. Then, similarly as it was done in the **Section 4.6**, we set one of the coefficient C_m to be equal to some nonzero value in order to obtain a non-homogeneous system of equations. To decide which one of the C_m to use we compute the norm of each column of the matrix of the system **(6.9)** and set a coefficient that corresponds to a minimal norm to be equal to one. Then the resultant non-homogeneous system of equations is solved numerically using *the LU-Decomposition method* (see [68]). Once obtained, the resultant solution set C_m is substituted into **(6.8)** and this yields an unnormalized wavefunction.

The eigenfunctions and the energy eigenvalues obtained by the method described in this section are in good correspondence with those obtained recently by the Rayleigh-Ritz method. This means that these two methods are in a good agreement with each other. An extensive outlook of the wavefunctions is given in the Appendix D **(Figure D.1)**. However, the method of matching the boundary conditions has an important advantage. As was mentioned earlier it allows one to obtain results for highly excited

states, when application of the Rayleigh-Ritz method becomes impossible because of the limited capabilities of the computational facilities available. A few eigenfunctions of highly excites states obtained by the method of matching of the boundary conditions are shown in **Figure 6.14.**

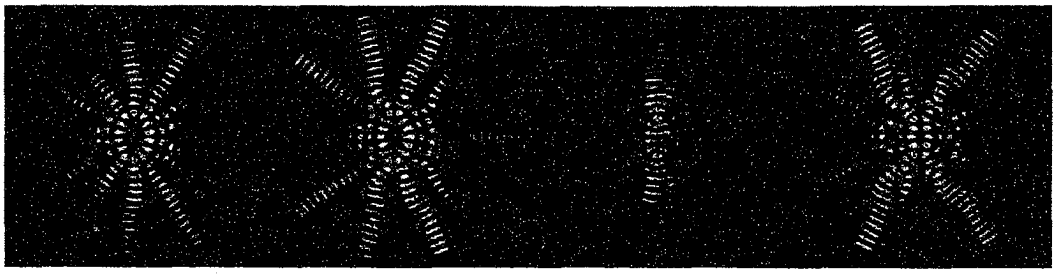

Figure 6.14: Wavefunctions of highly excited (≈ 500) states obtained by the method of matching of boundary conditions. Corresponding parameters of the system are $\alpha = 50$ and $X_0 = 0.3$.

The major disadvantage of the method of matching of the boundary conditions, as mentioned in **Section 4.6**, is that it does not give us all the energy eigenvalues. Some of the eigenstates can be missed. To avoid such losses we have to increase the amount of trial functions used which faces the same problem as we encountered while utilizing the Rayleigh-Ritz method: the limited power of available computers.

6.6 The time-dependent Schrodinger equation.

In the previous sections the Quantum Coulomb Billiard was examined based on the time independent Schrodinger equation. The eigenvalues as well as the eigenfunctions were obtained; they show clear signatures of an underlying classical chaos. As was observed when studying the square magnetic billiard **(Section 4.8)**, the time evolution of the system displays additional features that can be considered as the consequences of the underlying classical chaos. In this section we examine a time propagation of an initial wave pattern in the quantum coulomb billiard. To solve the problem of the time evolution we have to solve the time-dependent Schrodinger equation:

$$i\hbar\frac{\partial}{\partial t}\Psi = \hat{H}\Psi.$$

The quantum Hamiltonian operator of the system is the same as before **(6.1)**:

$$\hat{H} = -\frac{\hbar^2}{2m}\nabla^2 + \frac{\gamma}{\sqrt{(x-x_0)^2+(y-y_0)^2}}$$
$$\nabla^2 = \frac{\partial^2}{\partial x^2} + \frac{\partial^2}{\partial y^2}.$$

A formal solution of the time-dependent Schrodinger equation is expressed in terms of an exponential evolution operator acting on an initial wave pattern (see as an example [59]):

$$\Psi(\vec{r},t) = e^{-\frac{i}{\hbar}\hat{H}t}\Psi(\vec{r},0).$$

For numerical solution we use the same procedure as was applied when studying the square magnetic billiard **(see Section 4.8)** - the split operator method. First the Hamiltonian is represented as a sum of operators of the kinetic and potential energies $\hat{H} = \hat{T} + \hat{V}$. Next the following approximation for the exponential operator was used

$$e^{\hat{T}dt+\hat{V}dt} \approx e^{\hat{T}dt}e^{\hat{V}dt} \approx e^{\hat{V}\frac{dt}{2}}e^{\hat{T}dt}e^{\hat{V}\frac{dt}{2}}. \tag{6.10}$$

The approximation **(6.10)** is valid up to terms of an order $(dt)^3$ (see [59]). We then choose an initial wave-packet $\Psi(x,y,t_0)$ and act on it by the operator **(6.10)** to obtain a state at the moment of time $t_0 + \Delta t$

$$\Psi(x,y,t_0+\Delta t) = e^{-\frac{i}{\hbar}\hat{V}\frac{\Delta t}{2}}e^{-\frac{i}{\hbar}\hat{T}\Delta t}e^{-\frac{i}{\hbar}\hat{V}\frac{\Delta t}{2}}\Psi(x,y,t_0).$$

The operator $e^{-\frac{i}{\hbar}\hat{V}\frac{\Delta t}{2}}$ is diagonal in configuration space. Thus its action on $\Psi(x,y,t_0)$ leads to a phase-shift of the wavefunction in position space.

$$\tilde{\Psi}(x,y) = e^{-\frac{i}{\hbar}\hat{V}\frac{\Delta t}{2}}\Psi(x,y,t_0) = e^{-\frac{i\Delta t}{2\hbar}\frac{\gamma}{\sqrt{(x-x_0)^2+(y-y_0)^2}}}\Psi(x,y,t_0).$$

The operator of the kinetic energy is diagonal in momentum space. To represent $\tilde{\Psi}(x,y)$ in momentum space we express it in polar coordinates and expand it in the Bessel series (see [38]):

$$\tilde{\Psi}(\rho,\theta) = \sum C_k J_M(\mu_k^M \rho) e^{iM\phi},$$
$$x = \rho\cos\phi \qquad y = \rho\sin\phi.$$

In the formula above μ_k^M labels the $k-th$ root of the integer order Bessel function $J_M(\mu\rho)$. The ordering of the terms in the series is performed in the ascending order of μ_k^M. The Bessel functions $J_M(\mu\rho)$ are eigenfunctions of the Laplacian operator with the eigenvalues $-(\mu_k^M)^2$. Therefore, an action of the Laplacian operator Δ^2 on the Bessel function $J_M(\mu_k^M\rho)$ leads to its multiplication on $-(\mu_k^M)^2$. From the last follows that the action of the exponential operator $e^{-\frac{i}{\hbar}\hat{T}\Delta t}$ leads to the multiplication of each coefficient C_k in the Bessel series by a complex phase $e^{-\frac{i\hbar(\mu_k^M)^2}{2m}\Delta t}$

$$e^{-\frac{i}{\hbar}\hat{T}\Delta t}\tilde{\Psi}(x,y) = \sum -(\mu_k^M)^2 C_k J_M(\mu_k^M\rho)e^{iM\phi}.$$

Then, performing the inverse Bessel transform of the resultant Bessel series, we obtain a function in the configuration space $\tilde{\tilde{\Psi}}(x,y)$. The last operator $e^{-\frac{i}{\hbar}\hat{V}\frac{\Delta t}{2}}$ on the function $\tilde{\tilde{\Psi}}(x,y)$ yields the desired function $\Psi(x,y,t_0+\Delta t)$

$$\Psi(x,y,t_0+\Delta t) = e^{-\frac{i}{\hbar}\hat{V}\frac{\Delta t}{2}}\tilde{\tilde{\Psi}}(x,y).$$

Some examples of the time evolution are represented in **Figures (6.15) and (6.16)**. The first figure represents the time evolution of an initial wavepattern for the case with axial symmetry - this means the classical analogue is integrable. The initial wave

pattern exhibits some oscillatory motion - as is expected for the integrable quantum case. **Figure 6.16** represents the time evolution of the similar initial wave pattern governed by the Hamiltonian of an asymmetric dynamical system. The repulsive center is displaced one half - radius of the billiard. The classical analogue is known to exhibit a mixed phase space. The initial wave pattern was destroyed and the motion was suppressed to the left side of the billiard. This is a clear example of a non-integrable quantum system, which does not have a discrete spectrum of energy eigenvalues. Therefore, such a system can not be represented in terms of a series of functions, oscillating in time with the eigenfrequencies $\omega_j = \frac{E_j}{\hbar}$.

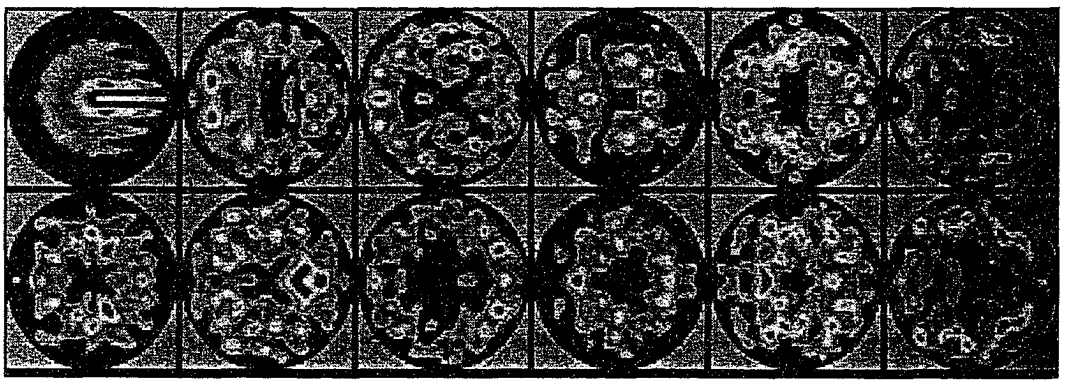

Figure 6.15: The Coulomb field is centered at the center of the billiard. The corresponding classical case is integrable. The wave pattern exhibits regular oscillatory motion.

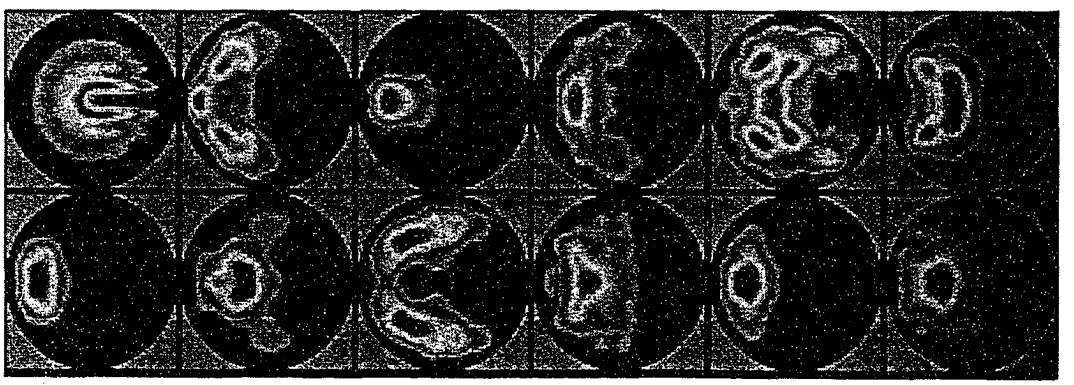

Figure 6.16: The Coulomb field is displaced from the center of the billiard to the right. The corresponding classical case is chaotic. The initial wave pattern is being destroyed, and late time evolution restricts the motion of the particle to the left side of the billiard.

6.6.1 The energy spectrum of the time evolution.

To find the energy spectrum of the Hamiltonian from a solution of the time-dependent Schrodinger equation we use the same procedure as the one described in Subsection 4.8.1 for the case of the square magnetic billiard. We compute a correlation of the initial wavefunction Ψ_0 and the wave function in future moments of time $\Psi(t)$. Let us assume that there exist a complete set (ϕ_j) of orthonormal eigenfunctions of the Hamiltonian $\hat{H}$, with a corresponding set of energy eigenvalues, E_j. We expand Ψ_0 in a series of ϕ_j:

$$\Psi_0 = \sum C_j \phi_j \, .$$

Based on the last expansion the time evolution is (see [59]):

$$\Psi(t) = \sum C_j e^{-\frac{i}{\hbar} E_j t} \phi_j .$$

The correlation function is

$$< \Psi_0 | \Psi(t) > = < \sum C_j \phi_j | \sum C_j e^{-\frac{i}{\hbar} E_j t} \phi_j > = \sum |C_j|^2 e^{-\frac{i}{\hbar} E_j t} .$$

The Fourier spectrum of the last expression is a linear spectrum with peaks corresponding to the subsequent values of E_j. In numerical computations we use the same set of parameters as everywhere throughout this Chapter:

$$\epsilon = \frac{2mE}{\hbar^2} \quad \alpha = \frac{2m\gamma}{\hbar^2} .$$

Figure (6.17) illustrates the Coulomb spectrum obtained from the solution of the time-dependent Schrodinger equation for the case $\alpha = 10$ and various displacements of the Coulomb center from the center of the billiard. It this is important to note that the energy eigenvalues obtained correspond to those acquired in the previous sections

of this Chapter as the result of solving of the time-independent Schrodinger equation. This is an indicator of a correspondence of all the methods used.

The next thing to examine is the appearance of spectral lines. For a small displacement from the center we clearly see a well-defined linear spectrum. This is the case when the corresponding classical dynamics are regular. As the displacement increases we see that the spectrum contains new lines and eventually becomes continuous. This is exactly what one expects for the non-integrable case. If the dynamics are non-integrable, a complete set of eigenfunctions does not exist and, therefore, the time evolution of the system can not be represented as a series of oscillatory terms:

$$\Psi(t) = \sum C_j e^{-\frac{i}{\hbar}E_j t}\phi_j.$$

Thus, our initial assumption about the existence of a complete set of eigenfunctions of the Hamiltonian is wrong when the classical analogue of a quantum system is chaotic. Hence, the real time evolution has a different character, not the one that was initially assumed. A time development of the quantum system that has a chaotic classic analogue is more complicated and it is not not expressible in terms of an oscillatory series.

6.6.2 Loschmidt Echo.

Let us investigate dynamics of the system using the concept of the *the Loschmidt Echo.* As mentioned in Section 2.1, according to an idea of Asher Peres **(see [64])** overlap of two identical wave packets, each evolving under two slightly different Hamiltonians, can be used as an indicator of underlying classical chaos. This overlap is also called the Loschmidt Echo, and in a case of its exponential decay the corresponding quantum system was shown to have a chaotic classical analogue. For computations we take an initial wave pattern Ψ_0 and propagate it under two slightly different Hamiltonians:

$$\Psi(t) = e^{-\frac{i}{\hbar}\hat{H}t}\Psi_0 \quad \tilde{\Psi}(t) = e^{-\frac{i}{\hbar}(\hat{H}+\hat{H}_1)t}\Psi_0.$$

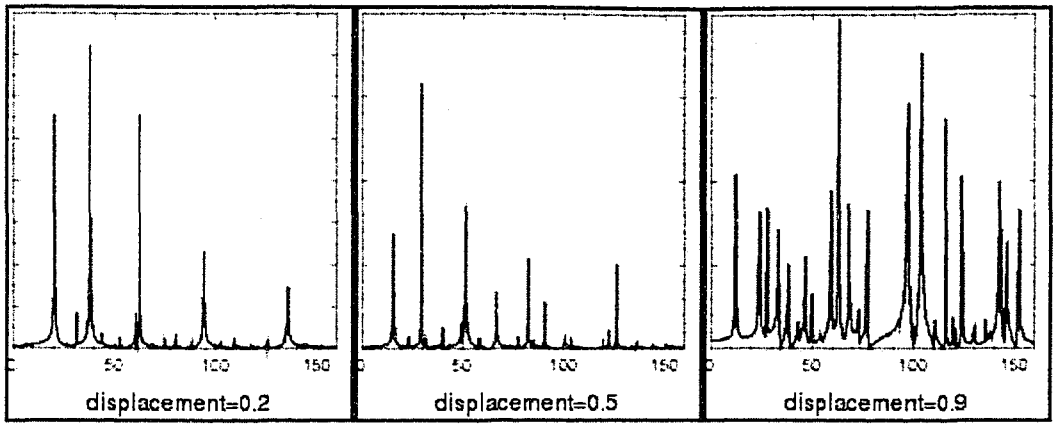

Figure 6.17: Energy spectrum corresponding to the same Coulomb interaction constant $\alpha = 10$ and the same initial wave packet, but different displacements of the Coulomb repulsive center from the center of the billiard. The last set of parameters corresponds to the classically chaotic analogue. The resultant spectrum of the time evolution appears to be continuous as the result of nonintegrability.

As the perturbation to the Hamiltonian $\hat{H}$ was taken to be a small displacement *(taken equal to* 10^{-4}*)* of the repulsive Coulomb center. How this small perturbation affects the time-evolution of the initial wave-packet is described quantitatively by an overlap integral

$$\langle \tilde{\Psi(t)} | \Psi(t) \rangle = \langle \Psi_0 | e^{\frac{i}{\hbar}(\hat{H}+\hat{H}_1)t} e^{-\frac{i}{\hbar}\hat{H}t} | \Psi_0 \rangle.$$

Some results of numerical computations of this overlap integral for various values of the displacement of the repulsive center are shown in **Figure (6.18)**. Values plotted on the pictures are logarithms of the overlap integrals. One can see that for small values of the displacement, the overlap integrals decay by a power law - the graph of the logarithm represents the logarithmic curve. For larger values of the displacement - the curve of the logarithm of the overlap integral becomes a straight line, therefore the Loschmidt Echo decays exponentially. This demonstrates that the quantum system that has a chaotic classical analogue exhibits an exponential decay of the overlap integral, which is one more manifestation of the underlying classical chaos.

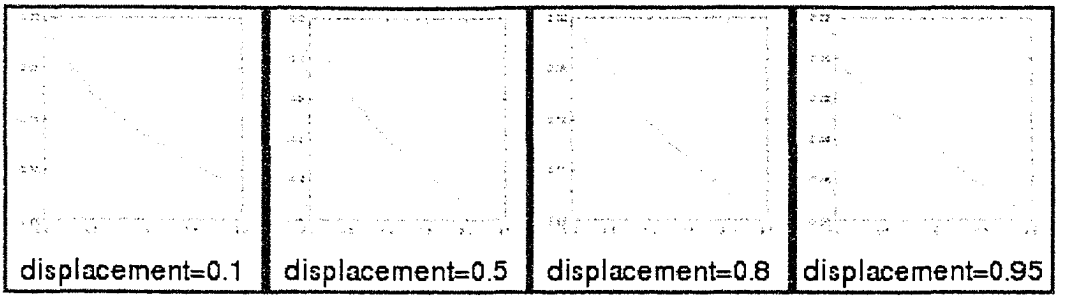

Figure 6.18: The same initial wave-packet was propagated under two slightly different Hamiltonians. The Hamiltonians differ by an extremely small displacement in the position of the repulsive center (taken equal to 10^{-4}). The logarithms of the overlap integrals (the Loschmidt Echo) versus time are given on the graphs for various positions of the repulsive center. First two graphs demonstrate a power law decay, while the last two show the exponential decay of the Loschmidt Echo, which is an indicator of the underlying classical chaos.

6.7 Transport properties.

Let us consider a quantum dot that confines an electron in a two-dimensional interlace of a circular shape **(Figure 6.7)**. An additional stationary charged pole produces an electrostatic field inside the confinement. Such a quantum dot is a possible experimental realization of the quantum system analyzed in this chapter. An electron enters the cavity through a tiny gate made at the point (x_0, y_0) on the boundary. There is another gate, made at the point (x_1, y_1), where we expect the electron to leave the cavity.

We approximate a wavefunction of the entering electron by a minimal uncertainty wavepacket localized at the point (x_0, y_0) with uncertainties in coordinates $\Delta x, \Delta y$ (see [59]).

$$\Psi_0(x,y) = \sqrt{\frac{1}{2\pi\Delta x\Delta y}} e^{-\left(\frac{x-x_0}{2\Delta x}\right)^2 - \left(\frac{y-y_0}{2\Delta y}\right)^2 + ik_{x0}x + ik_{y0}y}. \tag{6.11}$$

Then we expand the initial wave packet in series of ϕ_j - the eigenfunctions of the system that were found in Section 6.3:

$$\Psi_0(x,y) = \sum_j C_j\phi_j \quad C_j = \langle\phi_j|\Psi_0(x,y)\rangle. \tag{6.12}$$

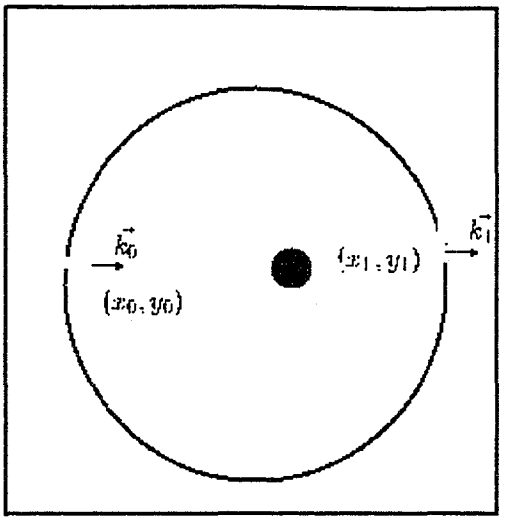

Figure 6.19: A model of a 'quantum dot' based on the circular coulomb billiard. A charged particle enters the dot through a gate (x_0, y_0) and leaves it through a gate (x_1, y_1).

The time evolution of the initial wavepacket is

$$\Psi(t,x,y) = \sum_j C_j \phi_j e^{-\frac{iE_j t}{\hbar}}. \tag{6.13}$$

In the last expression E_j labels energy eigenvalues of the set ϕ_j. A probability density for the electron to escape from the cavity through the second gate is equal to a projection of $\Psi(t,x,y)$ on a minimal uncertainty wavepacket, which is localized at the point (x_1, y_1). We denote such an outgoing packet as Ψ_1 and expand it in series of ϕ_j:

$$\Psi_1(x,y) = \textstyle\sum_j D_j \phi_j \quad D_j = \langle \phi_j | \Psi_1(x,y) \rangle. \tag{6.14}$$

The projection of $\Psi(t,x,y)$ on Ψ_1 is

$$\langle \Psi(t,x,y) | \Psi_1 \rangle = \langle \sum_j C_j \phi_j e^{-\frac{iE_j t}{\hbar}} | \sum_n D_j \phi_n \rangle = \sum_j C_j^* D_j e^{\frac{iE_j t}{\hbar}}. \tag{6.15}$$

To obtain a probability for the electron to escape the cavity through the second gate we square the last expression and take its time average. All the oscillating terms

will disappear as the result of an averaging, thus, an expression for transition of the quantum dot becomes:

$$T = |\langle \Psi(t,x,y)|\Psi_1\rangle|^2 = \sum_j |C_j|^2 |D_j|^2. \tag{6.16}$$

We examined numerically the transition properties of the circular coulomb billiard for two different positions of the entrance gate. The outgoing wavepacket was localized at the point with the coordinates $(1.0, 0.0)$ *(the right most point of the circular boundary)*. The repulsive center was placed on the $x-$axis. To distinguish cases corresponding to different allocations of the incoming wavepacket, the following notation was used:

- T_1 labels the transition probability for a case when the entering wavepacket is centered at the point with coordinates $(-1.0, 0.0)$ *(the left most point of the circular boundary)*.
- T_2 labels the transition probability for a case when the entering wavepacket is centered at the point with coordinates $(0.0, 1.0)$ *(the top most point of the circular boundary)*.

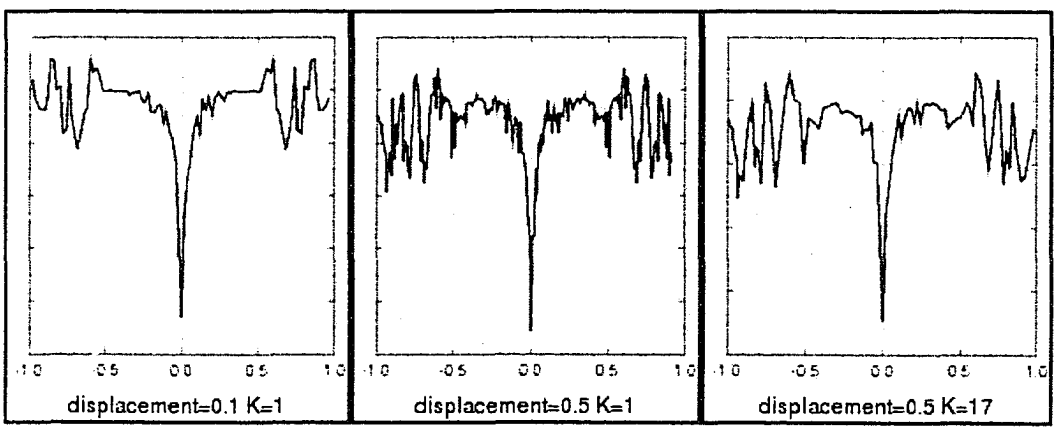

Figure 6.20: Transition T_1 of the quantum dot for various values of displacement of the Coulomb center from the center of the billiard and different wave-numbers K of the incident wavepackets.

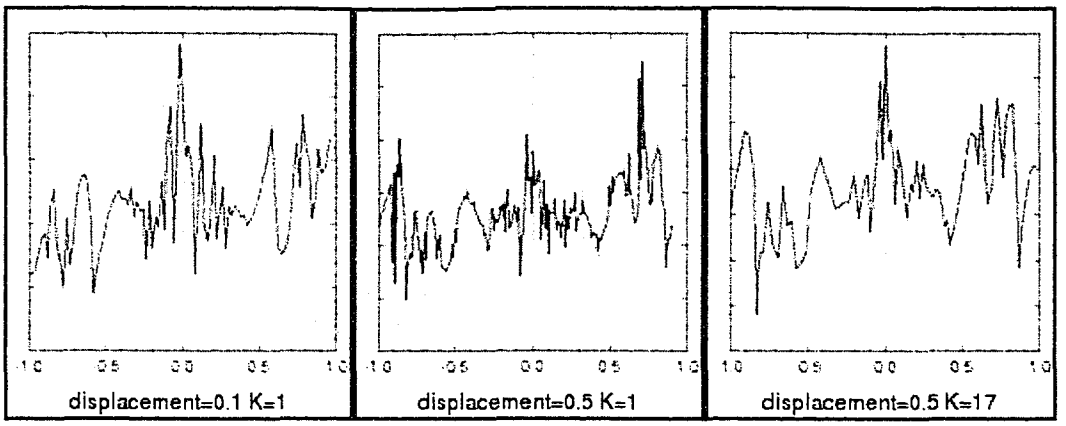

Figure 6.21: Transition T_2 of the quantum dot for various values of displacement of the Coulomb center from the center of the billiard and different wave-numbers K of the incident wavepackets.

Results of the computations for various sets of parameters are represented in **Figures 6.20 and 6.21**. Some general properties of the quantum dot in terms of its transition can be briefly summarized as the follows:

- The transition T_1 exhibits a sharp minimum in a case when the system is integrable ($X_0 = 0$). This situation persists for a wide range of values of the parameters of the system. This fact can be attributed to an existence of an unstable period 2 classical periodic trajectory *(the one when the particle simply bounces back and forth perpendicular to the boundary)*. A quantum analogue of this trajectory is a wavefunction, localized between the entrance gate and the repulsive center, thus a projection of the outgoing wave (which is localized at the opposite point) on the quantum state, corresponding to this trajectory, is zero. As a result the transition drops for this geometry of the quantum dot.

- The transition, T_2, shows noticeable maxima in the symmetric case ($X_0 = 0$) and when the displacement of the Coulomb center becomes approximately $X_0 \approx 0.75$. Examination of this phenomenon can not be done by means of simple considerations. It requires additional work which the author of this dissertation is planning to do in the near future.

In terms of an experimental realization the problem of two moving interacting charged particles inside a confinements appears to be more practical. However, this problem requires solution of a much more complicated quantum mechanical problem, which considers two light interacting particle inside a confinement. Work on this problem in the classical as well as in quantum mechanical case will be continued in the near future.

6.8 Summary.

The quantum dynamics of the circular Coulomb billiard billiard can be briefly summarized as the follows:

- As the Coulomb repulsion is weak $\alpha <\approx 2$ the system shows an uncorrelated energy spectrum. The time evolution in this case shows smooth oscillatory motion. All these results are consistent with the fact that the classical analogue for this range of parameters exhibits regular quasi-integrable character of the dynamics. As a result the quantum counterpart can be well described using perturbative methods. The energy levels are degenerate and uncorrelated, and the time evolution can be decomposed as a series of harmonics oscillating in time.

- A similar character of the dynamics was observed when the Coulomb repulsion is sufficiently strong, but the displacement of the Coulomb center from the center of the billiard is relatively small, such that $X_0 < \frac{\alpha}{\epsilon}$. The energy spectrum still consists of uncorrelated levels and the time evolution of the system exhibits regular oscillations of the initial wave pattern. These features are consistent with the dynamical phase space of the classical analogue, which displays a regular character of the dynamics for arbitrary values of the Coulomb repulsion as long as the degree of asymmetry of the system is sufficiently small.

  An interesting effect was observed in terms of the transport properties of a quantum dot based on the system analyzed in this chapter. An anomalous decay in

the conductance of the dot was detected for all values of the Coulomb repulsion in the symmetric case where the incident wave, the outgoing wave and the repulsive center are aligned along the diameter of the dot, and the Coulomb center is situated at the center of the circular confinement. Such behavior can be explained if we take into account an unstable period-2 trajectory, which corresponds to an incident particle re-bouncing backward. The quantum analogue of this trajectory appears to affect the dynamics of the quantum dot with this geometry, significantly reducing its conductivity.

- When the Coulomb repulsion is strong enough and the displacement of the Coulomb center from the center of the billiard is sufficiently large an entire spectrum of features that are called the quantum manifestations of the underlying classical chaos are detected:

  - The energy spectrum displays numerous repulsions of the closest levels, which indicates a strong inter-level correlation. However, an interesting feature of the level spacing distribution is that it does not obey the 'random walk' nor Wigner's statistics. Instead, a histogram of the level spacings turned out to consist of two distinct parts - the first part is close to the Poisson distribution, while the second one resembles Wigner's curve. This means that the energy spectrum of the system consists of correlated as well as uncorrelated levels. Such a dual structure of the energy spectrum is in agreement with the fact that the corresponding classical counterpart of the system is not entirely chaotic, but rather exhibits a mixed phase space.

  - The wave functions show a concentration of probability along narrow channels, corresponding to classical unstable periodic orbits. This effect was observed in numerous examples of classically chaotic quantum systems and it is called quantum scars.

  - The time evolution of an initial wave pattern does not look like a combination

of oscillating harmonics. Instead, the initial wave pattern becomes quickly destroyed, and gives rise to different type of wave patterns, not correlated with the initial one. The Loschmidt echo decays exponentially, all these facts display how an underlying classical chaos affects the time evolution of the system.

- The energy spectrum of the correlation function of the time evolution turned out to be continuous. This means that the motion can not be decomposed into a series of mutually independent oscillating harmonics. This is a clear manifestation of the nonintegrability of the classical analogue, which leads to the fact that the Schrodinger equation of the dynamical system is inseparable.

Appendix A

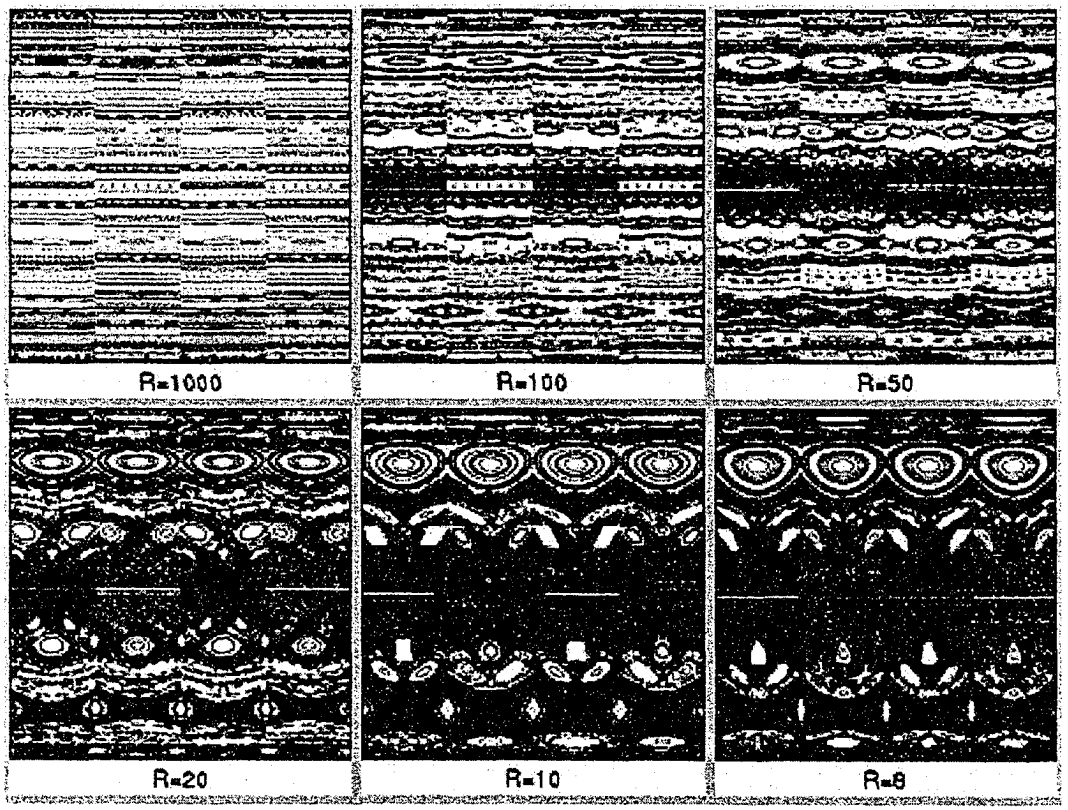

Figure A.1: Poincaré sections for relatively large values of the cyclotron radius. Initially the system is integrable, as the result the Poincaré sections consists of straight line segments. Then this straight segments are bent, forming KAM surfaces. Eventually this surfaces become destroyed, forming a chaotic part of the phase space. Such a combination of the KAM surfaces and a chaotic sea is a demonstration of the mixed phase space.

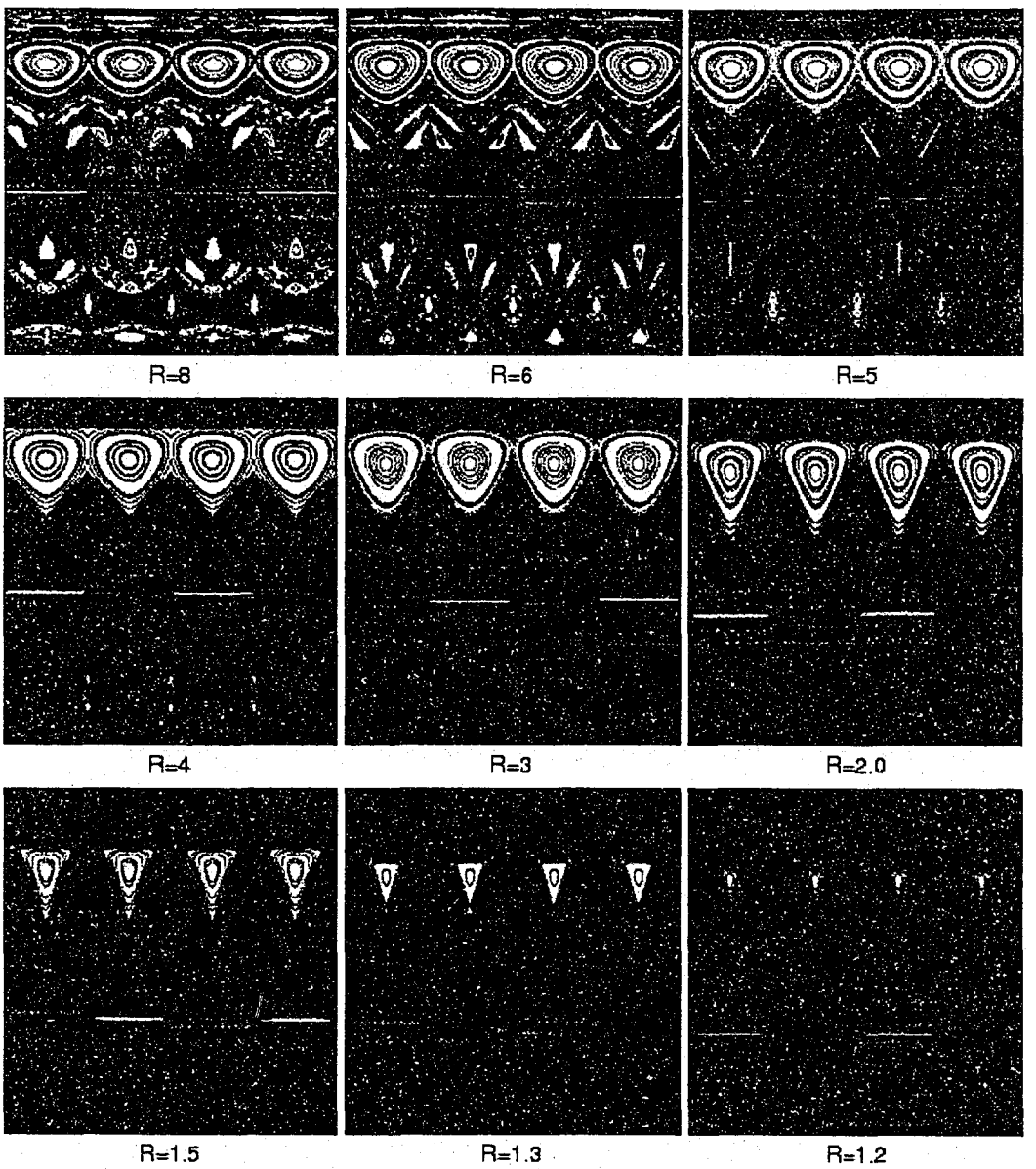

Figure A.2: Poincaré sections for medium values of the cyclotron radius. Initially the system is mixed, however, more and more KAM surfaces become destroyed as the cyclotron radius continues to decrease its value. As the cyclotron radius becomes approximately equal to the size of the system *(an approximate critical value is* $R_c \approx 1.1$*)*, almost all the KAM surfaces are destroyed and the system exhibits chaos.

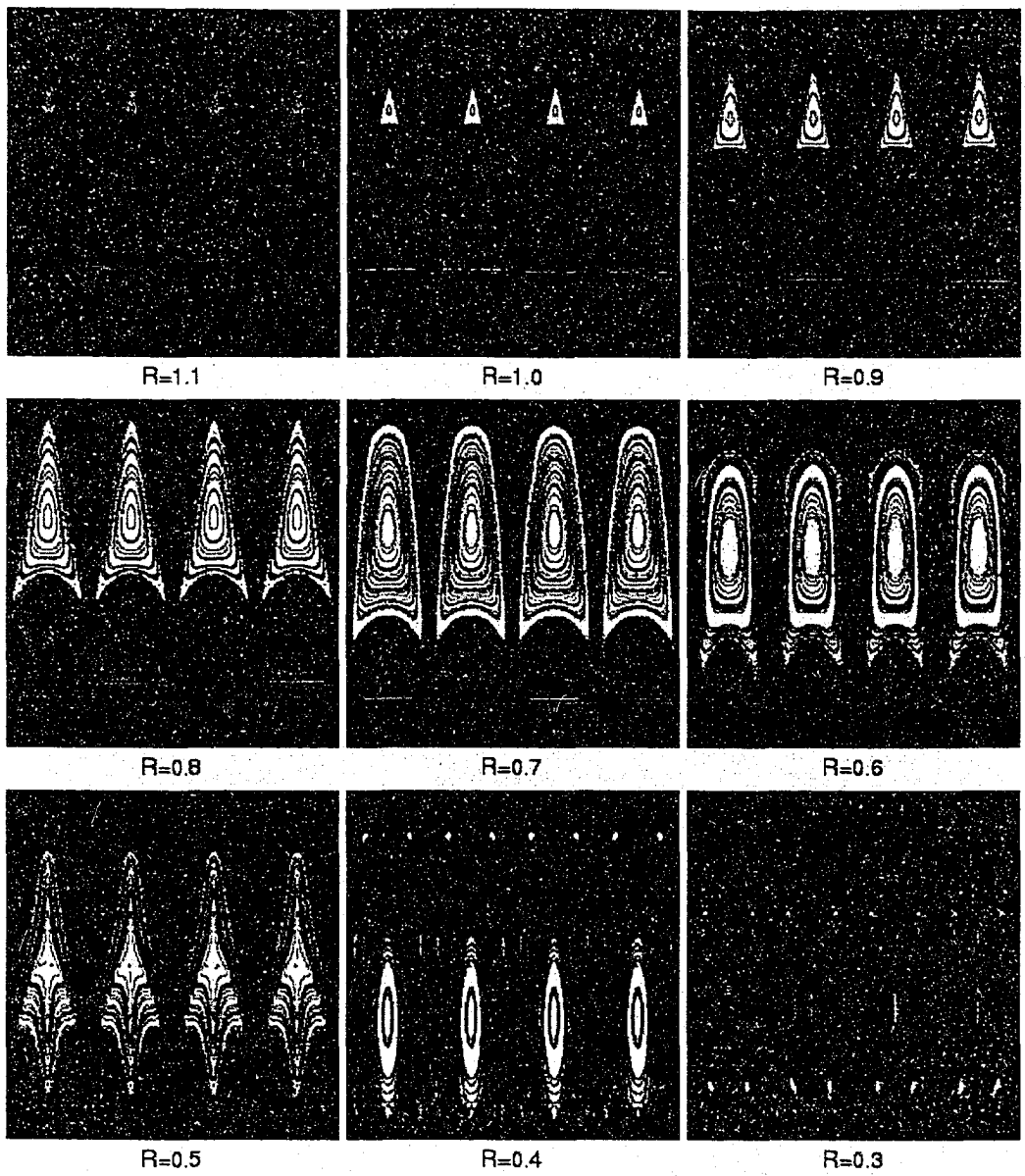

Figure A.3: Poincaré sections for small values of the cyclotron radius. Initially the system is chaotic, however, as the cyclotron radius decreases below its critical value ($R_c \approx 1.1$) the KAM surfaces are growing and system becomes mixed with increasing degree of regularity. Apparent growth of stochasticity as $R_c < 0.5$ is not a real characteristic of the system's dynamics. This happens because as $R_c < 0.5$ there exist trajectories that do not undergo collisions. Their relative amount is growing as R_c decreases. The bouncing map does not represent such kind of trajectory, therefore it does not adequately describe the dynamics of the system for $R_c < 0.5$.

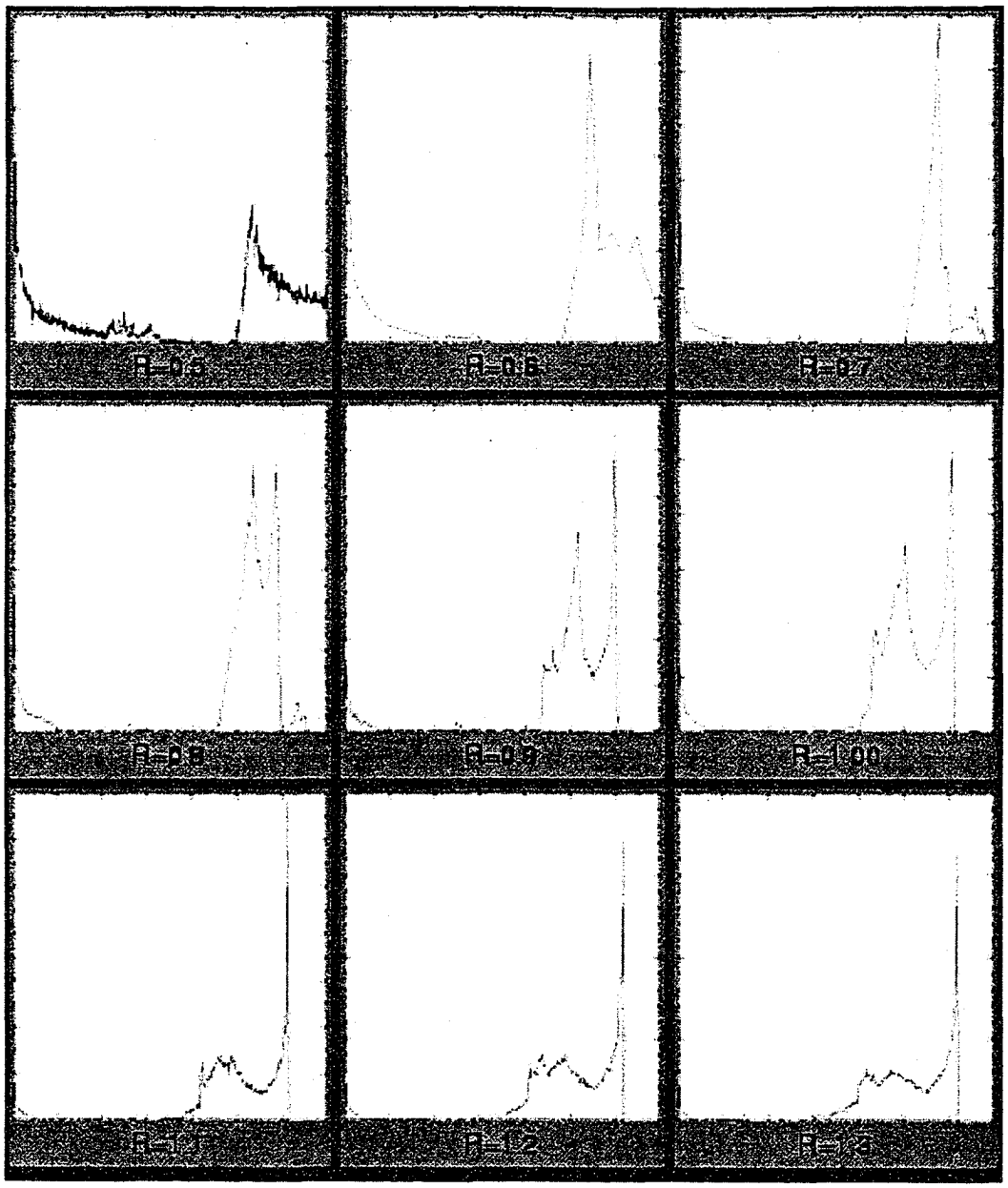

Figure A.4: Histograms of an action for small values of the cyclotron radius. As R_c tends to a critical value (the critical $R_c \approx 1.1$) the histogram becomes broader. Maxima on each histogram correspond to short periodic orbits, demonstrating their stickiness.

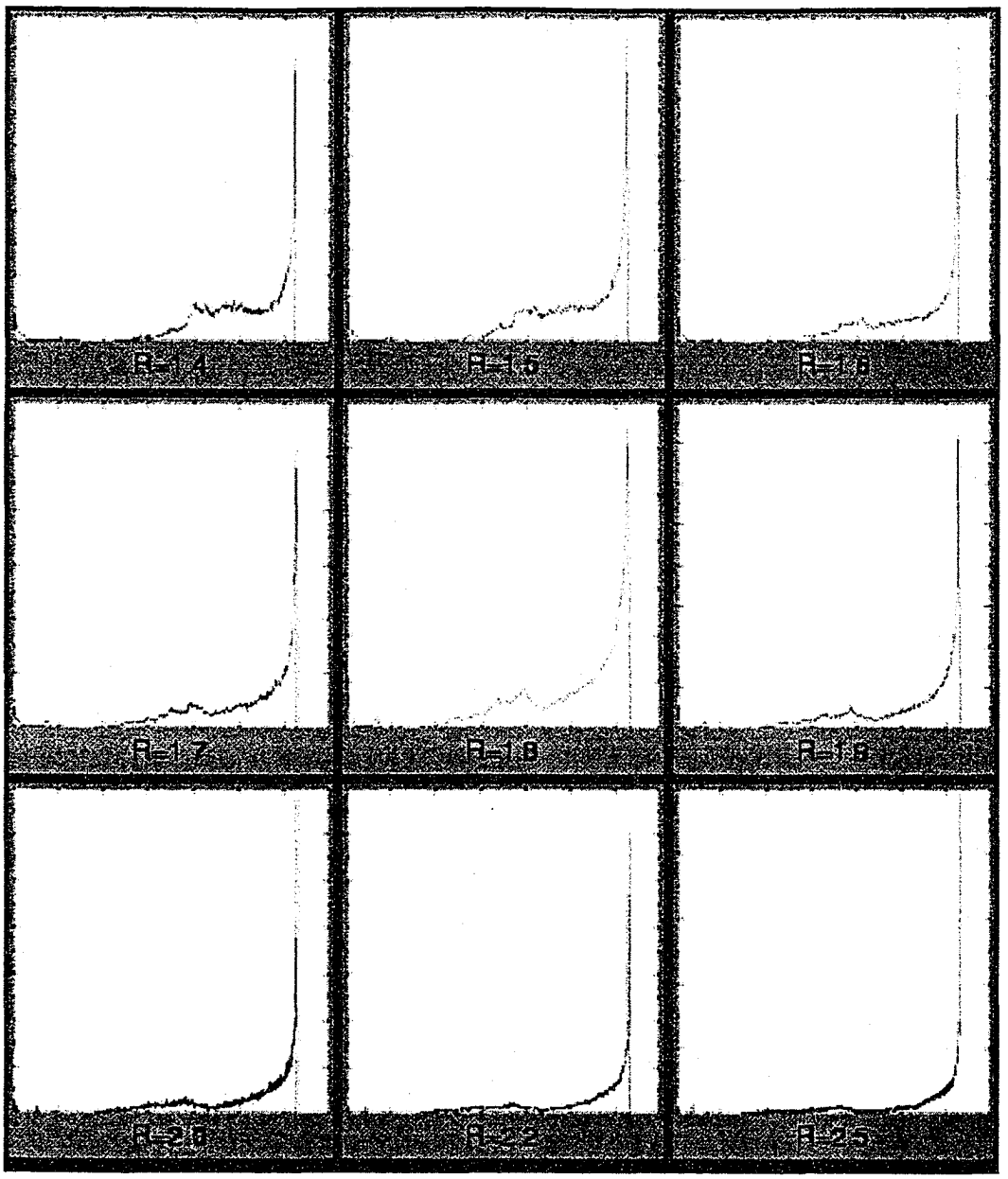

Figure A.5: Histograms of action for medium values of the cyclotron radius. As R_c goes far above its critical value (the critical $R_c \approx 1.1$) the histogram becomes more narrow, means that the action tends to become an integral of motion.

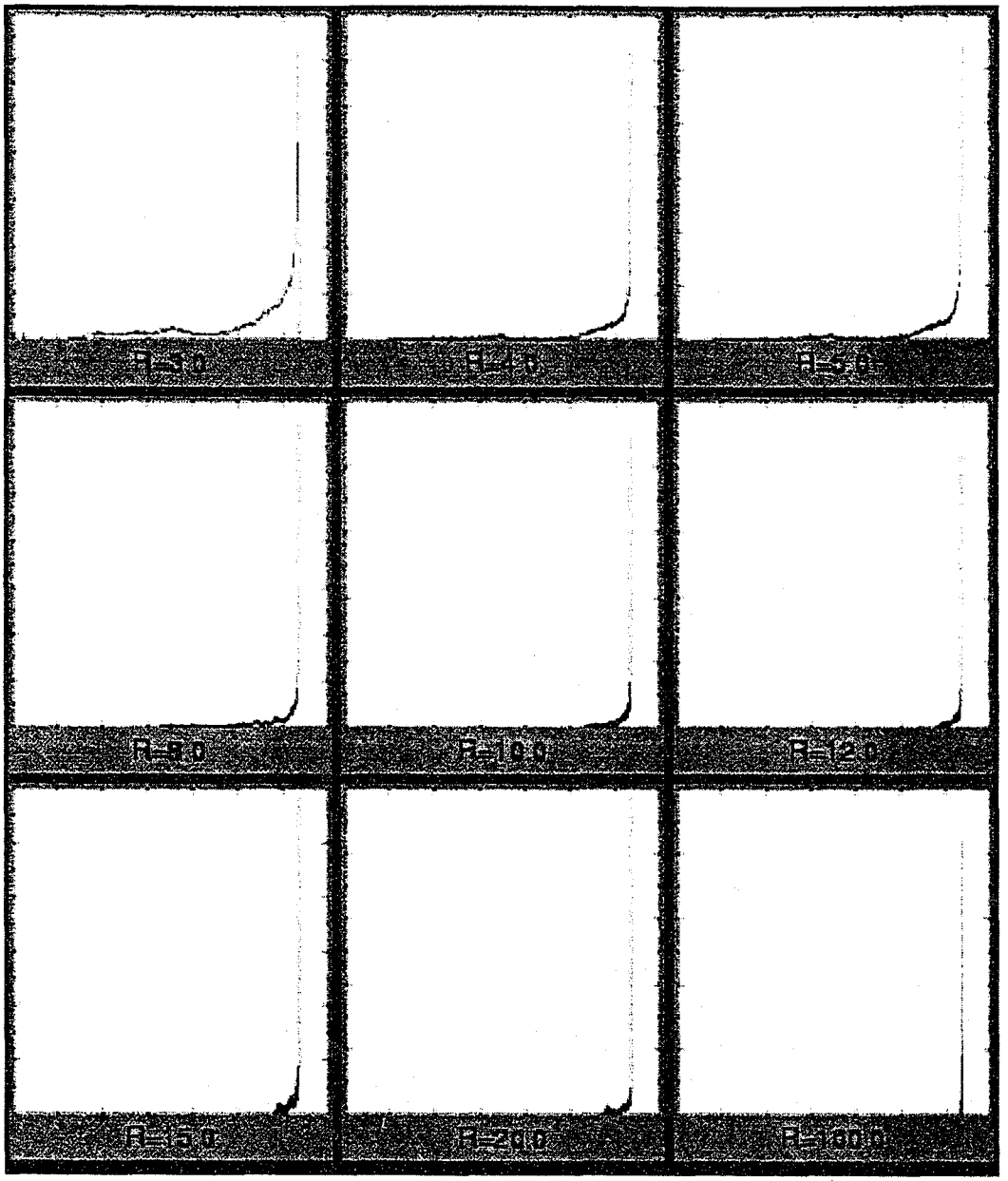

Figure A.6: Histograms of action for large values of the cyclotron radius. Dynamics eventually becomes integrable, hence all the action distribution tends to a single vertical line corresponding to a constant value.

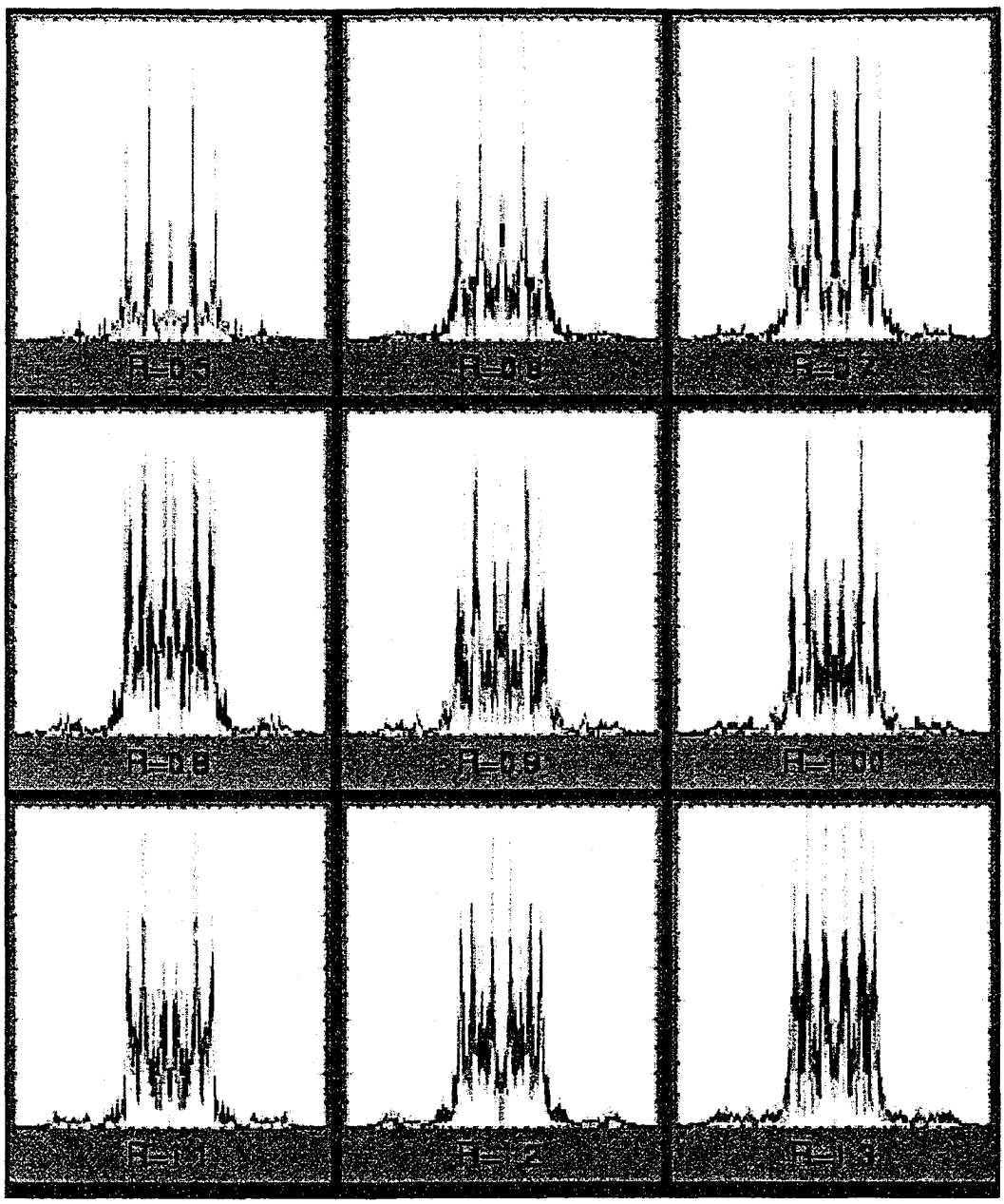

Figure A.7: Fourier spectrum of time evolution for small values of the cyclotron radius. Represented range of the cyclotron radius corresponds to mostly stochastic system's dynamics. As the consequence the Fourier spectrum in all the cases represented is continuous.

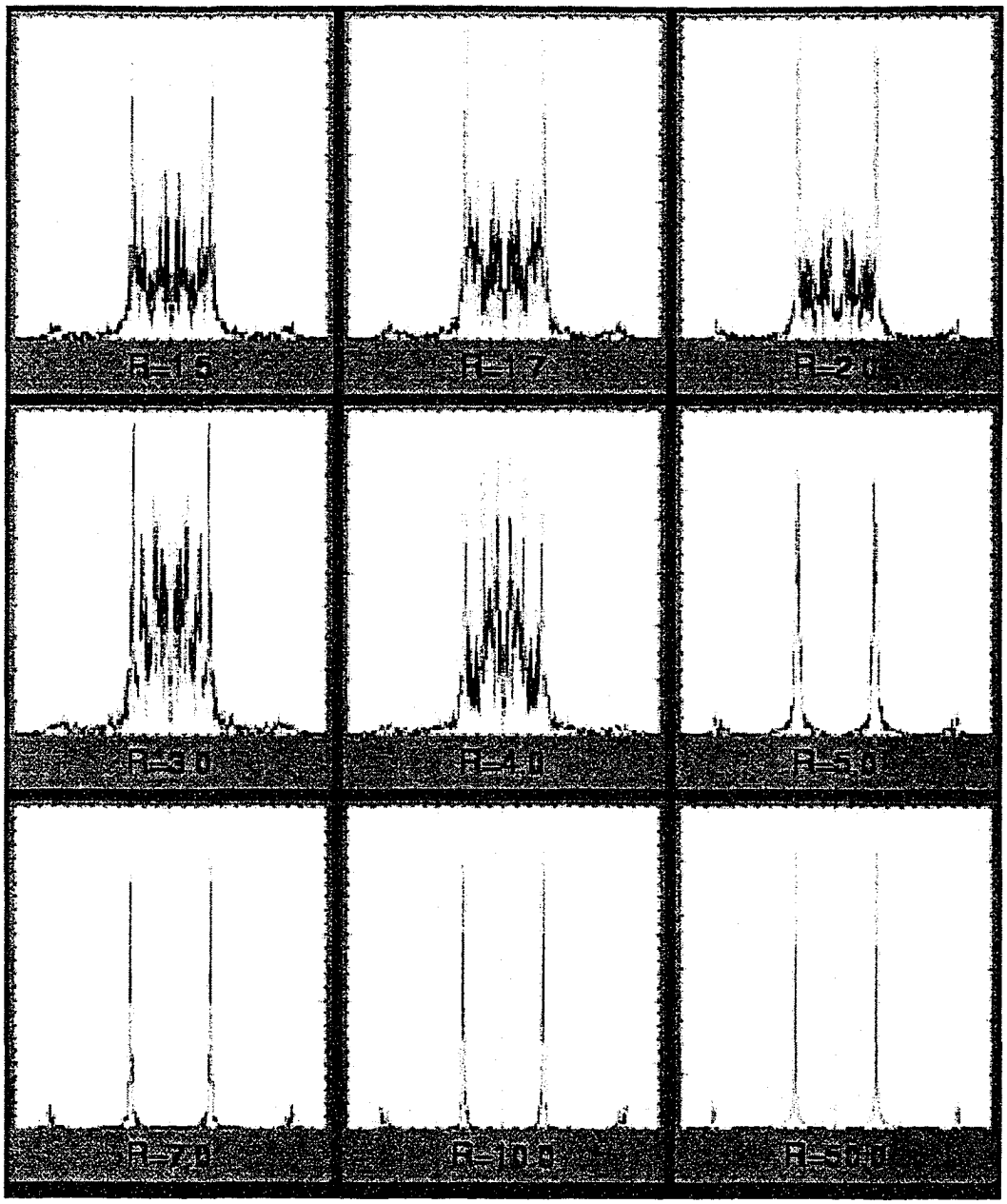

Figure A.8: Fourier spectrum of time evolution for relatively large values of the cyclotron radius. As the cyclotron radius is growing, the system changes character of its behavior from stochastic to regular. As the consequence, the Fourier spectra seen on the pictures initially are continuous, but eventually become discrete for large values of R_c.

Appendix B

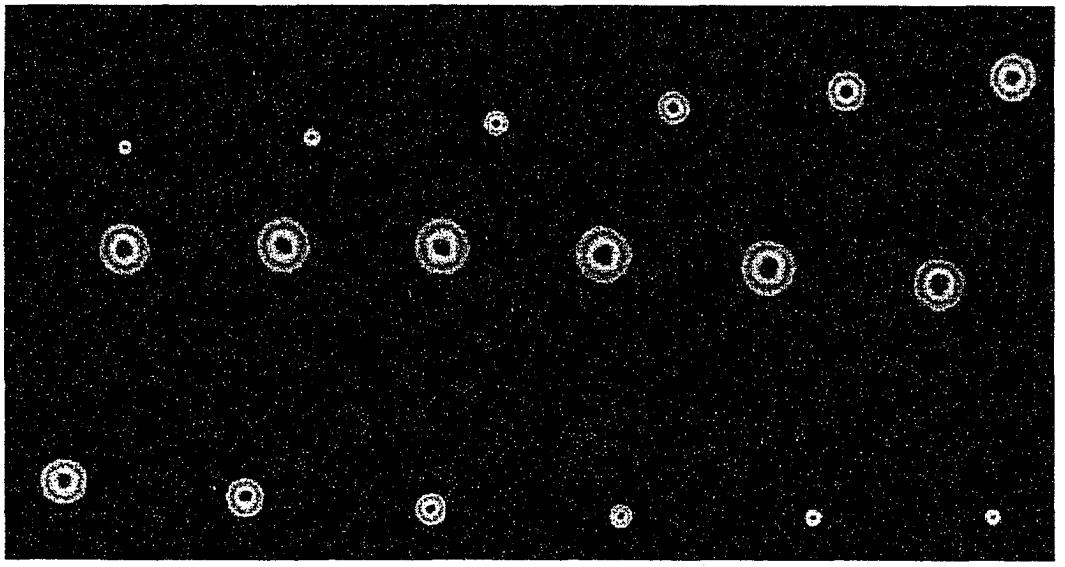

Figure B.1: Time evolution of a wavepacket inside the square magnetic billiard. Initial conditions and parameters of the billiard correspond to a periodic trajectory in the classical case $R_c = \frac{1}{5}$. The quantum motion is regular - the wavepacket oscillates and its center moves around a circular path.

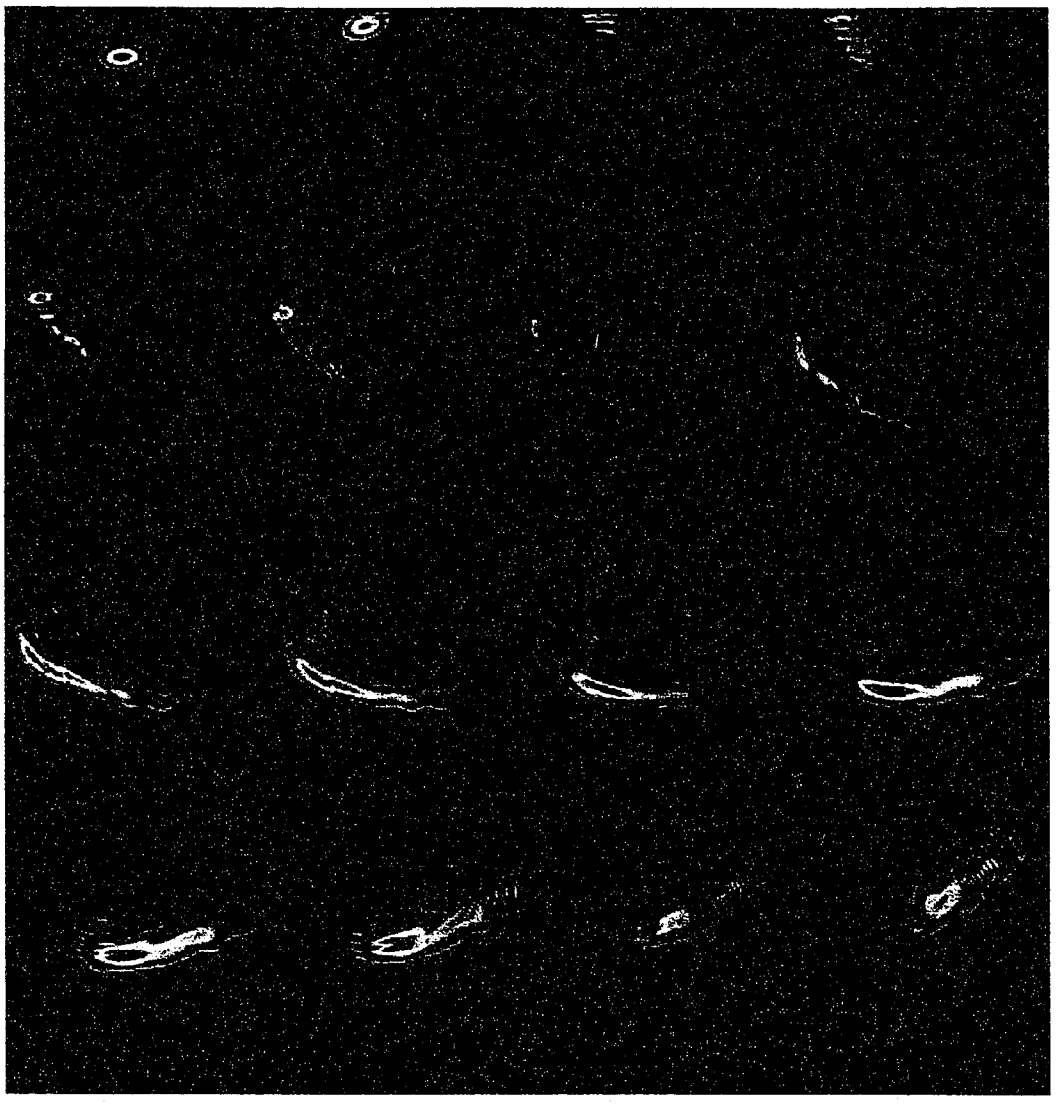

Figure B.2: Time evolution of a wavepacket inside the square magnetic billiard. Initial conditions and parameters of the billiard correspond to a chaotic trajectory in the classical case $R_c = 1$. The wave packet is being quickly totally destroyed.

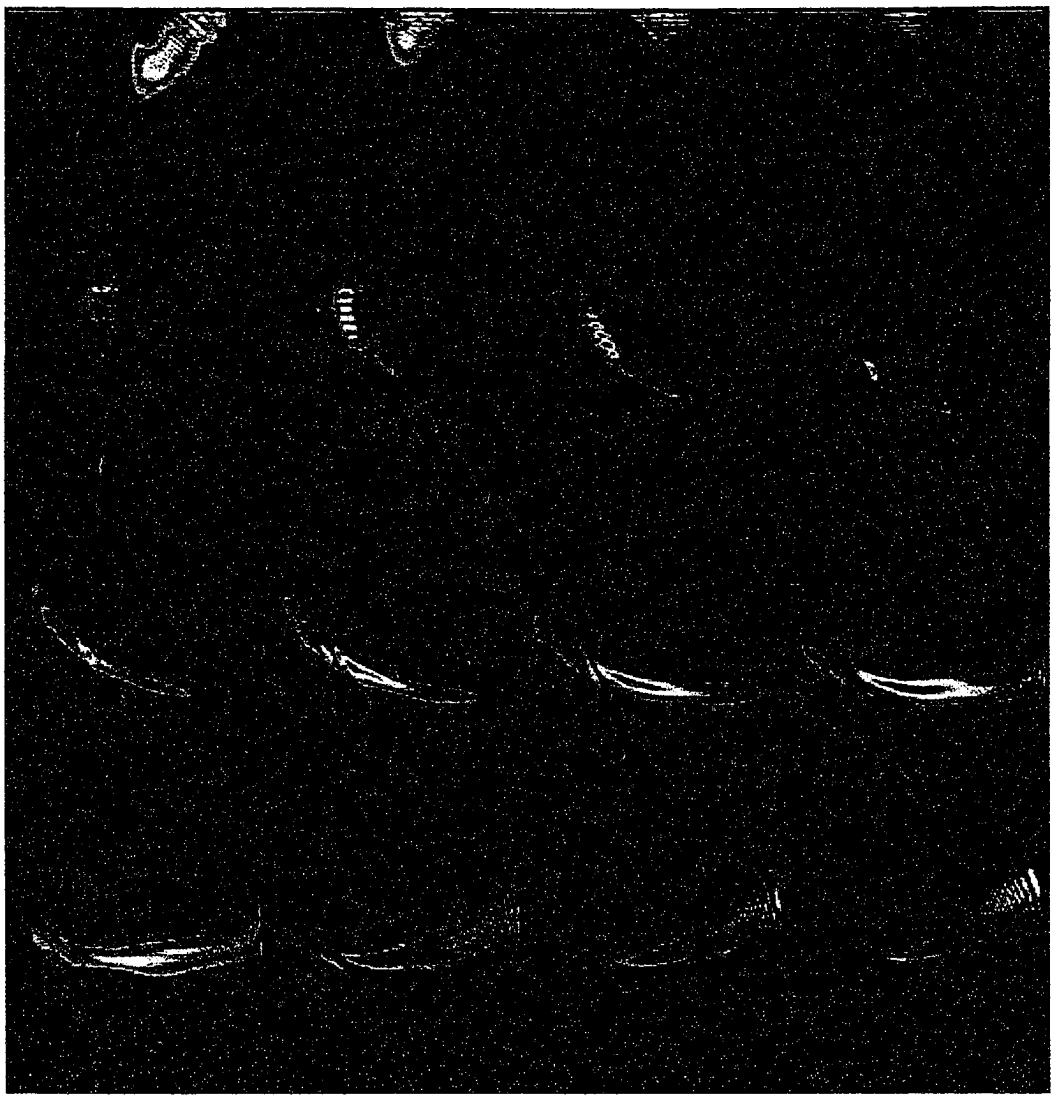

Figure B.3: Time evolution of a wavepacket inside the square magnetic billiard. Initial conditions and parameters of the billiard correspond to a chaotic trajectory in the classical case. The wave packet is being quickly totally destroyed. *(continued)*

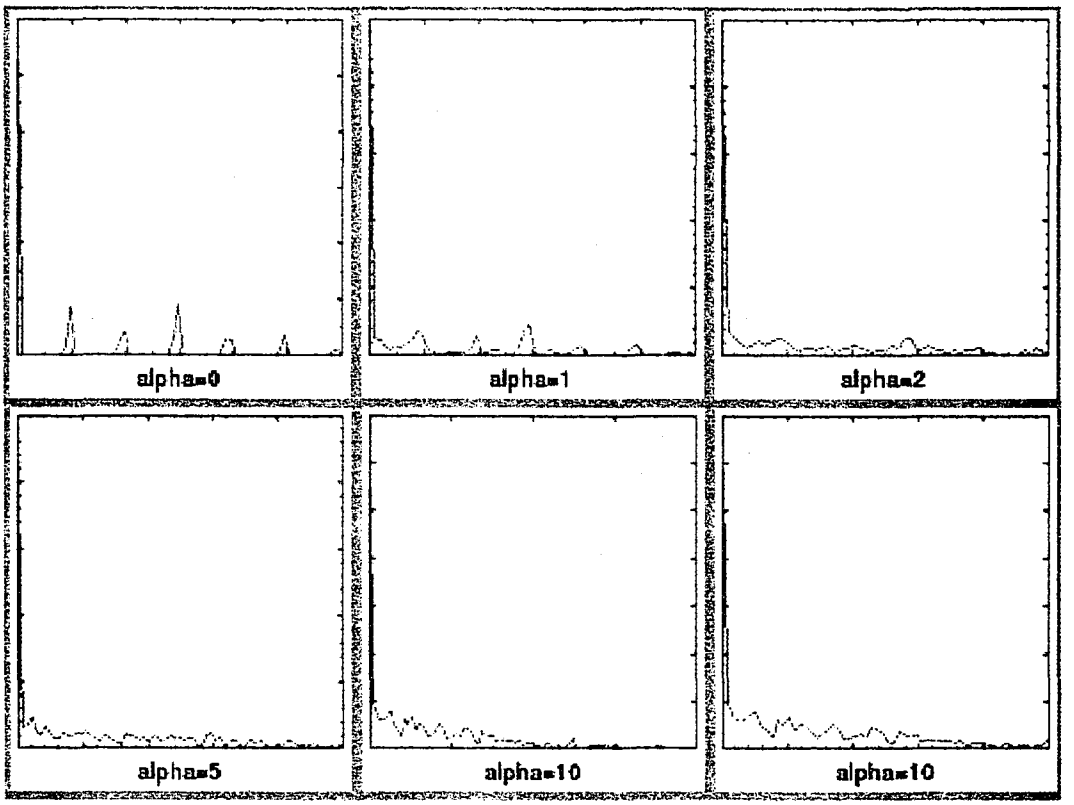

Figure B.4: Level spacing distribution for various values of α

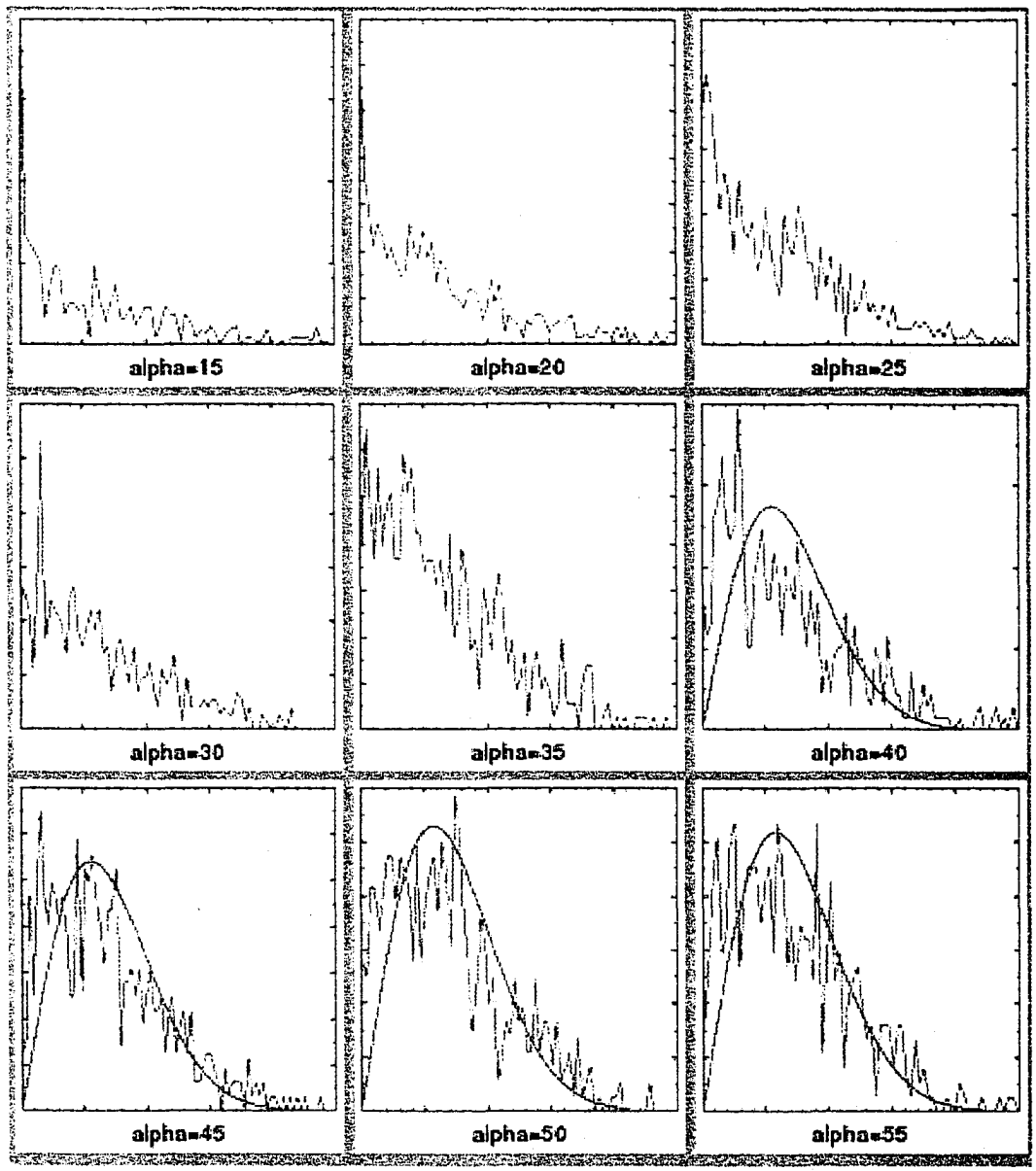

Figure B.5: Level spacing distribution for various values of α (continued) and the plot of corresponding Wigner's distribution (the green curve).

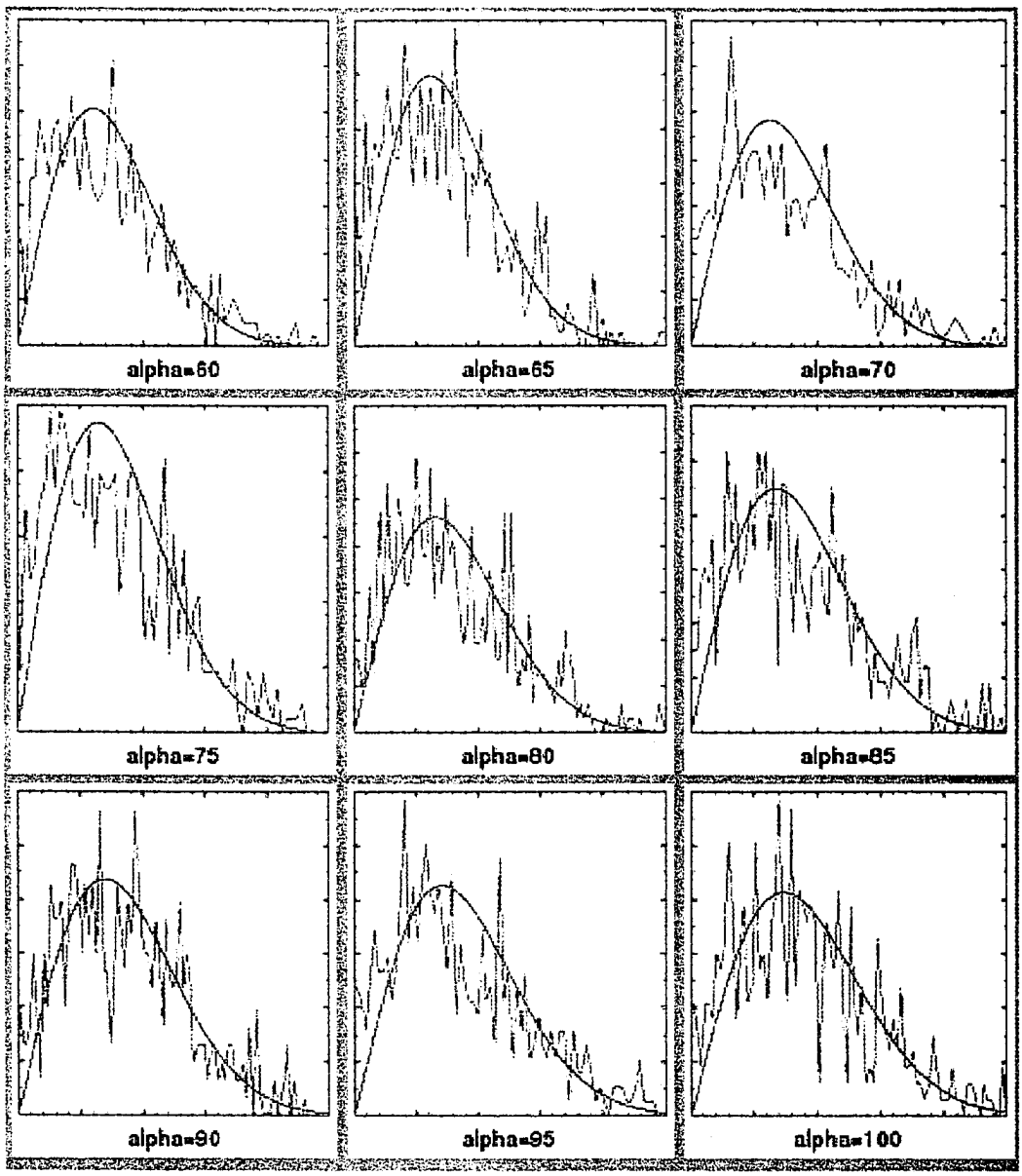

Figure B.6: Level spacing distribution for different values of α (continued) and the plot of corresponding Wigner's distribution (the green curve).

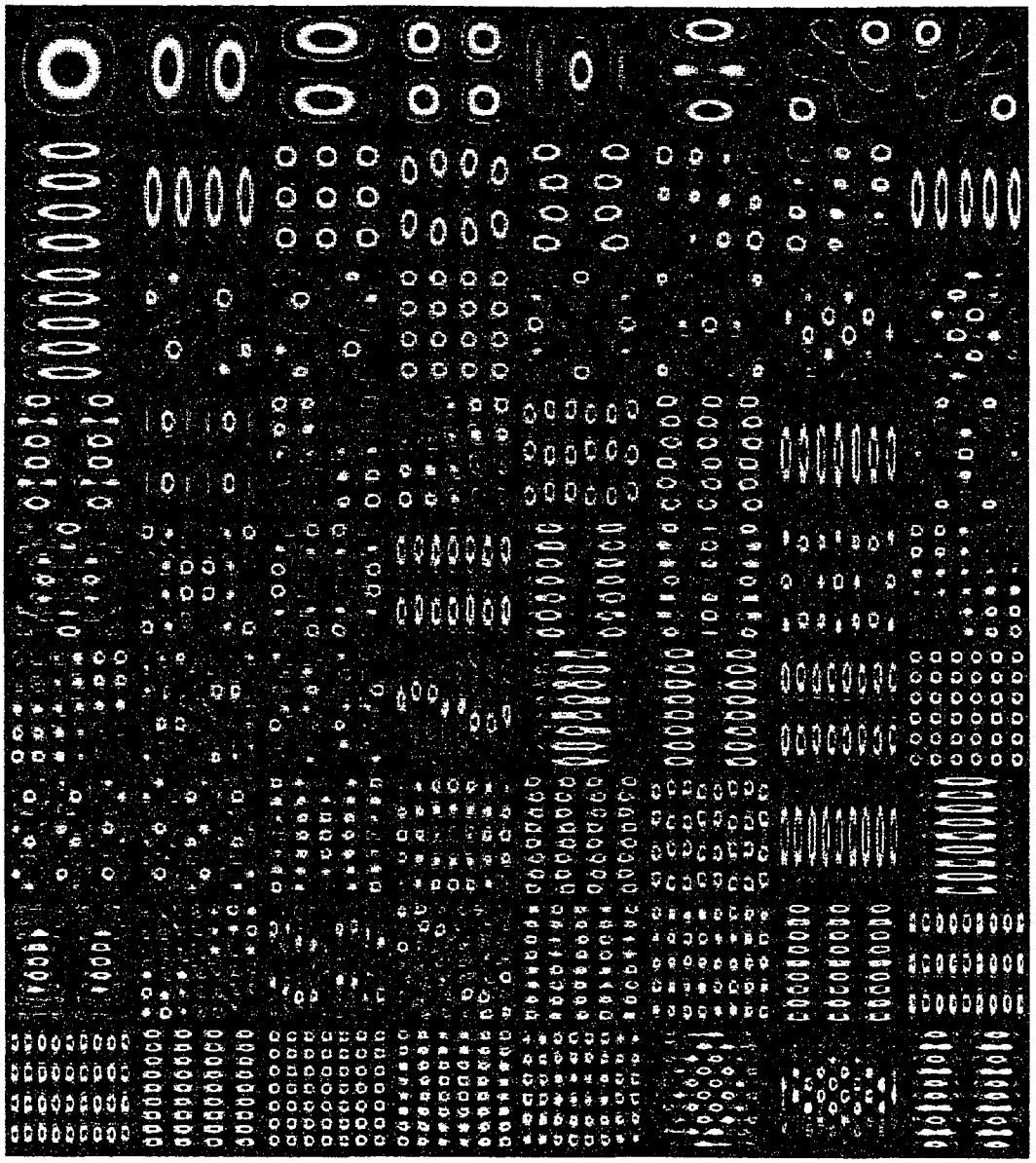

Figure B.7: Eigenfunctions of the lowest 72 states for the case $\alpha = 0$ (no magnetic field inside the billiard). An analitical expression for nonnormalized eigen functions are well-known sinusoidal standing waves: $\psi_{kn} = \sin(\pi k x)\sin(\pi n x)$

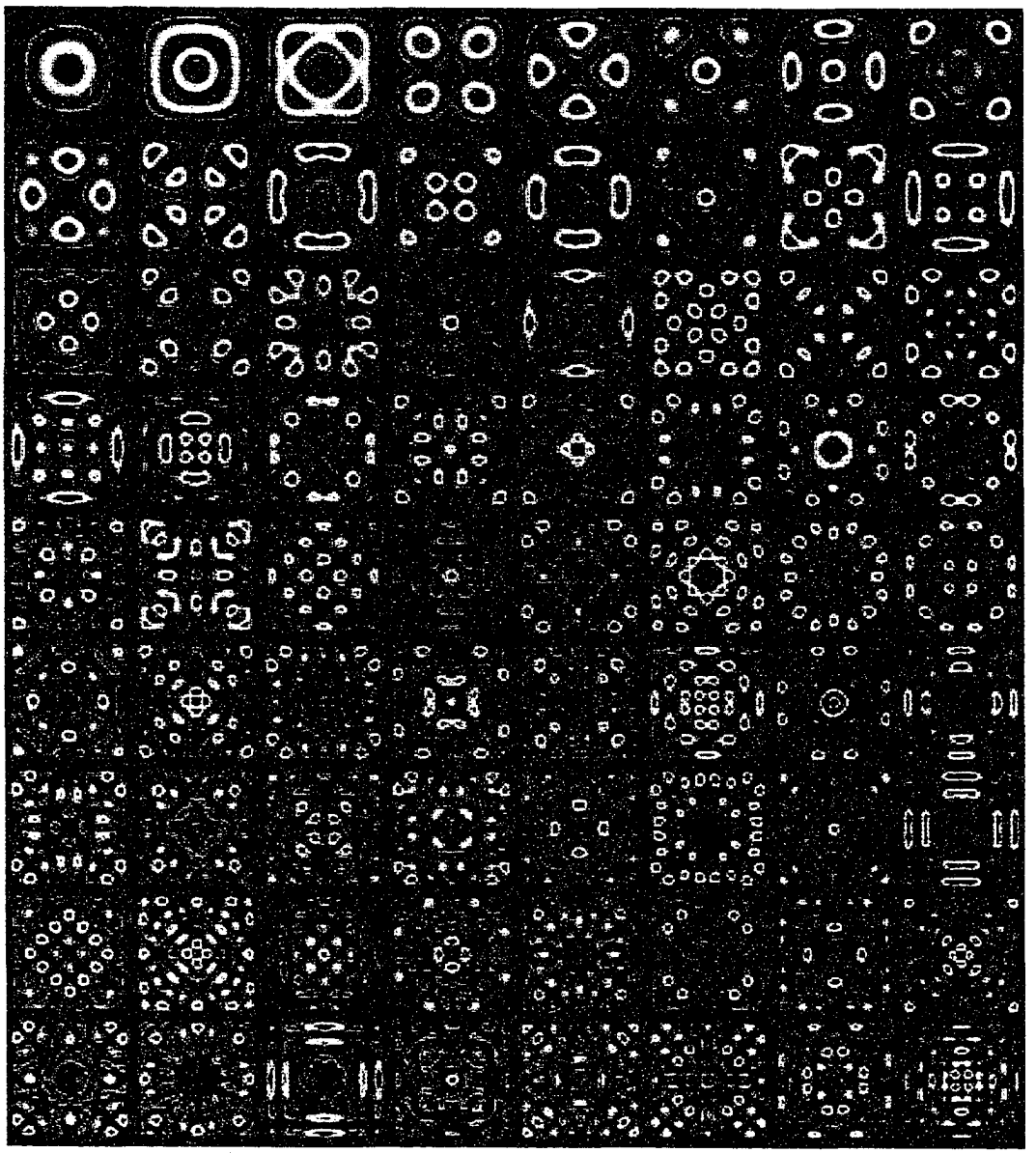

Figure B.8: Eigenfunctions of the lowest 72 states for the case $\alpha = 20$

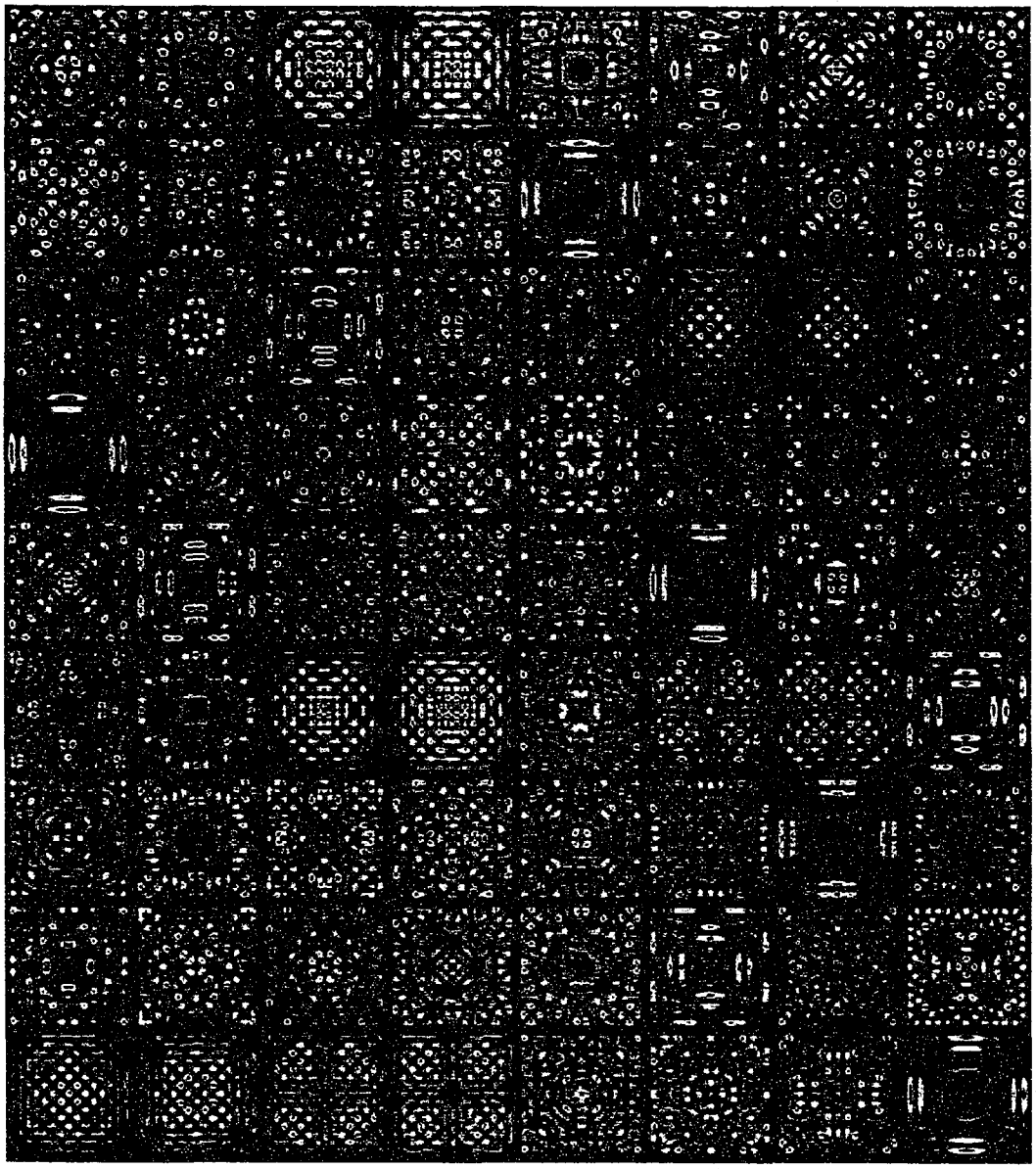

Figure B.9: Eigenfunctions of 72 excited states (the level numbers 100 to 171) for the case $\alpha = 20$

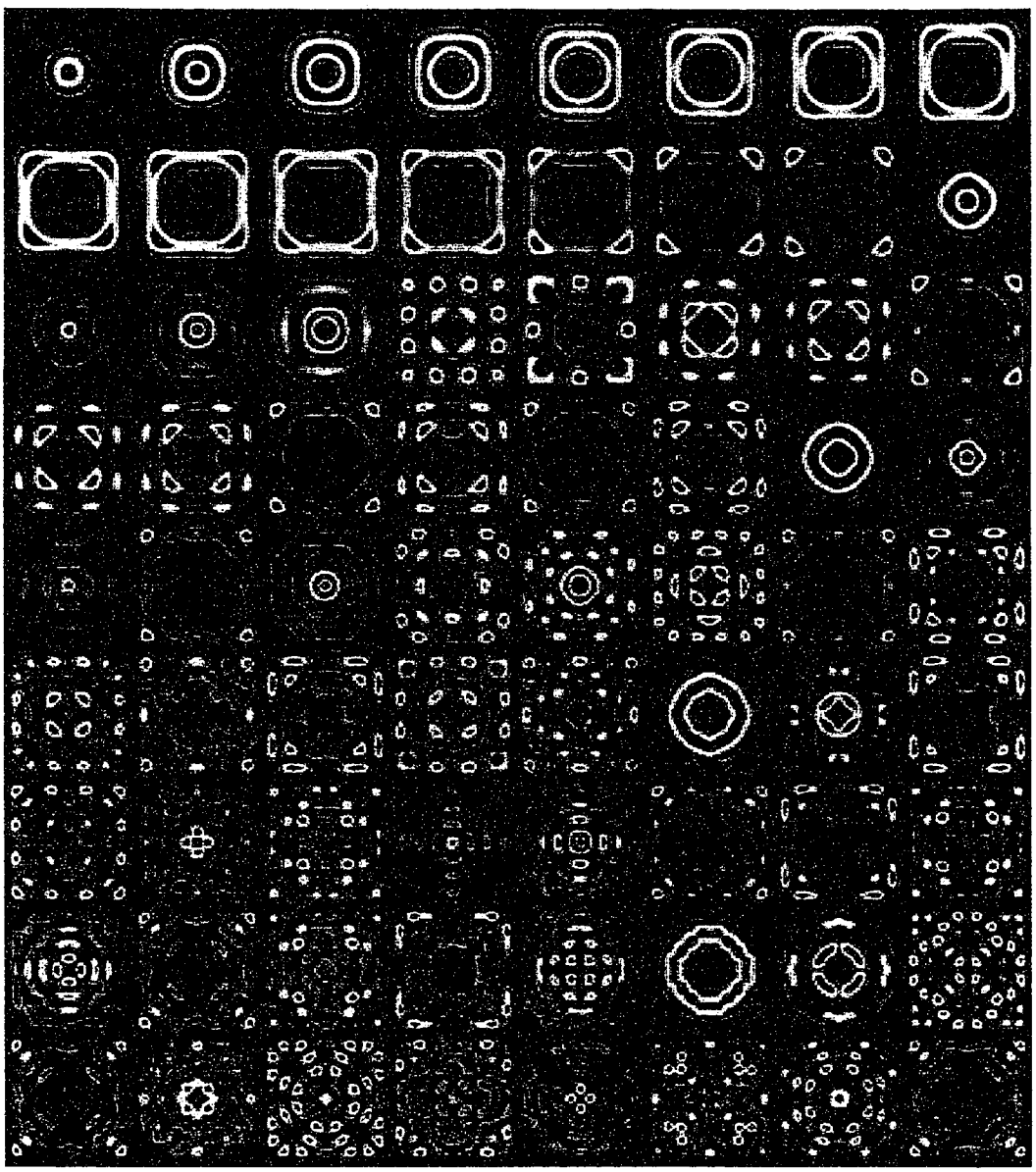

Figure B.10: Eigenfunctions of the lowest 72 states for the case $\alpha = 100$

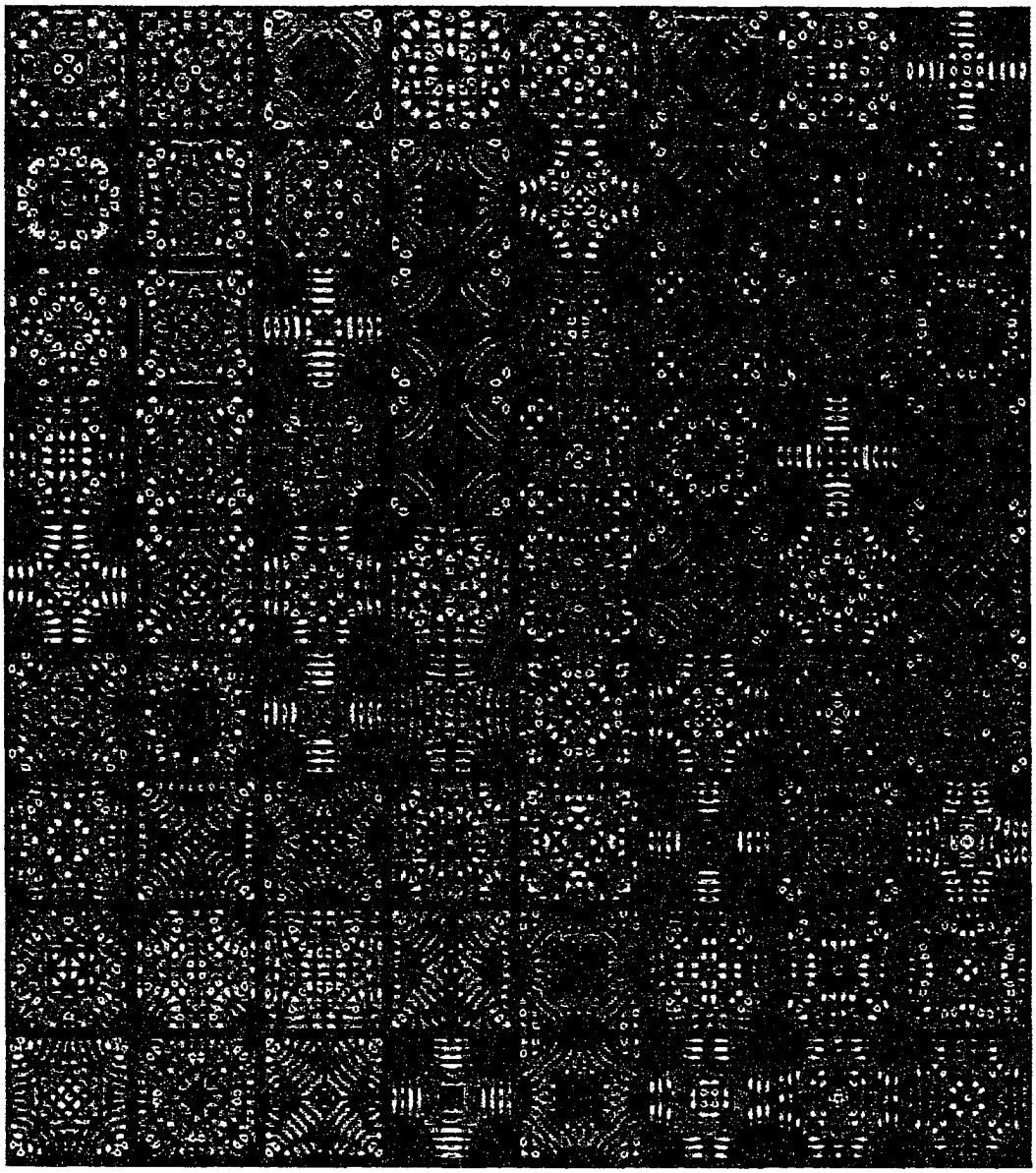

Figure B.11: Eigenfunctions of 72 excited states (the level numbers 100 to 171) for the case $\alpha = 100$

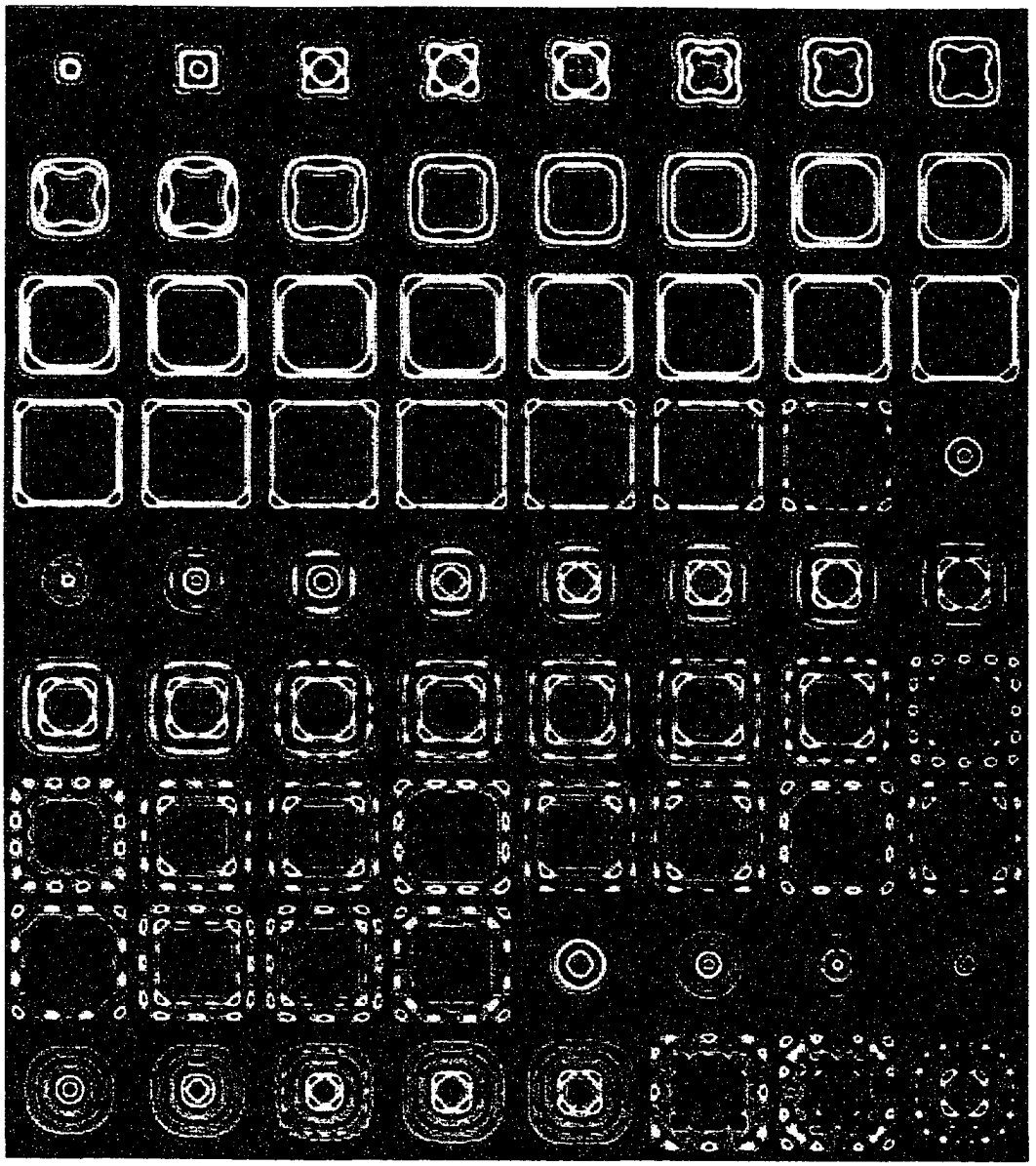

Figure B.12: Eigenfunctions of the lowest 72 states for the case $\alpha = 200$

Appendix C

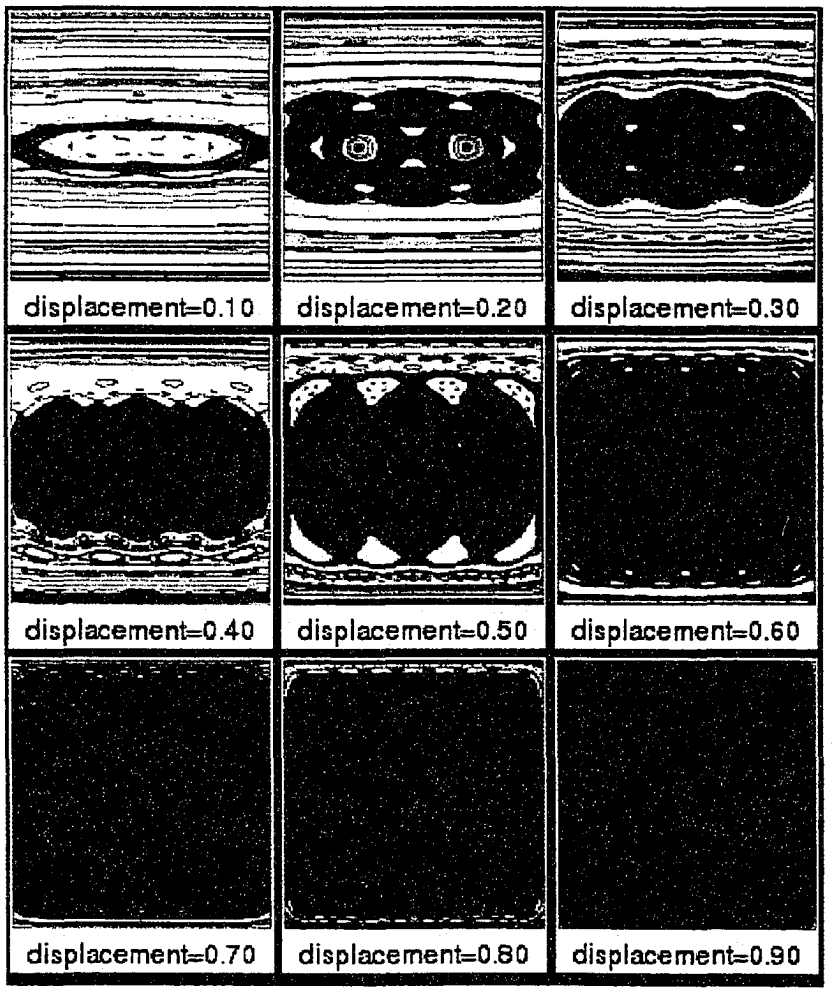

Figure C.1: Poincaré sections for different values of displacement of the Coulomb center. The Coulomb constant $\gamma = 0.1$

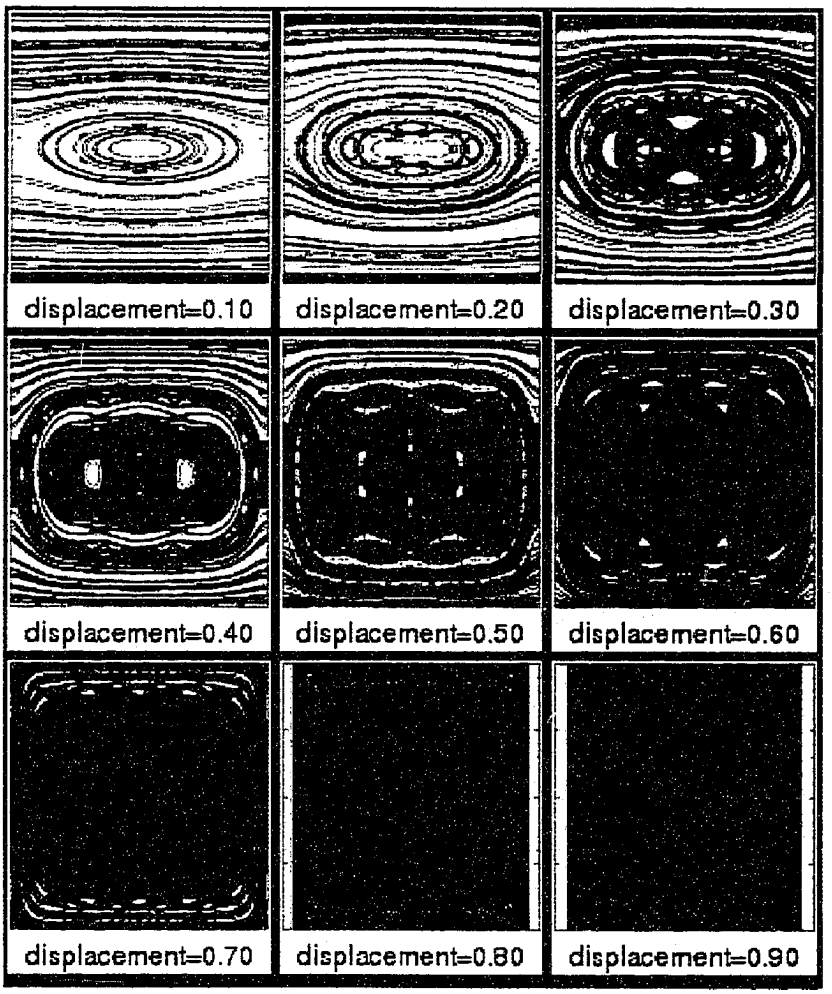

Figure C.2: Poincaré sections for different values of displacement of the Coulomb center. The coulomb constant $\gamma = 0.3$

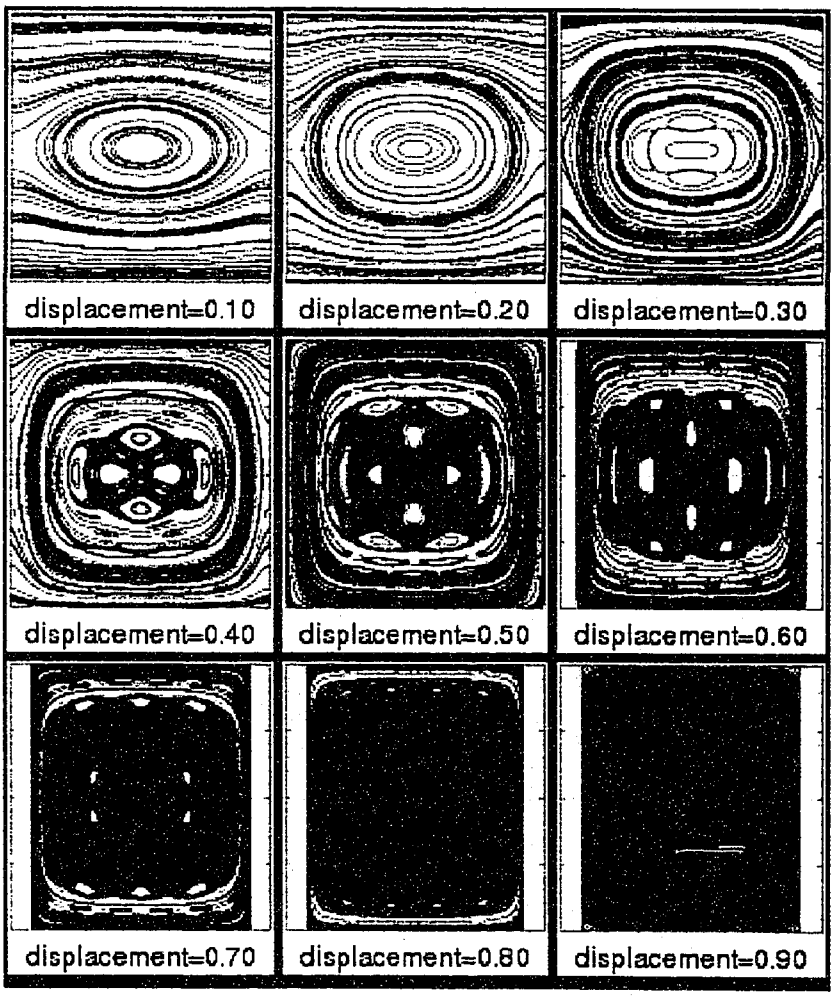

Figure C.3: Poincaré sections for different values of displacement of the Coulomb center. The coulomb constant $\gamma = 0.5$

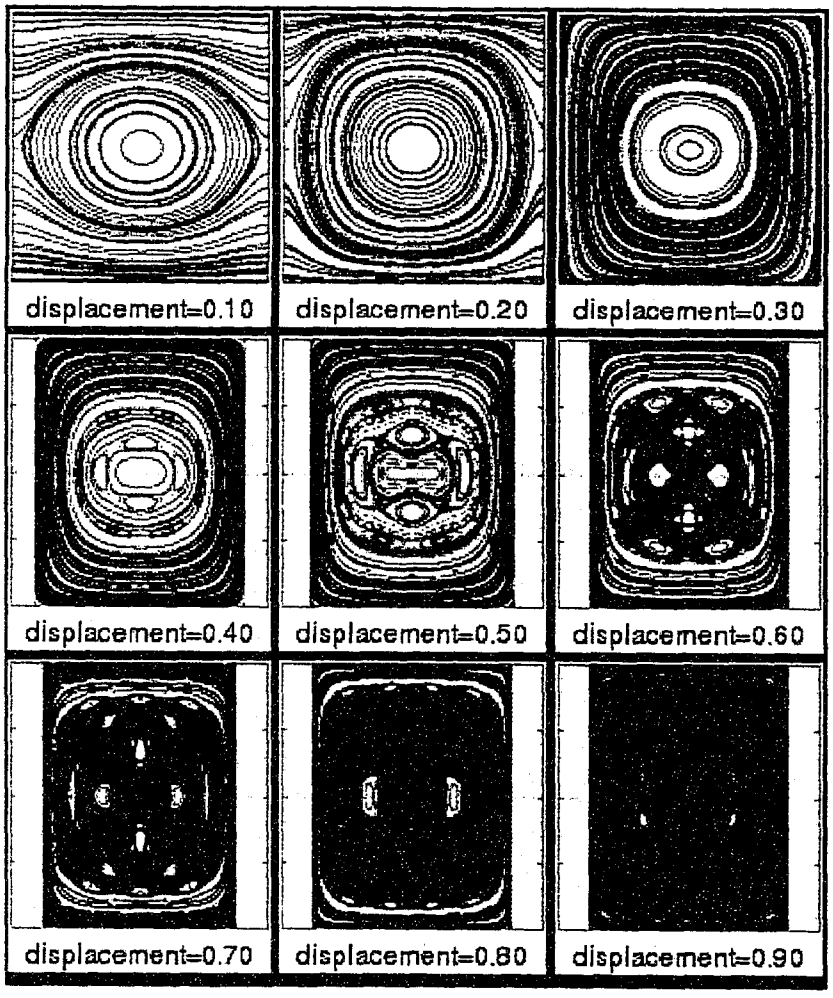

Figure C.4: Poincaré sections for different values of displacement of the Coulomb center. The coulomb constant $\gamma = 0.7$

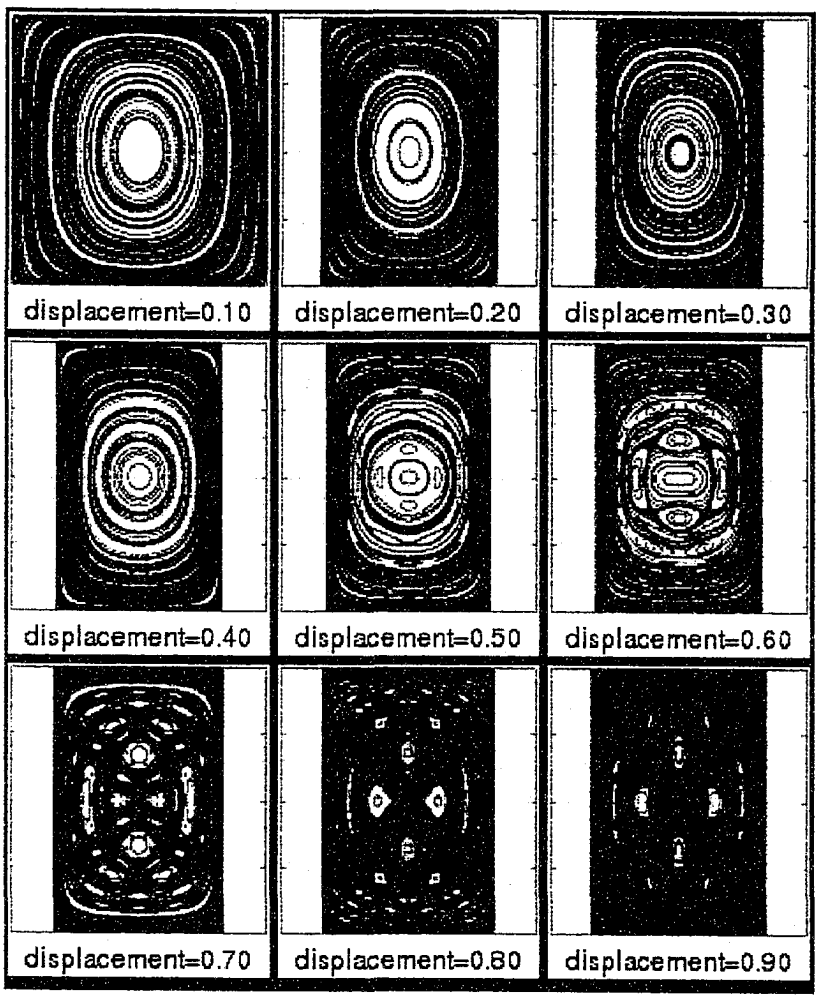

Figure C.5: Poincaré sections for different values of displacement of the Coulomb center. The coulomb constant $\gamma = 0.9$

Appendix D

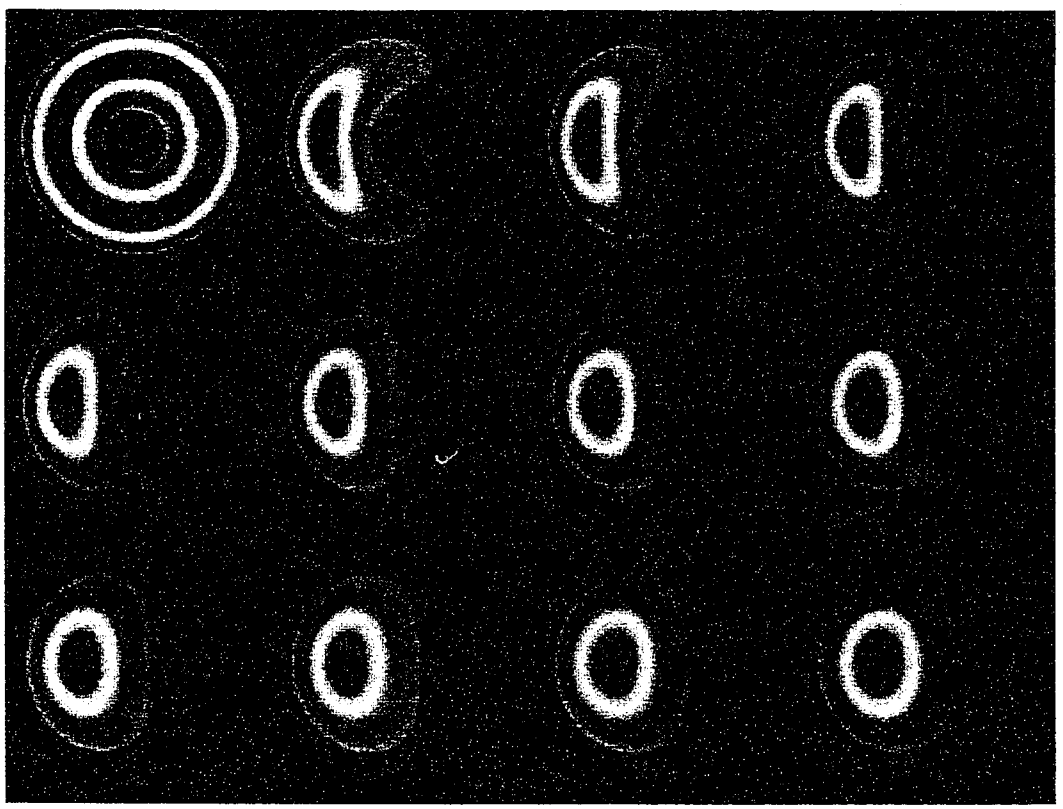

Figure D.1: Wave Functions of ground states for $\alpha = 20$. The values of the displacement of the Coulomb center from the center of the billiard are correspondingly 0.00 0.05 0.10 0.20 0.30 0.40 0.50 0.60 0.70 0.80 0.90 0.99

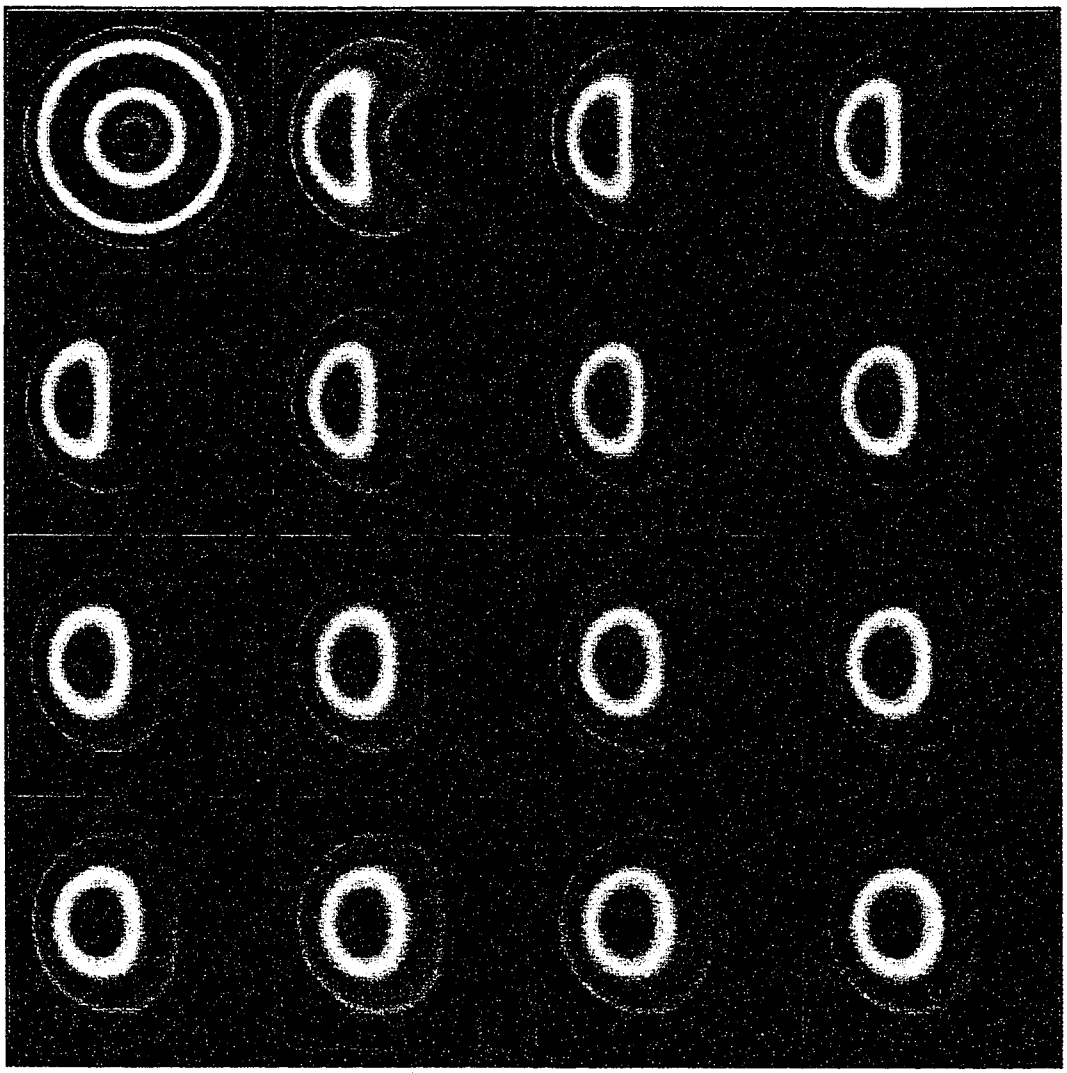

Figure D.2: Wave Functions of ground states for $\alpha = 10$. The values of the displacement of the Coulomb center from the center of the billiard are correspondingly 0.00 0.10 0.15 0.20 0.25 0.30 0.40 0.50 0.60 0.65 0.70 0.75 0.80 0.85 0.90 0.95

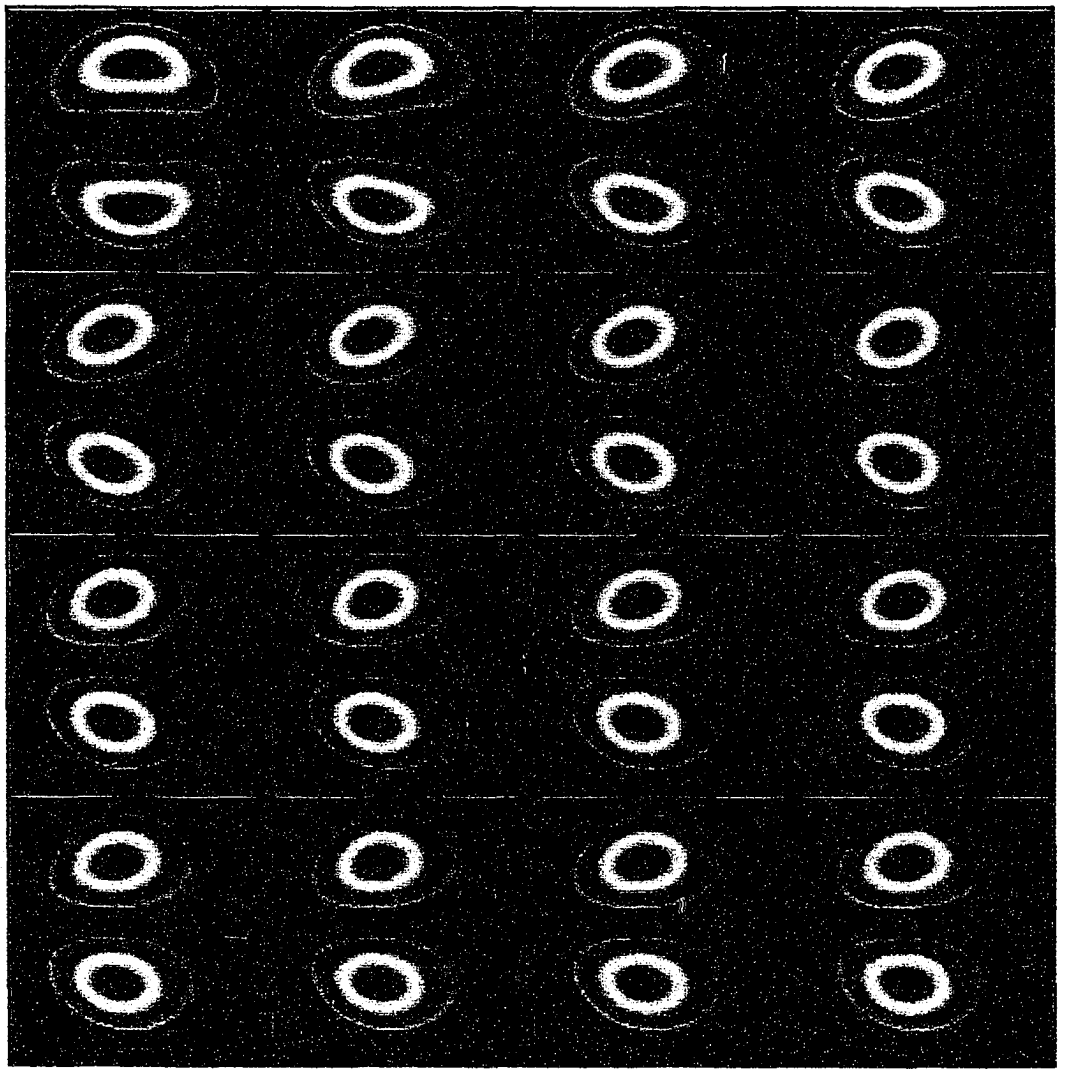

Figure D.3: Wave Functions of first excited states for $\alpha = 10$. The values of the displacement of the Coulomb center from the center of the billiard are correspondingly 0.00 0.10 0.15 0.20 0.25 0.30 0.40 0.50 0.60 0.65 0.70 0.75 0.80 0.85 0.90 0.95

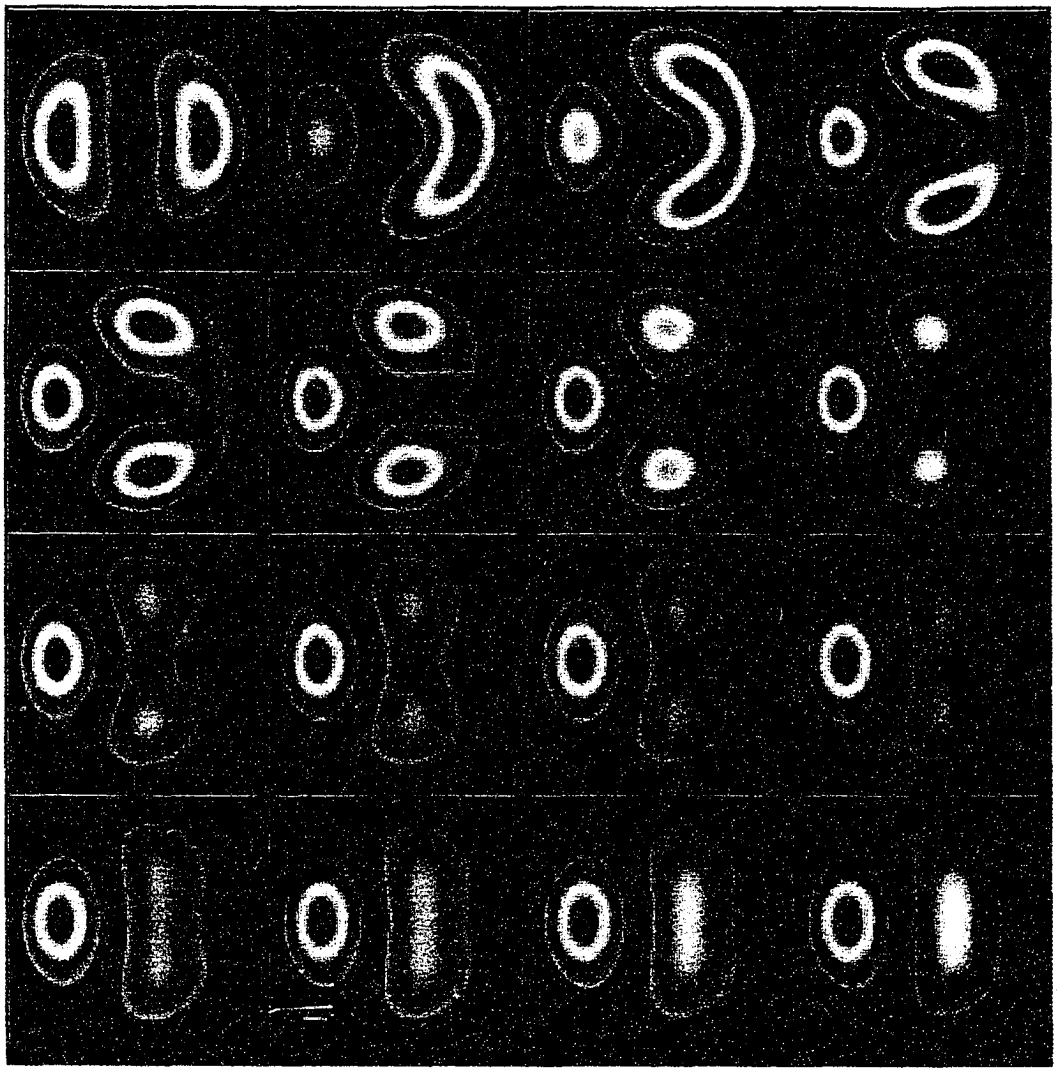

Figure D.4: Wave Functions of second excited states for $\alpha = 10$. The values of the displacement of the Coulomb center from the center of the billiard are correspondingly 0.00 0.10 0.15 0.20 0.25 0.30 0.40 0.50 0.60 0.65 0.70 0.75 0.80 0.85 0.90 0.95

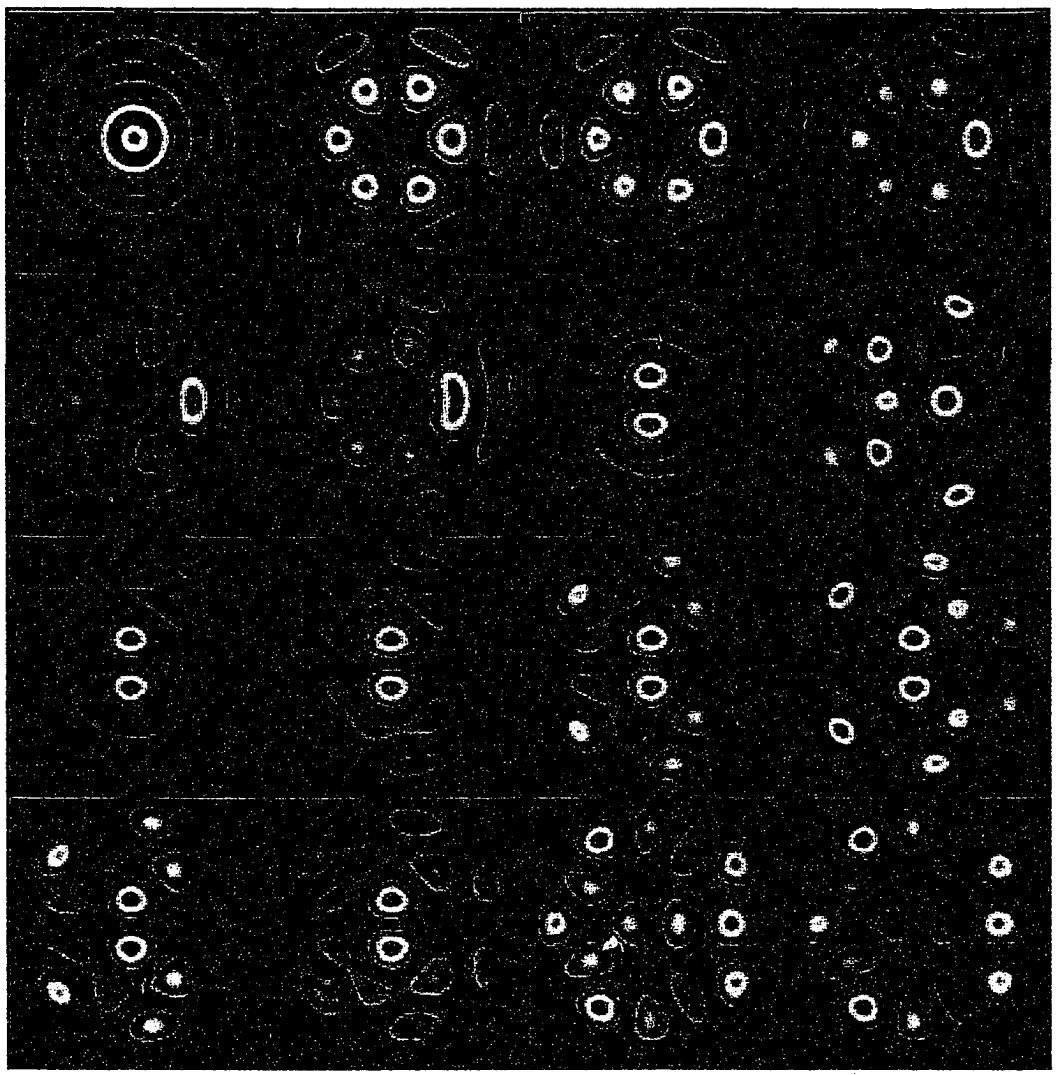

Figure D.5: Wavefunctions of states corresponding in the case with the axial symmetry to the state with the quantum numbers $K = 3$ $M = 0$. The constant of interaction $\alpha = 10$. The values of the displacement of the Coulomb center from the center of the billiard are correspondingly 0.00 0.10 0.15 0.20 0.25 0.30 0.40 0.50 0.60 0.65 0.70 0.75 0.80 0.85 0.90 0.95

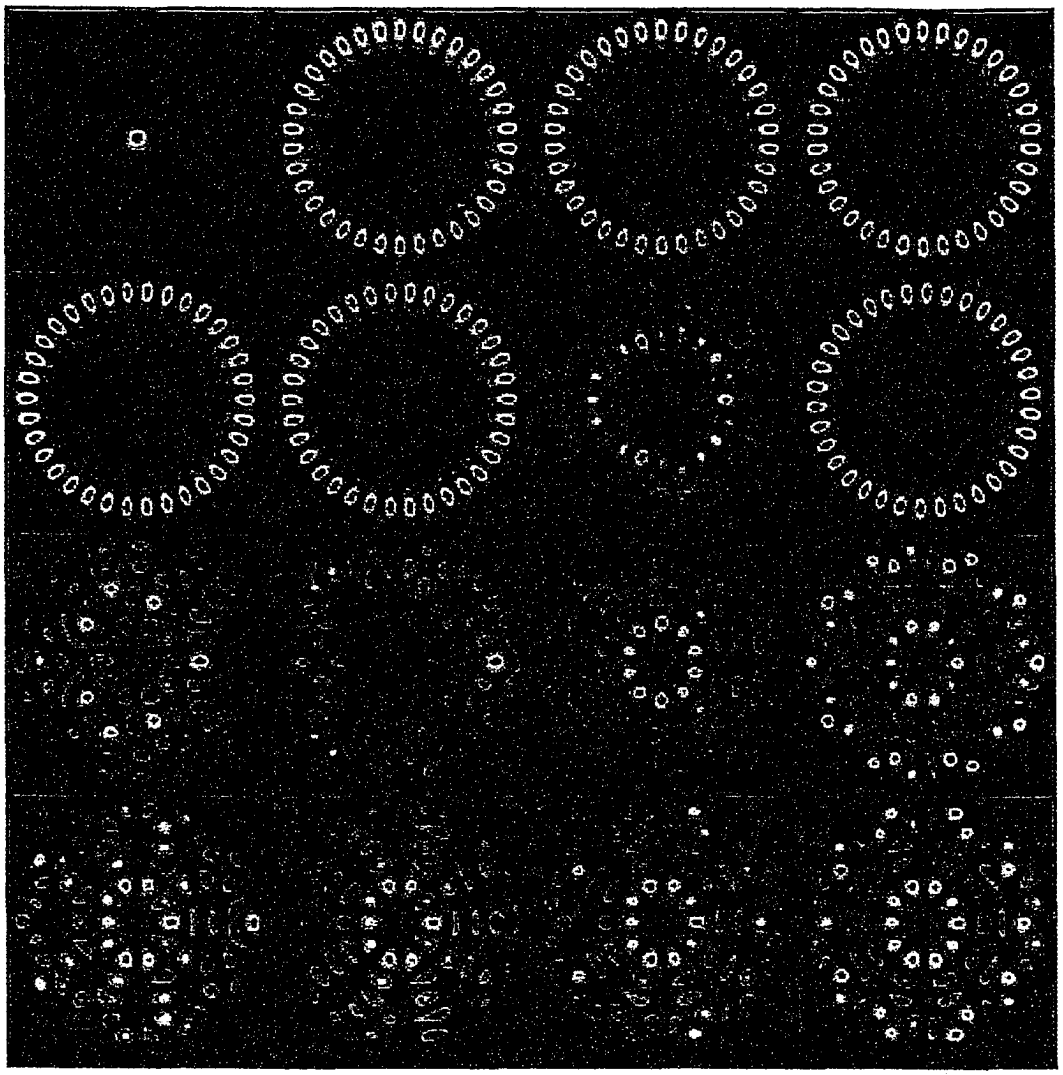

Figure D.6: Wavefunctions of states corresponding in the case with the axial symmetry to the state with the quantum numbers $K = 7$ $M = 0$. The constant of interaction $\alpha = 10$. The values of the displacement of the Coulomb center from the center of the billiard are correspondingly 0.00 0.10 0.15 0.20 0.25 0.30 0.40 0.50 0.60 0.65 0.70 0.75 0.80 0.85 0.90 0.95

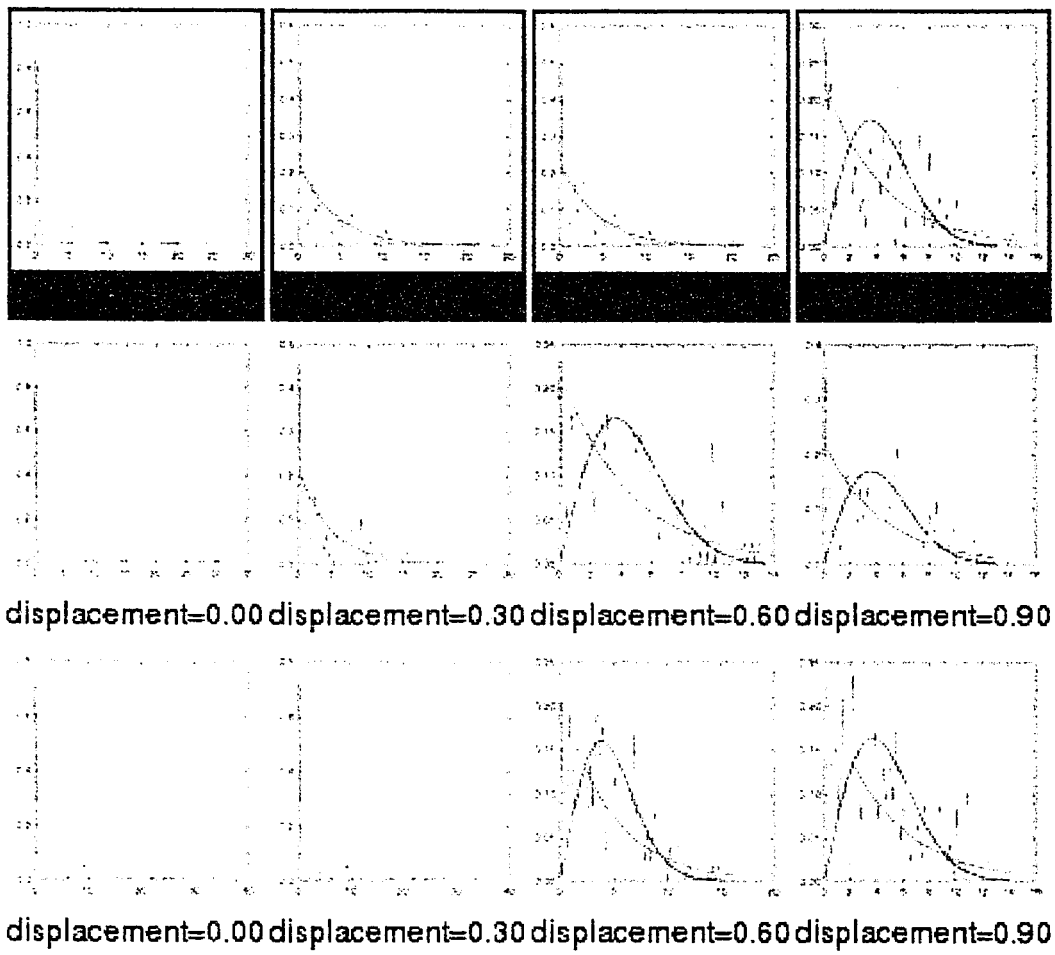

Figure D.7: The histograms of the level-spacing distribution (the red line) of the quantum circular Coulomb billiard. The upper row represents results for the constant of interaction $\alpha = 30$, the middle row corresponds to $\alpha = 60$ and the bottom row for $\alpha = 100$. The green lines given on some of the graphs represens corresponding Poisson distributions, while the blue lines - Wigner's distribution. It can be seen that the energy level distribution tends to Wigner's distribution as the strength of interaction as well as the displacement of the repulsive center is increasing. However, neither of the histograms displays a zero value at the origin which indicates a presence of an uncorrelated part of the energy spectrum.

Bibliography

[1] Abramovitz M. and Stegun A. , Handbook of Mathematical Functions with formulas, graphs and Mathematical tables, Dover Publications, INC., New York 1972.

[2] Arfken G. and Weber H. , Mathematical Methods for Physicists, Fourth Edition, Academic Press LTD., San Diego, California 1995.

[3] Backer A., Schubert R. and Stifter, Rate of quantum ergodicity in Euclidean billiards, Physical Review E, Volume 57, Number 5, pp 5425-5447, 1998.

[4] Baowen Li, Numerical study of scars in chaotic billiards, Physical Review E, Volume 55, Number 5, pp 5376-5379, 1997.

[5] Baranger H. U., Jalabert R. A. and Stone A. D., Weak localization and integrability in ballistic cavities, Physical Review Letters, Volume 25, Number 70, pp 3876-3879, 1993.

[6] Benettin G., Galgani L. and Strelcyn J. M., Kolmogorov entropy and numerical experiments, Physical Review A, Volume 14, Number 6, pp 2338-2345, 1976.

[7] Benettin G. and Strelcyn J. M., Numerical experiments on the free motion of a point mass moving in a plane convex region: Stochastic transition and entropy, Physical Review A, Volume 17, Number 2, pp 773-785, 1978.

[8] Benettin G., Froeschle C. and Scheidecker J. P., Kolmogorov entropy of a dynamical system with an increasing number of degrees of freedom, Physical Review A, Volume 19, Number 6, pp 2454-2460, 1979.

[9] Beresteckii V.B., Lifshitz E.M., Pitaevskii L.P., Relativistic Quantum Theory, Pergamon Press, Oxford, 1971.

[10] Berry M.V., Chaotic Behavior of Deterministic systems, edited by G. Iooss, R. Helleman and R. Stora, North-Holland, Amsterdam, 1983.

[11] Bies W., Kaplan L., Haggerty M., Heller E. R., Localization of eigenfunctions in the stadium billiard, Physical Review E, Volume 63, 066214, 2001.

[12] Bohigas O., Giannoni M.J. and Schmit C., Characterization of Chaotic Quantum Spectra and Universality of Level Fluctuation Law, Physical Review Letters, Volume 52, Number 1, pp 1-4, 1984.

[13] Bunimovich L., Mushrooms and other billiards with divided phase space, American Instite of Physics, Chaos, Volume 11, Number 4, pp 802-808, 2001.

[14] Casartelli M., Diana E., Galgani L. and Scotti A., Numerical computations on a stochastic parameter related to the Kolmogorov entropy, Physical Review A, Volume 13, Number 5, pp 1921-1925, 1976.

[15] Casati G. Quantum Chaos, American Instite of Physics, Chaos, Volume 6, Number 3, pp 391- 399, 1996.

[16] Casati G. and Chirikov B., Quantum Chaos. Between Order and Disorder, Cambridge University Press, 1995.

[17] Casati G., Chirikov B., Izrailev F. anf Ford J., Stochastic Behaviour of a Quantum Pendulum under a Periodic Perturbation, Lecture Notes in Physics, Volume 93, Number 13, 1979.

[18] Casati G. and Chirikov B., Energy-Level Statistics of Integrable Quantum Systems, Physical Review Letters, Volume 54, Number 13, pp 1350-1353, 1985.

[19] Chang A. M., Baranger H. U., Pfeiffer L. N., and West K. W., Weak Localization in Chaotic versus Nonchaotic Cavities: A Striking Difference in the Line Shape, Physical Review Letters, Volume 73, Number 15, pp 2111-2116, 1994.

[20] Cvitanović P., Artuso R., Mainieri R., Tanner G. and Vattay G., Classical and Quantum Chaos, `http://www.nbi.dk/ChaosBook/`, Niels Bohr Institute, Copenhagen 2001.

[21] Crespi B., Perez G. and Chang S., Quantum Poincare sections for two-dimensional billiards, Physical Review E, Volume 47, Number 2, pp 986-991, 1993.

[22] Cucchietti F., Universality of the Lyapunov regime of the Loschmidt echo: Irreversibility, decoherence, and the classical limit. Proceedings of the March Meeting of the American Physical Society, Austin, USA 2003.

[23] Delos J.B., Knudson S.K. and Noid D.W., Trajectories of an atomic electron in a magnetic field, Physical Review E, Volume 30, Number 3, pp 1208-1219, 1984.

[24] Dyson F.J. Journal of Mathematical Physics, Volume 3, page 140, 1962.

[25] Dyson F.J. Journal of Mathematical Physics, Volume 3, page 1191, 1962.

[26] Dyson F.J. and Mehta M.L., Journal of Mathematical Physics, Volume 4, page 489, 1963.

[27] Fishman S. E., Grempel D. R. and Prange R. E., Chaos, Quantum Reccurence, and Anderson Localization, Physical Review Letters, Volume 49, Number 8, pp 509-512, 1982.

[28] Frigo M. and Johnson S., FFTW: An Adaptive Software Architecture for the FFT, `http://www.fftw.org/fftw3_doc/`, ICASSP conference proceedings (vol. 3, pp. 1381-1384) , 1998.

[29] Galassi M., Davies J., Theiler J., Brian G., Jungman G., Booth M., Rossi F., GNU Scientific Library Reference Manual, Second Edition, http://sources.redhat.com/gsl/ref/gsl-ref_toc.html, Network Theory LTD., Bristol, UK 2003.

[30] Goldstein H., Classical Mechanics, Third Edition, Addison-Wesley, San Fransisco, 2002.

[31] Grempel D.R., Prange R.E. and Fishman S.E. Quantum dynamics of a nonintegrable system, Physical Review A, Volume 29, Number 4, pp 1639-1647, 1984.

[32] Gutzwiller M. C., Chaos in Classical and Quantum Mechanics, Springer-Verlag, New York 1990.

[33] Gutzwiller M. C., Quantum Chaos, http://www.maths.ex.ac.uk/mwatkins/zeta/quantumchaos.html, Scientific American, January 1992.

[34] Gutzwiller M. C., Classical Quantization of a Hamiltonian with Ergodic Behavior, Physical Review Letters, Volume 45, Number 3, pp 150-153, 1980.

[35] Gutzwiller M. C., Journal of Mathematical Physics, Volume 12, pp 1791, N.Y. 1971.

[36] Gutzwiller M. C., Journal of Mathematical Physics, Volume 11, p 1791, N.Y. 1970.

[37] Heller E. R., Bound-State Eigenfunctions of Classically Chaotic, Hamiltonian Systems: Scars of Periodic Orbits. Physical Review Letters, Volume 53, Number 16, pp 1515-1518, 1984.

[38] Jackson J. D., Classical Electrodynamics, Second Edition, John Wiley & Sons, INC., New York 1975.

[39] Jensen R. V., Stochastic Ionization of Surface-State Electrons, Physical Review Letters, Volume 49, Number 19, pp 1365-1368, 1982.

[40] Jensen R. V. and Shankar R., Statistical Behavior in Deterministic Quantum Systems with Few Degrees of Freedom, Physical Review Letters, Volume 54, Number 17, pp 1879-1882, 1985.

[41] Jensen R. V., Sanders M. M., Saraceno M. and Sundaram B., Inhibition of quantum transport due to "scars" of unstable periodic orbits, Physical Review Letters, Volume 63, Number 26, pp 2771-2774, 1989.

[42] Kaplan L., Heller E., Measuring scars of Periodic Orbits. Physical Review E, Volume 59, Number 6, pp 6609-6628, 1999.

[43] Kolmogorov A.N., On conservation of conditionally periodic motion for a small change in Hamilton s function, Dokl. Akad. Nauk SSSR, Volume 98, Number 4, pp 525-530, 1954.

[44] Kolmogorov A.N., Dokl. Akad. Nauk SSSR, Volume 119, p. 861, 1958.

[45] Kolmogorov A.N., Dokl. Akad. Nauk SSSR, Volume 124, p. 754, 1959.

[46] Kriecherbauer T., Marklof J. and Soshnikov A. Random matrices and quantum chaos Proceedings of the National Academy of Sciences (USA) Number 98, pp 10531-10532, 2001

[47] Landau, L. D. and Lifschitz, E. M., Mechanics, Third Edition, Oxford, England: Pergamon Press, 1976.

[48] Landau, L. D. and Lifschitz, E. M., The Classical Theory of Fields, Fourth Edition, Oxford, England: Pergamon Press, 1984.

[49] Landau, L. D. and Lifschitz, E. M., Quantum Mechanics (Non-Relativistic Theory), Third Edition, Oxford, England: Pergamon Press, 1977.

[50] Landau, L. D. and Lifschitz, E. M., Statistical Physics, Part 1, Third Edition, Oxford, England: Pergamon Press, 1980.

[51] Landau, L. D. and Lifschitz, E. M., Electrodynamics of Continuous Media, Oxford, England: Pergamon Press, 1984.

[52] Edward Lorenz, The essence of chaos, University of Washington Press 1993.

[53] Kastner M. A., The single electron transistor and artificial atoms, Annals of Physics, Volume 9, pp 885-894, Leipzig 2000.

[54] Kastner M. A., The single electron transistors, Physics Today, Volume 46, 1993.

[55] Lubcke M., Gutzwiller Trace Formula and Application, http://www.teorfys.uu.se/courses/exjobb/gutz.pdf, University of Uppsala, Sweden 2001.

[56] Marcus C. M., Rimberg A. J., Westervelt R. M., Hopkins P. F. and Gossard A. C., Conductance fluctuations and chaotic scattering in ballistic microstructures, Physical Review Letters, Volume 69, Number 3, pp 506-510, 1992.

[57] J. Marklof, Level spacing statistics and integrable dynamics, Proceedings of the XIIIth International Congress on Mathematical Physics, London 2000 (International Press, Boston, 2001), pp 359-363

[58] McDonald W. and Kaufman A., Wave chaos in stadium: Statistical properties of short-wave solutions of the Helmholtz equation. Physical Review A, Volume 37, Number 8, pp 3067-3086, 1988.

[59] Merzbacher E., Quantum Mechanics, Third Edition, John Wiley & Sons, INC., New York 1998.

[60] Meirav U., Kastner M. A., and Wind S. J., Single-electron charging and periodic conductance resonances in GaAs nanostructures, Physical Review Letters, Volume 65, pp 771-774, 1990.

[61] Moore F., Robinson J., Bharucha C., Sundaram B. and Raizen M., Atom Optics Realization of the Quantum $\delta-$Kicked Rotor, Physical Review Letters, Volume 75, Number 25, pp 4598-4602, 1995.

[62] Nakamura K. and Thomas H., Quantum Billiard in a Magnetic Field: Chaos and Diamagnetism, Physical Review Letters, Volume 61, Number 3, pp 247-250, 1988.

[63] Narimanov E. and Podolskiy V., Level Splitting Distribution in Chaos-Assisted Tunneling, Proceedings of the March Meeting of the American Physical Society, Austin, USA 2003.

[64] Peres A., Instability of Quantum Motion od a Chaotic System, Chaos and Quantum Chaos, Proceedings of the Adriatico Research Conference on Quantum Chaos, World Scientific, Singapore, 1991.

[65] Peres A., Chaotic Evolution in Quantum Mechanics, `http://arxiv.org/list/nlin.CD`, Department of Physics, Technion - Israel Institute of Technology, Israel 1995.

[66] Peres A. and Terno D., Evolution of Liouville density of a chaotic system, `http://arxiv.org/list/nlin.CD` Department of Physics, Technion - Israel Institute of Technology, Israel 1995.

[67] Piesin Y. G., Math. Dokl., Volume 17, p 196, 1976.

[68] Press W., Teukolsky S., Vetterling W., Flannery B., Numerical Recipes in C, The Art of Scientific Computing, Second Edition, Cambridge University Press, New York 2002.

[69] Raizen M.G., Koga G., Sundaram B., Kishimoto Y., Takuma H. and Tajima T., Stochastic cooling of atoms using lasers, Physical Review A, Volume 58, Number 6, pp 4757-4760, 1998.

[70] Raithel G., Fauth M. and Walther H., Quasi-Landau resonances in the spectra of rubidium Rydberg atoms in strong crossed electric and magnetic fields, Physical Review A, Volume 49, Number 3, pp 1646-1665, 1994.

[71] Raithel G. and Walther H., Ionization energy of rubidium Rydberg atoms in crossed electric and magnetic fields, Physical Review A, Volume 44, Number 3, pp 1898-1909, 1991.

[72] Reichl L.E., The Transition to Chaos in Conservative Systems: Quantum Manifestations, Springer-Verlag, Berlin 1992.

[73] Raichl L.E. and Zheng W.M., Field-induced barrier penetration in the quartic potential, Physical Review A, Volume 29, Number 4, pp 2186-2193, 1984.

[74] Raichl L.E. and Zheng W.M., Perturbed double-well system: The pendulum approximation and low-frequency effects, Physical Review A, Volume 30, Number 2, pp 1068-1077, 1984.

[75] Rihter K., Semiclassical Theory of Mesoscopic Quantum Systems, Springer-Verlag, Berlin 2000.

[76] Robnik M. and Berry M., Classical Billiards in magnetic fields, Journal of Physics A: Mathematical and General, Volume 18, pp 1361-1378, 1985.

[77] Robnik M., Regular and chaotic billiard dynamics in magnetic fields, In S. Sakar, editor, Nonlinear Phenomena and Chaos, pp 303-330. Adam Hilger, 1986.

[78] Shepelyansky D.L., Some statisticla propertiesof Simple Classically Stochastic Quantum Systems, Physica D, Volume 8, pp 208-222, 1983.

[79] Simonotti F. P., Vergini E. and Saraceno M., Quantitative study of scars in the boundary section of the stadium billiard Physical Review E, Volume 56, Number 4, pp 3859-3867, 1997.

[80] Sinai Y. G., Sov. Math. Dokl., Volume 4, p 1818, 1963.

[81] Solovyov E.A., Journal of Experimental and Theoretical Physics, Volume 82, page 1762, Soviet Union 1982.

[82] Solovyov E.A., Journal of Experimental and Theoretical Physics, Volume 85, page 109, Soviet Union 1983.

[83] Solovyov E.A. and Braun P.A., Journal of Experimental and Theoretical Physics, Volume 86, page 68, Soviet Union 1984.

[84] Steck D., Classical and Quantum Chaos, Lecture Notes for 2002 Los Alamos Summer School, Los Alamos 2002.

[85] Steck D., Quantum Chaos, Transport, and Decoherence in Atom Optics, Ph. D. Dissertation, The University of Texas at Austin, 2001.

[86] Suhan Ree and Reichl L., Classical and quantum chaos in a circular billiard with a straight cut, Physical Review E, Volume 60, Number 2, pp 1607-1615, 1999.

[87] Sundaram B. and Zaslavsky G. M., Wave analysis of ray chaos in underwater acoustics, American Instite of Physics, Chaos, Volume 9, Number 2, pp 483-492, 1999.

[88] Sundaram B. and Zaslavsky G. M., Anomalous transport and quantum-classical correspondence, Physical Review E, Volume 59, Number 6, pp 7231-7234, 1999.

[89] Tabor M., Chaos and integrability in nonlinear dynamics, John Wiley & Sons, INC., New York 1989.

[90] Weiss D., Richter K., Menschig A., Bergmann R., Schweizer H., Von Klitzing K. and Winmann G., Quantized periodic orbits in large antidot arrays, Physical Review Letters, Volume 70, Number 26, pp 4118-4121, 1993.

[91] Weiss, D., Lutjering, G., Richter, K., Chaotic Electron Motion in Macroscopic and Mesoscopic Antidot Lattices, Chaos, Soliton & Fractals, Volume 8, Number 7, pp 1337-1357, 1997.

[92] Wunner G., Woelk U.,Zech I., Zeller G., Ertl T., Geyer F., Schweitzer W. and Ruder H, Rydberg Atoms in Uniform Magnetic Fields: Uncovering the Transition from Regularity to Irregularity in a Quantum System, Physical Review Letters, Volume 57, Number 26, pp 3261-3264, 1986.

[93] Zaslavsky G.M., Stochasticity of Dynamic Systems, Nauka, Moscow, USSR 1984.

[94] Zaslavsky G.M., Chaos in Dynamic Systems, Harwood Academic Publishers, NY 1985.

[95] Zaslavsky G.M., From Hamiltonian chaos to Maxwell's Demon, American Instite of Physics, Chaos, Volume 5, Number 4, pp 653-661, 1995.

[96] Zaslavsky G.M., Chaotic Dynamics and the Origin of Statistical Laws, American Instite of Physics, Physics Today, August 1999, pp 39-45.

[97] Zaslavsky G.M., Edelman M. and Niyazov B.A.,, Self-similarity, renormalization, and phase space nonuniformity of Hamiltonian chaotic dynamics, American Instite of Physics, Chaos, Volume 7, pp 159-181, 1997.

[98] Zurek W.H. and Paz J.P., Decoherence, Chaos and the Second Law, Physical Review Letters, Volume 72, Number 16, pp 2508-2512, 1994.